Characterization of novel anti-EGFR single domain antibodies and their application in active targeting of superparamagnetic iron oxide nanoparticles to glioblastoma.

Ulrike Trojahn, MSc

Department of Biochemistry

McGill University, Montreal

January 2012

A thesis submitted to McGill University in partial fulfillment of the requirements of the degree of Doctor in Philosophy.

Acknowledgements

First and foremost I would like to thank my supervisor Dr. Maureen O'Connor-McCourt for her trust and confidence that she has put into my work over the past five years. I would also like to thank her for giving me the opportunity to travel to numerous Nanotechnology conferences to discuss my research with experts in the field. Her optimism and humor, as much as her profound scientific knowledge, have constantly been an inspiration. Furthermore, I would like to thank all the members of the O'Connor lab for their suggestions, discussions, collegiality and invaluable expertise. Particularly, I'm grateful to Maria for the smooth start back in 2006, as well as to her and Myriam for sharing their expertise in cell-based assays, to Beatrice for the crash-course in protein purification, to Cathy for everything she taught me about cloning, to Jason for turning me into a Biacore expert (or so I'd like to think), to Suzanne for great office companionship, and last but certainly not least to Anne for keeping me calm during the animal study.

I would also like to thank my RAC members, Dr Arnim Pause and Dr Kalle Gehring for allowing me to tap into their brains at our meetings, always providing me with many fresh thoughts and ideas. Many thanks also to my collaborators at the IBS-NRC in Ottawa, Umar Iqbal, Abdelnasser Abulrob (Naz), and Roger MacKenzie and their colleagues for their scientific contributions.

I would like to give special thanks to Dr. Barry Bedell for exploring out into the world of MRI phantom studies. I furthermore would like to thank Dr Traian Sulea for the critical reading of my manuscript, his challenging questions and generous feedback.

I thank CIHR for financial support of this project. Special thanks also to the Department of Biochemistry for the many discussion opportunities to discuss with scientific leaders, the two travel awards and especially to Dr Dave Thomas, Christine Laberge and Maureen Caron for their help when it was most needed.

Contributions

CHAPTER 2 – Characterization of single domain antibodies

Ulrike Trojahn conducted all Biacore and cell line experiments. Specifically, she characterized a panel of sdAbs (four monomeric, two bivalent and one pentavalent) against EGFR using surface plasmon resonance (SPR) and flow cytometry; investigated the effect of sdAb binding to cells by Western Blot and in a three-day growth assay; determined the affinity of monomeric and dimeric EG2 sdAbs on U87MG glioblastoma cells over-expressing EGFR in a competition binding assay with radio-labeled EG2; carried out confocal microscopy experiments to determine cell binding profiles and subcellular localization of two dimeric sdAbs (EG2-hFc and EG10-hFc) on three glioblastoma and one breast cancer cell line; and determined the specificity of two single domain antibodies for their targets in a cross-linking experiment with radio-labeled sdAbs on the glioblastoma cell line panel.

Dr Roger MacKenzie and colleagues provided the expressed proteins of the four monomeric single domain antibodies (sdAbs), as well as the bivalent and pentavalent constructs. They furthermore generated the plasmid of the EG2 sequence containing the additional cysteine at the C-terminus. Suzanne Grothe iodinated the sdAbs. Professor Maureen O'Connor, Dr Maria Jaramillo and Dr Jason Baardsnes oversaw the work.

CHAPTER 3 – EGFR-targeted nanoparticles

Ulrike Trojahn developed the nanoparticle conjugation strategy and carried out all experiments with the exception of the phantom MRI study, which was done by Professor Barry Bedell at the MNI. During the *in vivo* imaging study U. T. assisted Dr Anne Lenferink, who carried out the injections of tumor cells into nude mice, the tumor measurements, the preparation of animals for imaging, and

the image acquisition. U. T. did the planning and evaluation of the imaging study. Professor Maureen O'Connor oversaw the work.

Specifically, U. T. developed a purification strategy for particle conjugation; characterized iron oxide nanoparticles from commercial and non-commercial sources by dynamic light scattering and zeta potential measurements; carried out cytotoxicity assays on a panel of four cell lines representing target and non-target tissues; characterized the degree of surface amino-functionalization using the fluorescamine assay; characterized and tested polyethylene glycol (PEG) conjugation conditions using different commercially available PEG spacers and using varying stoichiometries and conjugation buffer conditions; carried out the expression, production and purification of EG2cys protein; conjugated the sdAb to the iron oxide nanoparticles and investigated nanoparticle binding to glioblastoma cells using confocal microscopy and SPR biosensor technology; prepared all conjugated nanoparticle samples used in the *in vivo* distribution study; and subsequently assisted in the mouse optical imaging study.

CHAPTER 4 - Thermodynamic analysis

Ulrike Trojahn performed all SPR experiments and carried out the data analysis. Professor Maureen O'Connor-McCourt and Dr Jason Baardsnes oversaw the work. Dr Traian Sulea helped with the interpretation of the results.

Abstract

Glioblastoma multiforme is the most lethal primary brain tumor with a mean patient survival of 12 - 15 months. The Canadian Cancer Society estimates that there are 2500 new cases of brain cancer every year in Canada. Compared to other solid tumors, efforts to treat glioblastoma with chemotherapeutics or radiation therapy have been largely ineffective, which is why the current treatment paradigm is predominantly based on surgery. Herein, it has been shown that the extent of surgical resection is correlated with patient outcome, i.e. less residual cancer cells result in a prolonged time to recurrence.

In glioblastoma patients, magnetic resonance imaging (MRI) is used in diagnosis, MRI-guided surgery, and monitoring of disease progression. Superparamagnetic iron oxide nanoparticles (IONPs) are currently receiving increased attention as MRI contrast agents for brain imaging. Their reported proton relaxation properties, biocompatibility, and retention times are superior to the commonly employed gadolinium-based contrast agents. In addition, their larger surface area allows for the conjugation of targeting moieties and/or labels used for multi-modal imaging (e.g. fluorophores, radioisotopes).

One of the most frequent genetic alterations in primary glioblastoma involves the epidermal growth factor receptor (EGFR). EGFR belongs to the ErbB family of receptor tyrosine kinases, whose members are crucially involved in the regulation of signaling pathways that control cell proliferation, differentiation, survival, and angiogenesis. EGFR over-expression due to gene amplification is observed in 50 - 71% of the patients and among these the simultaneous expression of EGFR mutants is frequently seen. The most common mutation is the deletion of exon 2 – 7 of the extracellular domain, which results in ligand-independent, constitutive activation of the intracellular kinase domain. This mutant is named EGFRvIII and has been intensely investigated as potential therapeutic target, since it is considered a tumor-specific antigen,

The objective of this project is to develop EGFR-targeted IONPs to improve the delineation of tumor outlines through targeted delivery of this MRI contrast agent to tumor cells. In addition, dual-labeling of the nanoplatform with near infrared fluorescent probes is expected to permit intra-operative optical imaging of infiltrative tumor cells, thereby decreasing the number of residual cancer cells left after surgical resection. To date antibodies have been the most successful targeting ligands and several immunoconjugates are already approved for molecular imaging in humans. However, small overall size (<100 nm) of the nanoparticle is crucial for achieving extended blood circulation times and high tumor penetration. Therefore, the use of smaller antibody fragments instead of the entire immunoglobulin molecule is preferred.

In this study, I characterized novel anti-EGFR single domain antibodies (sdAbs) for their application as targeting moieties for nanoparticulate contrast agents. I determined the specificity and binding kinetics of these sdAbs for their targets EGFR and EGFRvIII using surface plasmon resonance (SPR) biosensor analysis and cell-based assays. I then conjugated the sdAbs to the surface of commercial IONPs and, after thorough investigation of the physical properties, I tested the tumor-targeting ability of these immuno-IONPs in a glioblastoma xenograft model. My findings are in agreement with published observations on the *in vivo* distribution of targeted superparamagnetic iron oxide nanoparticles.

Modern SPR biosensors also allow the assessment of not only the binding affinity and kinetics, but also the thermodynamic parameters of protein-protein interactions. I therefore extended the use of this technology to study the interaction of a selected anti-EGFR sdAb with the extracellular domain of EGFR (EGFR-ECD), and compared this to binding of its natural ligand, the epidermal growth factor (EGF). I demonstrate that distinct thermodynamic driving forces govern sdAb and ligand binding to EGFR-ECD. My findings complement the available structural information and provide new insight into potential mechanisms of EGF-mediated receptor activation.

Resumé

Le glioblastome multiforme est la tumeur primaire du cerveau la plus mortelle avec un taux de survie moyen des patients de 12 – 15 mois. La Société canadienne du cancer estime qu'il y a 2500 nouveaux cas de cancer du cerveau chaque année au Canada. Comparés à d'autres tumeurs solides, les efforts pour traiter le glioblastome avec de la radiothérapie ou des agents chimiothérapeutiques ont été largement inefficaces, ce qui explique pourquoi le paradigme de traitement actuel est avant tout basé sur la chirurgie. Ici, il a été démontré que l'étendue de la résection chirurgicale est corrélée avec le pronostic des patients, c'est-à-dire, moins des cellules cancéreuses résiduelles mènent à une récidive plus tardive.

Chez les patients de glioblastome, l'imagerie par résonance magnétique (IRM) est utilisée dans le diagnostic, durant la chirurgie guidée par IRM, et pour le suivi de la progression de la maladie. Les nanoparticules superparamagnétiques d'oxyde de fer (IONPs) reçoivent actuellement une attention accrue comme agents de contraste en IRM pour l'imagerie cérébrale. Leurs propriétés de relaxation des protons, leur biocompatibilité et leur temps de rétention sont supérieurs aux agents de contraste à base de gadolinium couramment employée. En outre, leur surface plus grande permet la conjugaison des agents de ciblage et/ou étiquettes utilisées pour l'imagerie multimodale (par exemple, des fluorophores ou des radio-isotopes).

Une des altérations génétiques les plus fréquentes dans le glioblastome primaire implique le récepteur du facteur de croissance épidermique (EGFR), sa surexpression dû à l'amplification du gène est observée dans 50 – 71% des patients et parmi ceux-ci l'expression simultanée de mutants EGFR est fréquemment observé. L'EGFR appartient à la famille ErbB des récepteurs tyrosine kinases, dont les membres sont crucialement impliqués dans la régulation des voies de signalisation qui contrôlent la prolifération cellulaire, la différenciation, la survie et l'angiogenèse.La mutation la plus fréquente est la délétion de l'exon 2 – 7 de domaine extracellulaire, ce qui rend le EGFR

insensible au ligand, et mène à l'activation constitutive de la kinase intracellulaire. Ce mutant est connu sous le nom EGFRvIII, et puisqu'il est considéré comme un antigène spécifique de ce type de tumeur, il a donc été intensément étudié comme cible thérapeutique potentielle.

L'objectif de ce projet est de développer des IONPs spécifiques pour l'EGFR afin d'améliorer la délimitation des contours de la tumeur grâce à l'administration d'agents de contraste IRM ciblée vers les cellules tumorales. En outre, le double-étiquetage de cette nanoplateforme avec des sondes fluorescentes proche infrarouge permettra l'imagerie optique intraopératoire des cellules tumorales infiltrantes aidant à une résection chirurgicale plus précise et ainsi diminuant le nombre de cellules cancéreuses résiduelles après l'opération. À ce jour, les anticorps ont été les ligands de ciblage les plus efficaces et plusieurs immunoconjugués sont déjà approuvés pour l'imagerie moléculaire chez les humains. Cependant, la petite taille globale (<100 nm) de la nanoparticule permet d'atteindre une circulation sanguine prolongée et une pénétration tumorale élevée. Par conséquent, l'utilisation de fragments d'anticorps plus petits au lieu de la molécule d'immunoglobuline entière est préférée.

Dans cette étude, j'ai caractérisé des fragments d'anticorps contre l'EGFR (anticorps à domaine unique) pour leur application comme unité de ciblage et pouvant potentiellement servir comme agents de contraste nanoparticulaire. J'ai déterminé par résonance plasmonique de surface (SPR) et dans des tests cellulaires la spécificité et la cinétique de liaison de ces anticorps à domaine unique pour leurs cibles EGFR ainsi que pour le mutant EGFRvIII. J'ai ensuite conjugué ces anticorps à domaine unique sur la surface de IONPs commerciales et, après analyse approfondie de leurs propriétés physiques, j'ai testé la capacité de ciblage tumoral de ces immuno-IONPs dans un modèle de xénogreffe de glioblastome. Mes conclusions sont en accord avec les observations publiées sur la distribution *in vivo* des nanoparticules superparamagnétiques d'oxyde de fer ciblés.

Les biocapteurs SPR modernes permettent également la détermination des paramètres thermodynamiques pour les interactions protéine-protéine. J'ai donc

utilisé cette technologie pour étudier l'interaction d'un anticorps à domaine unique contre l'EGFR avec le domaine extracellulaire de l'EGFR (EGFR-ECD) en comparaison à la liaison avec son ligand naturel, le facteur de croissance épidermique (EGF). J'ai démontré que des forces motrices thermodynamiques distinctes conduisent l'interaction d'EGFR-ECD avec l'anticorps en comparaison d'avec le ligand. Mes conclusions sont en accord avec les informations structurelles disponibles et fournissent un nouvel éclairage sur les mécanismes potentiels de l'activation du récepteur par l'EGF.

Table of Contents

Acknowledgements ii

Contributions iii

Abstract v

Resumé vii

Table of Contents x

List of Tables xiii

List of Figures xiv

Abbreviations xvi

1 Introduction 1

1.1 Glioblastoma multiforme: disease state and treatment options. 1
1.2 The use of magnetic resonance imaging in GBM patients 3
1.3 Superparamagnetic iron oxide nanoparticles as emerging contrast agents for brain tumor imaging. 6
1.4 Tumor cell-targeted IONP contrast agents. 11
1.5 Single domain antibodies as targeting moieties for the systemic delivery of nanoparticles. 13
1.6 Dysregulation of the epidermal growth factor receptor in GBM patients. 20
1.7 Over-expressed EGF-receptors as molecular targets for the delivery of contrast agents to brain tumors 24
1.8 Short summary of the objective of my thesis project 26

2 Characterization of novel anti-EGFR single domain antibody fragments. 28

2.1 Introduction to surface plasmon resonance 28
2.2 Experimental Procedures 35
2.3 Results 41
2.3.1 Protein size and purity 41
2.3.2 Biacore SPR biosensor analysis 42
2.3.3 Cell-based assays 47
2.4 Discussion 56
2.4.1 Physical and structural properties of the novel sdAbs 57
2.4.2 Determination of binding kinetics of four novel sdAbs 59
2.4.3 Epitope mapping 62
2.4.4 Multimerization of single domain antibodies 63
2.4.5 Cell binding studies 66

2.4.6 Confocal microscopy 68
2.4.7 The effect of EG2 on EGFR receptor activation and cell growth 73
2.5 Conclusion 74
2.6 Publications 77

3 Development and characterization of EGFR-targeted iron oxide nanoparticles. 105

3.1 Introduction 105
3.1.1 Nanotechnology and the emerging field of nanomedicine 105
3.1.2 Synthesis and surface modifications of long-circulating IONPs 108
3.1.3 Bimodal imaging 110
3.1.4 The journey of a nanoparticle: from injection site to tumor 111
3.1.5 Delivery across the blood brain barrier 113
3.2 Experimental Procedures 115
3.3 Results 121
3.3.1 Conjugation strategy 121
3.3.2 Characterization of EG2cys 123
3.3.3 Characterization of commercial IONPs 125
3.3.4 Production and characterization of EGFR-targeted IONPs 128
3.3.5 U87MG.EGFR binding study of fluorescently-labeled IONPs demonstrated batch-dependent diversity 130
3.3.6 *In vivo* distribution study 132
3.4 Discussion 133
3.4.1 EG2cys for oriented conjugation to the nanoparticle surface 133
3.4.2 Commercial iron oxide nanoparticles – physical properties 135
3.4.3 Cytotoxicity study 138
3.4.4 Cell binding studies 140
3.4.5 *In vivo* distribution of targeted EG2-IONP-680 and non-targeted IONP-680 148
3.5 Conclusion 155
3.5.1 Future outlook 158

4 Thermodynamic analysis of EGFR extracellular domain binding to EGF versus binding to EG2 sdAb. 175

4.1 Introduction 175
4.1.1 Ligand-mediated receptor activation 177
4.1.2 Investigation of thermodynamic parameters using SPR biosensors 180
4.1.1 Ionic strength effects 182
4.2 Experimental procedures 183
4.3 Results 185
4.3.1 Kinetic analysis of EGFR-ECD/hEGF and EGFR(vIII)-ECD/EG2 interactions showed that these systems can be described by a simple bimolecular binding model. 185
4.3.2 Thermodynamic analysis of EGFR-ECD/hEGF and EGFR(vIII)-ECD/EG2 binding revealed that opposing thermodynamic forces are driving the receptor-ligand and the receptor-antibody interaction. 188
4.3.3 Ionic strength effects on the EGFR-ECD/hEGF and EGFR-ECD/EG2 interactions indicate a low degree of electrostatic steering 189
4.4 Discussion 190

4.4.1 Kinetic Analysis 190
4.4.2 Thermodynamic Analysis 193
4.4.3 Analysis of the EGFR-ECD/hEGF and EGFR-ECD/EG2 interactions demonstrates minor contributions of long-range electrostatic forces to complex formation 196
4.5 Conclusions 202
References 214

List of Tables

Table 1. Kinetic parameters for single domain antibody binding to immobilized recombinant EGFR and EGFRvIII extracellular domains. 80
Table 2. Overview of experiments carried out on the different nanoparticle batches..... 162
Table 3. Kinetic data derived from Langmuir fitting of SPR data for EGFR-ECD/rhEGF, EGFR-ECD/EG2 sdAb and EGFRvIII-ECD/EG2 sdAb interactions. 204
Table 4. Calculated thermodynamic parameters for the EGFR-ECD/hEGF, EGFR-ECD/EG2 and EGFRvIII-ECD/EG2 interactions obtained from linear van't Hoff analysis. 205
Table 5. Kinetic data obtained from the analysis of ionic strength dependence. 206

List of Figures

Figure 2-1. Analysis of purified proteins by SDS-PAGE. 81
Figure 2-2. Analysis of protein purity by dynamic light scattering (DLS). 82
Figure 2-3. Biacore analysis of single domain antibody binding to immobilized recombinant EGFR extracellular domain. 83
Figure 2-4. Biacore analysis of single domain antibody binding to recombinant EGFRvIII extracellular domain. 84
Figure 2-5. Comparison of sensorgrams obtained for the four sdAbs binding to EGFR-ECD and EGFRvIII-ECD. 85
Figure 2-6. Epitope mapping of single domain antibodies on EGFR-ECD. 86
Figure 2-7. Analysis of thermal stability of EG2 sdAb. 87
Figure 2-8. Biacore sensorgrams for monovalent and multivalent antibody constructs binding to the same EGFR-ECD chip surface. 88
Figure 2-9. Biacore sensorgrams showing the interaction of EG2, EG2-hFc and V2C-EG2 to immobilized EGFRvIII-ECD. 89
Figure 2-10. Comparison of rate constants measured for the interactions of monovalent and bivalent sdAb constructs on three different EGFR-ECD sensor chip surfaces. 90
Figure 2-11. Biacore analysis of the interaction of EGFR-ECD with immobilized EG2, EG2-hFc and V2C-EG2 91
Figure 2-12. Competition of EG2 sdAb constructs binding to EGFR extracellular domain 92
Figure 2-13. Biacore analysis of EGFR-ECD and EGFRvIII-ECD binding to immobilized 225 monoclonal antibody. 93
Figure 2-14. SPR biosensor epitope mapping experiment for EG2 and 225 binding to EGFR-ECD. 94
Figure 2-15. Analysis of sdAb binding to cell surface-expressed EGFR and EGFRvIII 95
Figure 2-16. Flow cytometry analysis of monovalent and multivalent anti-EGFR antibodies binding to the U87MG cell line panel. 96
Figure 2-17. Affinity labeling of cell surface expressed EGF-receptors using [^{125}I]-EG2 and [^{125}I]-EG10. 97
Figure 2-18. Competition binding assay with radiolabeled [^{125}I]-EG2 on EGF receptor over-expressing cell lines. 98
Figure 2-19. Confocal microcopy images of total EGF receptors on fixed cells from the U87MG cell line panel. 99
Figure 2-20. Comparative confocal analysis using EG2-hFc and 225 to label U87MG.EGFR and U87MG.EGFRvIII cells. 100
Figure 2-21. Confocal microscopy - colocalization experiment. 101
Figure 2-22. Confocal microscopy - EG2-hFc internalization study. 102
Figure 2-23. Western Blot of EGFR phosphorylation status. 103

Figure 2-24. Viability assay on the U87MG cell line panel treated with mono- and multivalent single domain antibody constructs..... 104
Figure 3-1 Nanoparticle conjugation scheme. 163
Figure 3-2 Production and purification of EG2-PEG. 164
Figure 3-3. Comparison of the physical properties of Ocean NanoTech and Genovis nanoparticles with amine surface functionalization. 165
Figure 3-4. Determination of Ocean NanoTech nanoparticle stability. 166
Figure 3-5. Conjugation of EG2cys to Ocean NanoTech IONPs. Determination of conjugation efficiency and changes in physical properties of the IONPs upon sdAb attachment. 167
Figure 3-6. Confocal microscopy images of U87MG.EGFR cells labeled with targeted and non-targeted IONPs. 168
Figure 3-7. Confocal microscopy images of fixed and permeabilized U87MG.EGFR cells labeled with targeted and non-targeted IONPs from different nanoparticle batches 169
Figure 3-8 Comparison of different batches of Ocean NanoTech IONPs. 170
Figure 3-9. *In vivo* distribution of targeted and non targeted IONP. 172
Figure 3-10. *Ex vivo* fluorescence imaging of organs and tumor tissue. 173
Figure 3-11. Schematic illustrating the potential charge interactions occurring on the surface of EG2-conjugated Ocean NanoTech iron oxide nanoparticles. 174
Figure 4-1. SPR biosensor analysis. 207
Figure 4-2. Temperature dependence of the EGFR-ECD/hEGF and EGFR-ECD/EG2 sdAb interactions 208
Figure 4-3. Temperature dependence of kinetic rate constants measured for the receptor-ligand and receptor-antibody interactions. 209
Figure 4-4. Linear van'Hoff plot assuming a temperature-independent ΔH. 210
Figure 4-5. Eyring plots. 211
Figure 4-6. Graphical representation of transition state energies at 25°C derived from the van'Hoff and Eyring analyses. 212
Figure 4-7. Ionic strength dependence of the association rate constants (k_a). 213

Abbreviations

ADCC	Antibody-dependent cell-mediated cytotoxicity
ApoE	Apolipoprotein E
BBB	Blood brain barrier
bp	Base pairs
BSA	Bovine serum albumin
CD	Circular dichroism
CDC	Complement-dependent cytotoxicity
CDR	Complementarity determining region
CED	Convection-enhanced delivery
CNS	Central nervous system
Da	Dalton
DLS	Dynamic light scattering
DMEM	Dulbecco's modified Eagle's medium
DMF	*N,N*-Dimethylformamide
DTT	Dithiothreitol
ECD	Extracellular domain
EDC	*N*-(3-Dimethylaminopropyl)-*N*′-ethylcarbodiimide hydrochloride
EDTA	Ethylenediaminetetraacetic acid
EGF	Epidermal growth factor
EGFR	Epidermal growth factor receptor
EGFRvIII	Epidermal growth factor receptor mutant variant III
EPR	Enhanced permeability and retention
FA	Folic acid
FACS	Fluorescent acquired cell sorting
FBS	Fetal bovine serum
FDA	Federal Drug Administration (USA)
Fe	Iron
FRET	Förster resonance energy transfer
GBM	Glioblastoma multiforme
GNM	Gaussian network modeling
HBS	HEPES-buffered saline
HEPES	2-[4-(2-hydroxyethyl)piperazin-1-yl]ethanesulfonic
IA	Injected amount
IDC	Indocyanine green
IONP	Iron oxide nanoparticle
IPTG	Isopropyl β-D-1-thiogalactopyranoside
ITC	Isothermal calorimetry
K	Kelvin
k_a	Association rate constant
K_D	Affinity constant, equilibrium dissociation constant
k_d	Dissociation rate constant

kDa	Kilodalton
LDH	Lactate dehydrogenase
M	Moles/liter
mAb	Monoclonal antibody
MAL	Maleimide
MES	2-(*N*-morpholino)ethanesulfonic acid
MPS	Mononuclear phagocyte system
MRI	Magnetic resonance imaging
MW	Molecular weight
MWCO	Molecular weight cut-off
NaOH	Sodium hydroxide
NHS	*N*-Hydroxysuccinimide
PAGE	Polyacrylamide gel electrophoresis
PBS	Phosphate-buffered saline
PBS^{++}	PBS containing 0.9 mM Ca_2Cl, 0.49 mM Mg_2Cl
PEG	Polyethylene glycol
PET	Positron emission tomography
pI	Isoelectric point
QD	Quantum dot
r^2	Relaxivity derived from T_2
ROS	Reactive oxygen species
RU	Resonance units
scFv	Single chain Fv
sdAb	Single domain antibody
SDS	Sodium dodecyl sulfate
SEC	Size exclusion chromatography
SMCC	4-(*N*-Maleimidomethyl)cyclohexanecarboxylic acid *N*-hydroxysuccinimide ester
SPECT	Single-photon emission computed-tomography
SPR	Surface plasmon resonance
T	Temperature
T_1	Longitudinal relaxation
T_2	Transverse relaxation
TCEP-HCl	Tris(2-carboxyethyl)phosphine hydrochloride
TGF-α	Transforming growth factor-α
TSDS	Tricine sodium dodecyl sulfate
VH	Heavy chain of conventional mammalian antibodies
VHH	Heavy chain of the camelid heavy chain antibodies
VL	Light chain of conventional mammalian antibodies
ΔG	Gibb's free energy change
ΔH	Enthalpy change
ΔS	Entropy change

1 Introduction

1.1 Glioblastoma multiforme: disease state and treatment options.

Gliobastoma multiforme (GBM) is also classified by the World Health Organization as grade IV astrocytoma, and is the most common and aggressive brain neoplasm. In North America, the estimated age-adjusted incidence of GBM is 3 per 100,000 population, with a prevalence for men (Mason et al., 2007). Based on clinical and genetic parameters, GBM is classified into primary and secondary GBM. Primary GBM originates *de novo* and accounts for up to 95% of all GBM. Secondary GBM slowly evolves from pre-existing low-grade diffuse astrocytoma and upon anaplastic changes reaches the GBM stage after several years. Neurologic symptoms depend on the area of the brain affected ranging from non-focal with headaches and/or seizures to focal deficits such as hemiparesis, aphasia and sensory loss (Binello and Germano, 2009). Despite decades of experimentation to improve the outcome of patients afflicted by this cancer, GBM remains fatal with a median survival of about 12 to 15 months. This is one of the worst 5-year survival rates among all human cancers. Interestingly subgroups of GBM patients survive for more the 36 months, highlighting the biological heterogeneity of this disease (Gadji et al., 2009). In general, primary GBM develops in older patients and typically shows EGFR over-expression, PTEN mutation, p16 deletions and less frequently MDM2 amplification. Secondary GBM develops in younger patients and often contains TP53 mutations as the earliest detectable alteration (Kuan et al., 2000). Histological hallmarks of GBM are high cellularity, anaplasia, neovascularization and necrosis (Vajkoczy and Menger, 2000).

The principal reasons for poor outcome in GBM are the high rates of recurrence and of resistance to chemotherapy. Choucair et al. estimated that more than 90% of gliomas recur (Mason et al., 2007). Virtually all glioblastoma multiforme tumors recur at the site of their initial treatment due to the presence of infiltrating

cancer cells in the surrounding normal brain that resist therapy or go untreated (Hadjipanayis et al., 2010). The notorious therapeutic resistance of GBM has been attributed to DNA-repair proficiency, a multitude of deregulated molecular pathways, and, more recently, to the particular biology of brain cancer stem/progenitor cells (Gadji et al., 2009). Nevertheless, the chemotherapeutic drug temozolomide (TMZ) has recently been shown to induce a dose and time-dependent decline of the brain cancer stem cell subpopulation (Beier et al., 2008). TMZ is an alkylating agent, whose cytotoxicity is mainly based on the methylation of guanine bases at the O6 and N7 positions, resulting in nucleic acid damage (Binello and Germano, 2009). Following this discovery, the current standard treatment paradigm since 2008 therefore consists of the gross total resection of the lesion to the extent that is safely feasible together with concurrent radiotherapy and TMZ, followed by 6 monthly cycles of adjuvant TMZ (Mason et al., 2007).

Extensive efforts are being conducted to develop effective chemotherapeutic treatments available for brain tumor patients. In order to be more effective, these therapeutic strategies will have to precisely target tumor cells, while minimizing collateral damage to neighboring cells (Sampson et al., 2008). For example, EGF receptor-targeted therapeutic approaches combined with existing treatment options are aimed at seeking and destroying the cancer stem cell compartment of GBM. For a review of EGFR-targeted therapy in GBM see Gadji et al. 2009 (Gadji et al., 2009). However, attempts to correlate EGFR molecular status to clinical response to EGFR inhibitors have previously been disappointing (Guillamo et al., 2009).

In a study involving 416 GBM patients Sawaya and colleagues demonstrated that gross surgical resection correlated with increased survival time (Lacroix et al., 2001). Therefore, until effective chemotherapeutic treatment strategies are available for GBM, the improvement of brain tumor surgery is a promising strategy to prolong patient survival. Herein, it would be important that the operating surgeon could clearly identify tumor outlines, as well as residual infiltrating cancer cells.

1.2 The use of magnetic resonance imaging in GBM patients

Imaging plays a vital role in the management of patients with cancer. Not only is it important for diagnosis, indicating sites of abnormality, and guiding biopsies, but also it is crucial in assessing disease extent and thereby determining treatment. Often the choice of surgery, radiotherapy or chemotherapy will rest entirely on the result of the imaging (Barentsz et al., 2006).

Magnetic resonance imaging (MRI) is currently the most powerful non-invasive technique available for the overall management of neurooncology patients. It is used in routine clinical practice to establish a differential diagnosis, guide tumor biopsy or resection, plan radiotherapy and monitor response to treatment and disease progression (Jenkinson et al., 2007; Sun et al., 2008). It has the advantage of providing exquisite anatomic resolution, down to 1 to 2 mm in plane at clinical field strength of 1.5 Tesla (T), and is the only imaging modality that can provide an assessment of function or molecular expression in tandem with anatomic detail (Delikatny and Poptani, 2005). In comparison to other clinical molecular imaging techniques, for example positron emission spectroscopy, magnetic resonance methods offer unparalleled image resolution without the use of ionizing radiation (Morawski et al., 2004).

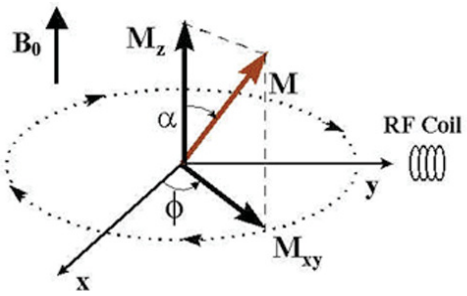

Figure 1-a. Precession of a magnetization vector in a static magnetic field aligned along the z-axis. *(Source: MRI Laboratory, Department of Radiology, Harvard Medical School, Boston, MA, USA)*

Clinical MR imaging is based on the property that hydrogen protons will align and precess around an applied magnetic field, B_0 (Figure 1-a). Upon application of a radiofrequency (RF) pulse perpendicular to the magnetic field, these protons are perturbed from alignment in B_0. The subsequent process, through which these protons return to their original state, is referred to as the relaxation phenomenon

(Sun et al., 2008). After the disappearance of the RF pulse the excited nuclei return back to their low energy state, either by relaxing back into the z-plane, called longitudinal or T_1 relaxation or by dephasing in the x/y plane called transverse, T_2, relaxation.

Herein, T_1 generates positive contrast, resulting in hyperintense (bright) areas, as shown in Figure 1-b B, whereas negative contrast enhancement through T_2 relaxation is hypointense, i.e. the image will appear darker (Yang et al., 2008). By systematically varying acquisition parameters, such as the repetition time (TR) or the echo time (TE) in an MR spin-echo or gradient echo imaging experiment, one can generate contrast that is weighted either toward T1 or T2. Short TR and short TE experiments lead to images with T1-weighted contrast, whereas T2-weighted images result from sequences using longer TR and TE (Delikatny and Poptani, 2005).

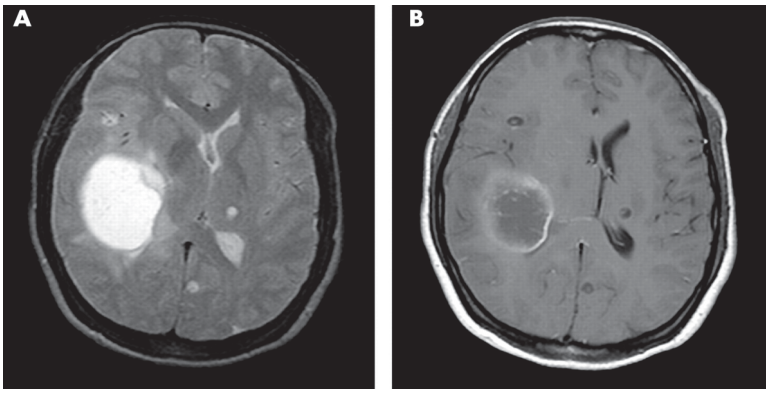

Figure 1-b. MR images of glioblastoma multiforme.

(A) T_2-weighted axial section. (B) Gadolinium-enhanced T_1-weighted axial section (Azad et al., 2003).

Local variation in relaxation, corresponding to image contrast, arises from proton density, as well as the chemical and physical nature of the tissue within the specimen (Sun et al., 2008). The signal to noise in an MR image depends on the density of protons present in the region of interest and the degree of polarization of the nuclear spin states. In the case of soft tissues with high water content, sufficient spin density is present to obtain high-quality images in short time periods (Delikatny and Poptani, 2005).

The MRI appearance of glioblastoma multiforme is typically characterized as an irregular enhancing lesion with central non-enhancing areas and marked mass effect secondary to vasogenic edema (Figure 1-b B). These findings mirror the histopathological description of central necrosis, solid tumor at the periphery with vascular proliferation and infiltrating cells within the surrounding normal brain (Jenkinson et al., 2007).

State of the art clinical MR imaging systems operate at magnetic field strengths 1.5 T. Modern magnet systems and small animal imaging systems can also be obtained at 3T and higher fields, and there are also lower-field magnets available, typically at lower cost for special purposes. In MR imaging there is always an opportunity to trade speed for quality (or vice versa), and the balance point of this compromise may yield an optimum study that maximizes benefit for the patient (McGowan, 2008). The application of magnetic contrast agents in MRI further improves the detection and characterization of lesions by enhancing the signal intensity of target tissues when compared with the surrounding normal, but often edematous, tissue. Contrast agents are used in approximately 25% of all MRI procedures (Yang et al., 2008). Contrast enhancement occurs as a result of the interaction between the contrast agents and neighboring water protons, hence they indirectly produce the contrast observed in MR images. The level of induced contrast depends on relaxivity (r), which is defined as the relaxation rate (R) of water protons in a 1 mM solution of contrast agents and is expressed in mM^{-1} s^{-1} (Delikatny and Poptani, 2005). Essentially, the relaxivity of a sample varies with the size and chemical structure of the contrast agent, as well as the accessibility of water molecules to the magnetic core. Experimental variables such as field strength, temperature, and medium in which the measurements are made, produce significant effects on the contrast agent. Therefore, these parameters should be considered when making comparisons of contrast agents found through the literature (Sun et al., 2008).

One of the hallmarks of GBM is the regional occurrence of prominent angiogenesis. The disrupted blood brain barrier in those regions allows magnetic resonance (MR)-based detection of these tumors by extravasation and

accumulation of contrast agents in the interstitial spaces (Claes et al., 2008). Gadolinium-chelates are the most commonly used paramagnetic contrast agents for T_1-weighted MR imaging and a series of clinically approved compounds exist, e.g. Magnevist® and Omniscan®. These complexes tend to be highly soluble and generate high and relatively uniform relaxivities (r_1) of 3.5 to 4 mM^{-1} s^{-1}. They have pharmacokinetic half-lives on the order of 1 to 2 hours, and, due to their small molecular weight, they are eliminated through the kidneys. Although gadolinium ions are inherently toxic, clinically employed chelates are chemically inert and thermodynamically stable. They demonstrate limited adverse effects mainly because of their efficient and rapid elimination, which minimizes exposure and possible cell internalization by endocytosis (Burtea et al., 2008; Delikatny and Poptani, 2005).

Another type of contrast agent that is rapidly gaining in popularity is superparamagnetic iron oxide nanoparticles (IONPs), which are generally composed of magnetite (Fe_3O_4), maghemite (γ-Fe_2O_3) or other ferrites. Superparamagnetic nanoparticles are recently receiving increasing attention because of their superior magnetic efficacy and biocompatibility compared to the traditional gadolinium contrast agents (Burtea et al., 2008). The next paragraph will focus on the properties and potentials of these novel superparamagnetic IONPs.

1.3 Superparamagnetic iron oxide nanoparticles as emerging contrast agents for brain tumor imaging.

IONPs provide MR contrast enhancement by shortening both the longitudinal and transverse relaxation of surrounding protons. However, as a result of their more pronounced T_2 effect, superparamagnetic nanoparticles are typically used to provide negative (hypointense) contrast enhancement using T_2-weighted pulse sequences. (Sun et al., 2008). Their relaxivities are in the range of 65 to 189 mM^{-1} s^{-1}, which is approximately 10 times greater than what is routinely seen for gadolinium (Burtea et al., 2008).

Because the relative changes in T_2-relaxivity induced by iron oxide nanoparticles depend on the size of the particles and the effective iron concentration, the modulation of these parameters can be exploited in the design of functional contrast agents (Delikatny and Poptani, 2005). In addition, several investigators generated metal-doped iron oxide nanoparticles that demonstrated enhanced relaxivities compared to conventional IONPs (Lee et al., 2007). For example Sung *et al.* showed relaxivities of 398 mM^{-1} s^{-1} at 1.5 T and 453 mM^{-1} s^{-1} at 3 T for cobalt-ferrite nanoparticles in an aqueous solutions, which is significantly higher compared to commercially available superparamagnetic IONPs (Sung et al., 2009). Superparamagnetism occurs when the size of the nanoparticles is smaller than the ferromagnetic domain (approximately 30 nm) and consequently they do not show any magnetic reminiscence (Xie et al., 2011).

Current clinical applications of iron oxide based MR contrast agents include bowel contrast, liver and spleen imaging, lymph node imaging, bone marrow imaging, perfusion imaging and MR angiography (Yang et al., 2008). In these applications, accumulation of the contrast agent within the tissue of interest relies primarily on nonspecific uptake by cells, such as macrophages of the mononuclear phagocytic system (MPS) (Sun et al., 2008). As a result, the blood half-life is dose-dependent due to progressive saturation of macrophage uptake and is generally longer in humans than in animals (Burtea et al., 2008).

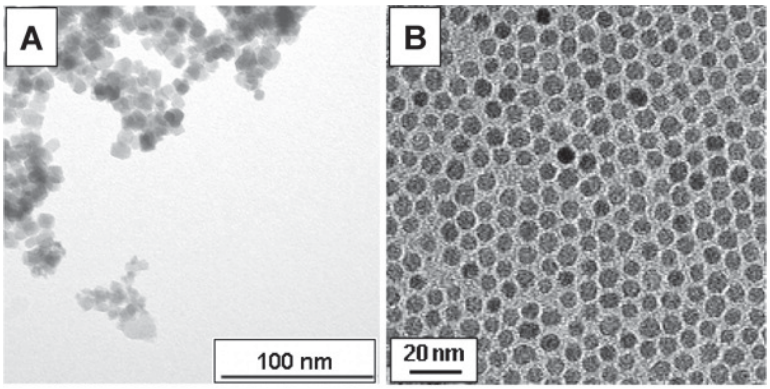

Figure 1-c. First and second generation iron oxide nanoparticles.

(A) IONPs generated using the coprecipitation method, which results in large particle size distribution due to aggregate formation. The nanoparticle formation can be achieved in the presence of stabilizing agents (e.g. dextran) (B) Thermal decomposition processes have recently been developed to produce high quality

monodisperse and monocrystalline IONPs of uniform size (Majewski and Thierry, 2007).

The IONP Feridex IV® (Advanced Magnetics), which is clinically used for liver imaging, has a r_2-relaxivity of 120 mM^{-1} s^{-1} at 1.5 T and is frequently used as point of reference for investigators developing novel IONP formulations. The particle cores are aggregates of iron crystals incompletely coated with dextran and have a large size distribution as well as irregularity in shape (58.5 nm ± 185.8) (Figure 1-c A). Feridex IV particles tend to be rapidly opsonized and taken up by the mononuclear phagocyte system (MPS) resulting in a short plasma half-life of 8-30 minutes (Varallyay et al., 2002). In contrast, Ferumoxtran-10 (29.5 nm ± 23.1), which is distributed under the names Sinerem® and Combidex® in Europe and the U.S, respectively, is significantly smaller than Feridex IV and consequently remains in the blood circulation for a long time (plasma half-life 25-30 hr). Ferumoxtran-10 has a reported r_2-relaxivity of 65 mM^{-1} s^{-1} (Burtea et al., 2008; Claes et al., 2008). These smaller size IONPs have been examined extensively as MRI contrast agents to improve the detection, diagnosis and therapeutic management of solid tumors (Sun et al., 2008), which account for over 85% of human cancers (Jang et al., 2003). Iron oxide nanoparticles are expected to accumulate at the tumor site due to the enhanced permeability and retention effect (EPR effect). This was first described by Matsumura and Maeda in 1986, who discovered that macromolecules passively accumulate at tumor sites due to the local defective vascular architecture and impaired lymphatic drainage (Matsumura and Maeda, 1986). However, passive tumor targeting requires the nanoprobes to have long plasma circulation times, which are typically achieved by shielding the IONPs with hydrophilic polymers. Most current clinical contrast agents are covered completely or partially with dextran. Among investigators developing second-generation IONPs, characterized by better-defined size, shape and surface chemistries, polyethylene glycol (PEG) conjugation has become the gold standard (Figure 1-c B). (The synthesis and surface chemistries of these second generation nanoparticles are presented in detail in Chapter 3 “3.1.2 Synthesis and surface modifications of long-circulating IONPs”, page 108)

Ferumoxtran-10 contrast enhancement has also been investigated for use in improving the delineation of brain tumor boundaries and quantification of tumor volumes (Enochs et al., 1999; Neuwelt et al., 2004; Varallyay et al., 2002). The somewhat smaller and more uniform size, compared with that of Feridex, may improve the ability of the ferumoxtran iron oxide particles to cross the damaged blood brain barrier (BBB) (endothelial junctions and basement membrane). A long plasma half-life (25 - 30 hrs) may create enough time for these iron oxide particles to "search for" the most leaky areas of the damaged BBB and, because of their uniform size, more iron oxide particles may cross the BBB resulting in good detectability with MR imaging (Varallyay et al., 2002). IONP accumulation and enhancement in malignant brain tumors peaks at 24 h after iron infusion and gradually decays in the following days. Histochemical staining for iron has demonstrated that long-lasting tumoral MR signal changes may result from intracellular trapping of the iron particle in reactive cells (e.g. macrophages, microglia), not tumor cells, at the tumor margin. Ferumoxtran signal intensity changes that persist for more than 24 hours may provide advantages over gadolinium for intra-operative MRI as well as post-operative assessment of surgical resection. One of the very important findings with ferumoxtran is the detection of areas that enhance with ferumoxtran but not with gadolinium. It is known that the gadolinium-enhancing tumor is just the "tip of the iceberg" and that the surrounding T_2 signal abnormality is a mixture of edema and infiltrating tumor in primary brain tumors (Neuwelt et al., 2004). It is widely accepted that BBB break down may be variable not only in the case of different histologic types of tumors but also within one tumor mass. The presence of ferumoxtran enhancement in regions of no gadolinium enhancement may suggest a mechanism of passing across the BBB other than via the intercellular junctions (Varallyay et al., 2002).

In a comparative study, Enochs and coworkers also found improved delineation of human brain tumors with long circulating IONPs over gadolinium. Likewise, micrometastases located some distance from the main tumor margin were observed (Enochs et al., 1999). Long lasting, as well as, better delineation of the

tumor with ferumoxtran as compared to the gadolinium chelate raise the possibility of the application of these iron oxide particles for preoperative and intraoperative surgical planning and postoperative assessment of surgical resection. Gadolinium enhancement caused by surgical BBB damage makes it difficult to correctly differentiate between residual tumor and postoperative enhancement. This difference may make ferumoxtran especially useful for intraoperative or postoperative MR imaging to assess the degree of resection (Varallyay et al., 2002). The need for image guidance during neurosurgical operations has always been a concern for neurosurgeons. Brain shift, which results from fluid shifts, tumoral volume resection, and change in arterial pCO_2 and cerebrospinal fluid (CSF) leakage after opening of the dura, may make preoperative data inaccurate. Intraoperative brain surface deformation greater than 10 mm has been documented within 1 hour of opening the dura prior to actual tumor resection in over half of the patients studied. Intraoperative imaging was in part created to overcome the effect of brain shift (Foroglou et al., 2009).

Since intraoperative MR imaging is a time-consuming procedure, as well as logistically difficult due to the large size of the instrument and need to remove all metal-containing operational tools in the vicinity of the MR imager, several researchers have sparked the idea to use optical instead of MR imaging during surgery (Kircher et al., 2003; Veiseh et al., 2005). Superparamagnetic iron oxide nanoparticles represent the ideal platform for multimodal imaging, since in addition to generating remarkably strong MRI contrast, IONPs also have a large surface area allowing for the introduction of functional molecules (Bulte and Kraitchman, 2004). Dual-mode imaging using magneto/optical nanoparticles is expected to give good anatomical information via MRI, along with more detailed subcellular information via fluorescence imaging at the same time point (Sung et al., 2009).

Currently, the major limitation of the multimodal probes is their low specificity and limited internalization by glioma cells (Veiseh et al., 2005). To overcome these limitations, the conjugation of target specific molecules, including monoclonal antibodies (mAbs), proteins, and peptides has been investigated to

increase site-specific accumulation of IONPs in tumor cells (Fang et al., 2011; Hatakeyama et al., 2011; Huang et al., 2011; Lee et al., 2008; Sun et al., 2006; Xie et al., 2011).

1.4 Tumor cell-targeted IONP contrast agents.

The concept of targeting lipid nanoparticles (liposomes) to cells by attaching antibodies to their surfaces was introduced more than 30 years ago (Kontermann, 2006). Later the concept of development of a small superparamagnetic probe conjugated to antibody was presented by Weissleder and colleagues (Wang et al., 2001). The ability to target nanomaterials to precise biological location would have wide-ranging impact in biology and medicine. In living systems, highly controlled transportation networks continually shuttle payloads to and from specific molecular addresses. The efficiency of these systems provides strong motivation for the advancement of targeted nanoparticles technologies, particularly for the diagnosis and treatment of human disease (von Maltzahn et al., 2008).

IONP contrast agents have no intrinsic affinity for particular tissues and are unable to discriminate between malignant and non-malignant tumors. Hence, their primary mode of tumor localization still relies on EPR-mediated passive extravasation (Xie et al., 2011). Upon intravenous injection, IONPs are mostly taken up by macrophages in the liver and spleen and are subsequently metabolized over several days. Several IONP agents with a variety of surface coatings that prevent the recognition by the MPS have also been extensively studied for the detection and diagnosis of solid tumors. The fate of intravenously injected IONPs is presented in more detail in Chapter 3 of this thesis ("3.1.4 The journey of a nanoparticle: from injection site to tumor", page 111). This is an active area of research since clinicians need contrast agents that can specifically target malignant tumors allowing for more accurate diagnosis of various stages of disease (Huang et al., 2011).

One way of targeting nanoparticle contrast agents to tumor tissue is based on the high magnetic moments generated by IONPs, which can be actively manipulated

by externally applied magnets making them suitable for use with magnetic targeting (Chertok et al., 2008). Another approach towards increasing the local concentration of superparamagnetic nanoparticles in tumor tissue is to conjugate these nanoparticles with targeting molecules that have a high affinity for tumor cells (Sun et al., 2006). In this "active targeting" approach, a high density of target antigens was shown to increase drug delivery and antitumor activity of nanocarriers (Hosokawa et al., 2003).

However, the challenge of tumor targeting is complex. The term "active targeting" has a flavor of guiding a drug/imaging agent to a target site like a cruise missile would. In reality, no technology or combination of technologies described to date has provided anything better than a few percent of the total administered dose reaching the site of solid tumors. The distribution of nanoparticles appears to be defined primarily by blood circulation, followed by EPR-mediated intratumoral retention, which eventually allows for extravasation. At this point, interactions between targeting ligands and cellular molecules are possible, since the two components are in close proximity (< 0.5 nm) (Bae et al., 2011). Therefore, active targeting is generally implemented to improve recognition and uptake by the target cell, and not necessarily to improve overall tumor accumulation (Lammers et al., 2011; Pirollo and Chang, 2008). For example, Kirpotin *et al.* showed that *in vitro* Her-2 targeted liposomes are taken up > 20 times more efficiently than are untargeted liposomes (Kirpotin et al., 2006). Similar findings have been reported by Davis and colleagues who showed that, overall, transferrin-targeted nanoparticles did not accumulate in tumors to a higher extent than did untargeted nanoparticles, but they improved the uptake of the particles by cancer cells (Choi et al., 2010).

Of the different targeting ligands, such as peptides, glycoproteins, carbohydrates, and polymers, mAbs are the most widely studied (Fahmy et al., 2005; Huh et al., 2005; Lee et al., 2007). Due to their high specificity monoclonal antibodies (mAbs) are popular targeting agents. Nevertheless, the large size of an intact antibody limits the ability of the IONPs to permeate through the vasculature into areas with tumor cells. In addition, the interaction of antibody with Fc receptors

on normal tissues could alter the specificity of tumor-targeted nanoparticles (Huang et al., 2011).

In my thesis project, I used single domain antibody fragments (sdAbs) to target IONPs to tumor cells with the objective of increasing uptake and retention of the contrast agent. The next paragraph provides detailed information about the physicochemical characteristics of sdAbs and the advantages for their use as targeting ligands compared to full-length antibodies.

1.5 Single domain antibodies as targeting moieties for the systemic delivery of nanoparticles.

Much of what we know about antibody-targeted nanoparticles has been learned from so-called "first generation" antibody-modified liposomes. Recently, a phase I clinical trial was carried out for an antibody-targeted liposome loaded with doxorubicin in 23 patients with metastatic or recurrent stomach cancer. This study is an impressive demonstration of the technical feasibility of the clinical application of antibody-conjugated liposomes (Schnyder and Huwyler, 2005).

Antibody-engineering is an important element in the design of novel targeting probes for *in vivo* or *ex vivo* applications, ranging from long-circulating antibodies for therapeutic targeting to chip- or array-immobilized antibodies for diagnostic purposes (Holliger and Hudson, 2005; Jain et al., 2007). Presently, the US Food and Drug Administration has approved 21 mAbs for therapy, mostly for the systemic treatment of cancer (Carter, 2006). The ability of antibodies to target their cognate antigen with high affinity and specificity has rendered them invaluable for a variety of applications in the management of human cancer. Targeting molecular markers over-expressed in tumors is expected to allow for selective drug delivery and improved tumor visualization. Despite the initial excitement over monoclonal antibodies (mAbs) as optimal therapeutic or imaging reagents, their entry into clinical use has been slower than expected. Their limited success in imaging applications may be attributed to the slow tumor penetration of mAbs due to their large size (150 kDa), and to unfavorable pharmacokinetics due to the long circulation times permitted by binding to the γ-Fc receptor, which

results in low tumor to blood ratio. Full-length antibodies can also trigger complement-mediated cytotoxicity (Torchilin, 2010). Another disadvantage of mAbs is their high production costs.

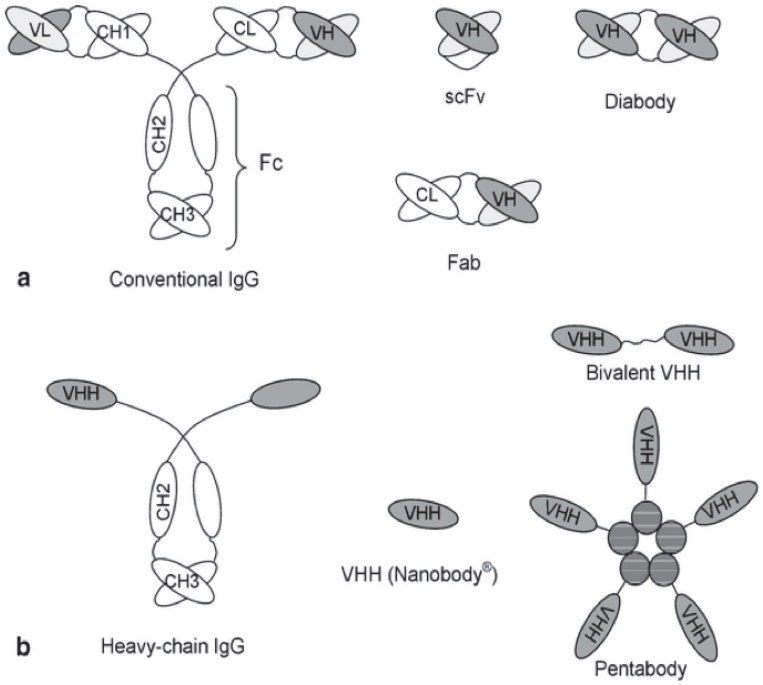

Figure 1-d. Schematic diagram of conventional (a) and heavy-chain (b) antibodies and fragments thereof.

Variable domains derived from the antibody heavy (VH) and light (VL) chains are shaded dark gray and light gray, respectively, whereas constant domains (CH and CL) are not shaded. Note the absence of the light chain and CH1 domain in heavy-chain antibodies. Antibody domains that pair by noncovalent interactions are indicated by overlaying them. The B-subunits of naturally pentamerizing toxins that are used to generate pentabodies are indicated as hatched spheres (Harmsen and De Haard, 2007).

Minimizing the size of an antibody from a multidomain protein to a smaller antigen binding entity has been one of the primary goals of antibody engineering. Minimization has the potential to improve production yield, stability, tissue penetration, blood clearance, and to reduce immunogenicity *in vivo* (Carter and Merchant, 1997; Funaro et al., 2000; Hoogenboom et al., 1998; Hudson and Souriau, 2003; Muyldermans, 2001). Several low molecular–weight antibody fragments against tumor antigens have been developed and investigated for their

application in tumor targeting (Holliger and Hudson, 2005). The most common antibody fragments are single chain Fv (scFv) and Fab. In addition to these, the variable domain of the heavy chain of the camelid heavy chain antibodies (HcAb) (VHH = sdAb) occupies a particular and perhaps undervalued position (Figure 1-d).HcAbs have been described in species belonging to the family of camelidae (i.e. dromedary, camel and llama) as a second class of antibodies different from the conventional (four chain) antibody repertoire (Hamers-Casterman et al., 1993). These molecules were shown to overcome, to a large extent, stability, aggregation and degradation problems often encountered with scFvs (Arbabi Ghahroudi et al., 1997; Hamers-Casterman et al., 1993; Omidfar et al., 2004a; van der Linden et al., 2000). With the advent of display libraries, direct screening of antibody fragment has become possible as a fast and cost-effective alternative to generating full-length antibodies. A plethora of alternative protein scaffolds are currently being engineered for immunodiagnostic and immunotherapeutic applications, e.g. affibodies, DARPins (Nuttall and Walsh, 2008).

Single domain antibodies (sdAbs).

The monomeric heavy chain antibody fragment derived from the variable domain of a camelid heavy-chain antibody is referred to as single domain antibody (sdAb), VHH or Nanobody™. The latter term was created by the company Ablynx, which specializes in the development of sdAbs for therapeutic application and currently has five molecules in Phase I or II clinical trials (http://www.ablynx.com). In order to differentiate the single domain antibodies investigated in this study, which were generated by our collaborators at the Institute for Biological Sciences (CNRC-IBS), from the commercial VHHs produced by Ablynx™, I will not use the term 'Nanobody' in this document.

With a size of only 12-15 kDa, VHH domains currently represent the smallest immunoglobulin-derived binding unit (Sheriff and Constantine, 1996). They are characterized by good expression yields in bacterial and yeast systems (Omidfar et al., 2007; Thomassen et al., 2005), high conformational stability (Dumoulin et al., 2002), and improved resistance to chemical and thermal denaturation compared to other IgG derived fragments. Their increased stability at elevated

temperatures and to extremes of pH has been largely attributed to their ability to correctly refold into their active conformation (Dumoulin et al., 2002; Ewert et al., 2002; Omidfar et al., 2007). Studies have shown that sdAbs retain functional activity in the oral cavity as well as in the gastro-intestinal tract (Kolkman and Law, 2010).

Another interesting feature of sdAbs is that they have been found to target novel epitopes, such as enzymatic clefts or phage receptors (De Genst et al., 2006; Lauwereys et al., 1998; Ledeboer et al., 2002). It was therefore hypothesized that their minimal size permits the targeting of hidden cryptic antigens that are inaccessible to larger antibodies (Stijlemans et al., 2004). As a result, single domain antibodies are anticipated to significantly expand the repertoire of antibody-based reagents (Holliger and Hudson, 2005). VHHs were shown to bind proteins with affinity constants in the low nanomolar range, which is of the same order of magnitude as Fabs or Fvs (Lauwereys et al., 1998; van der Linden et al., 2000). Single domain antibodies against hapten, peptide and protein antigens have been successfully generated (Souriau et al., 2004).

SdAbs most likely cause low immunogenicity because of their rapid blood clearance and the high sequence identity to the human variable domain of the heavy chain (VH). Two studies showed that they are non-immunogenic in mice (Cortez-Retamozo et al., 2002; Dumoulin et al., 2002) and Ablynx™ reported that no adverse effects of the VHH domain were seen in a phase I clinical trial of a VHH domain targeting von Willebrand factor in humans (http://www.ablynx.com). Still, humanization of sdAbs has been investigated and a VHH scaffold that serves as universal loop acceptor to graft antigen-binding loops from donor sdAbs has been proposed (Vaneycken et al., 2010; Vincke et al., 2009). The crystal structure of an isolated VHH indicated that it is a prolate shaped particle of 2.5 × 4 nm in diameter. All single domain antibodies belong to the same sequence family, closely related to that of the human VH of family III (VH3). The crystal and solution structures of several sdAbs have been solved and showed that their scaffolds consist of two β-sheeted structures similar to a VH immunoglobulin fold in a conventional antibody (Revets et al., 2005). By

contrast, whereas the VH domain of a classical antibody is rich in hydrophobic amino acids, which serve as anchoring places for the light chain, the VHH domain contains more hydrophilic amino acid residues, resulting in their overall better solubility. Specifically, a VHH differs from a human VH in about 10 amino acids spread over its surface to ensure maximal solubility and stability in the absence of a human variable domain of the light chain domain. The three complementarity determining regions (CDRs) also demonstrate important structural differences between the two classes of heavy chain fragments. The CDR3 loop of dromedary-derived VHHs is generally longer (average 18 residues) than in VH domains from human and mouse antibodies (average 13 or 12, respectively), thus the size of the paratope is increased in sdAbs (Muyldermans et al., 2009). However llama-derived VHH fragments revealed that the average length is not significantly different from human CDR3 (Kolkman and Law, 2010). Another group reported that a considerable fraction of the llama sdAbs seem to have a much shorter CDR3 of ~ 6 amino acids (Revets et al., 2005). Since sdAbs are devoid of the mechanism of paratope diversification that uses heavy and light chain pairing, the compensating mechanism for repertoire diversification is through novel conformations in the antigen-binding loops, deviating from the canonical structures reported for human VH3 (Decanniere et al., 1999; Decanniere et al., 2000; Muyldermans et al., 2001; Nguyen et al., 2000). Therefore, the CDR grafting from an antigen-binding human or mouse VH domain to the sdAb scaffold has little chance of success (Revets et al., 2005). The VHH paratope is often convex shaped and was shown to bind preferably to antigen surfaces with concave topology (Lauwereys et al., 1998). The compact shape and the protruding loop of the CDR 3 of some VHH domains have been proposed as determining feature that that allows them to interact with epitopes that are not antigenic for conventional antibodies (De Genst et al., 2006; Revets et al., 2005).

Immunizing a llama by repeated subcutaneous injections in presence of adjuvant is performed as in any other mammal (Paul-Murphy et al., 1989). After a short immunization step (6-7) weeks, lympohcytes are purified from a lymph node biopsy or a 50-100 ml peripheral blood sample and after an RT-PCR step the

VHH cDNA repertoire from the B-lymphocytes is cloned into phage display vectors (Nguyen et al., 2001). The VHHs are expressed at the tip of the phage particles and after 2-3 rounds of panning, individual clones can be identified that produce virions harboring the antigen-specific VHH. This method of identifying sdAbs from 'immune' libraries is much more efficient than corresponding methods to identify antigen binders from immune scFv or Fab libraries (Muyldermans et al., 2009). Once a clone with an antigen-specific VHH is identified it is normally straightforward to express mg quantities of the soluble, properly folded sdAbs (Revets et al., 2005). They are commonly cloned and expressed in the bacterium *Escherichia coli* (Bell et al., 2009), as well as in the yeasts *Saccharomyces cerevisiae* (Frenken et al., 2000; van der Linden et al., 2000) and *Pichia pastoris* (Omidfar et al., 2007) and, more recently *Nicotiana benthamiana*, a tobacco-related plant (Teh and Kavanagh, 2010). Microbial expression is a key advantage of the sdAb platform, because the average cost-of-good is 2-3 fold less compared to mammalian expression.

Applications for single domain antibodies

There are currently several applications for sdAbs ranging from *in vitro* biomarker recognition to their use as *in vivo* imaging agents. Tereshko et al, proposed the use of VHH domains as an inexpensive alternative to conventional antibodies and their fragments as crystallization chaperones (Tereshko et al., 2008). Their smaller size allows for higher density immobilization on sensor chip surfaces and therefore enables faster and more sensitive detection of a target protein in solution, e.g. biomarker recognition in a blood sample (Saerens et al., 2005a).

The pharmacokinetic requirements of a given antibody depend upon the nature of its application. In the case of therapeutic antibodies, which generally act either by inhibiting a signaling pathway or by inducing antibody-dependent cell-mediated cytotoxicity (ADCC) or complement-dependent cytotoxicity (CDC), a prolonged half-life is desirable, to achieve longer bioavailability and to avoid repeated injections (making it cost effective). Alternatively, if an antibody is being used as a vehicle for the delivery of a cytotoxic agent such as a radionuclide, drug, or

toxin, the rapid elimination of the untargeted conjugate is preferable to avoid non-target tissue toxicity (Jain et al., 2007). Like scFvs and Fabs, sdAbs can be used for generating immunoconjugates, and several reports have been published on this topic (Cortez-Retamozo et al., 2004; Harmsen and De Haard, 2007).

Critical determinants of the tumor targeting efficiency of recombinant antibodies are their specificity, affinity, and also their physical properties such as valency, surface charge and size.

Several studies on the *in vivo* distribution of sdAbs have shown that they are cleared rapidly from circulation (Bell et al., 2009; Harmsen et al., 2005). The blood half-life reported for different VHH fragments was within the range of a few minutes (Coppieters et al., 2006; Gainkam et al., 2008; Iqbal et al., 2010b; Vaneycken et al., 2010). At the same time, predominant renal accumulation was observed, which is expected, because their molecular weight is below the threshold of first-pass glomerular filtration in the kidneys, which is estimated to be 60-65 kDa (Behr et al., 1998). Further contributing to very short serum half-lives, compared to full-length antibodies, is the lack of an Fc domain. As a result, they do not bind the γFc-receptor, which prevents degradation of antibodies by the lysosomal pathway (Junghans, 1997). In a study by De Groeve and coworkers, the CDRs of the DC1.8 and DC2.1 VHHs were grafted onto the framework of the control BCII10 VHH, which resulted in biodistribution of the engineered sdAbs resembling that of the VHHs from which the antigen-binding loops were derived, therefore suggesting that biodistribution is mainly determined by their antigen-binding loops rather than by, for example, hydrophobic interactions with the framework sequences (De Groeve et al., 2010).

The short circulation times are incompatible with their use in tumor therapy, but hold large promise for radio-imaging applications (PET, SPECT), where long retention times are undesired and high tumor to blood ratios are crucial (Vaneycken et al., 2010).

Some differences in hepatic uptake have been reported, ranging from 2.5 % 18.9% of the injected amount (IA), which could be caused by variable degrees of

lipophilicity of the sdAbs, according to a previous study on scFvs (Gainkam et al., 2008; Huang et al., 2008; Thurber et al., 2008).

Roovers and colleagues demonstrated that serum half-lives of sdAbs could be significantly increased if they are bispecific, with one VHH domain binding to albumin (Gainkam et al., 2008). The conjugation to serum albumin has been shown to result in a greater overall molecular weight of the probe, which enables it to escape from the glomerular filtration in the kidneys (Dennis et al., 2007; Dennis et al., 2002). In addition, grafting of hydrophilic polyethylene glycol chains to antibody fragments, a process called PEGylation, has been applied to increase half-life of antibody fragments (Chapman, 2002; Jevsevar et al., 2010). However, since VHH domains are very small, there is a considerable danger that such chemical modification may diminish the immuno-reactivity of the molecule (Delgado et al., 1996; Kubetzko et al., 2005).

In order to improve functional affinity of *in vivo* targeted sdAbs several expression formats for sdAb multimer production have been described (Figure 1-d B) (Coppieters et al., 2006; Els Conrath et al., 2001; Harmsen et al., 2005; Roovers et al., 2007a; Zhang et al., 2004). Recently, VHH fragments have also been conjugated to the surface of metal nanoparticles and were shown to retain target-specificity *in vitro* and *in vivo* (Iqbal et al., 2010a; Oliveira et al., 2010; Van de Broek et al., 2011).

1.6 Dysregulation of the epidermal growth factor receptor in GBM patients.

Certain considerations should be taken into account when developing targeted preparations for *in vivo* imaging applications. First, a target should be identified that is present (over-expressed) on the surface of tumor cells in sufficient quantity, thus providing a good opportunity for the targeted nanoparticles to effectively bind to cancer cells (Torchilin, 2010). Growth factor receptors are attractive candidates for targeted therapy, since they are often over-expressed on the surface of cancer cells (Kuan et al., 2000). The epidermal growth factor (EGFR) is amplified, over-expressed, and/or mutated in a large percentage of glioblastoma

multiforme and therefore represents a compelling molecular target (Frederick et al., 2000; Heimberger et al., 2005; Ohgaki et al., 2004; Smith et al., 2001; Yoshimoto et al., 2008). Several researchers have investigated the EGFR status of high-grade gliomas by employing different molecular biological techniques. Herein, 71%, 51%, 69%, 50%, and 50% of tumors were found to have high EGFR expression levels by frozen section immunohistology, paraffin section immunohistology, radiolabeled ligand binding, Western Blot and enzyme-linked immunoassay, respectively (Liu et al., 2003).

EGFR belongs to the ErbB family of receptor tyrosine kinases, which contains four members: EGFR, ErbB2 (Her-2), ErbB3, and ErbB4. ErbB receptor signaling is normally very tightly controlled and its deregulation is linked to several epithelial cancers. Besides GBM, gene amplification, over-expression, and activating mutations of EGFR are seen in a large percentage of prostrate, breast, colorectal, non-small cell lung and squamous carcinomas (Dawson et al., 2005; Kuan et al., 2000). It was discovered early on that EGFR is homologous to the viral oncogene v-erb-b and its over-expression in transgenic mice was shown to be a transforming event, therefore identifying EGFR as a proto-oncogene (Downward et al., 1984; Lin et al., 1984; Ullrich et al., 1984; Xu et al., 1984).

The EGF receptor consists of a ligand-binding extracellular domain, a single pass transmembrane domain, and a cytoplasmic domain with intrinsic tyrosine kinase activity as well as conserved binding domains for adapter proteins (Figure 1-e) (Citri and Yarden, 2006). EGFR signals through homo- and hetero-dimerization with other members of the family, which are able to induce multiple downstream signaling events upon stimulation by a plethora of growth factors (Wells, 1999). Important downstream signaling pathways regulated by EGFR include the PI3K/Akt, phospholipase C and the MAPK pathways (Hynes and MacDonald, 2009). Increasing evidence shows that the internalized activated receptor continues to activate downstream signaling pathways from endocytic compartments through scaffold and adaptor proteins that are varying by subcellular distribution, further emphasizes the complexity of this pathway (Dard and Peter, 2006; Hoeller et al., 2005; Teis and Huber, 2003). The most abundant

EGFR ligands are epidermal growth factor (EGF) and transforming growth factor-α (TGF-α). Since there are no known antagonists for mammalian EGFR, the receptor is mainly regulated by the spatio-temporal expression of its activating ligands (Yarden and Sliwkowski, 2001). This autocrine receptor activation mediated through high affinity ligands was shown to produce short-range effects, (Wiley et al., 2003). How ligand-induced conformational changes in the extracellular domain of the receptor are thought to mediate receptor dimerization and activation of the cytoplasmic tail will be the focus of Chapter 4 of this thesis.

The two main strategies employed to interfere with EGFR functioning are, at the intracellular level, with small tyrosine kinase inhibitors (e.g. erlotinib and gefitinib) that compete with ATP for binding to the active site of the receptor, and at the extracellular level, with monoclonal antibodies (mAbs e.g. cetuximab) that prevent ligand binding to the receptor (Oliveira et al., 2010). A recent review summarizes the achievements and pitfalls of EGFR-targeted therapies for the treatment of glioblastoma multiforme (Gadji et al., 2009).

Gene amplification is the main mechanism of EGFR protein over-expression in tumors. Protein over-expression without gene amplification has only been reported in 12% - 38% of GBMs, suggesting that multiple systems of deregulation in EGFR expression may exist on translational and post-translational levels. In addition to over-expression, structural alterations are also frequently observed and several variants of EGFR have been identified to date and occur with different frequencies in gliomas. Herein, the most abundantly found variant is EGFRvIII, which occurs in 40 - 90% of GBM over-expressing EGFR as well as in breast, ovarian, prostate and lung carcinomas (Kuan et al., 2000; Wikstrand et al., 1997; Yamazaki et al., 1988). The mutant receptor variant EGFRvIII results from an in-frame deletion of 801 bp in the extracellular domain of the EGFR that removes exons 2 - 7 and produces a novel glycine at the fusion junction (Figure 1-e) (Gan et al., 2009; Sampson et al., 2009). Technically, that leaves the ligand binding site on subdomain III intact, however it has been shown that the tyrosine kinase is constitutively activated independent on ligand (Sugawa et al., 1990). Furthermore, it has been demonstrated that EGFRvIII fails to bind ligand in NIH3T3 and

glioblastoma cell models, but showed minimal low-affinity ligand binding in some other systems (O'Rourke et al., 1998; Tang et al., 2000).

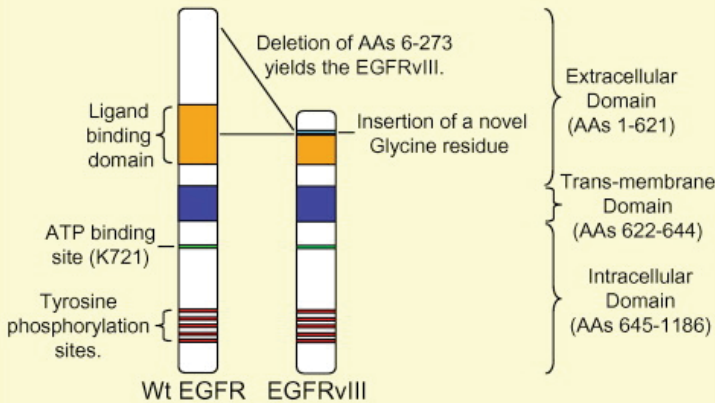

Figure 1-e. Schematic of the epidermal growth factor receptor (EGFR)vIII truncation.
The EGFRvIII variant receptor is characterized by a deletion of exons 2–7 of the wild type EGFR gene, which results in an in-frame truncation of amino acids 6 to 273 in the extracellular domain of the full length protein, yielding a constitutively active variant receptor that cannot bind ligand. The EGFRvIII also contains a novel glycine residue inserted at the fusion junction (Gan et al., 2009).

The deletions in EGFRvIII correspond to most of subdomains I and II of the EGFR and as a result this truncated mutant receptor has a molecular mass of 145 kDa versus 170 kDa for wild-type EGFR. The EGFRvIII mutation may occur as a result of multiple Alu repeats in introns 1 - 7 potentially contributing to alternative splicing or gene rearrangements (Ekstrand et al., 1992; Frederick et al., 2000; Wong et al., 1992; Yamazaki et al., 1990).

EGFRvIII transforms fibroblasts and enhances the tumorigenicity of cancer cells both *in vitro* and *in vivo*, suggesting that EGFRvIII plays an active role in tumorigenesis. In GBM and breast carcinomas the expression of EGFRvIII is correlated to a poor prognosis (Heimberger et al., 2005; Tang et al., 2000). The increased oncogenic potential of this constitutively active EGF receptor vIII deletion mutant likely depends on the enhanced downstream signaling of activated PI3K/Akt and MAPK pathways (Moscatello et al., 1995; Prigent et al., 1996). In addition, EGFRvIII can form homo- and heterodimers and phosphorylate EGFR and ErbB2 (Grandal et al., 2007; Johns et al., 2007; Luwor et al., 2004).

Since the expression of the EGFRvIII mutant is considered to be tumor-specific, several therapeutic approaches have been developed targeting this receptor variant. For example, Yamoutpour and colleagues demonstrated inhibition of tumor growth in a subcutaneous U87MG.EGFRvIII xenograft model by successful gene silencing after treatment with an anti-EGFRvIII lentivirus (Yamoutpour et al., 2008) A different approach was taken by Sampson and colleagues, i.e. they attempted to raise an immune response against EGFRvIII expressing tumor cells by administration of an anti-EGFRvIII vaccine (PEPvIII-KLH, AnaSpec Inc, San Jose, CA, USA), which showed encouraging results in phase I and II clinical trials (Sampson et al., 2008). In addition, toxin-conjugated anti-EGFRvIII scFvs have been developed and several other EGFRvIII-specific monoclonal antibodies and VHH domains have been generated with the potential of targeting therapeutics to cancer cells (Kuan et al., 2000; Lorimer et al., 1996; Omidfar et al., 2004b; Wikstrand et al., 1995).

1.7 Over-expressed EGF-receptors as molecular targets for the delivery of contrast agents to brain tumors.

Although EGFR is also ubiquitously expressed in normal tissues, predominantly in the liver and skin, the receptor is preferentially over-expressed on the surface of many tumors, which makes it an excellent candidate for broadly applicable tumor-targeted delivery (Arteaga, 2002). As a result, the ability to target immunoliposomes and nanoparticles to EGFR and EGFRvIII over-expressing cancer cells has been demonstrated *in vivo* for pancreatic (Yang et al., 2009b), breast (Sandoval et al., 2011) head and neck (Oliveira et al., 2010), and glioblastoma tumor models (Feng et al., 2009; Tsutsui et al., 2007). High-grade gliomas show predominant membrane staining pattern for EGFR and EGFRvIII as detected by immunohistochemical staining using specific monoclonal antibodies (Kuan et al., 2000; Nishikawa et al., 1994). By contrast, the gene encoding the EGFR and its mutant isoform EGFRvIII are low or undetectable in normal brain (Mendelsohn and Baselga, 2006). Herein, it was demonstrated that especially the invasive tumor cells on the boundaries of the tumors express high

levels of EGFR, due to the implication of the receptor in angiogenesis and enhanced migration (Lal et al., 2002; Wu et al., 2004). Data obtained from the analysis of cells from freshly disaggregated biopsy tissue have established that EGFRvIII positive gliomas contain approximately 40 - 90% EGFRvIII positive cell populations, the majority of which express receptors at a mean density of > 2 x 10^5 receptor/cell, a level established as supportive of receptor-mediated targeted therapeutic approaches (Wikstrand et al., 1997). However, it has also been demonstrated by immunohistology on GBM tissue samples that expression of EGFRvIII is heterogeneous within the tumor (Sampson et al., 2009). In another study by Biernat *et al*. it was shown that the occurrence of EGFRvIII in glioblastoma is even a rare event, whereas wild-type EGFR over-expression is often more extensive (Biernat et al., 2004). These findings provide the rational of using an antibody that binds both variants of the receptor for the development of a broadly applicable targeted contrast agent for improved imaging of GBM.

I pointed out earlier (paragraph 1.4 of this introduction) that the attachment of antibodies or antibody fragments is expected to generate prolonged retention at the tumor site due to the increased internalization mediated by the specific target. Antibodies with specific activity against the EGFRvIII mutant receptor have been developed that are internalized in the cell after receptor binding (Kuan et al., 2000; Reist et al., 1995). Monoclonal antibodies against EGFR, e.g. 225, have also been shown to internalize with the receptor (Goldstein et al., 1995; Jaramillo et al., 2006; Waksal, 1999). Furthermore, fragments of the anti-EGFR mAb 225, when coupled to drug-loaded liposomes, allowed for the substantially enhanced binding of such targeted liposomes to cancer cells over-expressing EGFR. The improved binding was shown to result in enhanced internalization (Mamot et al., 2003). A Fab fragment derived from the anti-EGFR antibody EMD72000 was also shown to provide efficient intracellular delivery of liposomal drugs into colorectal cancer cells (Torchilin, 2010).

I therefore conclude that the EGF receptor represents an excellent target for prolonged and specific retention of nanoparticulate MRI contrast agents in

invading glioblastoma cells, which could potentially improve delineation of tumor outlines and detection of infiltrating tumor cells.

1.8 Short summary of the objective of my thesis project

Despite aggressive, image-guided tumor resection, high dose external beam radiotherapy, and recent advances in chemotherapy, patients with glioblastoma multiforme (GBM) live less than 15 months from the time of diagnosis and patients with recurrent tumors usually survive less than 20 weeks. Moreover, the non-specific nature of conventional therapy for brain tumors often results in incapacitating damage to surrounding normal brain and systemic tissue. The spreading of tumor cells around the surgical cavity explains the recurrence of these tumors after resection. Furthermore, Guillamo and coworkers observed that tumors with EGFR amplification were much more invasive than those without amplification (Guillamo et al., 2009). In order to achieve high-resolution delineation of tumor boundaries the labeling has to be carried out on a cellular level. The difference in the level of EGFR expression between normal cells and tumor cells, coupled with the phenomenon of ü cellular internalization of EGFR-antibody complexes, suggests that EGFR is a potential marker for *in vivo* receptor-targeted molecular imaging with excellent tumor-to-background contrast (Yang et al., 2009b).

In this thesis, I investigated the development of an EGFR-targeted iron oxide nanoparticle contrast agent for MR imaging of GBM. Although gadolinium-based contrast agents are widely used in the clinic, they have relatively low contrast effects, short retention time *in vivo*, and their toxicity and biocompatibility is still unknown (Peng et al., 2008). One of the hallmarks of GBM is the regional occurrence of prominent angiogenesis. The disrupted blood brain barrier in those regions allows magnetic resonance (MR)-based detection of these tumors by extravasation and accumulation of contrast agents in the interstitial spaces (Claes et al., 2008). Specific targeting of IONPs to EGFR and EGFRvIII over-expressing cells in glioblastoma multiforme is expected to improve visualization of tumor outlines by MRI. Additional labeling of nanoparticles with fluorophores could

potentially allow for individual cell-labeling with emerging intra-operative microscopic devices (Valdes et al., 2009). Extending the visualization of GBM beyond tumor outlines and detecting residual tumor cells is essential for prolonging the survival of GBM patients.

Novel single domain antibodies (sdAbs) were generated against the extracellular domain of EGFR by my collaborators. These 15 kDa antibody fragments are suitable for imaging applications, because of their small size, high stability, and the absence of Fc-receptor mediated effector functions that could alter the distribution of the contrast agent *in vivo*. I present the characterization of these novel sdAb fragments in Chapter 2 and show the strategy I developed and implemented to conjugate them onto the surface of iron oxide nanoparticles in Chapter 3. Subsequently, I investigated the ability of these particles to localize to EGFR-over-expressing tumor cells *in vivo* in a subcutaneous glioblastoma xenograft model. The results of this study are also shown in Chapter 3.

Furthermore, the ability of single domain antibodies to bind unique epitopes, such as clefts and cavities, might provide additional information on structure and function, which cannot be assessed with conventional mAbs (De Genst et al., 2006; Stijlemans et al., 2004). Hence, these novel antibody fragments could potentially be useful for dissecting the mechanism involved in EGF receptor activation. In order to elucidate the mechanism of ligand-mediated receptor activation, I carried out a comparative thermodynamic study of sdAb binding to the extracellular domain of EGFR versus binding of the natural ligand EGF. This study is presented and discussed in detail in Chapter 4.

2 Characterization of novel anti-EGFR single domain antibody fragments.

The SPR biosensor data and the cell binding study using radiolabeled EG2 sdAbs have been partially published in two articles done in collaboration with my co-authors (Bell et al., 2009; Iqbal et al., 2010b). In this chapter I will also present additional findings to the previously published material, consisting of complementary SPR studies and cell-based assays, including flow cytometry and confocal microscopy. A detailed list of the published work and the individual contributions can be found at the end of this chapter (page 77).

2.1 Introduction to surface plasmon resonance

Large parts of the data presented in this thesis were generated using surface plasmon resonance (SPR) biosensor technology. In the following paragraph I will therefore provide a comprehensive introduction to SPR instrumentation and experimental design, in order to enable a good understanding of my data and the interpretations emerging from it.

All experiments presented in this thesis were carried out on a Biacore 3000 instrument available from GE Healthcare. SPR analysis allows for the label-free, real-time visualization of bimolecular interactions. Since the commercialization of biosensor platforms in the early 1990s a multitude of applications for SPR instruments have emerged, e.g. analysis of binding kinetics, calculation of thermodynamic parameters, epitope mapping of monoclonal antibodies, ligand searching for orphan receptors, study of protein-membrane interactions and analysis of drug candidates (Besenicar et al., 2006; Jason-Moller et al., 2006; Nice and Catimel, 1999; Rich and Myszka, 2004; Van Regenmortel et al., 1998). SPR Biosensors have now become standard instruments in biochemical and biophysical research centers. The magnitude of binding constants (K_D) that can be accurately determined in SPR experiments ranges from low picomolar to high micromolar K_D-values, which is close to the entire range of bimolecular affinities

found for biological complex formation (Myszka et al., 1997; Ohlson et al., 1997). Finally, compared to other methods like calorimetry or ELISA, the biosensor requires much less material and provides dynamic information about complex formation.

The Biacore 3000 biosensor system consists of a processing unit and a computer equipped with control and data evaluation software (Figure 2-a, left). In the processing unit a microfluidic system provides continuous buffer flow across the four flow channels (FCs) established between the exchangeable sensor chip and the integrated fluidic cartridge (IFC) (Figure 2-b).

Figure 2-a. Biacore 3000 optical biosensor (left) and CM5 sensor chip (not to scale, right). *Image: GE Healthcare.*

An SPR sensor chip typically consists of a glass support coated with a thin layer of gold onto which a hydrogel matrix of flexible, unbranched carboxymethylated dextran is grafted (Figure 2-a, right). This inert dextran layer serves as conjugation matrix for one of the binding partners, which then is termed “ligand”. The matrix provides a hydrophilic surface with low non-specific binding and maintains a solution-like environment for the immobilized protein (Day et al., 2002; Jason-Moller et al., 2006). Another property of the Biacore 3000 instrument is that the experimental temperature can be varied between 4 and 40°C, which is essential for thermodynamic studies.

The detection principle is schematically illustrated in Figure 2-b. Once the chip is inserted into the instrument, polarized light is focused onto the gold surface, leading to the formation of surface plasmons and a concomitant drop in the intensity of the reflected light measured in the optical unit. When a change in mass occurs near the sensor chip surface, e.g. as a result of a binding event, the angle of light at which SPR occurs shifts due to a change in refractive index near

the sensor chip surface. These changes can be measured in real time and are expressed in "resonance units", commonly abbreviated as "RUs". For proteins, a signal of 1 RU is equivalent to a surface mass of 1ng mm^{-2} (Stenberg et al., 1991).

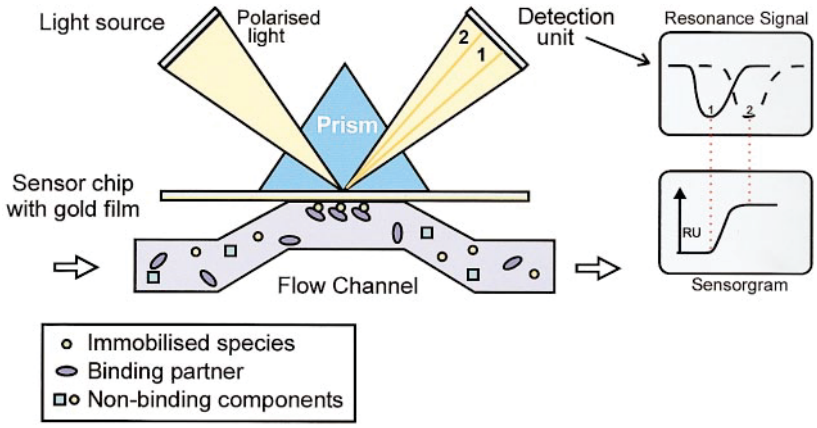

Figure 2-b. Surface plasmon resonance detection (Nice and Catimel, 1999).

A representative SPR sensorgram is shown in Figure 2-c. The continuous buffer flow is referred to as "baseline" and represents the reference point for the subsequent binding event. Upon sample injection, the mass on the surface increases, which is observed during the association phase.

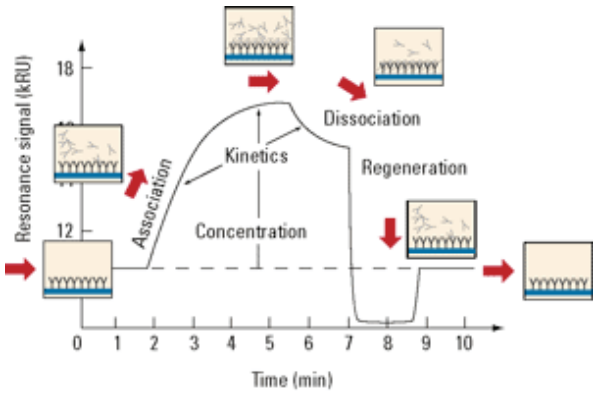

Figure 2-c. SPR sensorgram illustrating the different phases of an interaction monitored in real-time. *Image: GE Healthcare.*

At the end of the association phase, sample is replaced by buffer flow and the dissociation of the protein complex takes place. As mentioned above, the protein immobilized on the sensor-chip surface is generally referred to as "ligand" and the protein diluted in the running buffer, flowing over the surface, is termed

"analyte". Since in this study, I am investigating the interaction between the EGF receptor and its ligand EGF, I will stay clear of the "ligand" terminology and will refer to "bound protein" or "immobilized protein" instead, in order to avoid confusion between these two different applications of the term ligand.

Biacore chip surface preparation

In most of my experiments, proteins were immobilized by amine-coupling, which is also the most common method of immobilization seen in SPR studies. Herein, the carboxymethyl dextran coat is activated with N-ethyl-N'-dimethylaminopropyl-carbodiimide (EDC) and N-hydroxysuccinimide (NHS), resulting in the formation of covalent ester bonds between the dextran chain and primary amino-groups in the protein (Johnsson et al., 1995). Primary amino groups are present at the N-terminus and on lysine residues in the protein sequence. The drawback of this conjugation approach is that most proteins contain several lysines in addition to the N-terminal amino-group, which produces heterogeneous surfaces that may contain partially obscured binding sites. As a result, more than one class of interaction could be contributing to the investigated binding event.

In order to avoid the generation of heterogeneous surfaces, in the thermodynamic study presented in Chapter 4, I employed maleimide-coupling chemistry to immobilize a single domain antibody through an additional free cysteine engineered at the C-terminus of the protein. This is an approach that was previously used for other antibody fragments to achieve site-specific modification (Albrecht et al., 2004; Harmsen et al., 2007). Furthermore, it has been demonstrated that other sdAb fragments immobilized via C-terminal tags (e.g. His/NTA or Streptavidin/Biotin) retained their antigen-binding activity. This is not surprising, because relative to the tag, the paratope of the sdAb is located at the opposite end of the protein (Saerens et al., 2005a). The resulting biosensor surface is characterized by uniformly oriented bound protein, thereby reducing the risk of monitoring artifacts. For maleimide-coupling I used heterobifunctional succinimidyl-4-(N-maleidomethyl-cyclohexane-1-carboxylate) (SMCC-

hydrazide) to activate the surface by introducing thiol-reactive ethers (Jason-Moller et al., 2006).

Following surface activation, the ligand is injected in low salt buffer at a pH below the isoelectric point (pI) of the protein, usually pH 4 - 5. Under these conditions, the ligand acquires a positive charge and is efficiently pre-concentrated into the negatively charged carboxymethyl dextran matrix. Finally, after amino-coupling unreacted esters are blocked with ethanolamine and in the maleimide reaction unreacted thioethers are blocked with cysteine.

The approximate percentage of molecules on the surface that are active can be determined from the ratio of R_{max} obtained from model fitting versus the maximal binding capacity of the surface and is calculated according to the following equation (van der Merwe, 2000):

$$\text{Maximal analyte binding capacity (RU)} = \frac{\text{analyte MW}}{\text{ligand MW}} \times \text{immobilized ligand (RU)}$$

I carried out this calculation routinely for all surfaces to compare reproducibility within the investigated system.

Experimental design

Conventionally, the first of the four flow cells on a Biacore chip is used as reference channel to monitor bulk shifts in the refractive index that arise when running buffer is replaced by sample or regeneration solution. The manufacturer recommends Hepes buffered saline (HBS), pH 7.4, 3.4 mM EDTA and 0.005% p20 as running buffer, which I used in all my experiments. As in any other buffered system, the chelating agent EDTA functions to scavenge divalent metal ions and the detergent p20 reduces non-specific adsorption. In order to avoid large buffer shifts as much as possible, the sample is diluted in running buffer. When size exclusion chromatography was carried out to increase protein purity, the gel filtration column was operated in HBS buffer. Reliable detailed kinetic analysis requires data from four to six analyte concentrations, spanning the range of 0.1 to 10 times K_D (Jason-Moller et al., 2006). Following analyte injection and monitoring the dissociation phase, the residual amount of bound analyte is

removed with short injections of 20-50 mM HCl. This surface regeneration treatment generally does not affect the activity of the immobilized protein, which I verified in my experiments by comparing binding of two sequential injections of identical analyte concentration during each experimental run. In order to accurately determine the kinetic and/or thermodynamic constants of an interaction, every experiment is carried out in triplicate repeats, called "runs", to account for the intra-experimental error.

Considerations to maximize data quality

High quality data is essential for deriving reliable kinetic and thermodynamic constants from SPR studies. The following considerations should therefore be taken into account when designing biosensor experiments (Karlsson and Falt, 1997).

Besides the objective to create surfaces of homogeneously oriented proteins to measure rate constants accurately, it is equally important that the analyte is of highest purity, which is why the EGFR extracellular domain (EGFR-ECD) was purified by gel filtration prior to Biacore analysis. It is thought that most protein-protein interactions can be described by a simple bimolecular interaction model (Rich and Myszka, 2008). Impurities in the analyte, as well as other factors described in this paragraph, could cause apparent deviations away from a simple interaction model and accordingly affect accurate determination of binding constants.

As with all surface-based analysis methods, the phenomenon of mass transport should be considered. Under laminar flow conditions used in the Biacore instruments, the rate of transport of the analyte to the surface is proportional to the cube root of the flow rate and is also influenced by the dimensions of the flow cell and the diffusion properties of the analyte (Glaser, 1993). Optimal assay conditions that minimize mass transport limitations and enable accurate measurement of rate constants are a combination of high flow rates and low surface binding capacity (Myszka et al., 1997). High flow rates minimize the diffusion distance from the bulk flow to the surface, while low immobilized protein densities reduce analyte consumption in the surface layer. In practice this

translates into using immobilized protein densities that result in a maximum analyte binding response no greater than 50 – 150 RU and flow rates > 30 µl min^{-1} (Jason-Moller et al., 2006).

Another caveat of low flow rates is the occurrence of analyte rebinding during the dissociation phase, thereby artificially decreasing the dissociation rate constant, k_d (van der Merwe, 2000). Potential rebinding can also be minimized by including an excess amount of the same protein that was immobilized on the sensor surface, during the dissociation phase (Felder et al., 1993).

Measuring the kinetic parameters at several flow-rates as well as over different surface-densities are valuable controls that I routinely carried out to avoid documenting artifacts, which could have been generated from mass transport or rebinding effects. The most rigorous control is to confirm the affinity constant in the reverse configuration, i.e. the analyte is now immobilized and the previously bound protein is flowing. For two of the four investigated single domain antibodies this control was not possible, because, they could not be immobilized for reasons that are not clear.

Data treatment

Affinity values can be derived either from steady state values for interactions that have reached equilibrium or, in cases where the system does not reach steady state during the time frame of the experiment, from the ratio of the dissociation and association rate constants. Herein, analyte concentrations must be accurately known to determine correct association rate constants and ideally the investigated interaction should be monovalent. It is standard to include at least one zero concentration injection of analyte as part of the concentration series for the purpose of double-referencing (Myszka, 1999). With the Biacore 3000 instrument, on-rates between 10^3 and 10^7 M^{-1} s^{-1} and off-rates between 10^{-5} and 10^{-1} s^{-1} can be determined under optimal experimental conditions (Karlsson, 1999).

The most common method of analysis using the BIAevaluation software is global analysis, which is an iterative curve fitting routine that is applied simultaneously to complete sets of binding data (i.e. all analyte concentrations are included),

employing algorithms that are based on nonlinear least-squares analysis (NLLS). Selected parameters are constrained to a single solution for all curves, hence resulting in superior parameter estimates due to smaller errors compared to individual curve fitting (Karlsson and Falt, 1997; Myszka et al., 1997). Several binding models are available in the BIAevaluation software. Nevertheless, a biological understanding of the interaction is essential for the accurate choice of binding model, since the same data set can sometimes fit more than one model (Domagala et al., 2000; Karlsson and Falt, 1997; van der Merwe, 2000). Alternatively, equilibrium binding can be analyzed in the BIAevaluation software by plotting average RU values at equilibrium over the injected analyte concentration and then choosing the steady state affinity model, which fits the data by non-linear regression. Some antibody fragments are characterized by slow dissociation rates, and hence, it is difficult to reach equilibrium for these complexes in Biacore assays.

It has been proposed that most well designed Biacore experiments should fit a simple 1:1 binding model in the absence of experimental artifacts (Kalinin et al., 1995; Katsamba et al., 2006; Papalia et al., 2006; Rich and Myszka, 2004; Rich and Myszka, 2008). Therefore all the results presented in my thesis were obtained from global analysis of binding data using the 1:1 Langmuir binding model (A + L <=> AL) even though, like others, in some cases we observed non-random residuals after fitting the sensorgrams to the model. Although the traditional Scatchard representation of binding data has been shown to be less reliable for the determination of binding constants from Biacore data sets, linear plots nevertheless confirm that the application of a 1:1 binding model is justified (Chaiken et al., 1992; Schuck and Minton, 1996; van der Merwe, 2000). Hence, insets showing linear Scatchard plots are frequently included in Biacore data presentations to illustrate the accuracy of the 1:1 model.

2.2 Experimental Procedures

Protein production and purification

Human EGFR extracellular domain (EGFR-ECD) was produced in Sf9 cells and purified by two-step ion-exchange chromatography as reported previously (Brown et al., 1994). The production and purification of EGFRvIII-ECD was carried out as described by Campa *et al.* (Campa et al., 2000). Isolation of the single domain antibodies was achieved by llama immunization with EGFRvIII-ECD, construction of an immune phage display library and subsequent panning as previously described (Bell et al., 2009). Pentamerization of EG2 into V2C-EG2 was achieved by fusion to verotoxin subunit B1 (Zhang et al., 2004). EG2-hFc or EG10-hFc was constructed by fusion of EG2 or EG10 to a human Fc fragment and expression in a HEK293 expression system as described previously (Zhang et al., 2009).

The purity of the proteins was confirmed by SDS-PAGE and subsequent Coomassie staining to visualize proteins. Additionally, the single domain antibodies were detected by Western Blot using an antibody against the C-terminal 6× His-tag (Invitrogen). Monodispersity of the protein solutions was investigated by dynamic light scattering using a DynaPro™ Plate Reader™ (Wyatt Technology Corp., Santa Barbara, CA, US).

Biacore experiments

Experiments were performed using a Biacore3000 optical sensor platform equipped with research-grade CM5 sensor chips (GE Healthcare, Bethesda, US). All proteins were immobilized on the sensor chip surface by standard amine coupling using the amine-coupling kit from GE Healthcare according to the manufacturer's instructions (Ferguson et al., 2000). Briefly, 70 µl of a mixed solution NHS/EDC were injected to activate the carboxylated dextran, followed by manual injection of protein in 10 mM NaOAc (pH 4-4.5) until the desired surface density was reached. Ethanolamine, 1 M in water (pH 8.5), was then injected to deactivate residual NHS-esters on the sensor chip. All experiments were carried out in HBS buffer (10 mM Hepes, 150 mM NaCl, 3.4 mM EDTA, 0.005% p20, pH 7.4) at 25°C. Analytes were injected at serial dilutions ranging from 3.7 nM to 1 µM at flow rates of 20 and 30 µl/min, as indicated. After each injection the surfaces were regenerated with two 30 s injections of 10 – 50 mM

HCl. The amount of bound analyte after subtraction from the blank control surface is shown as relative resonance units (RU). The double-referenced sensorgrams from each injection series were analyzed for binding kinetics using the BIAevaluation software (GE Healthcare). Dissociation constants were calculated from the on- and off-rates (k_a and k_d, respectively), as determined by global fitting of the experimental data to a 1:1 Langmuir binding model ($Chi^2 < 1$). In addition, using the BIAevaluation software, the steady state affinities were determined for binding systems that exhibited fast association and dissociation constants and ultimately reached equilibrium during the applied injection times.

Cell lines and culture conditions.

The human glioblastoma cell line U87MG and the breast cancer cell line MDA-MB 468 were purchased from American Type Culture Collection (ATCC, Manassas, VA, US). The U87MG sublines U87MG.EGFR and U87MG.EGFRvIII, which over-express exogenous wild type EGFR and the EGFR type III variant (EGFRvIII), respectively, were obtained from the Ludwig Institute for Cancer Research (La Jolla, CA, USA), where they have been established and characterized previously (Nagane et al., 1996; Nishikawa et al., 1994). The glioblastoma cells were maintained in Dulbecco's modified Eagle's medium (DMEM) supplemented with 10% fetal bovine serum and 2 mM glutamine (Hyclone, Logan, UT, USA) at 37°C in a humidified atmosphere of 5% CO_2. The sublines U87MG.EGFR and U87MG.EGFRvIII were additionally kept under selective pressure in 400 µg/ml G418 (Geniticin®, Invitrogen, Grand Island, NY, US). The EGFR over-expressing human breast cancer cell line MDA-MB 468 was maintained in Leibovitz L-15 medium supplemented with 10% FBS and 2 mM glutamine (Hyclone) at 37°C under humidified atmosphere.

Flow cytometry

Semi-confluent U87MG cells were harvested by the addition of cell dissociation buffer (Sigma-Aldrich). A cell suspension containing 5×10^5 cells in 200 µl PBS/10% FBS was incubated with the indicated amounts of monovalent and bivalent sdAbs, as well as the two control anti-EGFR antibodies 225 and H11

(Lab Vision, Thermo Scientific, Fremont, CA, US). Following washes with PBS/10% FBS, the primary antibody was detected with anti-mouse Alexa Fluor® 488 secondary antibody (1:200, Life Technologies) and anti-human FITC secondary antibody for the commercial antibodies and the bivalent sdAbs, respectively. Monovalent sdAbs required an additional step of labeling with 1:500 dilution of anti-c-myc antibody (9E10, Santa Cruz Biotechnology, Inc, Santa Cruz, CA, US) prior to adding the fluorescently labeled antibody. Fluorescence analyses were performed on 10,000 viable cells gated on forward scattering, side scattering parameters and propidium iodide dye exclusion using a Coulter EPICSTM XL-MCL flow cytometer (Beckman-Coulter, Miami, FL) and standard filter set.

Affinity labeling of cell surface EGFR and EGFRvIII with [^{125}I]- EG2 sdAb

Radiolabeling was carried out using the [^{125}I]-Bolton-Hunter Reagent (PerkinElmer Life Sciences, Boston, MA, USA), which reacts with amino-groups of the protein through the formation of an amide bond (Bolton and Hunter, 1973). According to the manufacturer's instruction the benzene in the vial was evaporated and the reagent was dissolved in 15 µl 0.1 M sodium-borate buffer (pH 8.5) containing 15 µg EG2. The solution was incubated on ice for 15 minutes and frequently vortexed. 15 µl of sodium borate buffer were added again after 15 and 30 minutes of incubation. Finally the reaction was terminated through the addition of 165 µl 0.2 M glycine in sodium-borate buffer after 45 minutes. The mix of labeled protein and free reagent was loaded on a PD-10 pre-packed column (Amersham Biosciences, Uppsala, Sweden) and eluted with 0.05 M phosphate buffer (pH 7.5)/0.075 M NaCl/0.1% BSA. The fractions with highest amount of counts per minute (cpm) were pooled and aliquoted.

For cell binding experiments on the U87MG cell line panel 5×10^5 cells were seeded in duplicate wells in gelatin coated 6-well plates and allowed to adhere for 48 hours. 20 nM [^{125}I]-EG2 was added to the wells either treated or untreated with 2.5 µM unlabeled EG2. Plates were incubated for 2 hours at 4°C. SdAbs were cross-linked with 1 mM freshly prepared BS^3 (Pierce, Rockford, IL, USA) for 5 minutes. Cells were dissolved and cell lysates were separated in 8% SDS-PAGE.

The dried gel was exposed to a phosphorimage plate for 10 days, which was then scanned with a Typhoon Trio+ variable mode scanner (Amersham Biosciences, Uppsala, Sweden) using the storage phosphor mode.

In order to compare EGF receptor expression levels, cell lysates of the U87MG cell line panel were separated in a 10% SDS-PAGE and transferred on nitrocellulose membrane. The anti-EGFR cytoplasmic domain antibody, EGFR 1005 (sc-03) (Santa Cruz Biotechnology, Santa Cruz, CA, US), was used to detect the total amounts of EGF receptors by Western Blot.

[^{125}I]-EG2 competition binding assay

U87MG.EGFR and U87MG.EGFRvIII cells, 4 x 10^4, and MDA-MB 468 8×10^4 were seeded in gelatin-coated 48-well plates (Corning Incorporated, NY, USA) and grown in complete media for 48 hours. Wells were then washed twice with complete phosphate buffered saline, 0.9 mM Ca_2Cl, 0.49 mM Mg_2Cl (PBS^{++})/0.1% BSA and incubated with 20 nM [^{125}I]-EG2 and serial dilutions of unlabelled EG2 (0.01–10 μM) for 2 hours at 4°C. After three consecutive washing steps, cells were dissociated for 30 minutes in solubilization buffer (20 mM Tris, 1 mM EDTA, 10% (v/v) glycerol, 1% (v/v) Triton-X-100, pH 7.4) and transferred into plastic vials. The amount of radioactivity was counted in an automatic gamma counter (Wallac Wizard 1470, PerkinElmer Life Sciences, Boston, MA, USA). The resulting data points were fitted by non-linear regression to a one-site binding model using the GraphPad Prism software (La Jolla, CA, USA).

Confocal microscopy

5 x 10^4 cells were seeded in gelatin-coated 8-well glass chamber slides (Labtek, IL, USA) 48 hours prior to the experiment. Cells were washed three times in ice-cold PBS^{++}/0.1 % BSA and fixed in 4% paraformaldehyde (in PBS, pH 7.2) for 10 minutes at room temperature. The cells were then permeabilized for 5 minutes by adding 100 μl of 0.15% Triton-x-100 per well. In the experiments that required exclusively cell surface labeling, this step was omitted. The primary antibodies were added at 100 nM for EG2-hFc, EG10-hFc and 225 and at a dilution of 1:500 for anti-EEA1 antibody (BD Transduction Laboratories)

for 2 hours at room temperature. Wells were washed quickly with PBS^{++}/0.1% BSA and the corresponding secondary antibodies (Alexa Fluor® 488 and Texas Red®, Life Technologies, Grand Island, NY, US) were added at 1:500 dilutions for 1 hour at room temperature in the dark. Nuclei were counterstained using DRAQ5™ (biostatus limited, UK) and mounted in ProLong Gold (Life Technologies) as directed by the manufacturers.

Confocal images were taken on a laser scanning microscope (LSM) Pascal (Carl Zeiss Inc. Toronto, ON, Canada) equipped with a 30 mW Ar Ion laser (458/488/514 nm) and two 1 mW HeNe lasers (633 nm and 543 nm). Slides were visualized with 63× oil plan apo objective in the LSM 5 Image Browser software (Carl Zeiss). Acquisitions were carried out using 0.7 µm optical slices. Laser settings are indicated individually for each experiment. The 12-bit images were exported and analyzed using the free LSM 5 image examiner software (Carl Zeiss).

Western Blot analysis

U87MG and U87MG.EGFR cells were seeded in 6-well plates and allowed to adhere for 24 hours. U87MG cells were treated with 1 µM and 10 µM EG2, 0.5 µM EG2-hFc or 1 µM V2C-EG2. The control treatments were 10 nM 225, 1 µM AG1478 and mock-treatment with vector (PBS) alone. The cells were grown in the presence of antibody fragments and controls for 2.5 hours at 37°C. At the end of the incubation time 100 ng/ml EGF were added to half of the wells for 5 minutes. After treatment cells were washed twice with ice-cold PBS, lysed by sonication in radioimmunoprecipitation assay (RIPA) buffer and stored at -80°C. Protein concentrations were estimated with a BCA Protein Assay kit (Bio-Rad, Hercules, CA, US) and 20 µg of lysate were subjected to 8% SDS-PAGE followed by Western Blot analysis with the indicated antibodies and detected by chemoluminescence (Amersham Biosciences, Piscataway, NJ, US).

Growth assay

In a 96-well plate 3000 cells/well of each cell line were seeded and allowed to adhere over night. Triplicate wells were then treated with 5 µM monovalent

single domain antibodies (EG2, EG10, EG31 and EG43), 5 μM pentavalent V2C-EG2, 1 μM EG2-hFc or 10 μM AG1478. The final volume of each sample was 100 μl in DMEM containing low (1%) or high (10%) concentrations of serum. After 72 hours, 10 μl Alamar Blue® (Invitrogen) solution was added per well and the fluorescence was measured at 530 nm emission and 590 nm excitation in a CytoFluor® Microplate Reader (PerSeptive Biosystems, Framingham, MA, USA) after 2 and 4 hours. Values for control cells were considered 100% viability.

2.3 Results

2.3.1 Protein size and purity

Analysis of the four single domain antibodies, which I obtained from our collaborators in Roger MacKenzie's lab at the NRC-IBS, by gel electrophoresis under reducing and non-reducing conditions and subsequent Coomassie staining resulted in one distinct gel band for each protein, indicating that the sdAbs are of high purity (Figure 2-1 A). Additional Western Blotting for the C-terminal 6× His-tag also showed one distinct band for each sdAb. The EG2 single domain antibody ran higher in the gel than the three other sdAbs, which is in good agreement with its greater predicted molecular weight of approximately 16 kDa. Similarly, the dimer EG2-hFc and the pentamer V2C-EG2 were determined to be of high purity and showed distinct bands in the Coomassie stained gel (Figure 2-1 B). EG2-hFc resolved according to its predicted size of 80 kDa under non-reducing conditions, and at about half that size when reducing agent was added to the loading buffer. As expected, the five subunits of V2C-EG2 dissociated under reducing and non-reducing conditions, and ran at the predicted size of 23 kDa. Our collaborators showed by size exclusion chromatography (SEC) that the pentamer subunits remain associated in solution (Bell et al., 2009). The EGFR extracellular domain also ran as single distinct band near its predicted MW of 80 kDa, confirming the absence of aggregates and degradation products (Figure 2-1 C). These results demonstrate that the proteins I used for Biacore analysis were of excellent purity. In addition, size determination by gel electrophoresis reproduced

the results of our collaborators, thus indicating that the proteins remained stable after shipping.

In addition to SDS-PAGE, I determined the size and dispersity of the proteins in solution by dynamic light scattering (DLS), which is expected to provide information comparable to SEC. DLS measures the diffusion coefficient ("Brownian motion") of proteins in suspension. At a defined temperature and known viscosity of the solute, the diffusion coefficient relates to the size of the protein. This relationship is known as the Stokes-Einstein relationship and can be used to calculate the hydrodynamic diameter of a protein, from which the molecular weight can be derived (Online tutorial, Malvern Instruments Ltd, Worcestershire, England). EG2, EG10, EG43, EG2-hFc and EGFR-ECD showed narrow size distributions consistent with their predicted molecular weights, with the exception of V2C-EG2, which showed a significantly larger hydrodynamic diameter, thus indicating the presence of aggregates in solution (Figure 2-2).

2.3.2 Biacore SPR biosensor analysis

Kinetic analysis of monomeric sdAbs.

I determined the kinetic constants of the four sdAbs for binding to purified recombinant protein of the extracellular domains of the wild-type and mutant receptor, EGFR-ECD and EGFRvIII-ECD, by surface plasmon resonance. For each single domain antibody, serial dilutions (ranging from 3.7 nM to 1 μM) were injected over the same EGFR-ECD and EGFRvIII-ECD chip surfaces, which displayed receptor densities of 500 and 300 RU, respectively. Global fitting of the binding data to the 1:1 Langmuir binding model in the BIAevaluation software allowed the determination of the rate constants k_a and k_d, as well as the affinity constant K_D for all eight interactions (Figure 2-3 and Figure 2-4, left column; Table 1). The quality of the fittings was excellent with Chi^2 values smaller than 1 for all eight interactions. Since all antibody fragments exhibited fast association constants and therefore reached equilibrium (i.e. association equals dissociation = steady state) during the chosen experimental association time, it was possible to also determine the steady state affinities for these interactions in the

BIAevaluation software (Figure 2-3 and Figure 2-4, middle column). The affinities generated from steady state analysis (K_D^s) were comparable to the values obtained from Langmuir global analysis of the binding data (Table 1).

I obtained linear Scatchard plots for the interactions of the sdAbs with wild-type and mutant EGFR-ECD (Figure 2-3 and Figure 2-4, right column), which indicates that the investigated interactions follow a simple 1:1 binding mechanism (van der Merwe, 2000). I identified EG2 as the highest affinity binder for both receptors with K_D-values of 50 ± 6 nM and 98 ± 10 nM for EGFR-ECD and EGFRvIII-ECD, respectively. The differences in affinity between the four antibody fragments is mainly caused by their varying dissociation rate constants, whereas the association rates are relatively similar (Table 1), e.g. the k_d of EG2 is more than seven times slower than that of the lowest affinity binder EG31. A visual comparison illustrating the relative contributions of association and dissociation rates to the overall affinity difference is shown in Figure 2-5. The arrows indicate the range of variability in association and dissociation for the four investigated sdAbs.

Epitope mapping of monomeric sdAbs.

Monomeric sdAb fragments were then investigated for their ability to compete for binding to the EGFR-ECD among each other, as well as with the ligand EGF. For this experiment EG2 and EG43 were each immobilized on a Biacore chip at densities of 300 RU and 50 RU, respectively. Then, EGFR-ECD in the presence of increasing amounts of sdAbs or ligand was injected over the surface. Figure 2-6 A shows that EG2 successfully competes for binding with itself, as well as with EG43. Correspondingly, it is shown in Figure 2-6 B that EG43 competes for binding with itself as well as with EG2. Neither EG10, EG31 nor EGF competed with EG2 and EG43. Since neither EG10 nor EG31 bind EGFR-ECD in its solution conformation, competition among these two antibody fragments could not be investigated.

Analysis of thermal stability

The ability of the EG2 antibody to retain its binding properties towards EGFR-ECD at high temperatures was assessed. In one experiment, EG2 aliquots were incubated at 37°C for up to 50 hours. At several time points 100 nM dilutions were injected over a 400 RU EGFR-ECD surface and overall binding was measured. Figure 2-7 A shows the binding response in % relative to the control EG2 antibody, which had not been transferred to 37°C. The experiment showed that prolonged incubation at physiological temperature did not alter the affinity of the single domain antibody.

In the second experiment, EG2 aliquots were kept for 5 hours at temperatures between 4°C and 80°C. The affinity remained constant up to 60°C. At 70°C a decrease in affinity is observed and after 5 hours at 80°C the antibody fragment had lost 30% of its original activity (Figure 2-7 B).

Kinetic analysis of multimeric sdAb constructs.

Based on the above kinetic information, I then chose the two highest affinity binders, EG2 and EG10, which in addition do not share the same epitope on EGFR, for further investigation. As an approach to assess their potential to function as targeting moieties on the surface of iron oxide nanoparticles, I investigated their ability to interact with their target when presented in the context of multimeric constructs. Our collaborators at the NRC-IBS generated two dimeric and one pentameric construct derived from these monomeric binding units, using either a human IgG Fc domain or a verotoxin subunit as molecular scaffolds (Zhang et al., 2009; Zhang et al., 2004). The resulting constructs were termed EG2-hFc (dimeric EG2), EG10-hFc (dimeric EG10) and V2C-EG2 (pentameric EG2).

I first tested these novel constructs by SPR to investigate whether they retained their ability to bind EGFR-ECD and EGFRvIII-ECD. Figure 2-8 shows the sensorgrams obtained for the injection of serial dilutions of the monovalent and multivalent constructs over the same EGFR-ECD Biacore surface. As shown previously (Figure 2-3, Figure 2-4), the binding of monovalent antibodies to EGFR-ECD is characteristic of a simple 1:1 interaction shown by the fit to the Langmuir binding model (Figure 2-8, top row). In contrast, the sensorgram shapes

obtained for the two dimeric sdAbs and the pentavalent construct are significantly altered. Global fitting of the binding data in the BIAevaluation software showed the best fit when applying the bivalent analyte model (Figure 2-8). Apparent affinities on a 400 RU EGFR-ECD surface of 0.7 nM, 0.5 nM and 4 nM were obtained for EG2-hFc, EG10-hFc and V2C-EG2 respectively. This increase in apparent affinity resulting from multivalency is termed avidity, however the possibility that the scaffold structures are contributing to the improved affinity cannot be excluded at this point.

In order to further investigate the impact of avidity on the binding of multivalent constructs to immobilized targets, I next investigated the behavior of these constructs on three EGFRvIII-ECD chip surfaces with receptor densities of 300, 600 and 1400 RU, respectively (Figure 2-9). All constructs showed comparable binding to EGFR-ECD surfaces, confirming that none of the constructs differentiated significantly between the two receptor variants. Apparent affinities of 0.6 nM for EG2-hFc and 8 nM for V2C-EG2 binding to EGFRvIII-ECD were determined. After normalization of the sensorgrams obtained for 500 nM injections of sdAb constructs over the three surfaces, it can be seen that monomeric EG2 showed comparable sensorgram shapes for all surfaces, whereas the dimer EG2-hFc and the pentamer V2C-EG2 demonstrated a decrease in dissociation rate with increasing EGFRvIII-ECD chip surface densities. These findings are again illustrated in Figure 2-10 for binding of these constructs to three different EGFR-ECD surfaces, in which the dissociation rate constants, obtained from global fitting of the binding data, are plotted over the association rate constants for each of the investigated constructs. The graph shows that while the target density does not affect the association rate constants, the dissociation rate constants demonstrate clear dependence on the amount of EGFR-ECD immobilized on the chip surface. This experiment emphasizes the impact of surface receptor density on the measured apparent affinity (avidity) of multivalent constructs and illustrates how one should be careful when reporting these numbers. These two experiments additionally demonstrated that the avidity effect induced by the pentameric construct appears to be less efficient compared to the

dimer, since the decrease in off-rate observed for V2C-EG2 is less prominent, despite its multiple binding units.

I then decided to investigate whether the individual monomeric binding units on the multivalent scaffolds retained their original affinity for EGFR-ECD. I immobilized the different single domain antibody formats (monovalent EG2, bivalent EG2-hFc, and pentavalent V2C-EG2) on sensor chip surfaces and flowed serial dilutions of EGFR-ECD over these surfaces. This new experimental set-up allowed for the investigation of the interactions in the absence of avidity, since the analyte (EGFR-ECD) is monomeric. Hence, the simple 1:1 Langmuir binding model could be applied to describe the interactions. The results in Figure 2-11 indicate comparable sensorgrams for all three immobilized EG2 formats. K_D-values of 247 ± 37 nM, 143 ± 54 nM and 307 ± 30 nM were obtained for immobilized EG2, EG2-hFc and V2C-EG2, respectively. These results confirm that the increase in apparent affinities, observed when the multivalent constructs were binding to immobilized EGF receptors, were primarily mediated by avidity effects. The overall lower affinities for the EG2/EGFR interactions in this experimental orientation may have been caused by surface heterogeneities of the immobilized proteins due to random amino-coupling to the carboxymethyl matrix on the sensor chip, which may have resulted in obstruction or distortion of the EG2 paratope. On a side note, EGFR-ECD binding to immobilized EG43 also produced slightly lower affinities compared to the K_D-values measured when binding was analyzed in the inverse orientation, herein K_D = 602 ± 59 nM was obtained for EGFR-ECD as analyte and K_D = 311 ± 18 nM for EG43 as analyte.

Competition binding study

In the next experiment I assessed the potential of these three constructs to compete with each other for binding to EGFR-ECD. I used the same surfaces as in the previous experiment and injected again serial dilutions of EGFR-ECD, however this time in the presence of increasing amounts of competitor construct. As expected, EG2 competed for binding to EGFR with itself, EG2-hFc and V2C-EG2 (Figure 2-12 A). The same held true for EG2-hFc (Figure 2-12 B). However, whereas the pentameric construct V2C-EG2 successfully competes with EG2 and

EG2-hFc for binding to the receptor extracellular domain, it did not compete itself (Figure 2-12 C).

Analysis of the commercial anti-EGFR mAb 225

I was interested in employing the commercial anti-EGFR antibody cetuximab (225) as a reference antibody in the following cell-based assays, since our group and others have intensely investigated its specificity and binding properties in the past (Kamat et al., 2008; Li et al., 2005). Cetuximab was developed 20 years ago from a panel of antibodies that were derived from mice immunized with A431 epidermoid carcinoma cells, which express large amounts of EGFR. This antibody, marketed under the name Erbitux, has been the center of intensive study for its use as an anticancer agent and was approved by the FDA in February 2004 for use in treating advanced stage EGFR expressing colorectal cancer (Graham et al., 2004). I immobilized 225 by random amino-coupling at 200 RU on a CM5 Biacore chip and flowed EGFR-ECD and EGFRvIII-ECD in serial dilutions ranging from 3.7 nM to 1 μM. By fitting the data to the 1:1 binding model in the BIAevaluation software I obtained K_D-values of 2.8 nM and 26.1 nM for EGFR-ECD and EGFRvIII-ECD, respectively (Figure 2-13).
In the next experiment, I injected 500 nM EGFR-ECD pre-incubated with increasing amounts of monomeric EG2 (0.25 – 5 μM) over an 830 RU EG2 and 620 RU 225 surface. The overall response relative to binding of EGFR-ECD in the absence of EG2 is plotted over the concentration of competitor EG2 in Figure 2-14. Whereas binding to the EG2 surface decreased in the presence of increasing amounts of competitor EG2, binding to the 225 surface showed no competition. On the contrary, an increase in binding was observed with increasing amounts of competitor EG2, reaching saturation at approximately 1 μM. These results are consistent with 225 and EG2 binding to independent epitopes.

2.3.3 Cell-based assays

Flow cytometry

Next I investigated binding of the four single domain antibodies to the full-length receptors, EGFR and EGFRvIII, expressed on the U87MG

glioblastoma cell line panel. The parental cell line is known to express 5×10^4 wild-type receptors/cell (Johns et al., 2002). In contrast, U87MG.EGFR cells over-express the wild-type receptor and reportedly have cell surface expression levels of approximately 10^6 receptors/cell (Luwor et al., 2004). The U87MG.EGRvIII cell lines expresses $4 \times 10^5 – 1.3 \times 10^6$ mutant receptors/cell and endogenous wild-type EGFR expression levels are comparable to the parental cell line (Nishikawa et al., 1994) (Figure 2-17). One million live cells in suspension were incubated with 2.2 μM sdAbs for 2 hours at 4°C. The secondary antibodies anti-c-myc and fluorescently labeled anti-mouse were used to detect the bound fraction of single domain antibodies on the cells. The counted fluorescence for each sdAb on the three cell lines is shown in Figure 2-15. The highest fluorescence was seen for EG2 binding to the receptor over-expressing cell lines U87MG.EGFR and U87MG.EGFRvIII, followed by EG10 and EG31. The sdAb EG43, which showed comparable affinity to EG31 in the SPR analysis, does not appear to bind to any of the cells. However, a sterically obscured c-myc tag could be responsible for the lack of detection. Since EG43 was not one of the candidates chosen for further analysis, due to its low affinity, the possibility of the c-myc tag being defective was not further investigated.

The bivalent single domain antibody constructs EG2-hFc and EG10-hFc were also investigated by flow cytometry. By direct comparison, EG2-hFc labeled U87MG cells that over-express either EGFR or EGFRvIII (U87MG.EGFR and U87MG.EGFRvIII) showed more fluorescence than the same cells labeled with monovalent EG2 (Figure 2-16 A). In contrast, the same amount of fluorescence was observed for EG2 and EG2-hFc labeling on the parental cell line with low receptor expression levels (Figure 2-16 B). Surprisingly, no fluorescence was observed on all cell lines labeled with EG10-hFc (Figure 2-16 C).

Next, I wanted to investigate how EG2-hFc binding compared to the two commercial antibodies 225 and H11 (Ab-5), which both reportedly recognize wild-type EGFR and mutant EGFRvIII (Cochran et al., 2004). When labeling the three U87MG cell lines using these three antibodies, I observed that the ratio of fluorescent signal intensities between the three cell lines was comparable for each

antibody (Figure 2-16 C); i.e. in each case the fluorescence on the parental cell line corresponded to approximately 8% of the amount measured on labeled U87MG.EGFR cells, and the fluorescence measured on U87MG.EGFRvIII cells corresponded to about 66% of the intensity on U87MG.EGFR cells.

[^{125}I]-labeled monomeric single domain antibodies

To further analyze the affinity and specificity of the two lead single domain antibodies, EG2 and EG10, towards the full-length receptors in cell binding studies, the fragments were labeled with iodine-125. The advantage of using radioactive instead of fluorescent labels is the superior sensitivity of measuring radioactive counts in a gamma counter compared to the optical quantification of fluorescent tracers by spectrophotometry or flow cytometry. The introduction of a radiolabel is a crucial step, since it modifies the protein and might affect its binding to the target due to distortion of the protein fold that is needed for optimal affinity, or due to modification of amino acids involved in molecular recognition. Therefore, in order to assess their specificity, I covalently coupled the radiolabeled monomeric single domain antibodies EG2 and EG10 to the surface of the three U87MG cell lines using the cross-linking agent BS^3, which is a homobifunctional cross-linking reagent with amine reactivity. The cells were incubated for 2 hours at 4°C with [^{125}I]-sdAbs in the presence and absence of excess amounts of unlabeled antibodies and were subsequently treated with the cross-linking agent. The cells were then lysed and the cellular proteins were separated in 8% SDS-PAGE. The dried gels were exposed to a radiosensitive plate for ten days before reading. The intensity of the observed bands for the three U87MG cell lines labeled with [^{125}I]-EG2 correlates with the EGF receptor amounts detected by Western Blot (Figure 2-17). Wild-type EGFR reportedly runs as a single band with a molecular weight of approximately 175 kDa, whereas the mutant EGFRvIII is observed as two distinct bands of about 145-155 kDa in size, which are thought to represent two distinct post-translationally modified variants (Nishikawa et al., 1994). As expected, the lowest signal intensity was seen on the parental cells, which express ten times less EGF receptors compared to the EGFR and EGFRvIII over-expressing cell lines. The double bands observed

after radioactive labeling of U87MG.EGFRvIII cells run slightly lower in the gel indicating that the [^{125}I]-EG2 bound specifically to EGFRvIII (Figure 2-17 B). The intense band observed for labeled U87MG.EGFR cells corresponds to the large amount of EGF receptor expressed in these cells. Importantly, all bands were competed when an excess amount of unlabeled EG2 was added to the cells during cross-linking.

In a second cross-linking experiment, in which I only chose to use the receptor over-expressing cell lines, I also tested the specificity of [^{125}I]-EG10 for binding to full-length EGFR and EGFRvIII. Curiously [^{125}I]-EG10 recognized a band of smaller molecular weight than [^{125}I]-EG2 in the same assay. This band was also competed when an excess amount of unlabeled EG10 was added during cross-linking. Comparable intensities of this band were detected in U87MG.EGFRvIII and U87MG.EGFR cells (Figure 2-17 C).

Due to the fast dissociation rate of the monovalent antibody fragments their binding affinities could not be evaluated by flow cytometry. Accordingly, their affinities for cell surface expressed receptors were determined using competition binding studies with monovalent and bivalent competitors on U87MG.EGFR, U87M.EGFRvIII and MDA-MB 468 cells, all of which exhibit receptor expression levels of approximately 10^6 receptors/cell. In a homologous binding experiment the IC_{50} is the concentration of unlabeled competitor that reduces specific binding of labeled ligand by 50% (GraphPad Prism online tutorial). An IC_{50} value of 197 ± 147 nM was identified for binding of monovalent EG2 to wild-type EGF receptor expressed on the surface of MDA-MB 468 breast cancer cells (Figure 2-18 A). Competition binding on the two glioblastoma cell lines U87MG.EGFRvIII and U87MG.EGFR generated IC_{50} values of 60 ± 1 nM and 95 ± 47 nM, respectively (Figure 2-18 B, C). When plotting [^{125}I]-EG2 binding in % over competitor (cold EG2 or EG2-hFc) concentration, it becomes clear that the bivalent antibody more efficiently competes the radiolabeled EG2 sdAb from the cell surface of U87MG.EGFR cells (Figure 2-18 D). However, due to the relatively high concentration of [^{125}I]-EG2 (20 nM) in the competition experiment, these IC_{50} values are expected to underestimate affinities (for a more

accurate measure of affinity the concentration of radioligand should be much lower than the K_D of the competitor (Graph Pad Prism)). However, in my experiments I was not able to reduce the amount of [^{125}I]-EG2 below 20 nM, because the signal became too low for detection.

Confocal microscopy

Cell-labeling experiments for confocal microscopy analysis were carried out using exclusively the bivalent single domain antibody format. The reason for this choice was that the monomeric sdAbs needed to be detected with anti-c-myc antibody first, before applying the fluorescently labeled anti-Fc secondary, which required additional washing and incubation steps that resulted in very low overall fluorescence on the cells due to the fast dissociation rate of the monovalent fragment. The alternative would have been direct fluorophore labeling of the monovalent sdAbs. However, it was previously shown that the method of mAb labeling used could influence the selectivity and specificity of mAb distribution *in vivo*, which was attributed to the charge of the label (Kuan et al., 2000). This charge difference could affect the internalization properties of the sdAbs, which I intended to investigate in this study in order to assess the likeliness of the iron oxide nanoparticles to enter the cells when conjugated with sdAbs. The higher apparent affinities of the available dimeric constructs, in addition to their easy detection with fluorescently-labeled anti-human Fc secondary antibodies, made this an obvious choice rather than considering time-consuming and expensive direct fluorophore-labeling of the monovalent sdAb fragments. The pentavalent format was not considered, since the analysis of the protein revealed that it might form aggregates in solution (see DLS data - Figure 2-2), and in the Biacore competition experiment it demonstrated binding to itself, thus furthermore questioning its stability in solution (Figure 2-12). Another reason was that the pentamer would have required two secondary antibodies for detection (the first against the verotoxin scaffold followed by the fluorescently labeled antibody), if direct labeling steps were to be avoided.

In the first experiment, I assessed the overall labeling pattern of EG2-hFc for the three U87MG cell lines with different receptor expression levels. Hence, this is an

investigation similar to the flow cytometry study in Figure 2-15, but in this case the assessment would be visual instead of quantitative, i.e. additional information about the distribution of the antibody on the cell surface could be gained. In addition to investigating untreated cells, I also activated the EGF receptor with 100 ng/ml EGF for five minutes prior to fixation, which induces its rapid internalization. The receptors are then transferred to early endosomes and later either recycled back to the cell surface or degraded within lysosomes; a phenomenon referred to as EGF-induced down-regulation of EGFR (Sorkin and Goh, 2008, 2009). The confocal images of the permeabilized cells show that in untreated U87MG.EGFR cells the EG2-hFc-labeled EGF receptor is distributed evenly on the cell surface as well as in clusters at the protruding extensions of the cells (Figure 2-19, top row). Upon stimulation with EGF the cellular distribution of EGFR rapidly changes and numerous clusters, probably intracellular vesicles, are observed throughout the cytoplasm, but predominantly in the perinuclear area. U87MG.EGFRvIII cells also show prominent receptor labeling at the protruding edges of the cell, but additionally a significant amount of receptor can be found in clusters in the perinuclear area, even in the absence of EGF stimulation. This pattern is not significantly altered upon treatment with EGF (Figure 2-19, middle row). In contrast to the receptor over-expressing cell lines, the parental cell line exhibits significantly less overall fluorescence after labeling with EG2-hFc. Nevertheless, following stimulation with EGF, clusters in the perinuclear area can also be observed (Figure 2-19, bottom row). This experiment showed that detection of EGF receptors on EGF treated and non-treated cells using EG2-hFc reflected the expected cell surface and cytoplasmic distribution patterns of EGFR and EGFRvIII.

Next, I addressed the question how EG2-hFc binding to EGFR and EGFRvIII over-expressing cell lines compared to binding of the commercial 225 mAb on the same cells. This time I also included non-permeabilized cells in my investigation in order to distinguish surface-expressed EGF receptors from total receptors present both inside and outside of the cells. In Figure 2-20 A and B, fixed U87MG.EGFR cells, some of which were treated with EGF as indicated, were

labeled with either EG2-hFc or 225 mAb. Panel A shows the amount of cell-surface expressed EGFR and it can be observed that for both antibodies the amount of fluorescence decreases after cells were treated with EGF. For permeabilized cells stimulated with EGF, similar intracellular granular staining, most of which is localized in the vicinity of the nucleus, can be seen by detection with EG2-hFc as well as with 225 mAb (Figure 2-20 B). For U87MG.EGFRvIII cells, the observation that EGF induced relatively insignificant changes in fluorescence intensity and distribution was striking, and was equally obvious with both antibodies (Figure 2-20 C, D). Comparable results were found for the EGFR over-expressing human breast cancer cell line MDA-MB 468, in which both antibodies detected an EGF-induced decrease in fluorescence on non-permeabilized cells, and perinuclear vesicle formation in EGF-treated and subsequently permeabilized cells (data not shown).

The results so far indicate that EGFR and EGFRvIII recognition by EG2-hFc is comparable to 225 binding. The ultimate approach to assessing whether these two antibodies bind to the same target is a colocalization experiment. I therefore simultaneously labeled EGF treated and untreated parental U87MG cells that were fixed and permeabilized with EG2-hFc and 225 and detected these antibodies with fluorescently-labeled anti-human Fc and anti-mouse Fc antibodies emitting at 488 nm and 543 nm, respectively. (Note: the 225 antibody I was using in this study is the original mouse antibody and not the humanized version). In Figure 2-21, EG2-hFc labeling is shown in green and 225 detection is shown in red. When these two fluorophore-emitting signals overlap in the same voxel the resulting signal is shown in yellow. The results demonstrate close to perfect overlay of the fluorescence signals detected in the two channels (Figure 2-21 A). In contrast, EG10-hFc did not colocalize with 225. These results also suggest that the target of EG10-hFc does not become internalized upon EGF stimulation, since there are no visible intracellular clusters (Figure 2-21 B).

EGFR is known to locate to early endosomes shortly after its internalization (Sorkin and Goh, 2008). I therefore wanted to investigate whether the EG2-hFc antibody was able to internalize and follow the receptor into the early endosomal

compartment. Until now, all confocal microscopy studies were carried out on fixed cells. The next experiment addressed the question of the fate of EG2-hFc bound to cell surface of live cells. In this study, I treated U87MG.EGFRvIII and U87MG.EGFR cells for 5 minutes to 2 hours with the bivalent sdAb and stained for early endosomes after cell fixation and permeabilization using an anti-EEA1 antibody. The results are shown in Figure 2-22 A and B, respectively. In the absence of EG2-hFc the anti-EEA1 labeled early endosomes are green, as expected. When the cells were incubated for 5 minutes with EG2-hFc, a faint red staining of the invading edges of the cells can be observed. After 10 minutes, even more antibody was bound to the cells and some yellow (colabeled) endosomes start to appear; more so in the wild-type EGFR over-expressing cells than in the mutant EGFRvIII over-expressing cells. The difference becomes more obvious after 15 minute-exposure to EG2-hFc, when colocalization was observed in nearly all endosomes in U87MG.EGFR cells, while the majority of endosomes in U87MG.EGFRvIII cells remained green. This difference in the amount of colocalization observed between the two EGF receptor types (mutant and wild-type) and EEA1 in the glioblastoma cell lines continues to persist after two hours of incubation in the presence of EG2-hFc. Interestingly, in U87MG.EGFRvIII cells, the antibody appears to localize to intracellular compartments that do not stain positive for EEA1. This experiment demonstrates the ability of EG2-hFc to enter the EGFR over-expressing glioblastoma cells together with the receptor. As well, it shows that internalization appears to be more efficient in cells over-expressing EGFR compared to cells over-expressing EGFRvIII.

Investigation of the phosphorylation status of EGFR by Western Blot

The epidermal growth factor receptor is an intensely researched therapeutic target and monoclonal antibodies that interfere with receptor activation have been developed and are currently used for the treatment of human cancer (Ciardiello and Tortora, 2008; Jonker et al., 2007; Schmiedel et al., 2008). In the next experiment, I investigated whether EG2, in its monovalent or multivalent formats, affects the tyrosine phosphorylation status of EGF receptors in glioblastoma cells with low and high receptor expression levels. I treated

parental U87MG and U87MG.EGFR cells for 2.5 hours with 1 and 10 μM EG2, 0.5 μM EG2-hFc, and 1 μM V2C-EG2. The small molecule inhibitor AG1478 and the monoclonal antibody 225 are both known to inhibit EGF-mediated receptor activation and were therefore included as controls in this assay (Graham et al., 2004; Li et al., 2005; Zhu et al., 2001). After treatment, the cells were dissolved and the lysates analyzed by SDS-PAGE. I subsequently blotted for phosphorylation of tyrosine 1173 to observe the activation status of the intracellular kinase domain of EGFR, and for actin to compare the amount of protein loaded in the gel. The results are shown in Figure 2-23. As expected, relative to the mock-treated (PBS) U87MG and U87MG.EGFR cells, the treatment with 100 ng/ml EGF induced receptor activation. This activation was significantly reduced in cells that were either pre-incubated with 1 μM AG1478 or 10 nM 225. Treatment of both cell lines with monomeric EG2 at concentrations up to 10 μM resulted in activation levels comparable to mock-treated cells. In contrast, EG2-hFc induced receptor activation in cells that were not stimulated with EGF. This increase in tyrosine phosphorylation is more obvious in the EGFR over-expressing cell line than in the parental U87MG cells. Some activation can also be seen in cells treated with V2C-EG2, although much lower than for EG2-hFc.

The effect of sdAb treatment on cell growth and metabolic activity

The effect of single domain antibody treatment on U87MG cells was also investigated in a 3-day exposure assay. The effect of the treatment on cell growth and metabolic activity was assessed at the endpoint of the experiment by adding Alamar Blue® reagent to the culture wells. The Alamar Blue® assay is based on the ability of metabolically active cells to convert the reagent into a fluorescent and colorimetric indicator. Damaged and non-viable cells have lower innate metabolic activity and thus generate a proportionally lower signal (Life Technologies). The results are illustrated by plotting the percentage of measured fluorescence on the treated cells relative to the amount measured on untreated cells (Figure 2-24). The assay was carried out at normal and low serum concentration in the growth media since it is known that the sensitivity of cells to

growth/viability inhibition can be increased under serum-starvation conditions. None of the single domain antibodies significantly affected the viability of U87MG cells after the 3-day exposure period. In contrast, the EGFR inhibitor AG1478 demonstrated substantial inhibition of cell growth and metabolic activity, which was enhanced under low serum conditions.

2.4 Discussion

The search for tumor-specific targeting agents for therapeutic or diagnostic purposes has prompted several groups, including our own, to generate single domain antibodies against the extracellular domain of EGFR (Gottlin et al., 2009; Roovers et al., 2007a) and EGFRvIII (Cochran et al., 2004; Omidfar et al., 2004a; Omidfar et al., 2004b). Roovers and coworkers derived several EGFR-specific VHH domains from a llama immunized with EGFR-positive A431 cells. These VHH domains acted as antagonists, blocking EGF-induced tyrosine phosphorylation and cell proliferation and delayed tumor outgrowth in a mouse xenograft model (Roovers et al., 2007a). In the study by Gottlin and coworkers, the llama was immunized with a mixture of purified recombinant EGFR and EGFRvIII extracellular domain proteins. After several rounds of selection, they obtained two clones that specifically bound wild-type EGFR and not the mutant, but none of their clones was EGFRvIII specific (Gottlin et al., 2009). Similarly, our collaborators at the Institute for Biological Science (NRC-IBS) in Ottawa immunized llamas with purified recombinant EGFRvIII extracellular domain. I showed that all of these sdAbs recognize both wild-type and mutant receptor extracellular domain (Bell et al., 2010; Iqbal et al., 2010b). I published these results in two separate articles and additional unpublished data is presented in detail in this thesis.

It has traditionally been difficult to generate EGFRvIII-specific antibodies, since the epitope defined by the vIII mutation is small compared to the size of the protein (Pedersen et al., 2001). Of note, Omidfar *et al.* eventually overcame this problem by immunizing camels with a synthetic peptide corresponding to the mutated sequence of EGFR (Omidfar et al., 2004a; Omidfar et al., 2004b). This

approach has also been successfully employed for generating anti-EGFRvIII specific monoclonal antibodies (Yoshimoto et al., 2008).

2.4.1 Physical and structural properties of the novel sdAbs

Four VHH fragments were chosen by our collaborators from a panel of clones for further investigation of their binding properties and target specificity. I carried out these analyses using SPR biosensor technology and cell-based assays. The interpretation of the experimental results will be discussed in the following paragraphs. The sequences of the four sdAbs were determined by our collaborators and have been published (Bell et al., 2009). The calculated molecular weight of the sdAbs ranged from 14.7 kDa to 16 kDa (135–144 amino acids) and their theoretical isoelectric point (pI) varied between 6.30 and 7.22 (c-myc- and 6× His-tag included in calculation). This is useful information, since the molecular charge could also affect their clearance and retention in tumors (Pavlinkova et al., 1999). Similarly, Melkko and coworkers showed in an analysis of 13 derivatives of scFv(L19) (an anti-fibronectin antibody fragment) that molecules with isoelectric points between 5 and 9 had superior tumor penetration as compared to those outside this range (Melkko et al., 2002). The predicted molecular weights of the four sdAbs are in agreement with the size separation observed in a Coomassie-stained protein gel (Figure 2-1 A). Under reducing conditions the protein bands in the 10% poly-acrylamide gel are running higher than under non-reducing. The folded structure of single domain antibodies contains one disulfide bond, which is disrupted in the presence of reducing agent in addition to other intermolecular non-covalent bonds (hydrophobic and electrostatic interactions). The fully unfolded protein is therefore less compact than it would be in its partially unfolded (non-reduced) state and hence is expected to run slower through the gel. Most importantly, the Coomassie-stained gel showed no traces of aggregates or degradation products, hence demonstrating the excellent quality and purity of the VHH fragments investigated in this study. Analysis of the four sdAbs by dynamic light scattering, which allows the assessment of proteins in their solution states, confirmed their narrow size

distribution, except in the case of EG31, where small amounts of high MW contaminants affected the mass-weighted measurement (Figure 2-2). In the subsequent Biacore analysis, which was also carried out in solution, the presence of aggregates in the EG31 protein preparation could have caused deviations away from a simple binding model, however, this was not obvious.

Single domain antibodies contain three complementarity-determining regions (CDRs). Among the four anti-EGFR sdAbs EG2 exhibits the longest CDR3 region composed of 16 amino acid residues, whereas the other antibody fragments have shorter CDR3 loops of 14, 8, and 8 residues for EG10, EG31 and EG43, respectively. Short CDRs of approximately six amino acids have been reported for other llama VHHs, whereas long CDR1 and CDR3 regions are characteristic for dromedary sdAbs and frequently contain another disulfide bond to improve stability of the binding loop (Harmsen et al., 2000; Vu et al., 1997). It is not unusual for VHH antigen binding loops to adopt conformations other than the conserved canonical structures documented for human VH3 domains and the involvement of backbone residues in antigen binding has also been reported (Decanniere et al., 1999; Decanniere et al., 2000; Muyldermans et al., 2001; Nguyen et al., 2000). The great variety of CDR lengths observed in this panel of sdAbs therefore suggests the presence of several loop conformations, perhaps some of which have not been described yet.

Several studies have focused on the investigation of the amino acid composition in antibody paratopes. Summarizing these efforts, Olson and colleagues concluded that tryptophan, tyrosine, serine and asparagine residues were most abundant in the CDR domains of antibodies (Mian et al., 1991). With this information in mind, I analyzed the CDRs of the four VHH fragments and discovered that five of the eight tyrosine residues in the EG2 sequence were located within its antigen binding loops (three in CDR3). With only one tyrosine less than EG2, EG43 also displayed increased presence of tyrosine residues in or near the CDRs (two in CDR3, which, however, is only half as long as the CDR3 of EG2). Interestingly, I showed that these two VHH fragments share the same epitope on the extracellular domain of EGFR (Figure 2-6), which could indicate

that binding to this region on EGFR-ECD requires hydrophobic interactions. In contrast, EG10 contains multiple serine residues in its CDRs (six out of the eight in the whole sequence). The presence of polar residues within the antigen binding loops points towards electrostatic interactions as mediators of binding. Another interesting observation was seen with regards to the distribution and occurrence of lysine residues in the sdAb sequences. The lysines are of interest, because in the standard immobilization procedure for SPR sensor chips, primary amino-groups on the protein are linked to the carboxymethyl dextran surface using NHS/EDC coupling chemistry. Amino-groups are found on lysine residues, as well as the N-terminus of the protein. The number of lysine residues in the sequences of this sdAb panel varied from three to six. Also, the c-myc tag at the C-terminus provided an additional lysine for coupling.

One predominant feature of single domain antibodies is their superior stability when exposed to high temperatures or extreme pH, which is thought to arise from the ability of the protein to refold correctly after denaturation. I investigated the thermal stability of the EG2 antibody and observed that it retained its original activity even after 50-hour incubation at 37°C (Figure 2-7 A). In addition, incubation for 5 hours at 80°C only reduced its activity by 30% (Figure 2-7 B). These results compare well with previous reports that showed melting temperatures (T_m) of VHHs in the range of 60 - 80°C and approximately 60% recovered activity after heat denaturation and 80% after one week incubation at 37°C (Arbabi Ghahroudi et al., 1997; Dumoulin et al., 2002; Ewert et al., 2002; van der Linden et al., 2000). In contrast, fragments of conventional antibodies frequently aggregate after heat denaturation due to the dissociation of heavy and light chain and the subsequent exposure of hydrophobic surfaces (Dumoulin et al., 2002).

2.4.2 Determination of binding kinetics of four novel sdAbs

I monitored the interactions between the four single domain antibodies and their immobilized targets EGFR-ECD and EGFRvIII-ECD by surface plasmon resonance. The determined affinities are in the low nanomolar range, similar to

previously reported values for other VHH fragments (Table 1) (Arbabi Ghahroudi et al., 1997; Decanniere et al., 1999; Lauwereys et al., 1998). For example, the VHH122 antibody generated by Gottlin *et al.* binds to both EGFR and EGFRvIII with an affinity of approximately 40 nM (Gottlin et al., 2009). All interactions were fitted to the 1:1 Langmuir binding model in the BIAevaluation software to obtain the affinity constants (K_D) and the association and dissociation rate constants (k_a and k_d) (Figure 2-3 and Figure 2-4). Simple 1:1 models are commonly used to describe monovalent antibody-antigen interactions (Baerga-Ortiz et al., 2004; Katsamba et al., 2006; Papalia et al., 2006; Roden and Myszka, 1996; Vaneycken et al., 2010). Furthermore, a well-designed Biacore experiment is expected to reflect a simple 1:1 interaction (Rich and Myszka, 2008). The hallmarks of a well-designed study have been explained in the introduction to this chapter (page 28). In consideration of these recommendations, I immobilized the receptor at low concentrations (~ 500 RU) and flowed the analyte at high flow rates (20 – 30 µl min^{-1}) in order to avoid mass transport and rebinding effects. I furthermore verified that all protein solutions used in this study were of high purity. As a result, I was rewarded with excellent fits of the Biacore data to the 1:1 Langmuir binding model in the BIAevaluation software, confirmed by the resulting low Chi^2 values (< 1) (Table 1). A common internal control to validate if a protein-protein interaction is correctly represented in the Biacore experimental set-up is to inverse the immobilized protein and the analyte, provided, of course, both components of the binding system are monovalent. Since the kinetic constants were determined by flowing the sdAbs over immobilized EGF receptor surfaces, I now immobilized the single domain antibodies and injected serial dilutions of EGFR-ECD. The measured affinities compared well with the values obtained in the previous study carried out on the reverse orientation (Figure 4-1 B for EG2/EGFR-ECD, and data not shown for EG43/EGFR-ECD). Since EG10 did not immobilize on the Biacore surface, I used an anti-c-myc antibody to capture this sdAb on the chip surface. Another argument in support of the accuracy of the 1:1 binding model are the linear Scatchard plots obtained for all interactions (van der Merwe, 2000). Lastly, affinity constants obtained from fitting the Biacore data

to the steady state affinity model, which determines equilibrium binding constants in a manner similar to what is done in cell binding experiments or plate assays, were very similar to the affinity constants derived from global fitting to the 1:1 Langmuir model (Table 1, Figure 2-3, Figure 2-4).

EG2 was identified as the highest affinity binder for both receptors with K_D-values of 50 nM for EGFR and 97 nM for EGFRvIII. Nowadays most diagnostic and therapeutic antibodies have affinities in the low nanomolar range, which places EG2 as a good candidate for *in vivo* applications (Deyev and Lebedenko, 2008). Furthermore, Zhou and coworkers reported that they did not observe any difference in tumor localization for anti-Her-2 diabodies that were constructed from scFvs with intrinsic affinites ranging from 133 nM to 1 nM (Zhou et al., 2007). This finding suggests that in a multivalent format (i.e. on the nanoparticle surface) EG2 may function comparable to a single domain antibody fragment of 1 nM affinity.

When I compared the rate constants, k_a and k_d, of the four monovalent sdAbs for binding to EGFR- and EGFRvII-ECD, it became clear that the differences in affinity are mainly dictated by variations in the dissociation rate (Table 1). The dissociation rate of EG2 is approximately seven times slower than that of the lowest affinity binder EG31. In contrast, the maximal difference in association rate was only three-fold. The strong dependence of the affinity on the dissociation rate is visualized in Figure 2-5, by overlaying normalized sensorgrams of 500 nM sdAb injections. In a study on a series of mutant scFvs, specific to an identical epitope but with varying affinities, it has been shown that although the most uniform intra-tumoral distribution was achieved for the scFvs possessing affinities in the high nanomolar range (10^{-7} M), the best tumor retention and selectivity were obtained with the variants of K_D-values around 10^{-9} M (Adams et al., 2001). These findings support the choice of EG2 for conjugation to the surface of the nanoparticles, since the application is aiming for improved retention and selectivity.

The Biacore data in Table 1 furthermore suggested that all four sdAb recognize a similar fraction of the immobilized EGFR-ECD and EGFRvIII-ECD proteins on

the sensor surface. The obtained R_{max} values are comparable when taking into account the individual molecular weight of each single domain antibody. I determined that approximately 40% of the immobilized EGFR-ECD and EGFRvIII-ECD surfaces is recognized by the sdAbs (the calculation is explained in the introduction of this chapter). Other investigators reported similar levels of surface activity (Katsamba et al., 2006). The reason why higher activity surfaces are not obtained is not known, but steric interference related to the orientation of the immobilized protein within the carboxy dextran layer of the Biacore chip surface could be contributing to the effect.

2.4.3 Epitope mapping

Epitope mapping of the single domain antibodies showed that EG2 and EG43 share the same binding site, but do not compete with the natural ligand EGF for binding to EGFR-ECD (Figure 2-6). Therefore, their epitope does not overlap with the ligand-binding pocket that is constituted by subdomain I and III of the extracellular domain (Ogiso et al., 2002). Interestingly, Gottlin *et al.* discovered by competition binding studies with mAbs that their anti-EGFR sdAb clones could be classified into two distinct binding sites on EGFR (Gottlin et al., 2009). I furthermore determined that EG2 binding to EGFR-ECD is not inhibited in the presence of 225 (Figure 2-14). Since 225 is known to directly compete with ligand binding to subdomain III (Li et al., 2005), this finding is in agreement with the previous experiment in which I showed that EG2 does not compete with EGF for binding to EGFR-ECD.

Cochrane and coworkers carried out an intensive epitope mapping study on 11 monoclonal antibodies that were generated against the extracellular domain of EGFR and discovered two antigen ‘hot spots’ on subdomain III consisting of one group of antibodies that shared overlapping epitopes with cetuximab (225) and the second group that competed with H11. In contrast to 225, H11 does not compete with ligand (Cochran et al., 2004; Kamat et al., 2008). They furthermore discovered that none of the antibodies investigated in their study bound to subdomain I and they subsequently postulated that this particular region might not

be immunogenic (Ogiso et al., 2002). Since subdomain I is deleted in the mutant receptor EGFRvIII, it can be excluded as binding site for any of the sdAbs investigated in this study. For further elucidation of the potential epitope, I would like to point out the cell binding study, in which I showed that EG2 recognizes similar ratios of receptor on the U87MG cell line panel compared to 225 and H11 (Figure 2-15). It is therefore reasonable to say that EG2 is not specific for a low abundance conformational receptor species, as it is for example in the case of the 806 antibody, which was raised against EGFRvIII and shown to recognize a minor population of over-expressed wild-type EGFR (Johns et al., 2002). Although EG2 does not compete with 225, it is possible that the epitope of EG2 lies in the vicinity of the 225 and H11 binding sites, i.e. in the vicinity of the same "hot spots" of subdomain III that are preferentially targeted by multiple other antibodies. It would certainly be interesting to carry out a Biacore competition study with H11 and EG2 for binding to EGFR-ECD. Nevertheless, it has been suggested that sdAbs are capable of recognizing epitopes, which are not typically explored by conventional antibodies, e.g. enzyme binding clefts (Saerens et al., 2005b), which means that the epitope of EG2 and the other sdAbs investigated in this thesis could also be located in areas not yet explored by existing anti-EGFR monoclonal antibodies. Hence, the determination of their epitopes on EGFR-ECD might provide additional information on structure and function of the receptor, which could not be assessed with conventional mAbs (De Genst et al., 2006; Stijlemans et al., 2004).

2.4.4 Multimerization of single domain antibodies

The introduction of avidity is by far the easiest way to improve antigen-binding properties of antibody fragments in instances where the antigen is presented multivalently, e.g. an over-expressed cell surface receptor. Multimerization is therefore a particularly appealing strategy for the improvement of affinity and circulation times of single domain antibodies (Deyev and Lebedenko, 2008). The most important advantage of multivalent mini-antibodies over monovalent ones is the enhancement of specific binding avidity towards antigens. Theoretically, the

resulting binding constant (avidity) could be the product of the original binding constants (affinities). In practice this is however not the case. The precise increase in affinity gained through avidity depends on many factors, including steric effects, local concentration and accessibility of adjacent epitopes, and the conformational flexibility of both target antigens and binding molecules of the multimer (Deyev and Lebedenko, 2008). The production of bivalent (Cortez-Retamozo et al., 2002; Zhang et al., 2009), trivalent (Kolkman and Law, 2010), and pentavalent (Zhang et al., 2004) single domain antibody formats have been reported. In the study by Kolkman *et al.*, the comparison of the IC_{50} values of the monomer versus the trimer showed that the potency of the sdAb in their study was improved more than 4000-fold upon multimerization (Kolkman and Law, 2010). In my experiments, I determined that the apparent affinities of EG2-hFc, EG10-hFc and V2C-EG2 for EGFR-ECD and EGFRvIII-ECD were 50 to 100 times higher than the K_D-values of their monovalent counterparts. However, increased multivalency does not always cause an increase in antigen binding. Willuda and coworkers showed that the tetramer 4D5-p53 has no higher avidity than the dimer, presumably, because the simultaneous binding to more than two antigen molecules on the surface of cells is not possible due to steric hindrance (Willuda et al., 2001). Similarly, Roovers *et al.* reported that a divalent construct showed a half-life of 44 hours, whereas in a multivalent format, the construct had a half-life of only 1 hour (Roovers et al., 2007b). This observation is in agreement with the findings of our collaborators with respect to the serum half-lives of EG2-hFc and V2C-EG2. A half-life of 12 hours was determined for the dimer versus 70 minutes for the pentamer (Iqbal et al., 2010b).

I furthermore demonstrated that the individual EG2 binding unit on the multimerization scaffolds retained its original affinity to EGFR-ECD (Figure 2-11), which at the same time demonstrated that multivalency was the primary contributing force to the observed increase in affinity. Since the surface of an iron oxide nanoparticle also represents a form of multimerization scaffold, the density of the EGF receptor on tumor cells will crucially determine the effective affinity

of the EG2-conjugated nanoparticle, which will ultimately affect its retention time (Figure 2-9, Figure 2-10).

For pentamerization our collaborators chose the verotoxin 1 B-subunit (VT1B) monomer as the oligomerization domain because of its relatively small size and the nature of the multimeric structure that it forms by self-assembly. The 7.7-kDa VT1B subunit monomers self-assemble to form a 38.5-kDa homo-pentamer. The VT1B pentamer is a doughnut shaped structure with the N- and C-termini exposed at the periphery and on opposite sides of the molecule. The sdAb was fused to the C-terminus of verotoxin, which is considered to result in a highly dynamic structure (Zhang et al., 2004).

Our collaborators generated the bivalent sdAb formats by fusing the single domain antibody sequence to a human IgG1 Fc domain (Bell et al., 2010; Zhang et al., 2009). This approach bears a lot of potential, since for therapeutic applications, antibody fragments are often re-engineered back to resemble an intact antibody. Examples are adalimumab (Humira) and Erbicin, which were generated by this approach from Fab and scFv fragments, respectively. The fusion of scFvs with Fc not only prolongs the serum half-life and stability of the scFvs, but also improves their therapeutic efficacy owing to the antibody-dependent cell-mediated cytotoxicity (ADCC) and complement-dependent cytotoxicity (CDC) mediated by the Fc portion (Jain et al., 2007). Correspondingly, our collaborators showed increased *in vivo* circulation times for the bivalent EG2-hFc over monovalent EG2 (Bell et al., 2010; Iqbal et al., 2010b).

Dechant and coworkers made the interesting discovery that synergistic anti-tumor activity is likely to be observed when the EGF receptor is targeted by a combination of two IgG1 antibodies that recognize different, non-overlapping epitopes on the extracellular domain. The effect is attributed to potent complement activation, which is one of the most effective cell killing systems (Dechant et al., 2008). Therefore, our panel of single domain antibodies against EGFR could be exploited for the cost-effective production of bivalent sdAb Fc fusion constructs, which are expected to induce CDC in EGFR over-expressing tumors. In addition, they are expected to demonstrate enhanced tumor penetration

due to their reduced size (80 kDa) compared to conventional monoclonal antibodies. It could furthermore be envisioned to fuse different panels of anti-EGFR sdAb with Fc-domains produced in fucosyl transferase knock-out CHO cells, which were shown to exhibit a 100-fold higher ADCC compared with those expressed in wild-type cells (Natsume et al., 2006).

Furthermore, Sampson and colleagues demonstrated that antibodies could serve as specific and potent therapeutic agents within the CNS, if they are able to recruit effector cells to the tumor site. Macrophages, microglia and astroglial cells, all of which contain FcR, are abundant within brain tumors and throughout the substance of the brain (Sampson et al., 2000). For monoclonal antibodies, however, intracranial administration is a pre-requisite of treatment efficacy, since these large proteins are not able to cross the blood brain barrier (BBB). Fc-fused sdAbs that are only half the size of a conventional antibody could potentially penetrate the BBB in patients with brain tumors that already show increased vascular permeability.

Lastly, Shen and coworkers recently highlighted the usefulness of VHH libraries in the generation of bispecific antibodies. In the traditional hybrid hybridoma approach, the pairing between the heavy and light chains of two specificities is a purely random event and results in poor yields and purity of the bispecific antibodies (Shen et al., 2007). Since sdAbs have only one chain, this problem is not encountered when generating bispecific antibodies. Studies have demonstrated that Fc-containing bispecific antibodies and other fusion proteins do retain the full effector mechanisms of the Fc component (Zuo et al., 2000).

2.4.5 Cell binding studies

The overall fluorescence detected on live cells incubated with the four sdAb fragments reflected a similar binding “hierarchy” to the one determined by Biacore, with the exception of EG43 that did not show binding to any of the cell lines (Figure 2-15, Table 1). The lack of binding detected for EG43 could be caused by steric obstruction of the c-myc tag by the tertiary structure of the sdAb, which would interfere with binding of the fluorescently labeled secondary

antibody. Alternatively, EG43 could recognize a structural epitope specific to purified recombinant EGFR-ECD and EGFRvIII-ECD. The first explanation is more likely. The objective of the cell binding study was to assess specificity of the sdAbs to their targets EGFR and EGFRvIII. The flow cytometry data also supports the SPR results that showed that the increase in apparent affinity of EG2-hFc is dependent on avidity. Whereas for both receptor over-expressing cell lines a difference in fluorescent signal intensity between EG2 and EG2-hFc is observed, on the low density EGFR surface of the parental cell line the fluorescence between the two sdAb formats is comparable (Figure 2-16 A and B). This observation suggests that the distance between individual EGF receptors on the parental cell line may be too large to be bridged by EG2-hFc, thereby not giving rise to the avidity effect, which would also support the hypothesis that inactive monomeric EGF receptors are evenly distributed on the cell surface (Wikstrand et al., 1997). The specificity of EG2 for EGFR was supported by the finding that the relative amount of receptors recognized by EG2 on the U87MG cell line panel, was in good agreement to two commercial anti-EGFR antibodies (Figure 2-16 C).

Affinities to cell surface-expressed receptors are most commonly determined in homologous competitive binding experiments, which involve binding-site competition between a “hot” ligand (radiolabeled ligand) and a “cold” ligand (untagged ligand). This technique is known for its high sensitivity. For labeling of the single domain antibodies, I intentionally avoided the otherwise popular Iodogen method, which labels tyrosines, since it is well established that these residues occupy solvent-exposed locations in the CDRs (Cortez-Retamozo et al., 2002; Padlan, 1994). Furthermore, I established earlier in this chapter that the majority of tyrosines in the sequence of EG2 are located in the antigen binding loops. In contrast, lysines have a higher propensity to occur in the framework, away from the antigen-binding loop. Indeed, for EG2 only one out of six lysine residues is located in the vicinity of CDR2. The IC_{50} values obtained in the homologous competition binding experiment (197 nM for EGFR on MDA-MB 468 cells, 60 nM for EGFRvIII on U87MG.EGFRvIII cells, and 97 nM for EGFR

on U87MG.EGFR cells) compared well with the affinities of 50 nM for EGFR-ECD and 98 nM for EGFRvIII-ECD derived from the SPR kinetic study (Figure 2-18 A-C; Table 1). The IC_{50} of the multivalent constructs was likely skewed under these experimental conditions, because the concentration of the hot ligand was too high. However, by plotting the percentage of non-competed hot ligand over the concentration of monovalent and bivalent cold EG2 competitor, superior competition efficiency of EG2-hFc was still observed (Figure 2-18 D).

The cross-linking experiment confirmed the specificity of EG2 for EGFR and EGFRvIII; however, it became clear that EG10 binds specifically to a protein of approximately 110 kDa in size (Figure 2-17). In light of this experiment EG10 lost its position as a candidate sdAb for being conjugated to the nanoparticles. It would still be interesting to know what EG10 is binding to, since receptor variants of smaller molecular weight have also been observed with other anti-EGFR antibodies. For example, the RAb^{vIII} antibody recognizes the 145 kDa EGFRvIII protein band in U87MG.EGFRvIII. It also faintly recognizes the endogenous 170 kDa wild type EGF receptor and it strongly recognizes a 45 kDa protein band in both U87MG.EGFRvIII and parental U87MG cells. The authors speculated that the 45 kDa protein corresponded to another EGF receptor variant that they had recently identified (Gupta et al., 2010)

2.4.6 Confocal microscopy

The confocal microscopy analysis of cell-bound EG2-hFc for the U87MG cell line panel generally confirmed the ratio of fluorescence signal between the cell lines observed in the flow cytometry experiments: the lowest amount of signal was seen on the parental cells, followed by much higher fluorescence on the U87MG.EGFRvIII and U87MG.EGFR cell lines (Figure 2-19, left column). However, in contrast to the flow cytometry results, in the confocal microscopy analysis the fluorescence signal on the two receptor over-expressing cell lines appeared to be comparable. This discrepancy could be due to the fact that permeabilized fixed cells were assessed instead of live cells. Figure 2-20 illustrates that the fluorescence intensity measured on non-permeabilized cells

compared better to the hierarchy established in the FACS analysis, i.e. the EG2-hFc binding to U87MG.EGFR cells resulted in greater overall fluorescence than binding to U87MG.EGFRvIII cells. This observation suggests that large amounts of EGFRvIII receptors are contained inside the cells, with a smaller fraction present on the cell surface. The subcellular distribution of fluorescence in permeabilized U87MG.EGFRvIII cells supports this theory, since an intense punctate and tubular perinuclear pattern, consistent with the known distribution of EGFR in coated vesicles and perinuclear endosomes, is observed (Wikstrand et al., 1997) (Figure 2-19, Figure 2-20). These findings are, however, in disagreement with the reports on other EGFRvIII over-expressing cell lines (HC2 20 d2, NR6M), in which the receptor distribution between wild-type EGFR and EGFRvIII over-expressing cell lines was shown to be comparable, and cell surface localization of both EGF receptors types was predominant (Sorkin and Goh, 2009; Wikstrand et al., 1997). The U87MG.EGFR cells exhibited the EGFR distribution pattern described for other cell lines (e.g. A431, NR6W). That is, in the permeabilized cells few intracellular clusters were detected and protrusions at the cellular periphery were intensely labeled (Figure 2-20 B). It was reported previously that in most cells EGFR is constitutively internalized at the rate comparable to the rate of basal membrane recycling. After internalization, inactive ErbB receptors are mainly recycled back to the cell surface. Because the constitutive recycling rate is several times higher than the basal internalization rate, and because the distribution of EGFR is determined by the ratio of the internalization and recycling rates, a predominant localization of EGFR at the cell surface and a small endosomal pool is expected (Sorkin and Goh, 2009). At comparable laser settings for all cell lines, parental cells demonstrated weak but homogenous fluorescence intensities, indicating the absence of intracellular clusters (Figure 2-19). In addition, the receptor distribution on non-permeabilized U87MG.EGFR cells also correlated with previous reports, showing homogenous cell surface localization with intense clustering at the cell periphery and in areas of cell-cell apposition (Sorkin and Goh, 2009; Wikstrand et al., 1997).

All observations on the subcellular distribution of EGFR and EGFRvIII were reproducible with 225 as detection antibody, confirming the previous results from the [^{125}I]-EG2 cross-linking study that EG2 is indeed specific for EGFR (Figure 2-17). In addition, the flow cytometry results are supported, which suggested that EG2-hFc and 225 recognize the same receptor population on the U87MG cell lines (Figure 2-16). The reason why the overall fluorescence observed for EG2-hFc-labeled cells was weaker than for 225 in the flow cytometry study could have been caused by the different fluorophores on the secondary antibodies that I used in this study (FITC versus Alexa Fluor® 488). By contrast, in the confocal microscopy experiments both secondary antibodies were labeled with Alexa Fluor® antibodies (Life Technologies). A final colocalization experiment between EG2-hFc and 225 confirmed once more that EG2-hFc is highly specific for the extracellular domain of EGFR (Figure 2-21). With respect to EG10, the colocalization study corroborated the findings from the cross-linking study, in which [^{125}I]-EG10 specifically recognized a protein that was not the full-length EGFR or EGFRvIII receptor (Figure 2-17). This protein appears to be insensitive to EGF-mediated receptor activation, since no changes in EG10-hFc distribution on ligand-treated compared to untreated cells was observed (Figure 2-21).

Ligand-activated EGFR enters the early endosomal compartments positive for EEA1 within 2-5 minutes of internalization (Sorkin and Goh, 2009). Furthermore, spatial trafficking of the early endosomes from the cell periphery to the cell center is critical for their ability to generate endosomal vesicles that bud from early endosomes and fuse with late endosomes or mature into late endosomes (Chen et al., 2009c). During the endosomal maturation process, receptors either recycle back from endosomes to the cell surface or the complexes are degraded in lysosomes. The half-life of the EGF receptor is reduced dramatically when the internalization of receptors is induced by EGF, which subsequently leads to down-regulation of EGFR from the cell surface (Sorkin et al., 1991). I observed this characteristic distribution of EG2-hFc-detected EGFR-containing vesicles trafficking along the endosomal pathway in all cells that were pre-treated with 100 ng/ml EGF for five minutes prior to fixation (Figure 2-19 - Figure 2-22). In

addition, co-localization between EG2-hFc and the early endosomal protein EEA1 was observed in fixed EGF-treated U87MG.EGFR cells (results not shown).

Next, I investigated whether EG2-hFc is able to enter the cells and follow the cytoplasmic receptor trafficking route to the perinuclear area. It has been known for a long time that antibodies can induce receptor clustering on the cell surface, which in turn leads to increased endocytosis (Huet et al., 1980; Schreiber et al., 1983; Schwartz et al., 1986; Winkler et al., 1989). This suggests that receptor dimerization may be a prerequisite for antibody internalization. Becerril *et al.* showed that dimeric IgG, but not monomeric Fab, dimerize and activate the ErbB2 receptor, which subsequently undergoes endocytosis. Alternatively, monomeric receptor ligands can activate receptors and undergo endocytosis either by causing a conformational change in the receptor favoring the dimeric form or by simultaneously binding two receptors (Becerril et al., 1999). For example, three internalizing scFvs were discovered by Souriau and coworkers (Souriau et al., 2004).

My results showed that in U87MG.EGFR cells the antibody appeared in early endosomes within 10 minutes of incubation at 37°C. After 15 minutes practically all EEA1-positive endosomes contained EG2-hFc (Figure 2-22 B). Rapid internalization has previously been described for several anti-EGFR mAbs, including 225, 425, and C10 (Goldstein et al., 1995; Jaramillo et al., 2006; Miyamoto et al., 1996; Waksal, 1999; Zhou et al., 2007).

Comparatively less co-stained endosomes were found in U87MG.EGFRvIII cells after 10 and 15 minutes and the antibody mainly located to the cell surface and to protrusions at the cell periphery. After two hours, some co-localization with EEA1 was observed, although the majority of early endosomes did not contain EG2-hFc. Interestingly, the presence of multiple intracellular vesicles containing EG2-hFc, which did not stain positive for EEA1, were observed at this time point, thus indicating an alternative route of antibody internalization (Figure 2-22 A). These findings are in agreement with observations on TB 829 human glioma cells that showed little or no recycling of EGFRvIII (Sorkin and Goh, 2009). Grandal and coworkers also described that EGFRvIII retained its ability to become

internalized, but at a significantly lower rate than that of unstimulated EGFR. Furthermore, the small fraction of internalized EGFRvIII is recycled to the plasma membrane rather than delivered to lysosomes. In their study, EGFRvIII was present in intracellular compartments after 1h of incubation at 37°C, presumably in peripheral sorting endosomes and in perinuclear endosomes (Grandal et al., 2007). These findings would explain, why EG2-hFc (bound to EGFRvIII) does not colocalize with the early endosomal marker EEA1. In contrast, EGFRvIII-specific mAbs were internalized by HC2 20d2 cells to intracellular vesicles within 5 minutes (Reist et al., 1995).

Due to the discrepancy in reports on the ability of EGFRvIII to recycle, it is possible that other cell line-specific factors, besides the expression level of EGFRvIII, contribute to its internalization. For example, Cvrljevic *et al.* showed that EGFRvIII is localized in the mitochondria upon Src activation (Cvrljevic et al., 2011). Another potential explanation for the origin of these non-endosomal EG2-hFc positive intracellular compartments could be provided by the observations reported by Al-Nedawi *et al.* for EGFRvIII over-expressing U373 glioma cells. They postulated that the expression of EGFRvIII triggers production of microvesicles derived from membrane lipid rafts into which this transmembrane receptor becomes incorporated and subsequently shed into the pericellular micromilieu (Al-Nedawi et al., 2008). It would therefore be worthwhile to investigate whether the intracellular compartments, to which EG2-hFc was shuttled after 2 hours of incubation on U87MG.EGFRvIII cells, correspond to mitochondria or lipid raft-derived microvesicles.

In the light of the above-presented observations, I conclude that targeting EGFR on the cell surface of cancer cells promises the potential of efficient internalization of the receptor-specific iron oxide nanoparticles. Due to the multivalent character of the EG2-conjugated nanoparticulate contrast agent I would expect to observe receptor clustering on the cells surface, which was shown to induce receptor-mediated internalization. This concept has already been verified by three different investigators in studies on EGFR-targeted immunoliposomes, the most recent one of which was also carried out with an anti-

EGFR targeted single domain antibody (Heitner et al., 2001; Mamot et al., 2003; Oliveira et al., 2010).

2.4.7 The effect of EG2 on EGFR receptor activation and cell growth

The capacity of the single domain antibodies to induce receptor phosphorylation was investigated by Western Blot in the U87MG cell line panel. Antagnostic anti-EGFR VHH fragments that competed for ligand binding were previously described by Roovers and coworkers (Roovers et al., 2007a). In contrast, monovalent EG2 had no effect on activation of the intracellular kinase of the receptor, however, the bivalent antibody induced receptor activation (Figure 2-23). It is well established that intact antibodies can induce clustering, activation and internalization of plasma membrane receptors. In line with this, incubation of EGFRvIII over-expressing NR6M cells with a monoclonal antibody (clone 528) against an extracellular epitope of EGFRvIII resulted in an increase in phosphorylation of the receptor, whereas the Fab fragments of the same antibody did not induce phosphorylation (Grandal et al., 2007). The unligated, monomeric receptor does not appear capable of signaling; the receptors need to oligomerize (Schlessinger, 2002; Teramura et al., 2006). EGF receptors on the cell surface are thought to engage in short-lived dimeric complexes (predimers) in the absence of ligand that result in low levels of intracellular kinase domain activation (Burgess, 2008). Cross-linking of two receptors on the cell surface would result in increased stability of these temporary complexes and have been shown to induce internalization (Heitner et al., 2001).

It has been postulated that there is a correlation between the ability of an antibody to block ligand binding to the receptor and its ability to inhibit tumor growth, e.g. the antagonistic antibody 225 directly competes with ligand binding to domain III (Li et al., 2005). The correlation has however been questioned since it became clear that the monoclonal antibody matuzumab (425) does not compete directly with ligand binding, but instead sterically blocks the domain rearrangement that is required for high affinity ligand binding and receptor dimerization (Kamat et al., 2008; Schmiedel et al., 2008). The antagonistic effect of 225 on EGF-induced

tyrosine phosphorylation can be clearly seen in the Western Blot. However, whereas the tyrosine kinase inhibitor tyrphostin (AG1478) appeared to entirely eradicate phosphorylation in EGF treated and untreated cells, 225 only reduced activation, but not below the basal level, which is consistent with its ability to block ligand binding, but probably not the formation of predimers (Figure 2-23). The treatment of U87MG cells with monovalent and multivalent sdAb constructs showed that none of them affected the proliferation or metabolic activity of these cells (Figure 2-24). Nevertheless, these findings alone are insufficient to conclude that EG2-hFc has no potential therapeutic efficacy. In a study by Johns *et al.* it was observed that neither mAb 528 or 806 inhibited the growth of U87MG.EGFRvIII cells *in vitro* but both antibodies displayed robust anti-tumor activity *in vivo*. It can be argued that the observed effect is caused by host-related ADCC, but it was shown that another mutant cell line was not sensitive to treatment with mAb 528 (Johns et al., 2007). Likewise, the *in vitro* binding properties of the antagonistic sdAbs described by Roovers *et al.* did not correlate with their *in vivo* anti-tumor effect (Roovers et al., 2007a). Interestingly, the same group reported that one of their homobivalent anti-EGFR sdAbs, which inhibited tyrosine phosphorylation at concentrations of 10 and 50 nM, suddenly induced activation at 100 nM. Since in its monovalent form, this antibody inhibits tyrosine phosphorylation, these findings demonstrate that the effect of receptor clustering induced by multivalent binders is a potent driving force of receptor activation. It would be interesting to investigate how "clustering"-induced EGFR activation differs from ligand-mediated activation of the downstream signaling pathways. Since the objective of this study was the application of sdAb as targeting ligands for the delivery of contrast agents, the potential therapeutic efficacy of these antibodies was not further investigated.

2.5 Conclusion

I determined the binding kinetics of four novel single domain antibodies for their targets EGFR and EGFRvIII by surface plasmon resonance. The rate constants and affinities were derived by global fitting of the sensorgrams to the 1:1

Langmuir binding model in the BIAevaluation software. Their affinities (K_D-values) ranged from 50 to 440 nM, which corresponds to affinities commonly seen for monovalent binding fragments. Competition binding studies furthermore showed that at least two of the four antibodies have overlapping epitopes on EGFR. Based on the results obtained from the Biacore experiments, I identified EG2 as the highest affinity binder to wild-type EGFR-ECD (K_D = 50 nM) and EGFRvIII-ECD (K_D = 98 nM).

Flow cytometry analysis validated the hierarchy in binding affinity determined by SPR for cell surface expressed EGF receptor in U87MG glioblastoma cells. The fast dissociation rate constants of these monomeric binding units ($2 \times 10^{-2} – 1.8 \times 10^{-3}$ s^{-1}), were not compatible with flow cytometry–based affinity studies and I therefore carried out homologous competition binding experiments using radio-labeled [^{125}I]-EG2. I determined IC_{50} values for binding to cell surface expressed EGFR (IC_{50} = 97 nM) and EGFRvIII (IC_{50} = 60 nM) that were comparable to the affinities measured in the SPR experiments. The sdAb EG10, the second highest affinity sdAb, was also investigated in more detail. However, in a cross-linking experiment, I showed that EG10 recognizes a protein on the cell surface of U87MG cells that does not correspond to EGFR or EGFRvIII.

Three multivalent constructs were subsequently generated by our collaborators, namely EG2-hFc (dimeric EG2), EG10-hFc (dimeric EG10) and V2C-EG2 (pentameric EG2). At present, it is evident that favorable biodistribution and pharmacokinetics in *in vivo* applications often require multivalent formats of antibody derivatives. The rational design of these formats should ensure the optimal molecular mass, stability under physiological conditions and high functional avidity. I demonstrated in SPR biosensor experiments that the multivalent constructs EG2-hFc, EG10-hFc and V2C-EG2 exhibited increased apparent affinities compared to their monovalent counterparts. I furthermore showed that this increase in apparent affinity was primarily based on avidity mediated by multimerization of the sdAb binding units on the scaffold structures, i.e., Fc-domain and verotoxin subunit.

To validate the specificity of binding of EG2 to EGFR, I carried out a series of cell-based assays. By confocal microscopy, I determined comparable binding patterns for EG2-hFc and the monoclonal antibody 225 on the U87MG cell line panel, consisting of cells with low and high EGF receptor expression levels. I also confirmed colocalization of EG2-hFc with 225, as well as with the early endosomal marker EEA1. EG10-hFc failed to colocalize with 225 antibody as well as with EEA1 (data not shown), which supports the results of the cross-linking experiment. These findings gave rise to the hypothesis that EG10 recognizes an unidentified splice variant of the EGF receptor, since other investigators have previously reported the occurrence of a variety of smaller EGFR variants. Based on these results EG10 lost its position as a candidate antibody for coupling to iron oxide nanoparticles. EG2 was chosen as the targeting moiety for conjugation to the IONP contrast agent. Favoring my choice are the low nanomolar affinity (50 nM) and high specificity of EG2 towards its epitope on the extracellular domain of EGFR and EGFRvIII.

2.6 Publications

Some of the work presented in the above chapter was published in two publications in collaboration with Roger MacKenzie's group and Danica Stanimirovic's group at the Institue for Biological Sciences (NRC-IBS). My contributions to the individual manuscripts are described below.

Differential tumor-targeting abilities of three single domain antibody formats.
Bell A, Wang JZ, Arbabi-Ghahroudi M, Chang TA, Durocher Y, **Trojahn U**, Baardsnes J, Jaramillo ML, Li S, Baral TN, O'Connor-McCourt M, MacKenzie R, Zhang J. Cancer Letters (2010) 280, 81-90. (Published online September 1, 2009)

I determined the kinetic constants for binding of the four monovalent single domain antibodies (EG2, EG10, EG31 and EG43) to the extracellular domain of wild-type EGFR (EGFR-ECD) by surface plasmon resonance. The results are shown in Table 1 and Figure 3 A. I furthermore, showed that the multivalent constructs EG2-hFc and V2C-EG2 bound with higher apparent affinity to the EGFR-ECD sensor chip surface due to significantly slower dissociation rates. I illustrated, by using two different sensor chip surfaces (one with low density and one with high density immobilized EGFR-ECD), that the dissociation rate was dependent on the receptor density (Figure 3 A and B). This dependence on surface receptor density is a phenomenon that is routinely observed for multivalent constructs and is referred to as avidity. In Figure 3 C, I immobilized the three formats of the EG2 sdAb (monovalent EG2, EG2-hFc and V2C-EG2) on three different chip surfaces over which I injected EGFR-ECD, thereby generating a 1:1 interaction between immobilized protein and the monovalent analyte. Overlay of the normalized sensorgrams, showed that in this orientation the interactions were comparable, hence confirming that avidity was the primary contributing force to the increased apparent affinity of these multivalent sdAb constructs over the monovalent form. These findings furthermore validated that the conformational

representation of the monovalent binding unit engineered into the multimerization scaffold retained its original binding properties.
Roger MacKenzie and colleagues carried out the immunization of the llama with EGFRvIII-ECD and the isolation of EGFR-specific sdAbs from a llama immune phage display library (Figure 1 and 2). They subsequently expressed the sdAbs and based on my identification of EG2 as highest affinity binder they constructed the bivalent EG2-hFc and the pentavalent V2C-EG2 format. The *in vivo* distribution and blood clearance of these three EG2 formats was also assessed by our collaborators (Figure 4 and 5).

Kinetic analysis of novel mono- and multivalent VHH-fragments and their application for molecular imaging of brain tumours.

Iqbal U*, **Trojahn U***, Albaghdadi H, Zhang J, O'Connor-McCourt M, Stanimirovic D, Tomanek B, Sutherland G, and Abulrob A. British Journal of Pharmacology (2010), 160, 116-1028

* Both authors contributed equally.

I determined the binding kinetics for EG2 to EGFRvIII-ECD and demonstrated that the bivalent EG2-hFc and the pentavalent V2C-EG2 bound to immobilized EGFRvIII-ECD with higher apparent affinities than in their monovalent format (Figure 2 A). I furthermore demonstrated that this increase in apparent affinity was dependent on receptor chip surface density (Figure 2 B - D). I also generated a graph in which the association constants (k_a) were plotted over the dissociation constant (k_d), which demonstrated that the association constants were independent of receptor density within each construct (yet they did differed between constructs). In contrast, large variability was seen in the dissociation rates and herein, the dimer outperformed the pentamer, despite its two binding units versus five on the pentamer. In addition, I showed that the increase in apparent affinity originated primarily from avidity effects, because the immobilized sdAb constructs showed 1:1 binding to EGFRvIII-ECD in solution,

which was comparable to the interaction measured between immobilized monovalent EG2 and EGFRvIII-ECD (Figure 2, E).

I furthermore contributed cell binding data to this publication, which I generated using radio-labeled [^{125}I]-EG2 for binding to U87MG glioblastoma cells over-expressing either the wild-type EGF receptor or its mutant variant EGFRvIII. In order to determine the specificity of the of the EG2 antibody for its targets, I carried out a cross-linking experiment (Figure 3 A). In a competition binding study, I also determined the affinity of the single domain antibody to the cell surface of these two cell lines and obtained comparable IC_{50} values of 70 nM for binding to U87MG.EGFR and 60 nM for U87MG.EGFRvIII (Figure 3 B).

Danica Stanimirovic and colleagues performed the pharmacokinetic analysis of the fluorescently labeled monomeric and multimeric EG2 construct in nude mice. They furthermore investigated the ability of the different sdAb formats to accumulate in an orthotopic glioblastoma xenograft models. In addition, they carried out a histological analysis of human brain tumor sections comparing the ability of the pentavalent V2C-EG2 antibody to recognize EGFR expressing cells with a commercial polyclonal anti-EGFR antibody.

Table 1. Kinetic parameters for single domain antibody binding to immobilized recombinant EGFR and EGFRvIII extracellular domains.

The values are derived from global fitting of data sets obtained from sdAb injections (0.4 nM – 1 μM) over a 500 RU EGFR-ECD and a 700 RU EGFRvIII-ECD surface. The affinity constants K_D and K_D^s were calculated using the 1:1 Langmuir model and the steady state binding model in the BIAevaluation software, respectively. The standard deviation is representative of three independent experiments.

	sdAb	k_a (10^5 M^{-1} s^{-1})	k_d (10^{-2} s^{-1})	K_D (10^{-9} M^{-1})	R_{max} (RU)	Chi^2	K_D^s (10^{-9} M^{-1})
EGFR	***EG2***	4.01 ± 0.26	2.00 ± 0.23	50 ± 6	58 ± 6	< 0.8	72 ± 3
	EG10	2.55 ± 0.03	3.21 ± 0.19	126 ± 8	47 ± 4	< 0.4	159 ± 15
	EG31	3.43 ± 0.44	14.77 ± 2.03	439 ± 112	41 ± 4	< 0.3	461 ± 67
	EG43	1.23 ± 0.02	3.82 ± 0.17	311 ± 18	49 ± 8	< 0.8	392 ± 6
EGFRvIII	***EG2***	2.59 ± 0.19	2.53 ± 0.01	98 ± 10	71 ± 3	< 1.0	129 ± 5
	EG10	2.52 ± 0.29	3.27 ± 0.14	131 ± 20	72 ± 4	< 0.6	150 ± 19
	EG31	6.16 ± 0.67	18.07 ± 0.98	294 ± 16	67 ± 2	< 0.3	259 ± 33
	EG43	2.08 ± 0.21	6.04 ± 0.74	289 ± 7	58 ± 3	< 0.5	342 ± 28

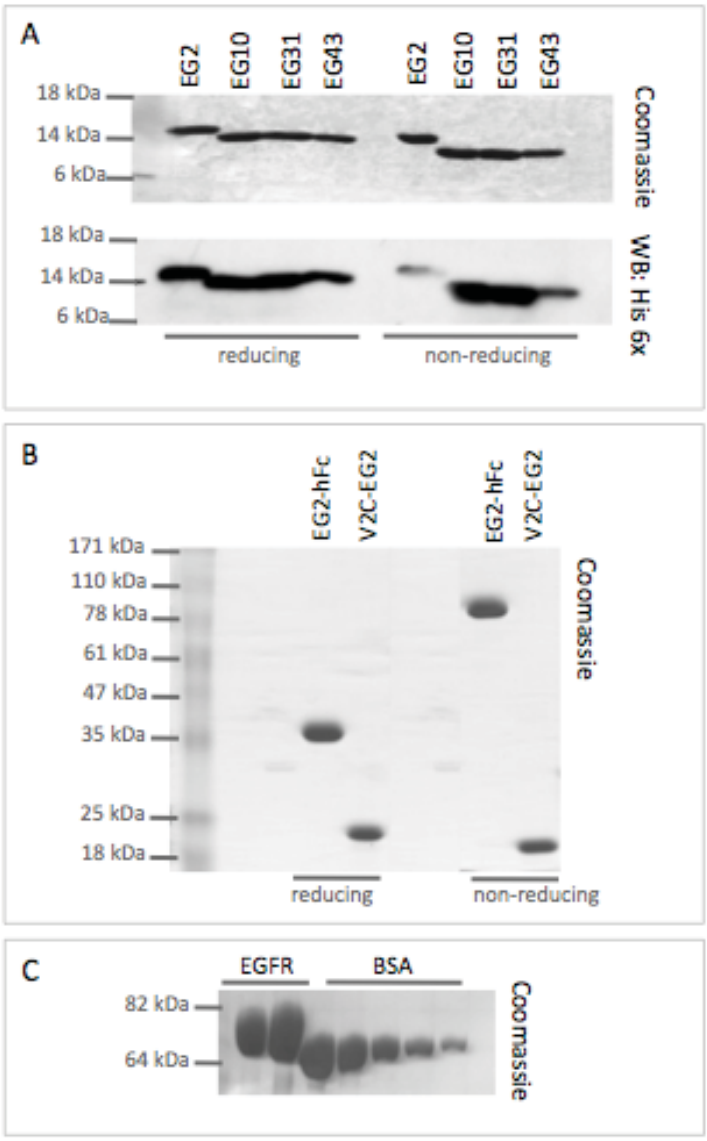

Figure 2-1. Analysis of purified proteins by SDS-PAGE.

(A) The anti-EGFR sdAb panel was separated in a 10 % protein gel under reducing and non-reducing conditions followed by Coomassie blue staining (top) and Western Blotting against the C-terminal 6× His-tag (bottom). The predicted sizes based on the protein sequences are 16 kDa for EG2, 14.4 kDa for EG10, 13.6 kDa for EG31 and 13.8 kDa for EG43, which are in good agreement with the distribution in the gel. (B) Bivalent EG2-hFc and pentavalent V2C-EG2 under reducing and non-reducing conditions. The predicted molecular weight for EG2-hFc is approximately 80 kDa. Reduction of EG2-hFc separates the dimer in its two subunits. The expected molecular weight of the pentamer is 126 kDa. However, the pentamer dissociated even under non-reducing conditions into its individual subunits that are 23 kDa in size. (C) Purified recombinant EGFR extracellular domain: 9 and 18 µg, BSA: 0.6-10 µg.

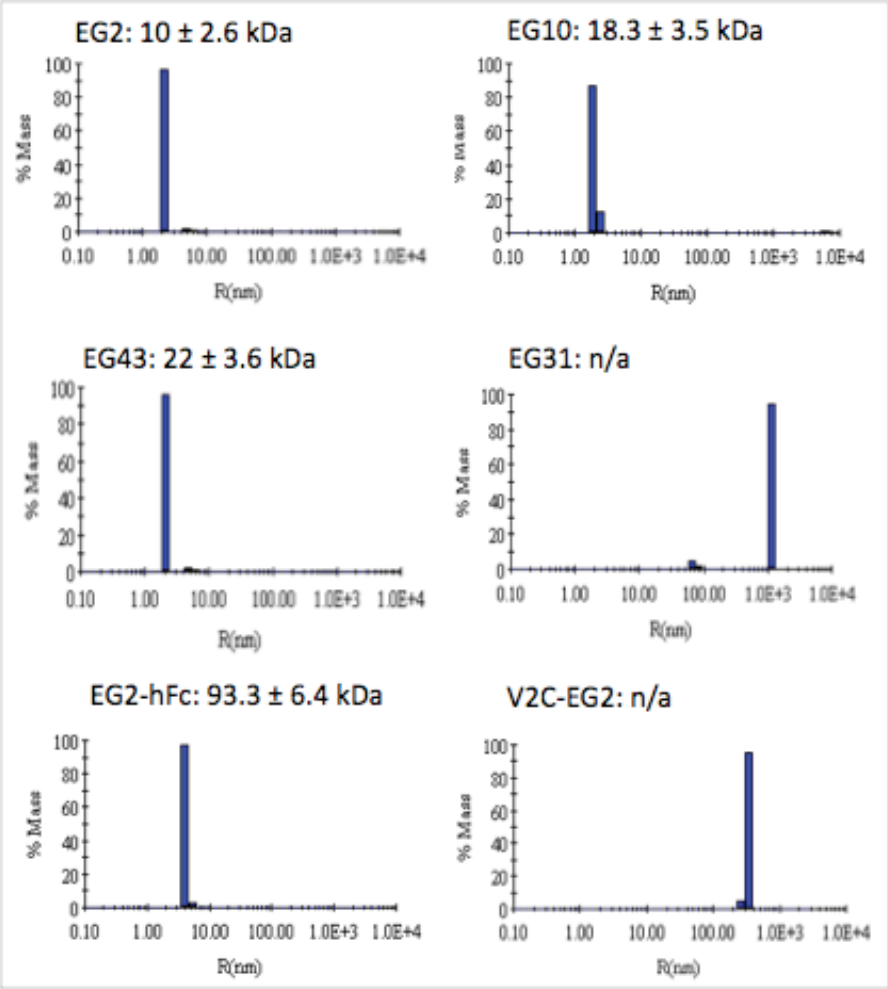

Figure 2-2. Analysis of protein purity by dynamic light scattering (DLS).

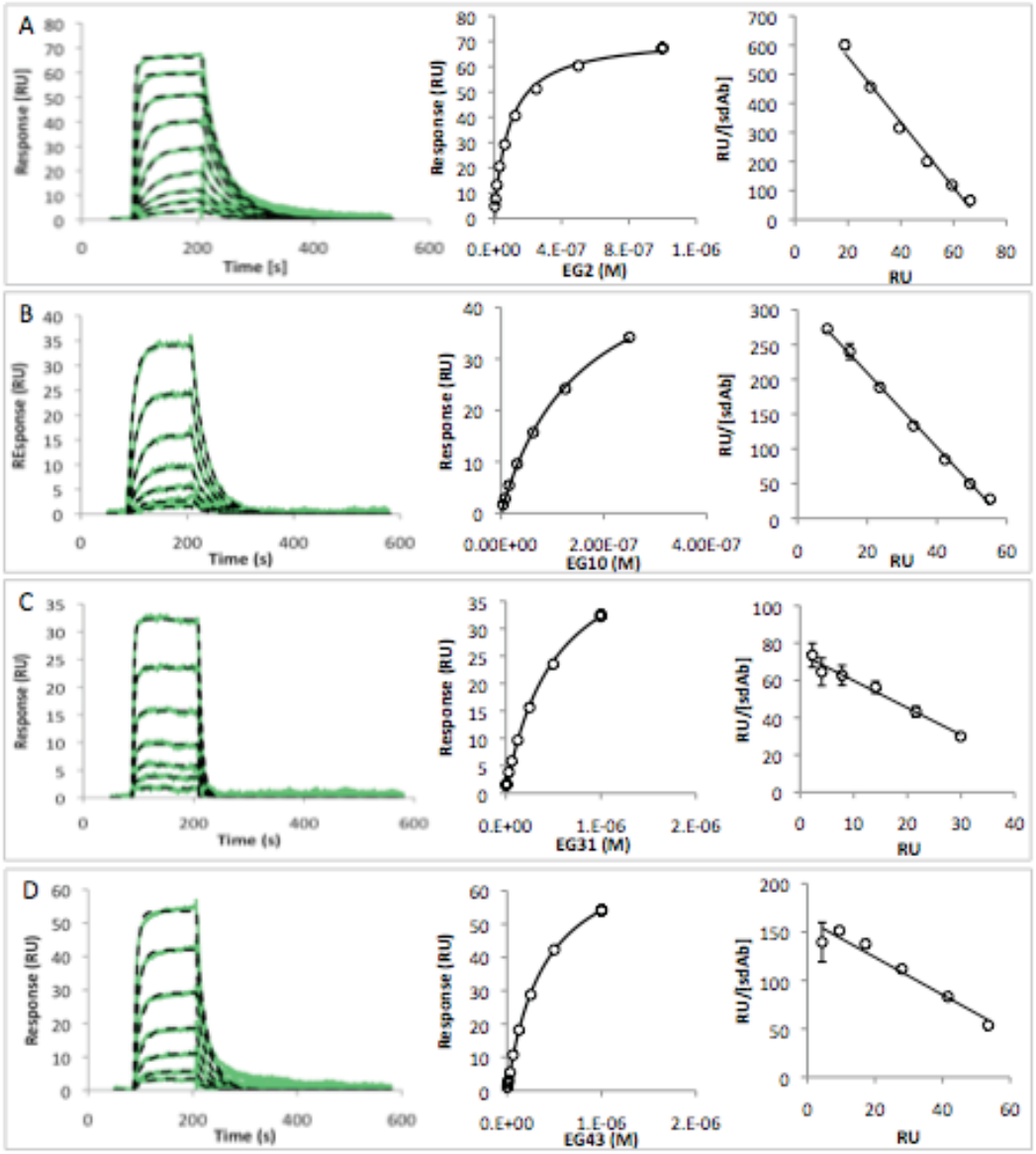

Figure 2-3. Biacore analysis of single domain antibody binding to immobilized recombinant EGFR extracellular domain.

Kinetic analysis of four sdAbs binding to immobilized EGFR-ECD by surface plasmon resonance. The first column shows sensorgrams for sdAb concentrations ranging from 3.7 nM to 1 μM on 500 RU EGFR-ECD immobilized on a CM5 sensor chip. The raw data (green) is overlaid with the global fit to the 1:1 Langmuir binding model in the BIAevaluation software (dashed black line). The plots in the second column show the equilibrium binding data fitted to the steady state affinity model in the BIAevaluation software. The third column illustrates the same data in Scatchard format. EG2 (A), EG10 (B), EG31 (C), EG34 (D).

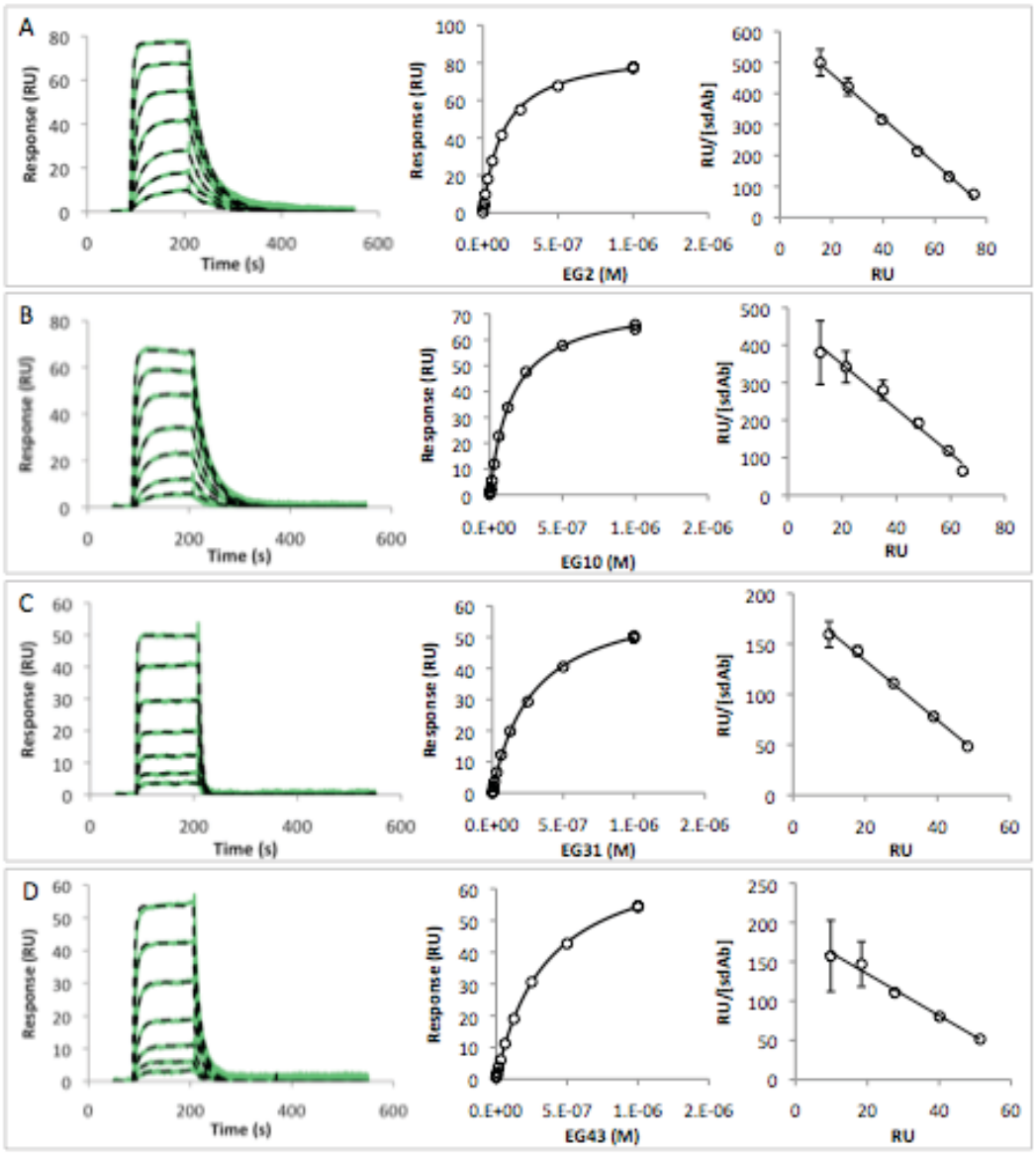

Figure 2-4. Biacore analysis of single domain antibody binding to recombinant EGFRvIII extracellular domain.

Kinetic analysis of four sdAbs binding to immobilized EGFRvIII-ECD by surface plasmon resonance. The first column shows sensorgrams for sdAb concentrations ranging from 3.7 nM to 1 μM on 700 RU EGFRvIII-ECD immobilized on a CM5 sensor chip. The raw data (green) is overlaid with the global fit to the 1:1 Langmuir binding model in the BIAevaluation software (dashed black line). The plots in the second column show the equilibrium binding data fitted to the steady state affinity model in the BIAevaluation software. The third column illustrates the same data in Scatchard format. EG2 (A), EG10 (B), EG31 (C), EG34 (D).

* I published the 1:1 Langmuir fit in panel A (EG2 binding to immobilized EGFRvIII) in Iqbal *et al.* 2010 (Iqbal et al., 2010b).

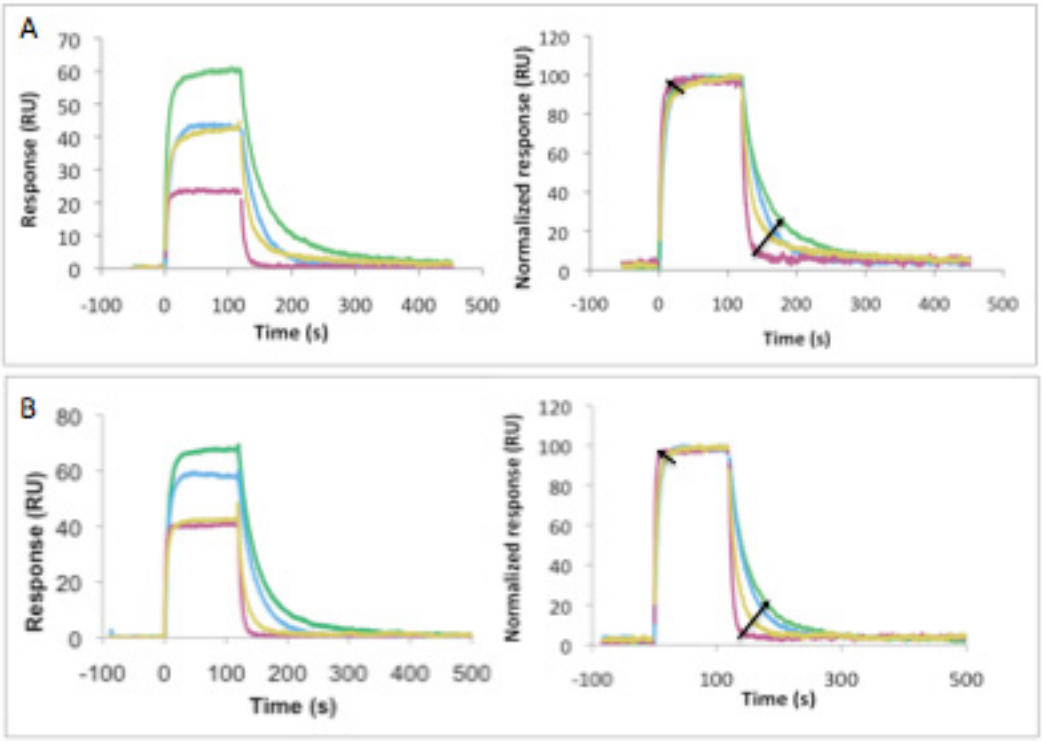

Figure 2-5. Comparison of sensorgrams obtained for the four sdAbs binding to EGFR-ECD and EGFRvIII-ECD.

Overlay of sensorgrams of 500 nM injections of the four monomeric single domain antibody fragments over a 500 RU EGFR (A) and a 700 RU EGFRvIII (B) surface. The data on the left represents the original sensorgrams, which were subsequently normalized to 100 RU for better comparison of the binding responses. EG2 (green), EG10 (blue), EG31 (red), EG43 (yellow). Black arrows emphasize the variability in association and dissociation rate between the four sdAbs.

* I published the left figure in panel A in Bell *et al.* 2009 (Bell et al., 2009).

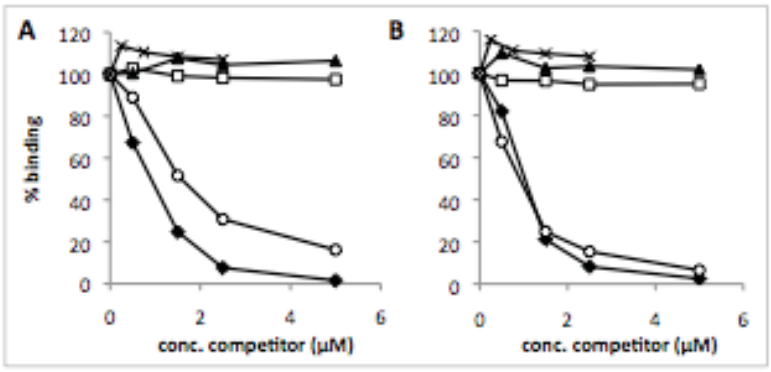

Figure 2-6. Epitope mapping of single domain antibodies on EGFR-ECD.

Competition binding study for binding of EGFR-ECD to a 300 RU EG2 surface (A) or a 50 RU EG43 surface (B). Besides competing with themselves for binding to EGFR-ECD, EG2 and EG43 also compete with each other for binding to EGFR-ECD, indicating that they share the same epitope on the extracellular domain of the receptor. Due to a five-fold lower affinity of EG43 towards EGFR-ECD compared to EG2, its competition for binding of EGFR-ECD to the EG2 surface is less effective than competition with EG2 (A). EGF does not compete with binding of EG2 and EG43. The sdAbs EG10 and EG31 did not bind to EGFR-ECD in its solution conformation, therefore competition between these two fragments could not be investigated. EG2 (◆), EG10 (▲), EG31 (□), EG43 (○).

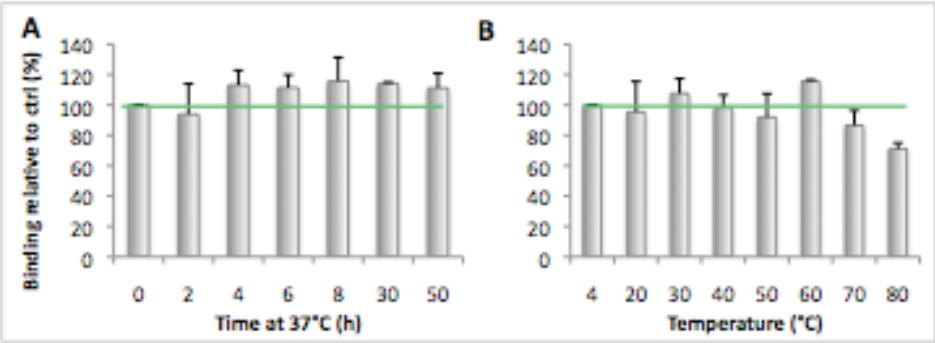

Figure 2-7. Analysis of thermal stability of EG2 sdAb.

(A) EG2 was kept at 37°C for up to 50 hours after which the samples were transferred back to 4°C and subsequently analyzed for their binding ability to a 400 RU EGFR-ECD surface. The control sample was kept at 4°C. The total binding response for each aliquot was measured after 50 µl injection of 100 nM EG2 at a flow rate of 30 µl/min. (B) Alternatively, EG2 was kept for 5 hours at temperatures between 4 and 80°C and analyzed by SPR as described before.

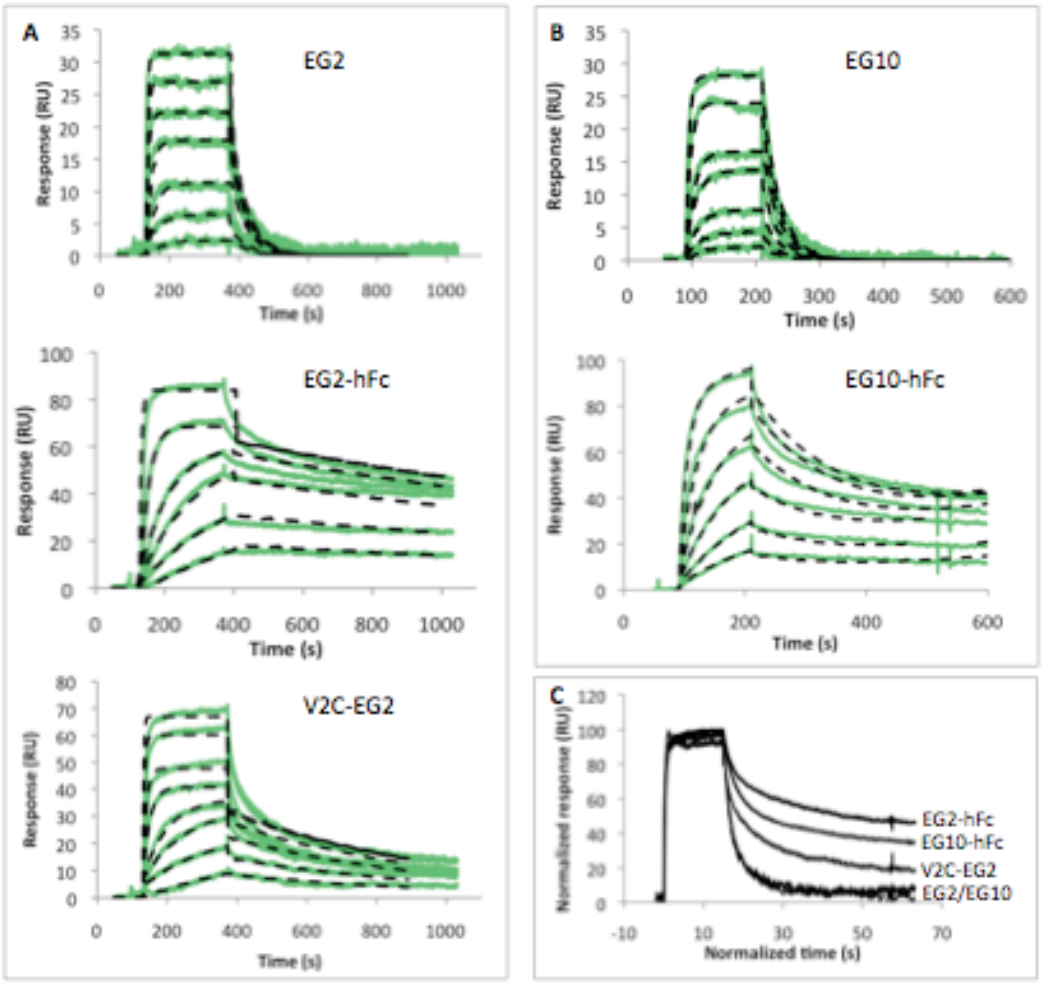

Figure 2-8. Biacore sensorgrams for monovalent and multivalent antibody constructs binding to the same EGFR-ECD chip surface.

The antibody formats were injected at serial dilutions ranging from 3.7 nM to 1 µM over a 400 RU EGFR-ECD sensor chip surface at a flow rate of 20 µl/min. (A) EG2 constructs: the sensorgrams for monomeric EG2 were globally fitted to a 1:1 binding model whereas the bivalent analyte model showed better fit to the sensorgrams obtained for EG2-hFc and V2C-EG2 binding. (B) EG10 constructs: the interaction of EG10 with the EGFR-ECD surface is represented well by a 1:1 Langmuir model. Binding of bivalent EG10-hFc fit well to the bivalent analyte binding model in the BIAevaluation software. The raw data is shown in green and the modeled fits are overlaid in black dashed lines. (C) Overlay of the normalized sensorgrams obtained for the injection of 500 nM antibody constructs (mono- or multivalent).

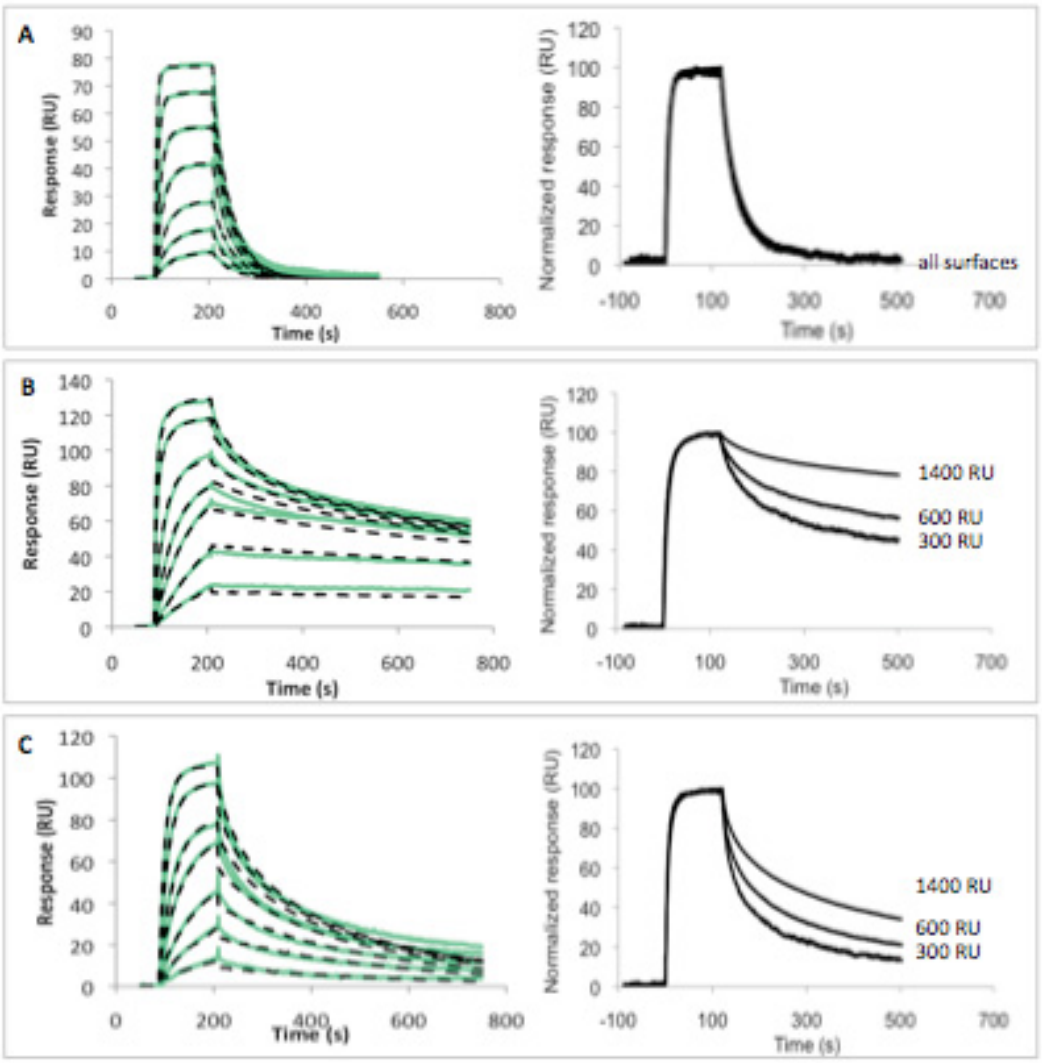

Figure 2-9. Biacore sensorgrams showing the interaction of EG2, EG2-hFc and V2C-EG2 to immobilized EGFRvIII-ECD.

Binding of EG2, EG2-hFc, and V2C-EG2 to immobilized to 600 RU EGFRvIII-ECD is shown in the left column. The constructs were injected at concentrations ranging from 3.7 nM to 500 nM at a flow rate of 20 µl/min. The interaction between monovalent EG2 and the receptor was best described in a 1:1 binding model as shown earlier (Figure 2-4). Similar to the wild-type EGFR-ECD surface the binding of EG2-hFc and V2C-EG2 fit well to a bivalent analyte binding model using the BIAevaluation software. In the right column, overlaid normalized sensorgrams of 500 nM injections over EGFRvIII-ECD surfaces of three different densities are shown. EG2 (A), EG2-hFc (B), V2C-EG2 (C).

* I published the sensorgrams in panel A, as well as the overlaid normalized sensorgrams in the right column of panel B and C in Iqbal *et al.* 2010 (Iqbal et al., 2010b).

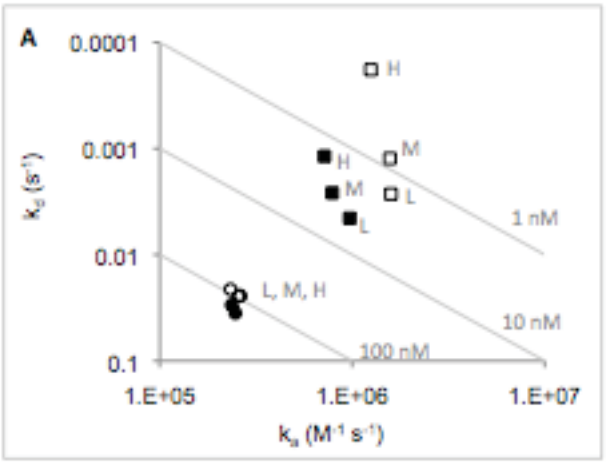

Figure 2-10. Comparison of rate constants measured for the interactions of monovalent and bivalent sdAb constructs on three different EGFR-ECD sensor chip surfaces.

The rate constants of EG2, EG10, EG2-hFc and EG10-hFc binding to immobilized EGFR-ECD on three SPR chips with different receptor densities (400 (L), 750 (M) and 1400 RU (H)) is shown. The association and dissociation rate constants were derived from global fitting to the Langmuir binding model, herein, a 1:1 interaction was also assumed for the multivalent constructs in order to determine apparent affinities. The monovalent constructs are shown as circles and the bivalent constructs are indicated by squares. EG2 (white), EG10 (black).

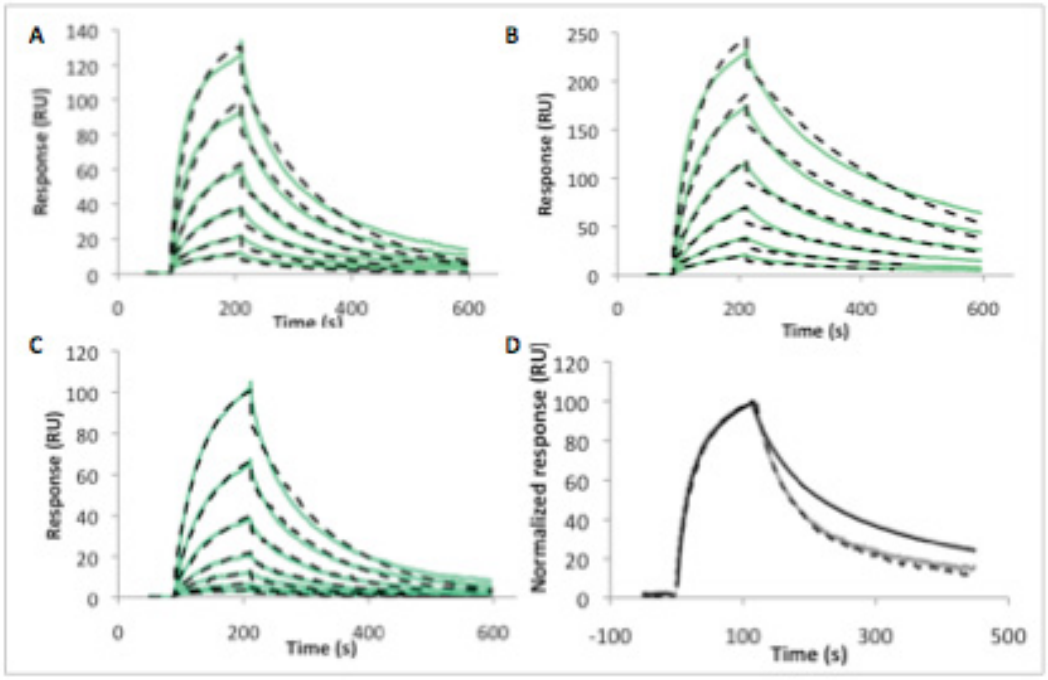

Figure 2-11. Biacore analysis of the interaction of EGFR-ECD with immobilized EG2, EG2-hFc and V2C-EG2.

EGFR-ECD was injected in serial dilutions over a 140 RU EG2 (A), a 300 RU EG2-hFc (B) and a 500 RU V2C-EG2 surface (C). K_D-values of 247 ± 37 nM, 143 ± 54 nM and 307 ± 30 nM were obtained for EG2, EG2-hFc and V2C-EG2, respectively. The 500 nM injections were normalized and overlaid to allow for the comparison of the binding profiles. EG2 (grey line), EG2-hFc (black line), V2C-EG2 (dashed line) (D).

* I published Figure 2-11 D in Bell *et al.* 2009 (Bell et al., 2009).

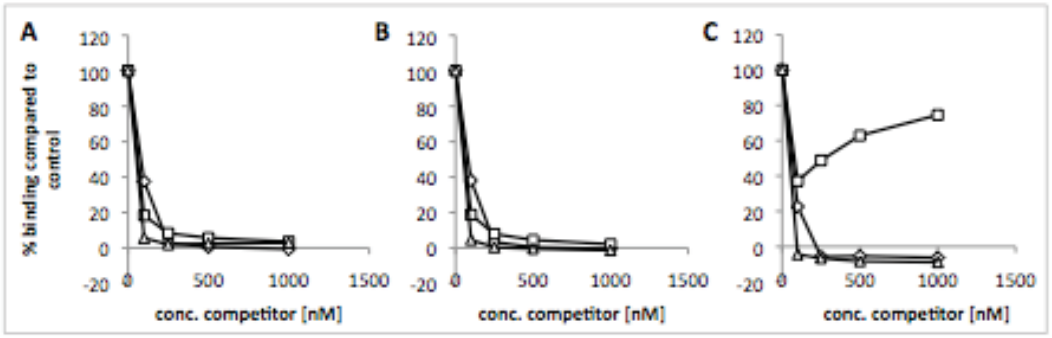

Figure 2-12. Competition of EG2 sdAb constructs binding to EGFR extracellular domain.

500 nM EGFR-ECD was injected over the three surfaces in the present of increasing amounts of competitor (0.25 – 5 μM): EG2 (◇), EG2-hFc (△), V2C-EG2 (□). (A) - 140 RU EG2 surface, (B) - 300 RU EG2-hFc surface, (C) - 500 RU V2C-EG2 surface.

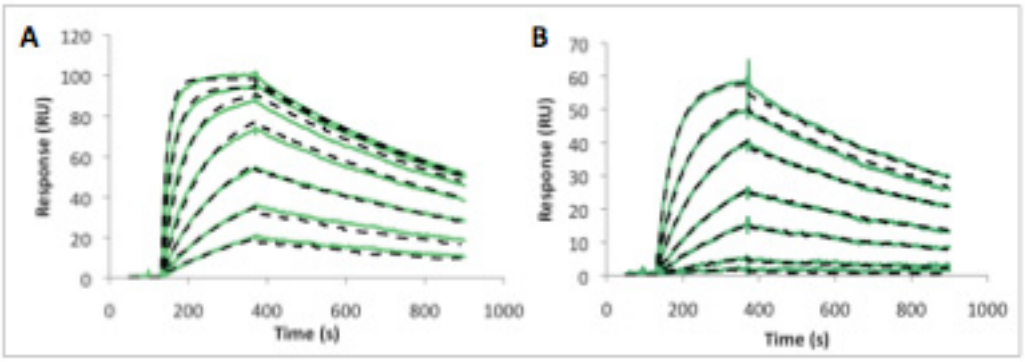

Figure 2-13. Biacore analysis of EGFR-ECD and EGFRvIII-ECD binding to immobilized 225 monoclonal antibody.

225 was immobilized at 200 RU and the receptors were injected over the surface at concentrations ranging from 3.7 nM to 1 uM. The data sets were fit globally to a 1:1 binding model and K_D-values of 2.8 nM and 26.1 nM were obtained for EGFR-ECD and EGFRvIII-ECD, respectively.

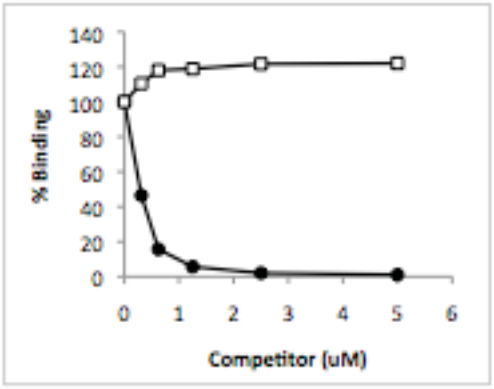

Figure 2-14. SPR biosensor epitope mapping experiment for EG2 and 225 binding to EGFR-ECD.

500 nM EGFR, pre-incubated with increasing amounts of EG2 (0.33 – 5 μM), were injected over 830 RU EG2 (●) and 620 RU 225 (□) surfaces. As shown previously in Figure 2-6, EG2 successfully competes with itself for binding to EGFR. In contrast the response for EGFR binding to immobilized 225 increases with greater amounts of competitor, therefore indicating that EG2-bound EGFR is still able to interact with 225.

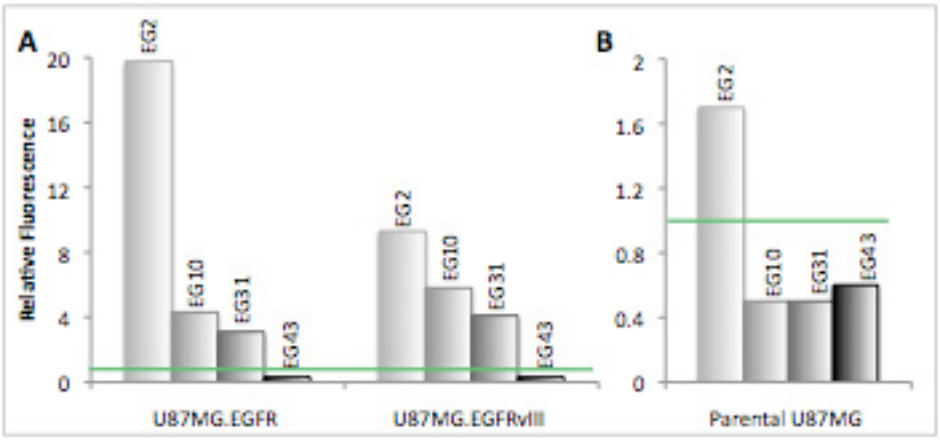

Figure 2-15. Analysis of sdAb binding to cell surface-expressed EGFR and EGFRvIII

Flow cytometry analysis of 2.2 μM single domain antibody binding to U87MG cell lines over-expressing wild-type EGFR and mutant EGFRvIII (A) and the parental cell line with endogenous EGF receptor expression levels of 1×10^5 receptors/cell (B). In contrast, both mutant cell lines are reported to have cell surface receptor expression levels of 1-2 $\times 10^6$ receptors/cell. The green line represents the error threshold of the method.

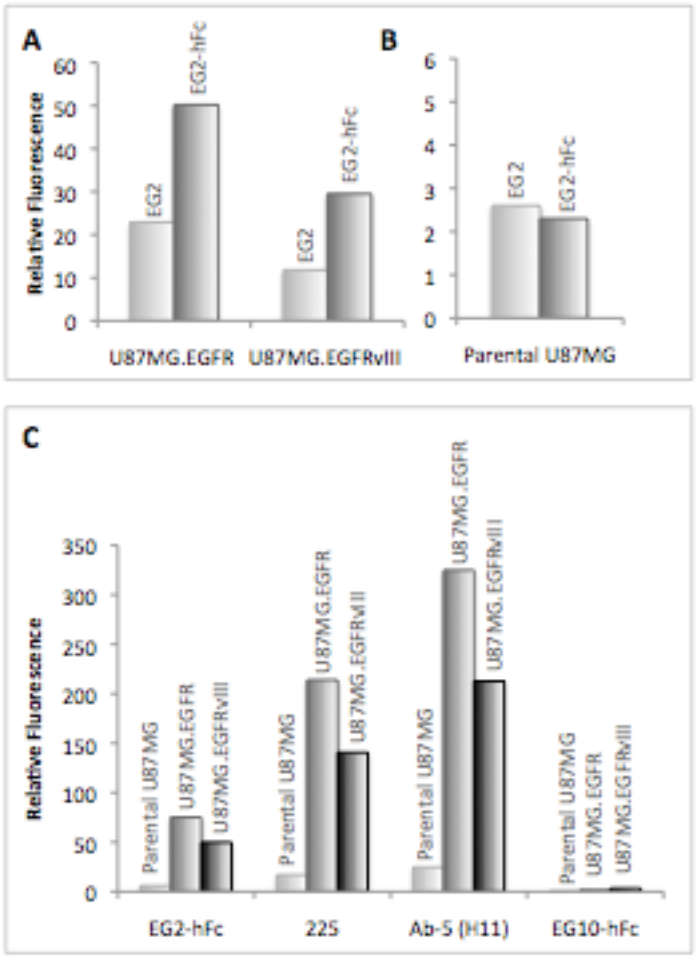

Figure 2-16. Flow cytometry analysis of monovalent and multivalent anti-EGFR antibodies binding to the U87MG cell line panel.

Flow cytometry analysis of monovalent and multivalent EG2 sdAb constructs on U87MG.EGFR and U87MG.EGFRvIII cells (A) and parental U87MG cells (B). EGFR expression levels on the parental cell lines are approximately 10 to 20-fold less than on the EGFR- and EGFRvIII over-expressing cell lines
(C) The binding profile of EG2-hFc (0.3 μM) to the U87MG cell line panel is comparable to that of two commercial anti-EGFR antibodies: 225 and H11 (0.1 μM). The ratio of binding between these three antibodies is consistent, which indicates that they recognize the same population of receptors on the cell surfaces of the U87MG cell lines. In contrast, EG10-hFc (0.5 μM) shows very low labeling efficiency.

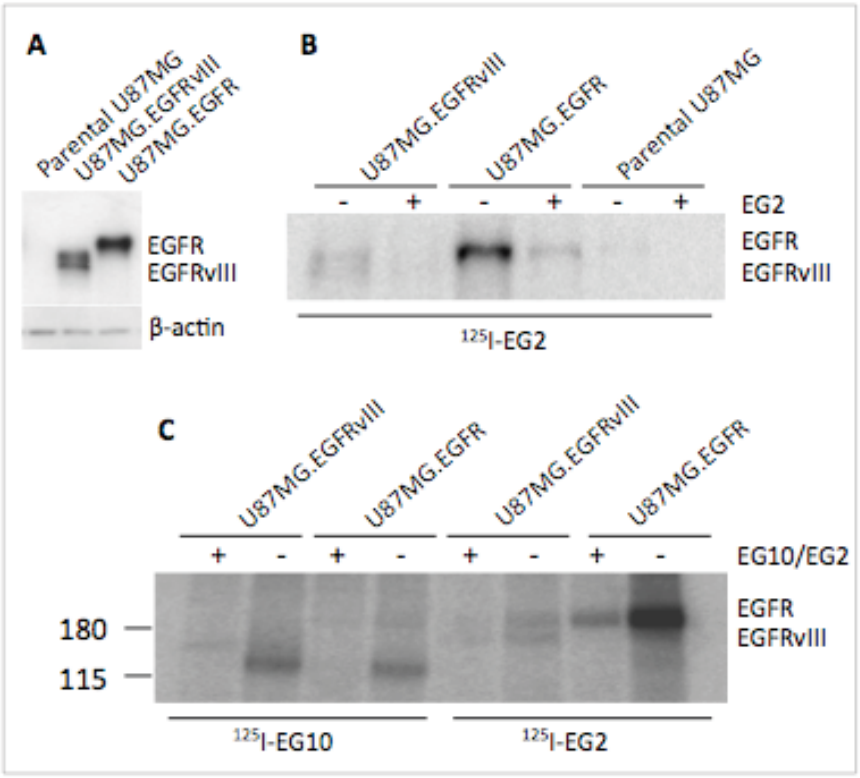

Figure 2-17. Affinity labeling of cell surface expressed EGF-receptors using [^{125}I]-EG2 and [^{125}I]-EG10.

(A) Western Blot of whole cell lysate. EGFR and EGFRvIII were detected with the anti-EGFR antibody sc-03, which recognizes the cytoplasmic domain of the receptor. (B), (C) Whole cell lysates of U87MG cells cross-linked with radiolabeled EG2 and EG10 sdAbs were separated in 8% polyacrylamide gels. The dried gels were exposed to radiosensitive imaging plates for detection.

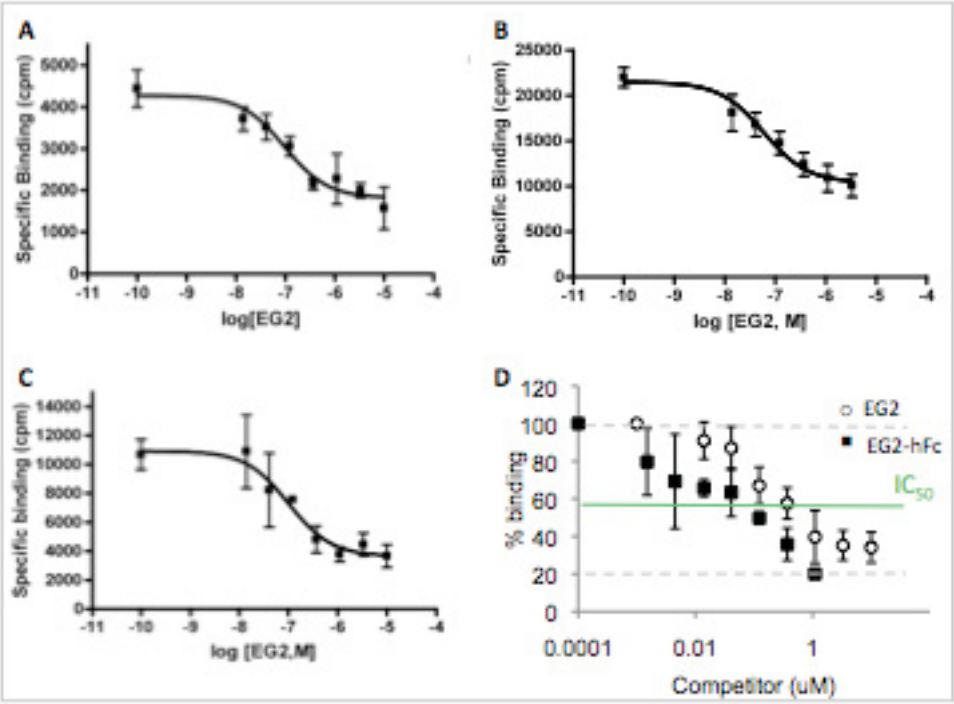

Figure 2-18. Competition binding assay with radiolabeled [^{125}I]-EG2 on EGF receptor over-expressing cell lines.

Representative data fits for the competition of 20 nM radiolabeled [^{125}I]-EG2 for binding to EGFR with unlabeled monovalent EG2 sdAb. IC_{50} values of 197 ± 147 nM for MDA-MB 468 (A), 60 ± 1 nM for U87MG.EGFRvIII (B) and 95 ± 47 nM for U87MG.EGFR cells (C) were obtained. Figure D shows that the bivalent EG2-hFc competes more efficiently with [^{125}I]-EG2 on the cell surface of U87MG.EGFR cells compared to its monovalent counterpart. The error bars indicate the standard deviation for the radioactive counts in a triplicate data set.

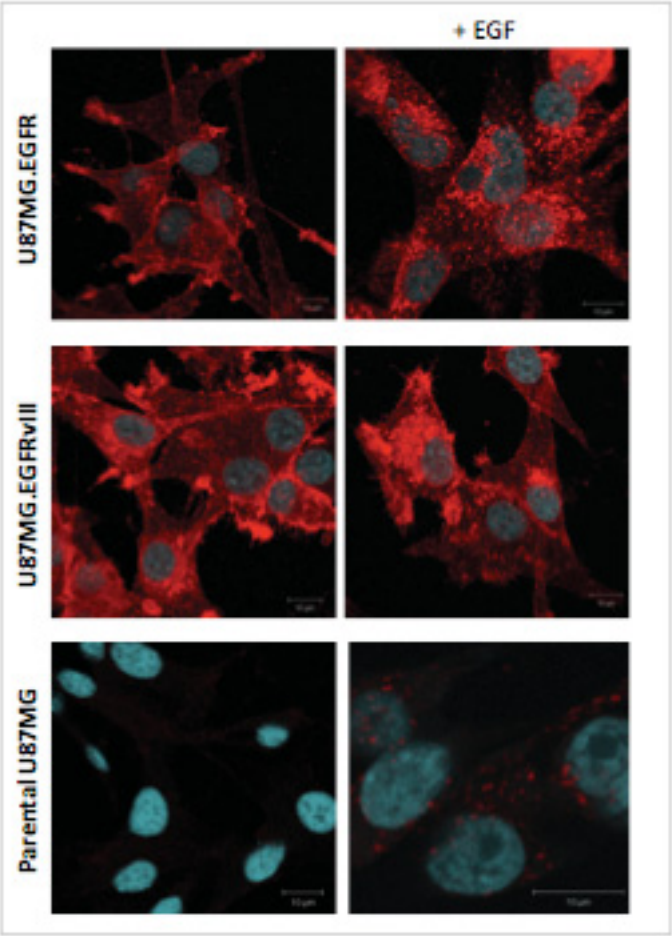

Figure 2-19. Confocal microcopy images of total EGF receptors on fixed cells from the U87MG cell line panel.

Prior to fixation, half of the cells were treated with 100 ng/ml EGF for five minutes. Fixed and permeabilized cells were labeled with 100 nM EG2-hFc for two hours at room temperature. The images were taken under identical acquisition settings: HeNe (633 nM): 10%, Arg (488 nm): 2%. The size bar represents 10 micron.

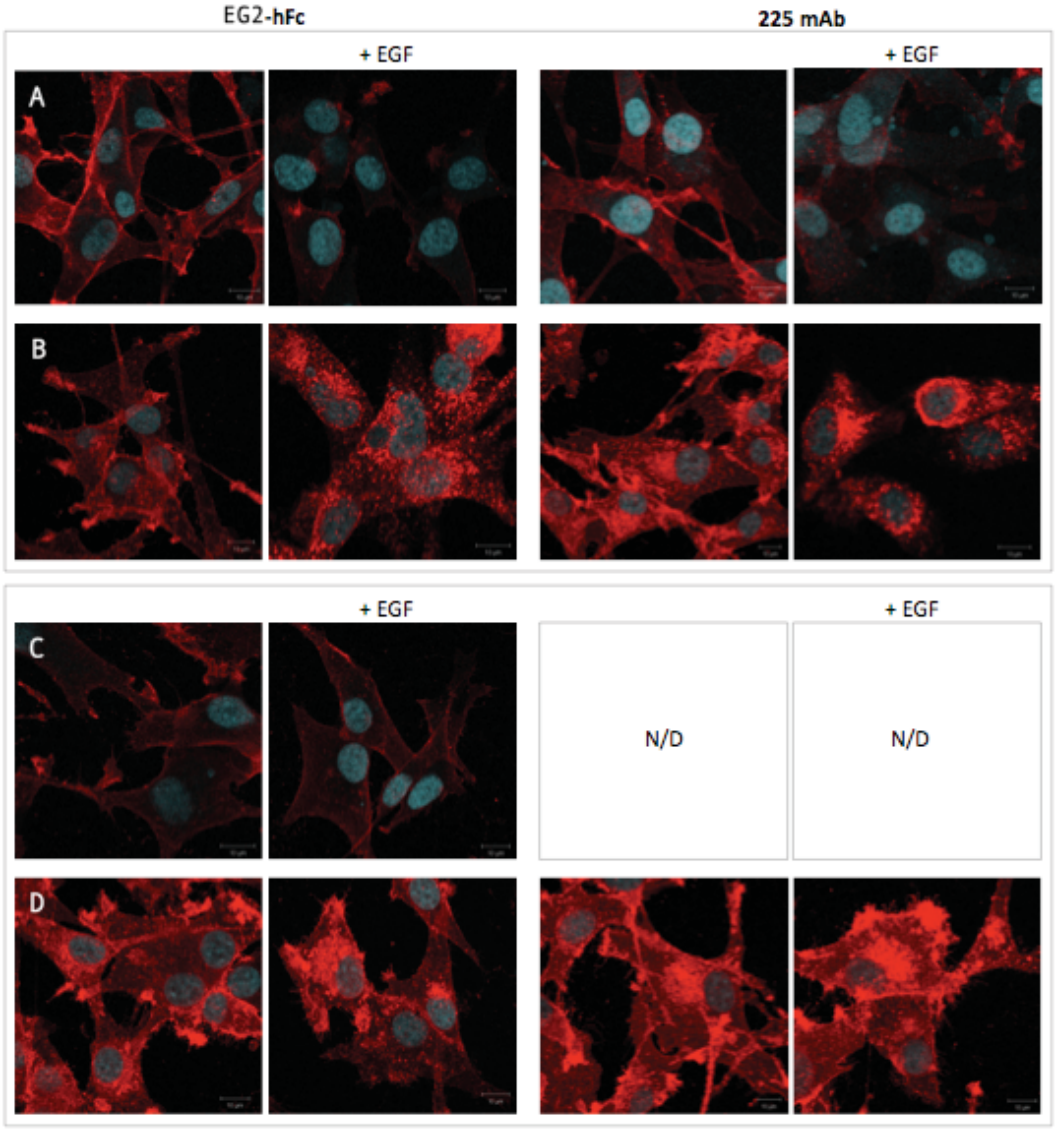

Figure 2-20. Comparative confocal analysis using EG2-hFc and 225 to label U87MG.EGFR and U87MG.EGFRvIII cells.

Confocal microscopy images of fixed U87MG.EGFR (A, B) and U87MG.EGFRvIII (C, D) cells. In half of the cells, EGFR was activated with 100 ng/ml EGF prior to fixation. Surface receptor levels (A, C) and total receptor levels on permeabilized cells (B, D) were investigated with two different antibodies. EGFR was labeled with either EG2-hFc or 225 mAb for two hours at room temperature. The images were acquired under identical settings using the 63× objective: HeNe (633 nm): 10%, Arg (488 nm): 2%. The scale bar in each image represents 10 µm.

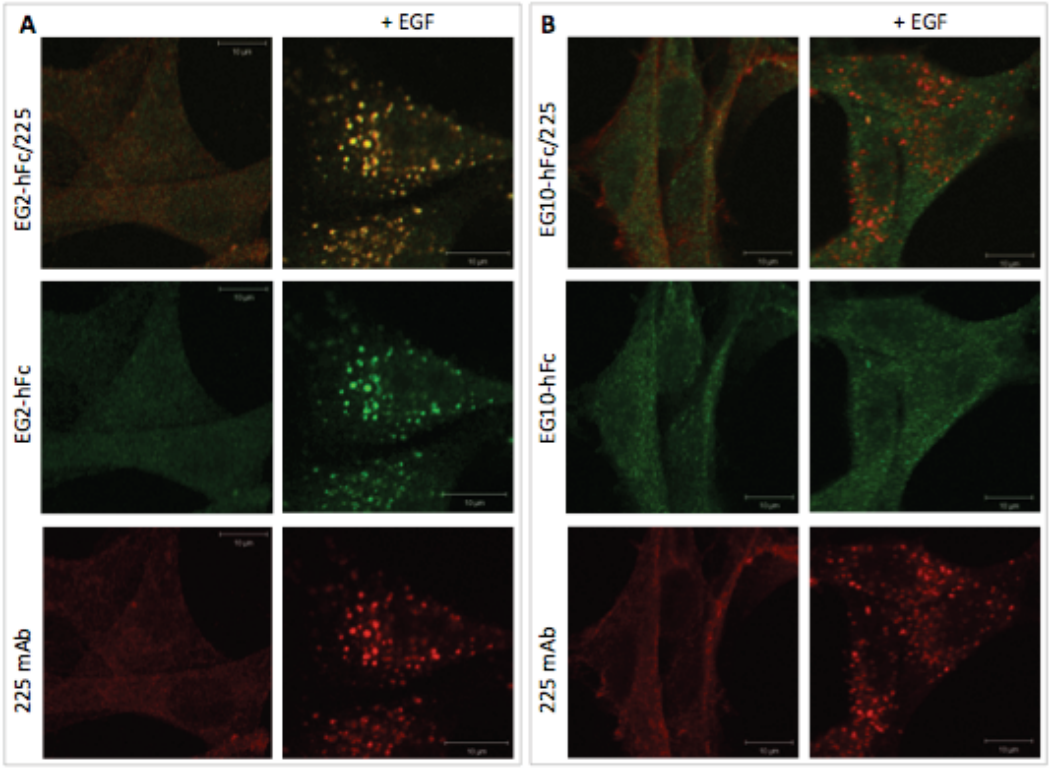

Figure 2-21. Confocal microscopy - colocalization experiment.

Parental U87MG cells were labeled simultaneously with 225 and the bivalent sdAb constructs EG2-hFc or EG10-hFc. EGF-treated and untreated cells were fixed and permeabilized with Triton-x-100 before co-labeling with EG2-hFc and 225 (A) or EG10-hFc and 225 (B). Settings: Arg (488 nm): 1%, HeNe (543 nm): 60%. The size bar represents 10 micron.

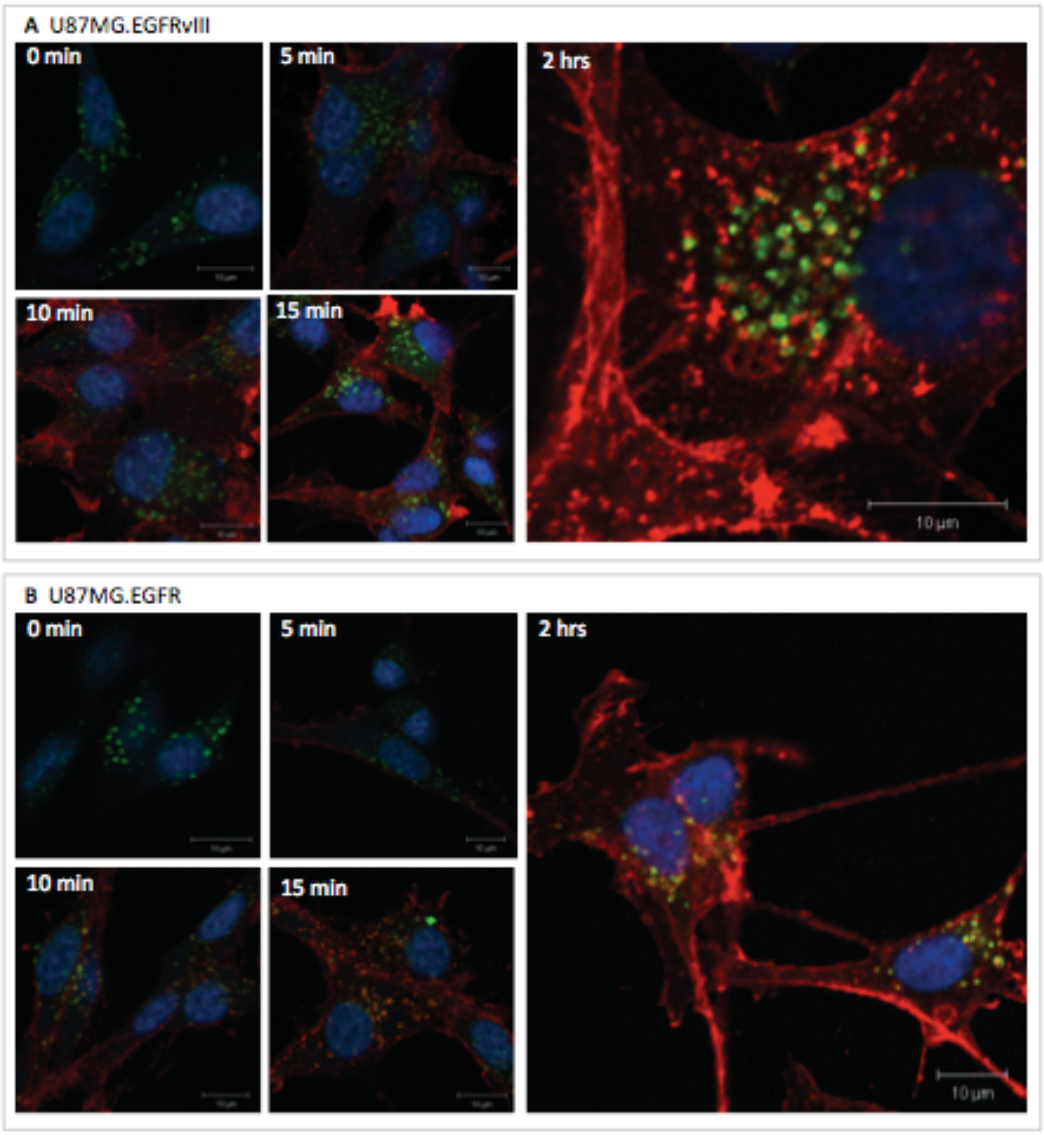

Figure 2-22. Confocal microscopy - EG2-hFc internalization study.

Confocal microscopy image of bound EG2-hFc after different incubation times at 37°C on U87MG.EGFRvIII (A) and U87MG.EGFR (B) cells. The cells were incubated for up to 2 hours with 100 nM EG2-hFc in complete growth media at 37°C. Cells were then fixed, permeabilized and subsequently labeled with anti-EEA1 antibody for 1.5 hours at room temperature. All images were acquired using the same microscope settings: HeNe (543 nm): 70%, HeNe (633 nm): 10%, Arg (488 nm): 2%. The size bar represents 10 micron. EG2-hFc (red), EEA1 (green), nuclei (blue), colocalization (yellow).

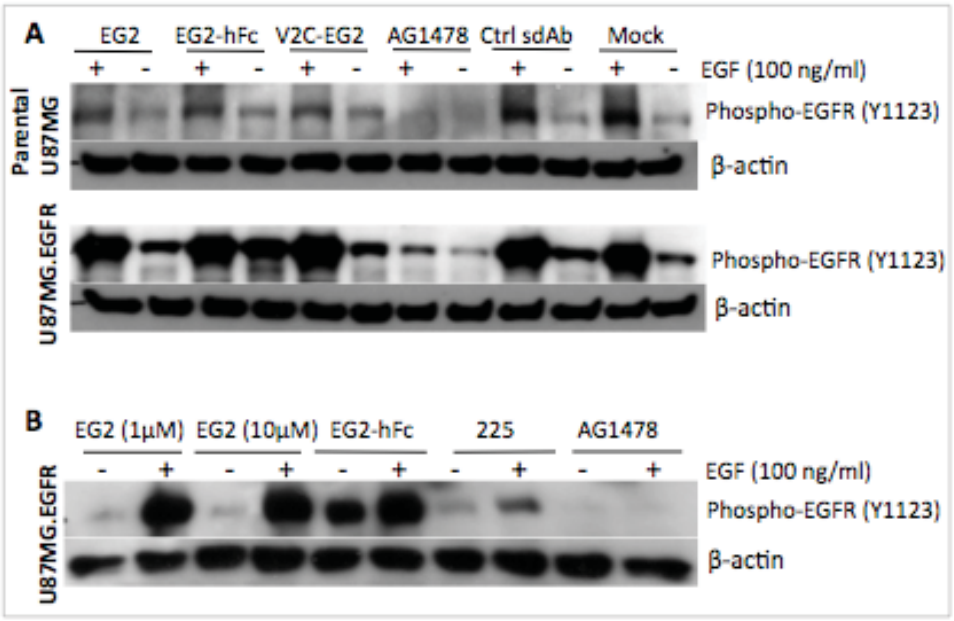

Figure 2-23. Western Blot of EGFR phosphorylation status.

Parental U87MG cells and EGFR over-expressing U87MG.EGFR cells were treated with mono- and multivalent EG2 single domain antibody constructs for 2.5 hours at 37°C followed by 5 minutes of EGF induction, where indicated. A non-specific monovalent sdAb, 225 and AG1478 were included as controls.

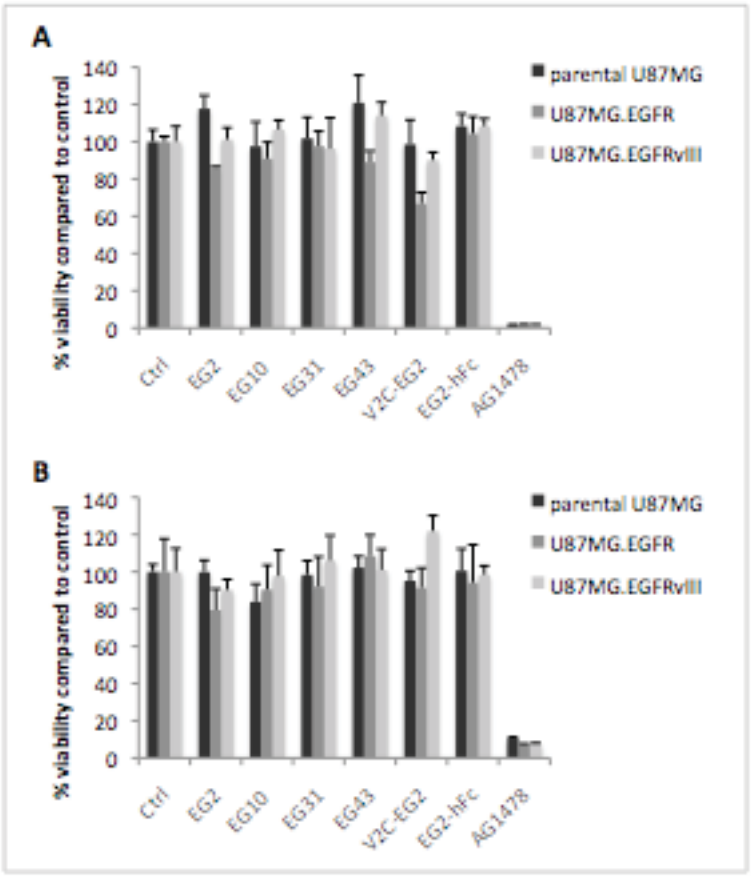

Figure 2-24. Viability assay on the U87MG cell line panel treated with mono- and multivalent single domain antibody constructs.

Parental U87MG. U87MG.EGFR and U87MG.EGFRvIII cells were treated with 5 μM monovalent sdAbs and V2C-EG2, and 1 μM EG2-hFC for 3 days. AG1478 was included as control. At the end of the incubation time the metabolic activity of the cells was measured using Alamar Blue®.

3 Development and characterization of EGFR-targeted iron oxide nanoparticles.

3.1 Introduction

3.1.1 Nanotechnology and the emerging field of nanomedicine

In 1959, the physicist Richard Feynman articulated the concept of nanotechnology in his lecture "There is plenty of room at the bottom" in which he challenged the scientific community to think small (Porter and Youtie, 2009). Today, nanotechnology is a fast-growing, multidisciplinary field that applies engineering and manufacturing principles at a molecular level. Nanomedicine is one category of nanotechnology bearing fruit from the considerable investments being made in nanotechnology research. It is defined as the application of nanotechnology to detect, monitor and treat disease. Within this domain, the research into delivery and targeting of therapeutic and diagnostic agents with nanoparticles is of primary interest (Emerich and Thanos, 2007). Nanoparticles are attractive as therapeutic and imaging agents in oncology due to their unique physical and/or chemical properties. The high surface area to volume ratio associated with nanoparticles, in concert with facile surface functionalization chemistries, allows for loading a large amount of cargo including chemotherapeutic drugs, plasmid DNA and siRNA. Specifically for cancer, nanoparticles between 10 and 100 nm in size preferably accumulate at tumor sites due to the enhanced permeability and retention (EPR) effect. With these properties nanoparticles have the potential to radically improve cancer diagnostic for early tumor detection and serve as customizable therapeutic devices for combined imaging and therapy ("theranostics") (Huang et al., 2011). Drug delivery applications, using lipid- and polymer-based nanoparticle formulations, are currently dominating the field of Nanomedicine with a share of 76% of the scientific papers, 59% of the patents and 25 formulations already approved for the clinical application, examples being Doxil® and Abraxane® which are the nano-encapsulated versions of the chemotherapeutic drugs doxorubicin and paclitaxel (Porter and Youtie, 2009). A

recent review by Wang *et al.* summarizes already approved nanoparticle drug formulations, as well as novel formulations that are currently undergoing clinical investigation (Wang et al., 2012).

Inorganic nanoparticles have gained significant attention in the recent past due to their unique material- and size-dependent physicochemical properties, which are not possible with traditional lipid or polymer-based nanoparticles. In particular, optical, magnetic and other physical properties, in addition to inertness, stability, and ease of functionalization make inorganic nanoparticles attractive alternatives to organic nanoparticles for imaging and ablation of malignant tissue (Huang et al., 2011). Several studies of human brain tumor enhancement using the commercial IONPs Ferumoxtran-10 have been published in the past decade. Herein, it has been demonstrated that ultrasmall superparamagnetic iron oxide nanoparticle (USPIO) contrast agent enhancement constitutes a rim at the margins of human brain tumors, thereby improving their delineation on magnetic resonance images (Kremer et al., 2007; Neuwelt et al., 2004).

The purpose of the study presented here was to develop a superparamagnetic iron oxide nanoparticle for the improved delineation of glioblastoma multiforme (GBM) by magnetic resonance imaging (MRI). GBM is a highly aggressive tumor with distinct histopathological features, including high proliferation, necrosis and considerable neo-vascularization leading to vessels that exhibit morphological abnormalities and 'leakiness' (see "1.1 Gliobastoma multiforme", page 1). MRI has been regarded as a powerful imaging tool as a result of its noninvasive nature, high spatial resolution and tomographic capabilities (see "1.2 Magnetic resonance imaging in GBM patients", page 3). Clinically benign iron oxide based magnetic nanoparticles (IONPs) have been widely explored for such signal-enhancing purposes (see "1.3 Superparamagnetic iron oxide nanoparticles", page 6). Iron oxide nanoparticles are biocompatible and can be degraded safely by macrophages/microglia. Upon degradation the free iron ions released do not significantly increase the body's native iron pool, but instead get incorporated in hemoglobin in erythrocytes and are thus degraded along normal iron recycling pathways (Huang et al., 2011). Both sharper tumor margins and the potential

detection of micrometastases on pre-operative MR images enhanced by an IONP not only may increase the accuracy of stereotactivity biopsy guided by MRI, but also may aid in surgical planning and thereby increase the efficacy of tumor resections (Claes et al., 2008; Enochs et al., 1999; Gambarota and Leenders, 2011). A single particle can be conjugated with a large number of targeting ligands, thereby increasing the affinity of the nanoparticle to its biological target through a phenomenon known as multivalency (see "1.4 Tumor cell-targeted IONPs", page 11). Initially, molecular imaging with paramagnetic agents was performed with gadolinium-conjugated antibodies; however the concentration of metal ions was not sufficient to achieve diagnostic contrast enhancement (Morawski et al., 2004).

In the following chapter I describe the characterization of IONPs from two commercial sources (Ocean NanoTech, Springdale, AR, USA and Genovis AB, Lund, Sweden), one of which I chose to conjugate with the anti-EGFR single domain antibody EG2 to allow for internalization of the contrast agent into EGFR over-expressing tumor cells. The development of a conjugation strategy, analyses of the intermediate conjugation products, as well as the final EG2-IONP complex are subsequently described. Furthermore the binding properties of the immunoparticles were characterized by SPR, confocal microscopy and *in vivo* in a subcutaneous glioblastoma xenograft mouse model.

Chapter 1 of this thesis contains a detailed discussion of the advantages of using tumor-cell targeted iron oxide nanoparticles as contrast agents for MR imaging of brain tumors (see "1.4 Tumor cell-targeted IONPs", page 11 and "1.7 Over-expressed EGF-receptors as molecular targets for the delivery of contrast agents to brain tumors", page 24). However, I did not yet describe the physiological factors influencing toxicity and systemic, as well as intracranial delivery of IONPs. The following paragraphs therefore aim to provide an overview of the information available on IONP synthesis and surface functionalization and their effects on cytotoxicity and *in vivo* distribution.

3.1.2 Synthesis and surface modifications of long-circulating IONPs

Recent advances in nanoscience have led to the development of novel nanomaterials for molecular and cellular imaging, including iron oxide nanoparticles (Jain, 2005). Key requirements for the successful use of these nanoparticles in biomedical applications are good dispersity, colloidal stability in biological media, internalization efficiency and low toxicity. Nanoparticle production approaches for applications in humans furthermore need to be well-characterized, display low batch to batch variability, and easy to prepare in a cost-effective manner (Prestwich, 2008).

Synthesis of the iron oxide core

There are many different methods that have been used in the past to synthesize magnetic nanoparticles, including vapor deposition, mechanogrinding, microemulsion, sol-gel processes and co-precipitation of ferrous and ferric salts (Yang et al., 2008). First generation IONPs (e.g. Feridex IV) are made from alkaline co-precipitation of $Fe(OH)_2$ and $Fe(OH)_3$ suspensions. The resulting particles exhibit size variations between several nanometers and several hundred nanometers in diameter (Huang et al., 2011) (Figure 1-c). However, particle size is an important parameter as it can directly affect their magnetic properties, physical stability, cellular uptake and biodistribution. In addition, the magnetism of IONPs and its effect on MR imaging can depend significantly on their morphology, crystal structure, and uniformity (Yang et al., 2008). Therefore, second-generation IONPs are produced by thermal decomposition (pyrolysis), which yields particles of narrow size distribution (Figure 1-c) (Hyeon et al., 2001; Jun et al., 2005). The superior crystallinity of the second generation IONPs generates larger r_2-relaxivities (Xie et al., 2010). Both commercial IONP formulations that I investigated in this study are generated by thermal decomposition chemistry.

Functionalization of the particle surface with biocompatible polymers

Surface coatings are an integral component of all MNP platforms. Due to their superparamagnetic properties, nanoparticles still have significant tendency to

agglomerate as a result of their high surface energy. Polymeric coatings provide a steric barrier to prevent nanoparticle agglomeration and represent a means to tailor the surface properties of IONPs such as surface charge and chemical functionality (Sun et al., 2008). A variety of methods have been employed to functionalize IONPs with coatings of inert polymers including dextran, polysaccharides, PEG and polyethylene oxide, in order to increase their stability, circulation half-life and biocompatibility (Huang et al., 2011). PEGylation has evolved as gold standard for surface modification of all kinds of organic and inorganic nanoparticles. The PEG moiety forms an aqueous layer on the surface of nanoparticles and confers steric hindrance, which results in the inhibition of protein (opsonin) adsorption and prevents recognition by the mononuclear phagocytic system (MPS) located in the liver and spleen (Hatakeyama et al., 2011). The effect of PEGylation depends on the molecular structure of PEG and the extent of PEGylation (Bae et al., 2011). PEG polymer chains are generally considered safe and can be prepared synthetically at high purity and in large quantities, which has led to their approval by the FDA (Schnyder and Huwyler, 2005; Veronese and Pasut, 2005). PEG is not biodegradable and PEG molecules with molecular weights below 40 kDa are readily excreted from the body via the kidneys. It should be noted however, that recent evidence showed that PEG-liposomes previously considered biologically inert, could still induce certain side-reactions via activation of the complement system (Torchilin, 2011). PEGs used for the modification of drugs and drug carriers usually have a molecular weight from 1,000 to 20,000 Da (Torchilin, 2010). From the practical point of view, PEGs are commercially available in a wide range of molecular weights and customized conjugation approaches can be easily effectuated when choosing the appropriate functional group from a variety of “activated” PEGs (Peng et al., 2008). To achieve better selectivity of PEG-coated nanoparticles, it is advantageous to attach the targeting ligand at the terminal end of the PEG spacer arm so that the ligand is extended outside of the dense PEG layer, hence reducing steric hindrance for ligand recognition of the target (Torchilin, 2010). The most commonly employed conjugation chemistries are thiol reactive (e.g. maleimide,

2-pyridyldithio, iodoacetyl) and amine reactive (NHS, epoxy, aldehyde EDC) chemistries. Ligand attachments on tumor-targeting nanomaterials must remain stable against *in vivo* degradation for hours while they circulate systemically and identify their molecular targets (von Maltzahn et al., 2008).

3.1.3 Bimodal imaging

The idea of a multimodal nanoparticles for pre-operative MR imaging and intra-operative optical brain tumor delineation was sparked by the groups of Josephson and Weissleder at Harvard Medical School (Kircher et al., 2003). Multimodality imaging combines two or more distinct imaging modalities in a way that leverages the respective strength and weaknesses of each imaging technology. The large surface of IONPs allows for the attachment of different imaging agents: examples include combined PET-CT, PET-MR, and MR-fluorescence imaging (Glaus et al., 2010). The dual modal imaging using magneto/optical nanoparticles is expected to give good anatomical information via MRI, along with more detailed information on a cellular level using fluorescence imaging, thus allowing for better correlation of pre-operative MR images with intra-operative optical imaging in the absence of ionizing radiation (Bertorelle et al., 2006; Sung et al., 2009; Veiseh et al., 2005). In the absence of tumor cell specific labels, neoplastic tissue is virtually indistinguishable from normal brain (Koo et al., 2006). Clinical studies have demonstrated the benefit of fluorescence-guided surgery, which translated into higher progression-free survival (Stummer et al., 2006). However, the development and distribution of NIRF based clinical imaging systems lie well in the future, while MRI is an established imaging modality with the ability to visualize probe accumulation deep within the human body (Schellenberger et al., 2004).

In mice optical probes in the wavelength of 680 nm (e.g. Cy5.5) are most frequently used and were shown to provide sufficient penetration depths (Schnall and Rosen, 2006). For *in vivo* bimodal imaging in humans, the fluorescent dyes indocyanine green (IDC) could be conjugated to IONPs. IDC is approved by the

FDA and is characterized by near-infrared absorption and emission maxima near 780 and 820 nm (Malicka et al., 2003).

3.1.4 The journey of a nanoparticle: from injection site to tumor

There is currently a good understanding of how IONPs distribute within the body upon systemic administration and several strategies have been developed to increase their circulation times (e.g. by employing the aforementioned PEGylation strategy) and to enable them to target solid tumors. Herein, a large number of barriers need to be overcome ranging from hepatic and enzymatic degradation, to high interstitial fluid pressure that is typical of tumors, and to cellular membranes. The following paragraph will therefore give a short overview of this vast field of knowledge that was recently summarized in a number of excellent reviews (Bae et al., 2011; Bertrand and Leroux, 2011; Hamad and Moghimi, 2008; Islam and Josephson, 2009; Lammers et al., 2011; Moghimi et al., 2005).

The fate of IONPs upon intravenous administration is highly dependent on their size, morphology, charge and surface chemistry (Sun et al., 2008). Large proportions of magnetic iron oxide nanoparticles are sequestered relative quickly by the mononuclear phagocyte system (MPS) in the liver and spleen and then are subsequently metabolized or used for iron storage (Bulte and Kraitchman, 2004). The ability of IONPs to evade uptake by the MPS is critical for achieving a long blood half-life, therefore the ability to control size and surface modification of IONPs is of crucial importance for their *in vivo* targeting success.

Most studied IONPs have an overall size of around or larger than 50 nm, a size range that facilitates phagolytic clearance. The “tagging” of nanoparticles by adsorption of complement proteins, such as fibronectin and immunoglobulins, is called opsonization and is highly dependent on the surface properties of the carrier. Negatively- or positively-charged, highly hydrophobic or irregular surfaces promote the adhesion of complement protein. Adsorption can furthermore result in nanoparticle aggregation, which also contributes to rapid MPS recognition and sequestration (Bertrand and Leroux, 2011; Moghimi et al., 2001). The conjugation of a range of polymers (e.g. PEG) has therefore been

developed to prevent particle aggregation. While positively charged polymers tend to non-specifically stick to cells, strong negative charges on the particle surface are also detrimental in that they result in increased liver uptake. Therefore, it is generally agreed that nanoparticles with a neutral surface experience extended blood circulation times (Fang et al., 2011; Roser et al., 1998; Shi et al., 2007; Sun et al., 2008).

I explained in the first chapter of this thesis that for nanoparticles the primary mode of tumor localization relies on EPR-mediated passive extravasation (see "1.3 Superparamagnetic iron oxide nanoparticles", page 6). In tumors, the vessel-wall structure is abnormal with wide inter-endothelial junctions, an abnormally thick or thin basement membrane, large numbers of fenestrae and trans-endothelial channels formed by vesicles and pore diameters as large as several hundred nanometers (Jain and Stylianopoulos, 2010). Together with the fact that solid tumors tend to lack functional lymphatics and therefore are unable to eliminate extravasated nanonmaterials, this increase in vascular leakiness allows long-circulating nanomedicines to accumulate in tumors over time (Lammers et al., 2011). The requirement for achieving efficient tumor targeting is therefore the presence of a favorable EPR-effect. There are certain human tumors which are very leaky, e.g. because they express high levels of VEGF. However, even within a single tumor there are huge differences with regards to vascular permeability and in many cases there are parts in which particles as large as 200 nm are able to extravasate, whereas in (the vast majority of) other parts not even molecules in the size range of albumin (i.e. 3-4 nm) are able to enter the interstitium (Bae et al., 2011). Thus, depending on the tumor model used and/or the human malignancy in question and on how well they allow for extravasation and penetration, it can be more or less easy for nanoparticles to find and bind cancer cells (Lammers et al., 2011). Unfortunately, practical information is still lacking on the extent of the EPR effect of most solid tumors (Bae et al., 2011).

But there is good news, too. Several mechanisms to enhance the EPR effect have been proposed and are currently being investigated for their use in the clinics. For example, Maeda and colleagues developed methods to achieve a more

homogeneous delivery to tumors by elevating blood pressure or by applying nitric oxide-releasing agents. Nitric oxide is known to play a key role in angiogenesis, cell proliferation and the EPR-effect (Fang et al., 2011).

Translocation from the blood compartment to the tumor tissue is governed by convection and diffusion. The driving force behind convective flow is the pressure gradient. In contrast, the main mechanism of transport within tumors is diffusion (Bae et al., 2011). The rate of diffusional extravasation at a given concentration gradient across tumor vascular fenestrae can be controlled by nanoparticles parameters such as size, shape, surface properties and concentration within the tumor blood vessel, as well as by the physicochemical properties of the interstitial matrix. The collagen content is the major determinant of interstitial transport. Tumors rich in collagen hinder diffusion to a greater extent than tumors with low collagen content. Another determinant of interstitial transport is the sulfated glucosaminoglycan content. These thin and elongated fibers not only significantly increase the viscosity of the interstitial fluid, but they also carry a highly negative charge such that even in small quantities can inhibit the transport of materials by forming aggregates (Bae et al., 2011; Jain and Stylianopoulos, 2010).

Finally, another barrier that comes into play when targeting specifically to the brain is the blood brain barrier (BBB).

3.1.5 Delivery across the blood brain barrier

The BBB is composed of brain capillary endothelial cells connected by tight junctions (zonulae occludens), astrocyte end-feet ensheathing the vessels and pericytes. Pericytes are the least-studied cellular component of the BBB but appear to play a key role in angiogenesis, structural integrity, and formation of endothelial tight junctions (Ballabh et al., 2004). Currently, iron oxide nanoparticles destined for brain tumor imaging are systemically administered and were shown to penetrate the BBB. IONP contrast agent enhancement constitutes a rim at the margins of human brain tumors, thereby improving their delineation on MR images (Enochs et al., 1999; Kremer et al., 2007; Neuwelt et al., 2004;

Varallyay et al., 2002). Angiogenesis in glioblastoma is comparable to that in other solid tumors resulting in leaky vasculature and impaired lymphatic drainage, which promote the EPR effect, as described above. It has been reported that in the diseased state, the fenestrations of the BBB increase from 5 to 10 nm up to a micron (Emerich and Thanos, 2007). In addition, the brain cancer may enhance the BBB permeability by increased pinocytosis (Koo et al., 2006).

Nevertheless, efforts are being undertaken to increase the delivery of nanoparticles to the brain and improve their distribution by developing strategies that are independent of pre-existing BBB permeability. These approaches could also prove useful in the delivery of therapeutic agents for the treatment of neurodegenerative diseases, in which the BBB might be unaltered. CNS delivery may be achieved by transient opening of the tight junction using artificially created osmotic pressure by administration of hyperosmolar agents such as mannitol. Barrier opening however poses significant risk for CNS toxin entry and subsequent damage (Lockman et al., 2003). Convection-enhanced delivery (CED) is a minimally invasive surgical procedure that provides fluid convection in the brain by a pressure gradient that bypasses the BBB. High concentrations of therapeutic agents can be delivered into the brain by CED without toxicity to normal tissue and organs commonly associated with systemic delivery. Perlstein *et al.* demonstrated the intracranial delivery of dextran-coated NPs with an average hydrodynamic diameter of 80 nm in a rat brain model using CED (Perlstein et al., 2008). Recently, phase I/II clinical trials have been performed for using CED for the treatment of recurrent GBM (Hadjipanayis et al., 2010; Lidar et al., 2004; Sampson et al., 2003). Another strategy uses peptides derived from apolipoprotein E (ApoE) to decorate the surface of liposomes for delivery across the BBB, via receptor-mediated endocytosis (Re et al., 2011). ApoE participates in the transport of lipids into the brain via the LDL receptor, which is essential for maintaining cholesterol homeostasis (Wohlfart et al., 2011). Transcytosis of nanoparticles can also be mediated by other receptors expressed in the BBB, such as for example the transferrin and the lactoferrin receptors (Xie et al., 2011). Examples of brain targeting vectors include cationized albumin, the OX26

monoclonal antibody to the rat transferrin receptor, or monoclonal antibodies to the insulin and lactoferrin receptors (Schnyder and Huwyler, 2005; Xie et al., 2011). Another example is a recent study by Reddy *et al.* in which the F3 peptide, that binds to nucleolin expressed on tumor endothelium and cancer cells, was utilized to deliver multifunctional IONPs to brain tumors (Reddy et al., 2006). Of interest are also the two VHH domains that were recently reported to cross the BBB and promote targeting to the brain (Iqbal et al., 2010a; Muruganandam et al., 2002). Additionally, in a number of the biodistribution studies it has been shown that PEGylation of the nanocarriers can considerably improve their uptake in the brain. Nevertheless, coating with most surfactants does not lead to an enhanced transport of nanoparticle-bound drugs into the brain. Among the surfactants investigated as nanoparticle coatings, polysorbate 80 has long been considered to represent a gold standard, which proved to be effective for brain delivery of different types of the nanoparticles, for example, solid lipid nanoparticles (Wohlfart et al., 2011). Herein, the effect of polysorbate 80 coatings was attributed to surfactant-mediated specific adsorption of ApoE (Ramge et al., 2000). Finally, reducing pericyte coverage of tumor blood vessels by using a TGF-β inhibitor was recently reported to greatly increase the intratumor uptake of nanoparticles in the brain (Fang et al., 2011).

In summary, nanoparticles possess ideal prerequisites to function as carriers that cross the BBB, since they may be decorated with numerous combinations of polymers, surfactants and targeting ligands for optimized BBB penetration.

3.2 Experimental Procedures

Nanoparticles

Iron oxide nanoparticles with amino-functionalized surfaces were purchased from Ocean Nanotech (Springdale, AR, US) and Genovis (Lund, Sweden).

Expression, production and purification of EG2cys sdAbs

The cDNA encoding the EG2 sequence was cloned into the *Eco*RI and *Bam*HI sites of a pSJF2 periplasmic expression vector, which added an additional cysteine at the C-terminus of the sdAb ("EG2cys"). Roger MacKenzie's group at the NRC-IBS did the cloning. I subsequently carried out the production and purification of EG2cys according to the procedure described previously for single domain antibodies (Bell et al., 2010). In short, following IPTG induction, the protein was expressed periplasmically and purified by metal affinity chromatography on a HiTrap chelating column (GE Healthcare), followed by gel filtration on a Superdex 75™ column (GE Healthcare). The purity of the protein was assessed by SDS-PAGE using Coomassie staining and anti-His antibody (Invitrogen) for protein detection. EG2cys antibodies intended for the *in vivo* animal studies were additionally purified on an EndoTrap™ column (Hyglos GmbH, Bernried, Germany) according to the manufacturer's recommendations.

Production and purification of mono-pegylated EG2 sdAb.

EG2cys was reduced with TCEP-HCl (Sigma-Aldrich) in the presence of 20 mM EDTA for 30 minutes at room temperature. Mono-functional maleimide-activated PEG (MAL-PEG, 2 kDa) (NOF Corporation, Tokyo, Japan) was added to a final ratio of 10 : 1 (MAL-PEG : EG2cys), unless otherwise stated. The reaction was terminated by quenching unreacted maleimide functional groups through the addition of excess amounts of glutathione (Sigma-Aldrich). The sample was purified at a flow rate of 0.5 ml/min on a Superdex 75™ gel filtration column, pre-equilibrated in PBS. The purity of the fractions was analyzed by 14% TSDS-PAGE and subsequent Coomassie staining for visualizing the protein in the gel. Highest purity fractions were pooled and concentrated by centrifugation using Amicon® filter units, MWCO 10,000 Da (Millipore, Billerica, MA, US).

SPR binding studies

(a) EG2 sdAb was bound to a maleimide-activated surface through an additional cysteine, at the C-terminus of this protein. Briefly, the protein was reduced prior to injection in the presence of 10 mM TCEP-HCl/10 mM EDTA to disengage intermolecular disulfide bonds. 50 µl of a 2.5:1 solution of SMCC (17.8

mM in 40% DMF)/EDC (1.16 mM in 100 mM MES buffer, pH 5) was injected over the chip surface at a flow rate of 5 µl/min, followed by manual injection of protein in 10 mM NaOAc, pH 4 until the desired density was reached. 50 µl of glutathione (50 mM in 10 mM NaOAc, pH 4) was then injected to block residual maleimide groups on the chip surface. Serial dilutions of EGFR-ECD (15.6 nM – 1 µM) were injected over different EG2cys surfaces (15 – 84 RU) and a 1:1 Langmuir binding model was applied to determine the kinetic parameters.

(b) Alternatively, mono-PEGylated EG2cys (EG2-PEG) was injected at concentrations from 3.9 nM to 1 µM over a 700 RU EGFRvIII-ECD surface at 20 µl/min. In the competition experiment, 500 nM EGFR-ECD were co-injected with either EG2 or EG2-PEG (0.25 – 5 µM) over a 800 RU EG2 surface at 5 µl/min. Binding in RU was measured after 20 µl of analyte were injected and plotted over the concentration of competitor.

(c) Purified EG2-IONPs and control IONPs were diluted in HBS and injected over three different densities of immobilized EGFR-ECD (40, 150 and 570 RU) on a Biacore sensor chip, followed by injection of 8.5 µM EG2 at a flow rate of 5 µl/min.

Dynamic light scattering

Nanoparticle light scattering experiments were carried out using a Malvern High Performance Particle Sizer (HPPS) 3.3 (Malvern Instruments, Worcestershire, UK), equipped with a 3 mW He-Ne laser (λ = 632 nm). Measurements were performed at 25°C and at a constant angle of 173°. The hydrodynamic size and size distribution were determined using the cumulant method in the HPPS software. Final results were determined from at least three independent measurements, each consisting of 10 cycles.

Zeta potential measurements

Zeta-potential measurements were performed at 25°C on a Zeta Plus S/N Analyzer, (Brookhaven Instruments Corp., USA). In short, a palladium electrode (AQ-479) was placed in the center of a disposable plastic cuvette containing 1.5 ml of sample and connected to the instrument. A reference nanoparticle solution

was analyzed before and after each series of measurements to confirm the integrity of the experimental conditions. The values were calculated using the Smoluchowski model in the BIC Pals software (Brookhaven Instruments). The final values were averaged from at least 5 runs, each consisting of 15 cycles.

Fluorescamine Assay

Nanoparticles were suspended in 100 mM boric acid/NaOH (pH 8) and transferred to a 96-well plate. A stock solution of 0.03% fluorescamine/acetone (w/v) (Sigma-Aldrich) was added to a final concentration of 0.0025% to each well and the plate was incubated in the dark for 10 minutes at room temperature (Corsi et al., 2003). The plates were subsequently measured in a SpectraMax Gemini XS spectrophotometer (Molecular Devices, Sunnyvale, CA, US) at 390 nm excitation and 480 nm emission settings. Serial dilutions of glycine (0.02 – 3 mM) were used to generate the standard curves.

Cell viability assay

Parental U87MG and MDA-MB 468 cells were cultured as described in Chapter 2. HepG2 cells and RAW264.7 cells were cultured in DMEM supplemented with 10 % FBS and 2 mM glutamine (HyClone) under humidified atmosphere, 5% CO_2. Three times 10^3 cells were seeded in 96-well plates and allowed to adhere over night. IONP dilutions ranging from 3.7 to 300 μg/ml in complete media were added to triplicate wells. The plates were incubated for 72 hours after which the metabolic activity of the cells was measured using Alamar Blue® reagent (see "2.2 Experimental Procedures ", page 35).

Phantom MRI experiments

The phantom MRI experiments were carried out on serial dilutions of targeted EG2-IONPs and non-targeted control IONPs in deionized water. Iron concentrations of the particle solutions ranged from 50 – 400 μM. T_2 relaxation was measured on a 7 T Bruker Pharmascan 300 MRI scanner (Bruker BioSpin Ltd, Milton, ON, Canada).

Production of EGFR-targeted nanoparticles (EG2-IONPs)

The conjugation process was done in three steps. In step 1, amine-functionalized iron oxide nanoparticles were conjugated with DyLight680 NHS-reactive dye (Thermo Scientific Rockford, IL, US) at a ratio of 400 : 1 (dye : particle) in PBS, pH 7.2 at 2 hours at room temperature or alternatively at 4°C for 12 hours in the dark. In addition, the reaction mix was bubbled with argon gas to remove oxygen that would contribute to the accelerated oxidization of the functional groups. Excess free dye was removed by gel filtration using a self-packed 25 ml Sepharose 6B column that allows the separation of molecules up to 4000 kDa (Sigma-Aldrich). The purified fractions were concentrated in an Amicon® Ultra-4 centrifugal filter (Millipore) and stored at 4°C until further modification. In step 2, the SMCC crosslinker (Molecular Biosciences, Boulder, CO, US) was added at a ratio of 5000 : 1 (SMCC : particle), i.e. ~10 : 1 (SMCC : amino-group), to the previously fluorophore-labeled particles. The reaction was incubated for 2 hours at room temperature in the dark. Non-conjugated cross-linker and excess free dye were removed by gel filtration in a self-packed 25 ml Sepharose 6B column (Sigma-Aldrich) at a flow rate of 0.5 ml/min. The purified maleimide-activated IONP-680 were concentrated by centrifugation using an Amicon® Ultra-4 filter. In the next step, monomeric EG2cys was prepared by TCEP-HCl reduction as described previously and added to the maleimide-activated nanoparticles at a ratio of 100 :1 (protein : particle). After one hour incubation at room temperature, the unreacted maleimide groups were quenched by adding glutathione at a final concentration of 16 mM to the sample. EG2-IONPs were subsequently purified by gel filtration and concentrated as described.
The quantity of immobilized sdAb was assessed using a Bradford protein assay in reference to BSA standards according to the manufacturer's instructions (Pierce). The final concentration of nanoparticles in the solution was determined by measuring the optical density (OD) at 500 nm in comparison to a series of IONP dilutions of known concentration (personal communication with Ocean NanoTech). The EG2cys protein did not absorb significantly at this wavelength and contribution of conjugated protein to the measured OD of the particle solution was therefore considered negligible (data not shown).

Laser scanning (confocal) microscopy

Cell culture and slide preparation was carried out as described in Chapter 2 of this thesis (see "2.2 Experimental Procedures", page 35). IONPs used for cell labeling were either conjugated with Alexa Fluor® 488 NHS-activated fluorophores (Invitrogen) or detected indirectly using an anti-PEG (backbone) antibody (Epitomics, Burlingame, CA, US), according to the manufacturers's instructions.

Tumor xenografts

Six to 8-week old male and female nude mice (nu/nu), weighing 20-25 g each, were purchased from the specific pathogen-free breeding colony at Charles River Laboratories (Senneville, QC, Canada). The animals were kept in well-ventilated polypropylene cages with a 12-hour light-dark cycle and fed sterilized standard laboratory diet and water *ad libitium*. Approval from the institutional animal committee was obtained for all experimental procedures. The documentation was submitted along with this thesis. Near confluent U87MG.EGFR cells grown in culture flasks were harvested using 0.05% trypsin-EDTA (HyClone), counted with a hemocytometer and assessed for viability using trypan blue (Invitrogen). The cells were washed once and resuspended in sterile saline to obtain a final cell concentration of 6×10^6 cells per 100 µl, which was injected subcutaneously in the left hind leg of the mice. After injection, tumor growth was monitored every three days and tumor size was measured using a digital caliper. The tumor volume was determined according to the following formula: $\pi/6$ (length × width × height). Tumors are rarely round and this formula is considered the most accurate for determination of ellipsoid volumes (Tomayko and Reynolds, 1989). *In vivo* imaging experiments were initiated when tumors reached a size of 100 mm^3.

In vivo optical imaging

The IVIS imaging system (Caliper Life Sciences, Hopkinton, MA, USA) consists of a dark chamber with a heated stage and gas anesthesia inlet and outlet ports. A 150-W quartz halogen lamp is used as the excitation source, and the

emitted signal is collected using a cryogenically cooled (-105°C), back thinned, back-illuminated grade-1 CCD camera.

The mice were injected intravenously with EG2-IONP-680 or IONP-680 at a dose of 10 mg Fe/kg body weight in sterile saline. For imaging, mice were first anesthetized with isofluorane, and then positioned on the animal stage so that administration of gaseous anesthesia was maintained. The images were taken at 670 nm excitation and 720 nm emission wavelengths and 5 sec acquisition time. The NIRF images were acquired at several time points up to 72 hours post injection. Background measurements were taken prior to the injections of the fluorophores-labeled nanoparticles.

Euthanasia and tissue collection

Following the last imaging time point (72 hours), anesthetized animals were euthanized by heart puncture. Immediately after euthanasia, the organs were harvested and imaged in the IVIS imaging system using the same excitation and emission settings used for the animal. The tissues were subsequently embedded in a plastic cassette containing optimal cutting temperature (OCT) medium and cooled over dry ice in ethanol. The tissues are currently stored at -80°C and are awaiting histological analysis.

3.3 Results

3.3.1 Conjugation strategy

Prior to all manipulations, I developed a strategy to conjugate EG2 to the IONPs, which is illustrated in Figure 3-1. In this approach the two most common covalent conjugation chemistries were employed, maleimide- and NHS-chemistries. Both chemistries have already been introduced in the previous chapter, as immobilization approaches for proteins to SPR chip surfaces (“ 2.1. Introduction to surface plasmon resonance”, page 28). Maleimide-reactive groups are specific for sulfhydryl (= thiol) groups, which, in proteins, are exclusively available on cysteine residues. Cysteines are hydrophobic and therefore most naturally occurring disulfide bonds are buried within the protein (Hagihara et al., 2007).

The presence of reducing agents, such as DTT, β-mercaptoethanol and TCEP-HCl, will disengage disulfide bridges, thereby producing free thiol-groups for conjugation. In contrast to DTT and β-mercaptoethanol, which compete for binding to free sulfhydryls and therefore require a buffer exchange step before conjugation, TCEP-HCl does not interfere with maleimide-bond formation (Getz et al., 1999). Thus, in addition to being odorless, TCEP-HCl enables faster conjugation, because reduction and conjugation can be done in one step. This is especially important in the application described here, in which bifunctional linkers were used. NHS and maleimide reactive groups are both relatively short-lived in aqueous solutions, with half-lives of 4 hours and 64 hours at 4°C in PBS, pH 7, respectively (Thermo Scientific).

Another objective I had in mind when designing the conjugation strategy, was to achieve site-specific conjugation of the sdAb to the surface of the nanoparticles. The rationale here is the same as described previously for SPR chip surfaces, in which heterogeneous immobilization should be avoided in order to prevent partial or complete obstruction of the antibody's paratope. There are only two conserved cysteines in the sequence of EG2, which are engaged in a disulfide bond. I proposed to add another cysteine residue to the sequence of EG2, a strategy that has previously been shown to be effective for the introduction of individual conjugation sites in other antibody fragments (Albrecht et al., 2004; Harmsen et al., 2007). Our collaborators in Roger MacKenzie's group at the NRC-IBS therefore generated an EG2 clone expressing an additional cysteine residue at the C-terminus, which I subsequently expressed and purified.

In consequence of using the maleimide-chemistry on the bifunctional PEG chain to conjugate to EG2, the NHS-chemistry on the bifunctional PEG chain was available for conjugation to the nanoparticle surface. I therefore proposed that either primary amino-groups or carboxyl-groups should be available on the nanoparticle surface. Originally the nanoparticles for this project were to be manufactured by our collaborators at the CNRC-IMI, who were co-authors on the CIHR research grant that funded my project. Thus, I developed the conjugation strategy in consideration of the production objectives communicated by our

collaborators, who chose NH_2-derivatization over COOH for conjugation. In addition to allowing for sdAb conjugation via bifunctional PEG spacers, derivatizing the nanoparticle surface with primary amino-groups was also ideal for attaching fluorescent dyes. Fluorophore labels in a large variety of wavelengths are routinely available with amino-reactive NHS groups (e.g. Alexa Fluor™, DyLight).

Originally, my plan was to compare the targeting ability of EG2-IONPs with different PEG chain lengths and densities, since it was shown previously that polymer length crucially influences the optimal presentation of targeting moieties on the surface of nanoparticles (Sawant et al., 2008). Unfortunately, our collaborators encountered difficulties during up-scaling of the nanoparticle production process, which affected batch reproducibility and quality. I demonstrated this batch variability in DLS, zeta potential, fluorescamine and cytotoxicity assays (data not shown), and I finally had to rely on commercial nanoparticle sources in order to carry on with my project. I purchased iron oxide nanoparticles with surface amino-groups from two different companies with the objective to comparatively evaluate their physical properties and chose one of them for sdAb-conjugation and further investigation. Since the surface of the commercial nanoparticles was already modified with amino-terminal PEG chains, a short bifunctional linker (SMCC) was used for EG2 sdAb conjugation. This evaluation process of the commercial IONPs will be described in the following paragraphs.

3.3.2 Characterization of EG2cys

The yield of EG2cys production was approximately 15 mg/L. Purification was carried out on a metal affinity column via the His-tag at the C-terminus of the sequence. However, when generating the EG2cys clone, the sixth histidine residue was replaced by a cysteine, which decreased the affinity of the protein towards the Ni^{2+}-resin compared to the original antibody fragment and resulted in elution in the presence of lower concentrations of imidazole. Therefore, in order to remove contaminating proteins that eluted in the same fractions as EG2cys, the reduced

protein was further purified by gel filtration. I tested several different TCEP-HCl concentrations to determine the least amount of reducing agent necessary to generate monomeric EG2cys and determined a ratio of 100 : 1 (TCEP : protein) (Figure 3-2 A, lane 1 and 2).

The first step in the characterization of the modified EG2 protein was to determine whether the introduction of the additional C-terminal cysteine affected its affinity and specificity for EGFR. I chose surface plasmon resonance technology for this analysis. EG2cys was immobilized by maleimide chemistry using the cross-linker SMCC-hydrazide to connect the free cysteine in the sdAb sequence to the carboxydextran layer on the SPR chip, followed by injections of serial dilutions of EGFR-ECD or EGFRvIII-ECD over the oriented EG2cys surface (Figure 4-1 B and C). SPR data fitting to the 1:1 Langmuir binding model produced affinities (77 nM for EGFR and 34 nM for EGFRvIII) similar to the previously determined K_D-values from EG2 binding to immobilized EGFR-ECD (50 ± 6 nM) (Figure 2-3) and EGFRvIII-ECD (98 ± 10 nM) (Figure 2-4, Table 1).

Next, I investigated whether the conjugation of polyethylene glycol to the C-terminus of the protein affected binding to its target. I tested several PEG to protein ratios for the conjugation of 2 kDa maleimide-reactive PEG chains to monomeric EG2cys and found the ideal ratio was 10 : 1 (PEG : protein) (Figure 3-2 A lane 3). The conjugation product exhibited an apparent molecular weight of ~25 kDa in Coomassie-stained 14% TSDS-polyacrylamide gels, although the calculated MW would be only 18 kDa (16 kDa EG2cys + 2 kDa PEG). This, however, is not surprising, since PEG is known to generate a hydrophilic shell around proteins, which could significantly contribute to its hydrodynamic size and/or disguise charges on the protein surface (Hatakeyama et al., 2011). At higher PEG concentrations two additional protein bands appeared in the gel, which could correspond to the consecutive PEGylation of the two other cysteine residues in the sequence that are normally involved in the internal disulfide bond (Figure 3-2 A, lane 4 and 5). The results demonstrate that, using the right stoichiometry, site-specific PEGylation can be achieved for proteins containing internal and external cysteine residues. Mono-PEGylated EG2cys (EG2-PEG)

(Figure 3-2 A, lane 3), was subsequently purified by gel filtration and analyzed for binding to immobilized EGFR-ECD (Figure 3-2 B and C). EG2-PEG showed binding to EGFR-ECD comparable to EG2, however the dissociation was incomplete, which suggests non-specific interaction of PEG with the chip surface. Interaction between EG2 and EGFR-ECD appeared to be a necessary prerequisite for this non-specific interaction, since it was not observed on the control surface.
The possibility that PEG was interacting non-specifically with immobilized EGFR-ECD was excluded in the following experiment. The interaction of EG2-PEG with EGFR-ECD in solution was shown in a competition experiment, in which EG2-PEG demonstrated a competition profile for EGFR-ECD binding to an EG2 surface comparable to non-PEGylated EG2 (Figure 3-2 D). Hence, if PEG contributed to binding of EG2-PEG to EGFR, then this increase in affinity should have been visible in the competition study.

3.3.3 Characterization of commercial IONPs

Comparative analysis of nanoparticles from Genovis and Ocean NanoTech

I compared the iron oxide nanoparticles from Genovis and Ocean NanoTech for their size, surface charge, and number of amino-groups available for conjugation. In addition, I carried out cytotoxicity assays on a panel of four cell lines (Figure 3-3). Both IONP samples have iron oxide (Fe_2O_3) cores of 10 nm. Genovis reports that, including the coating layer, the overall diameter of these particles is 18 nm, whereas the Ocean NanoTech NPs possess an estimated diameter of 25 nm when coating thickness and 5 kDa PEG layer are considered (Figure 3-1).
The hydrodynamic diameter of particles in suspension can be determined by dynamic light scattering (DLS). DLS measures Brownian motion and relates this to the size of the particles using the Stokes-Einstein equation. It does this by illuminating the particles with a laser and analyzing the intensity fluctuations in the scattered light (Malvern). DLS also provides information about the degree of polydisperity, i.e. the degree of uniformity of the particle size in the sample. Figure 3-3 A shows the overlaid intensity-weighted DLS spectra for IONPs

obtained from Ocean NanoTech and Genovis. The Ocean NanoTech nanoparticles show an average hydrodynamic diameter of 36 nm and the Genovis particles are approximately 65 nm in size. The differences between TEM- and DLS- measured sizes are attributed to the fact that TEM measures the diameter of dried particles on a metal grid, while light scattering determines the hydrodynamic diameter, which takes the hydrated layers on the particle's surface into account.

Next, I monitored the zeta potential of these particles in water over the first 3 months after shipping (Figure 3-3 B). The zeta potential indicates the degree of repulsion between adjacent, similarly charged particles in solution. Colloids with high zeta potential (negative or positive) are electrically stabilized while colloids with low zeta potentials tend to aggregate. The zeta potential of a nanoparticle solution is crucially influenced by the pH. Generating a zeta potential versus pH plot therefore provides information about the isoelectric point of the nanoparticles (Malvern, Zeta Potentiometer handbook).

The zeta potential of the Ocean NanoTech nanoparticles significantly decreased during the investigated time period from -2.7 to -11.1 mV, which suggests that changes on the particle surface may have been occurring (possibilities are for example, adsorption of buffer ions or dissociation of the coating layer). In contrast, the IONPs from Genovis did not alter their surface charge over the investigated three months. The data presented in Figure 3-3 B corresponds to the average zeta potential values of two independent measurements (consisting of 10 measurement cycles each) and their associated standard deviations.

The presence of amino-groups on the surface of the commercial IONPs was confirmed using the fluorescamine reagent. Fluorescamine, which is not fluorescent in itself, binds to primary amino groups, thereby forming highly fluorescent products, which can be quantified in a spectrophotometer (Udenfriend et al., 1972). The method showed good reproducibility and an approximation of the number of free amino groups was generated in comparison to a linearized glycine standard. Routinely, the concentration of nanoparticles is expressed in mg/ml, which commonly indicates the concentration of iron (Fe) in the sample, since iron content is the parameter that determines the most relevant property of a

nanoparticulate MRI contrast agent, its relaxivity. The particle concentration is commonly determined by inductively coupled plasma (ICP) analysis, which is a type of mass spectrometry that measures the elemental composition of a sample (Xie et al., 2008). For Ocean NanoTech nanoparticles, 1 mg/ml Fe sample corresponds to 0.86 μM nanoparticles. In the case of Genovis nanoparticles a sample containing of 1 mg/ml Fe was calculated to correspond to 0.5 μM particles, suggesting that the overall iron content per particle was lower for Ocean NanoTech nanoparticles (Ocean NanoTech, Genovis). Using the fluorescamine assay, I determined that the IONPs from Ocean NanoTech contained 40 times more free amino-groups on their surface than the Genovis particles. I calculated approximately 4 - 5 × 10^3 amino groups/particle for Ocean NanoTech IONPs and 0.1 × 10^3 amino groups/particle for Genovis IONPs. I next investigated whether the addition of NHS-PEG (2 kDa) or the bifunctional cross-linker SMCC would reduce the number of free amino groups on the particle surface. The reaction was carried out at a ratio of 5000 : 1 (linker: particle). The conjugation of NHS-PEG to Ocean NanoTech IONPs reduced the amount of free amino groups by over 50% and addition of the bifunctional crosslinker SMCC at the same concentration occupied 25% of the reactive groups. Similarly, NHS-PEG and SMCC conjugation to Genovis nanoparticles demonstrated reduction of 48% and 15% of free amino groups, respectively (Figure 3-3 C). The results showed that amino-group mediated conjugation was achieved on IONPs from both commercial sources.

Cytotoxicity study

IONPs from both commercial sources did not significantly affect the proliferation of a panel of cell lines representing target (glioblastoma cells: U87MG, breast cancer cells: MDA-MB 468) and non-target tissue (hepatocytes: HepG2, macrophages: RAW 264.7) up to a concentration of 100 μg/ml (Figure 3-3 D). At the highest tested concentration of 300 μg/ml three out of the four cell lines treated with Ocean NanoTech IONPs showed an approximately 40% decrease in cell viability in a three day growth assay. The Genovis particles inhibited only HepG2 viability by 40% and MDA-MB 468 viability by 25%.

Comparable toxicity profiles were obtained from colony formation assays for HEK 293, RAW264.7 and MDA-MB 468 cells, in which cell growth was assessed over a period of 7 days (data not shown). The parental U87MG cells were least affected in growth among the investigated cell lines. The results indicated that cell line specific characteristics are underlying the observed effects of IONPs on cell viability.

Stability of Ocean NanoTech IONPs over time

Due to the better size distribution and the availability of significantly more amino groups for conjugation, I subsequently selected the Ocean NanoTech IONPs for conjugation with EG2 sdAbs. While I was optimizing the conjugation protocol, I regularly measured size, zeta potential and number of amino groups on the surface over a period of 4 to 16 months (Figure 3-4). The measured number of amino-groups and the hydrodynamic diameter of the particles were consistent over a period of 16 and 6 months, respectively (Figure 3-4, A B). However, the zeta potential decreased from -2.7 to -13.4 mV over the investigated 4 months (Figure 3-4 C).

3.3.4 Production and characterization of EGFR-targeted IONPs

The amino-terminated PEG layer on Ocean NanoTech IONPs was conjugated with EG2 sdAb using the bifunctional crosslinker SMCC, which consists of an amino-reactive NHS and a sulfhydryl-reactive maleimide functional group. I achieved excellent separation by gel filtration between the nanoparticles and the reaction compounds of much smaller molecular weight (SMCC: MW 330, fluorophore: MW 643-1150, EG2: 15 kDa) (Figure 3-5 A). The elution profile shows that the nanoparticles elute in the void volume of the column, and that their MW is above 670 kDa, which was the size of the largest protein in the gel filtration standard. This observation is in agreement with previous findings by Dreher and coworkers, who reported that the molecular weight of a 50 nm dextran coated IONP corresponded to approximately 2000 kDa (Dreher et al., 2006).

I confirmed successful EG2 conjugation by measuring the zeta potential, the hydrodynamic diameter, the binding specificity by surface plasmon resonance and

the r_2-relaxivity by MRI (Figure 3-5). The zeta potential became more negative upon fluorophore and single domain antibody conjugation demonstrating values of -7.8 mV for control IONPs, -8.31 mV for IONP-488 and -13 mV for EG2-IONP-488 (Figure 3-5, B). The overall hydrodynamic diameter of the particles dispersed in PBS increased from 56 nm for bare IONPs to 95 nm for EG2-IONP-488 (Figure 3-5 D).

The ability of EG2-IONP to bind to immobilized EGFR-ECD was investigated by surface plasmon resonance (Figure 3-5 C). The immunoparticles were injected over three different density EGFR-ECD surfaces (40 – 570 RU) and showed corresponding amounts of binding, as well as no binding to the control surface. Avidity effects could be responsible for the slow dissociation rate observed for EG2-IONPs on these surfaces. In contrast, non-conjugated control IONPs did not bind to any of the surfaces (data not shown). I injected monomeric EG2 sdAbs at concentrations between 0.08 – 10 μM and observed a concentration-dependent acceleration in EG2-IONP dissociation. Figure 3-5 C shows one representative EG2 injection of this experiment to illustrate the competition potential of the monomeric sdAb. These results confirm the specificity of EG2-IONPs for binding to EGFR-ECD. Furthermore, the slow dissociation of the multivalent immunoparticle is expected to generate a significantly higher apparent affinity compared to the affinity of monovalent EG2, which holds great promise for increasing the retention of the EGFR-targeted nanoprobe on cells over-expressing the EGF receptor.

Finally, I investigated the changes in r_2-relaxivity of EG2-conjugated nanoparticles (Figure 3-5 E). Herein the T_2-relaxation of non-targeted control nanoparticles and targeted EG2-IONPs was measured using a 7 T small animal MRI scanner at Fe concentrations ranging from 50 to 400 μM. The IONPs significantly reduced the transverse relaxation time (T_2) compared to the water control and the signal intensity (brightness) decreased at higher particle concentrations. As expected, the T_2-relaxation times are linearly proportional to the concentration of contrast agent. I obtained relaxivities of 65 mM^{-1} s^{-1} for

control IONPs and 42 mM^{-1} s^{-1} for EG2-IONPs, which renders them suitable for use as a negative MRI contrast agent in T_2-weighted imaging.

The Bradford method was adopted to determine the quantity of EG2 sdAbs conjugated to the surface of the amino-functionalized iron oxide nanoparticles. An average of 6-8 sdAbs were obtained per particle. This number was derived from measurements on six individual batches. Comparing the amount of fluorescence on IONP-680 and EG2-IONP-680 to serial dilutions of free NHS-reactive DyLight 680 fluorophore allowed for quantification of conjugated fluorophore on the nanoparticles. I calculated that there was, on average, one fluorophore per nanoparticle.

3.3.5 U87MG.EGFR binding study of fluorescently-labeled IONPs demonstrated batch-dependent diversity.

The targeted and non-targeted nanoparticles were either labeled directly with NHS-reactive Alexa Fluor® 488 or detected indirectly using an anti-PEG (backbone) antibody followed by a fluorescent anti-species secondary antibody. I compared the cell binding data obtained for control IONPs and EG2-IONPs derived from several batches of nanoparticles that I received from Ocean NanoTech. The fluorescence intensity observed for IONP binding to fixed U87MG.EGFR was generally very low (Figure 3-6 A). Herein, only EG2-IONP-488 derived from batch 4 demonstrated uniform distributions on the cell surface of U87MG.EGFR cells. In contrast, the cells labeled with targeted and non-targeted nanoparticles originating from batch 8 showed punctate staining at the cell periphery.

Live cells incubated with 100 μg/ml nanoparticles from batch 4 showed fluorescence in clusters predominantly localized in the perinuclear region, suggesting that the particles were contained within intracellular vesicles (Figure 3-6 B). Herein, the fluorescence intensity in cells labeled with targeted nanoparticles was higher than in cells labeled with the non-targeted IONP. Fluorescence images obtained for live U87MG.EGFR cells that were incubated with particles from the sixth batch showed fluorescence in clusters inside the cells

as well as on the cell periphery. The distribution is much more uneven than in the images obtained for batch 4. Non-targeted IONPs from batch 7 were not detected on live U87MG.EGFR cells. In contrast EG2-conjugated nanoparticles from the same batch labeled the cell periphery in bright clusters, but did not suggest the presence of internalized particles.

Finally, I also investigated the degree of nanoparticle-mediated cell labeling that could be achieved on fixed and permeabilized U87MG.EGFR cells (Figure 3-7). With the exception of EG2-conjugated IONPs from the first batch, all nanoparticles showed intense staining of permeabilized cells. Whereas particles from batch 8 and non-targeted IONPs from batch 1 demonstrated even staining of the entire cell, non-targeted nanoparticles from batch 6 located to distinct clusters within the cells.

In summary, the results show high variability in cell staining patterns obtained for different nanoparticle batches, indicating that factors other than EG2-mediated binding to EGFR are governing the interaction with the cells.

Table 2 presents an overview of the experiments that I carried out on each individual IONP batch. When comparing their physical properties, such as hydrodynamic diameter, zeta potential and number of amino groups on the particle surface, I noticed that these parameters were also subject to large variability between batches (Figure 3-8). DLS analysis showed that particle size generally ranged between 36 and 55 nm, with the exception of batch 7 that was highly polydisperse resulting in a significantly higher average hydrodynamic diameter of 210 nm (Figure 3-8 A). Next, I compared the relative fluorescence intensities obtained at comparable iron concentrations of different nanoparticle batches in the fluorescamine assay (Figure 3-8 B). The results showed that the number of amino-groups on nanoparticles from batch 2 and 3 was more than ten-fold lower compared to the other investigated batches. Significant diversity was also seen in the zeta potential values of the different nanoparticle batches, suggesting high variability in particle surface charge (Figure 3-8 C). In addition to the zeta potential measurements carried out in water, I investigated the zeta potential of Ocean NanoTech nanoparticles dispersed in low salt buffer at pH

values ranging from 4 to 10, in order to determine the isoelectric point (pI) (Figure 3-8 D). The Ocean NanoTech nanoparticles demonstrated pH-dependent changes in zeta potential values, which correlated to pI values of approximately 5.2 and 6.2 for batch 1 and 3, respectively, which suggests that these IONPs were charged negatively at physiological pH.

3.3.6 *In vivo* distribution study

Distribution and tumor accumulation of targeted EG2-IONP-680 and non-targeted IONP-680 was investigated by optical imaging of subcutaneous U87MG.EGFR xenograft tumors in mice. The U87MG.EGFR tumor model is an established tumor model that reportedly demonstrates acceptable proliferation rates, high vessel density and adequate blood perfusion, with few signs of inflammation. In addition, a high level of EGFR expression was retained *in vivo* (Abourbeh et al., 2007; Claes et al., 2008). When the tumor size reached approximately 100 mm^3, animals were intravenously injected with targeted and non-targeted nanoparticles at the dosage of 10 mg Fe/kg body weight. The animals were imaged up to 72 hours post-injection in the IVIS small animal imager at 670 nm excitation and 720 nm emission, which are the optimal settings indicated by the manufacturer of the fluorophore (Thermo Scientific) (Figure 3-9). Increased fluorescence was observed with targeted as well as non-targeted IONPs in the tumor-carrying flank at 1 h post-injection, which persisted until 72 hours post-injection. The highest fluorescence in the tumor area was observed at 24 h and 48 h post-injection in untargeted IONP-680 and EG2-IONP-680, respectively (Figure 3-9, white arrows). No signs of toxicity were observed in any of the animals injected with nanoparticles (n = 8) throughout the duration of the study.

After 72 hours the animals were sacrificed and the organs and tumor tissue removed for *ex vivo* imaging (Figure 3-10). It has been reported that the fluorescence intensity determined in *ex vivo* imaging is an accurate reflection of amount of fluorescence-labeled nanoparticles accumulated inside organs due to the deep penetration in the near-infrared region and negligible autofluorescence in *ex vivo* organs (Gao et al., 2004). Imaging of the organs showed that the highest

accumulation of fluorescence was observed in liver and spleen for both particles. The EG2-IONP-680 nanoparticles were additionally retained in the lung, which was not observed for the control IONP-680. Overall fluorescence intensity in the tumor tissue was similar to the intensities seen in heart and kidneys.

Non-specific fluorescence signals were seen in the stomach of all imaged animals. Likewise, Ke *et al.* observed fluorescence originating from the gastrointestinal tract when imaging their animals at 660 nm. They attributed this phenomenon to the mouse diet and suggested to use fluorescence-depleted mouse chow for future studies (Ke et al., 2003).

3.4 Discussion

Research in the field of rational delivery of nanoparticulate contrast agents and therapeutic nanocarriers to tumor sites is at the forefront of projects in nanomedicine. In the current study, I comparatively analyzed the physical properties of iron oxide nanoparticles from two different commercial sources, among which I chose one for further modification. I developed a strategy to attach a targeting ligand to the particle surface based on well-known protein conjugation chemistries and subsequently monitored and evaluated each conjugation step using an array of biochemical and biophysical approaches (Figure 3-1). Earlier in this thesis, I established that the single domain antibody fragment (EG2) used for targeting the IONPs to glioblastoma cells is specific for the extracellular domain of the epidermal growth factor receptor, which is a well-established molecular target (see "1.7 Over-expressed EGF-receptors as molecular targets for the delivery of contrast agents to brain tumors", page 24). I investigated the interaction of the targeted and non-targeted nanoparticles with cultured glioblastoma cells over-expressing EGFR and monitored their *in vivo* distribution in mice carrying subcutaneous xenograft tumors of the same cancer cell line.

3.4.1 EG2cys for oriented conjugation to the nanoparticle surface

The EG2 single domain antibody specifically binds the extracellular domain of the wild-type EGF receptor as well as the mutant variant EGFRvIII with affinities

of 50 and 98 nM, respectively (Bell et al., 2010; Iqbal et al., 2010b). The detailed binding kinetics of this VHH fragment were described in detail in the previous chapter of this thesis (see "2.4.2 Determination of the binding kinetics of four novel sdAbs", page 59) The rationale for using single domain antibody fragments instead of full-length antibodies is their smaller overall size, as well as the absence of Fc-mediated effector functions, which could potentially influence the distribution of the immunoparticles *in vivo*. An immunoglobulin G (IgG) antibody has an average size of 14.5 × 0.5 × 4 nm^3 and a molecular weight of 160 kDa (Yang et al., 2009b). In contrast a VHH fragment is a prolate-shaped protein with reported dimensions of only 2.5 × 4 nm (Revets et al., 2005) .

In order to achieve homogenous conjugation of active sdAb to the surface of the particle, our collaborators cloned an additional cysteine to the C-terminus of the EG2 sequence (EG2cys), which was expected to allow sdAb conjugation by means of a site-specific thioether bond. In contrast random coupling methods (e.g. using amino-reactive PEG lipids) risk antibody inactivation and nanoparticle aggregation by cross-linking.

I showed in SPR binding studies that the altered EG2 sdAb retained its affinity for binding to EGFR and EGFRvIII, when immobilized to the Biacore chip using maleimide chemistry (Figure 4-1 B and C, respectively). I furthermore demonstrated that conjugation of a 2 kDa polyethylene glycol chain was achieved with high site-specificity when using optimal stoichiometries of protein and PEG (Figure 3-2 A). Other investigators showed previously that by varying the concentration of reducing agent and maleimide-reactive PEG in the reaction, site-specific conjugation of antibody fragments could be achieved (Natarajan et al., 2005; Xiong et al., 2006; Yang et al., 2003).

Purified EG2-PEG bound EGFR-ECD with affinities similar to the original EG2 sdAb, but non-specific interactions between the PEG chain and the carboxydextran layer of the Biacore chip were observed (Figure 3-2 B). Yang and coworkers also obtained reduced dissociation rates for some of their scFv-PEG constructs, but they only monitored the dissociation period over a relatively short time frame and therefore did not assess whether the system would eventually

return to baseline (Yang et al., 2003). It is possible that I am one of the first to describe non-specific interactions between PEG and the dextran coating on SPR chip surfaces. The ability to make this observation likely results from the fact that the dissociation rate of EG2-PEG is faster than that of any other PEGylated protein investigated by SPR to date; accordingly, the slow dissociation rates in these other published interactions may have masked potential contributions due to non-specific binding (Knight et al., 2004; Kubetzko et al., 2005).

The conjugation of single domain antibodies via maleimide-terminated PEG chains has recently been carried out by another group that coupled anti-EGFR sdAbs onto liposomes (Oliveira et al., 2010). However, instead of introducing an extra cysteine in the protein sequence they generated protected sulfhydryl-groups on primary amino-residues using SATA reagent. They demonstrated sdAb activity in an ELISA assay, but it is probable that this approach resulted in heterogeneous orientation of the immobilized fragments.

3.4.2 Commercial iron oxide nanoparticles – physical properties

Based on their superior physical properties, I selected IONPs from Ocean NanoTech for conjugation with fluorophores and EG2 sdAbs (Figure 3-3).

These IONPs are coated with a PEGylated triblock copolymer consisting of a polybutylacrylate segment, a polyethylacrylate segment, a polymethacrylic acid segment and a hydrophobic hydrocarbon side chain resulting in a bilayered coating structure with multiple exposed amino-terminated polyethylene glycol (PEG) chains of 5 kDa length. This coating layer was initially designed to render fluorescent quantum dots biocompatible (Chen et al., 2009a; Gao et al., 2004). To my knowledge there are currently six published reports showing *in vitro* and *in vivo* studies of cancer cell-targeted IONPs from Ocean NanoTech (Chen et al., 2009a; Hadjipanayis et al., 2010; Xie et al., 2010; Yang et al., 2009a; Yang et al., 2009b; Yang et al., 2009c). However, in contrast to the amino-PEG functionalized nanoparticles that I used in my experiments, all but one of the previously published studies investigated IONPs, which were coated with the above-

mentioned amphiphilic polymers containing carboxyl-groups for conjugation but no further modifications with amino-functionalized PEG.

Despite the significantly increased blood circulation times achieved by PEGylation, disadvantages of PEG modification of nanoparticle surfaces have also been reported. For example, PEG-coated IONPs may have limited binding sites available for further ligand modification, since the number of functional groups on the surface of each IONP is limited (Gupta and Gupta, 2005).

Chen *et al.* determined the number of amine groups per PEGylated Ocean NanoTech particle by labeling the IONPs with excess amount of Cy5.5-NHS and followed by quantification of the fluorescence signal. According to their analysis there are about 25-50 amines available for conjugation per particle. They state, however, that the actual number could be slightly higher given the potential quenching effect of multiple fluorophores in proximity (Chen et al., 2009a; Kircher et al., 2004). Another group, working with IONPs from a different source, reported the introduction of approximately 30 amino groups/nanoparticle using monofunctional PEG (Sun et al., 2008). In contrast to these studies, quantification of amino-groups using the fluorescamine assay showed 5- to 100-fold variations from these values in my study, depending on the investigated batch (Figure 3-8 B). This discrepancy suggests that there might be a difference between the number of amino-groups detectable in the fluorescamine assay and the amount of amino-groups that are actually freely available for conjugation with biomolecules. From my own experience, fluorophore conjugation to the amino-functionalized distal end of the PEG chains resulted in very low yield, even at ratios of 400 : 1 (fluorophore : particle). I calculated a labeling efficiency of approximately one fluorophore per particle. Similarly, ratios of 1.22 fluorophores/particle were achieved for conjugation to the terminal ends of polyethylene glycol chains by Veiseh *et al.* (Veiseh et al., 2009). Furthermore, Schellenberger and coworkers reported 1.8 fluorophores per 50 nm dextran coated IONP (Schellenberger et al., 2004). Higher labeling efficiencies, however, have been reported for nanoparticle preparations in which the protein conjugation was either carried out prior to fluorophore-labeling or when already fluorescently-labeled proteins were attached

to the polyethylene glycol chains, as well when fluorescent dyes were incorporated directly into the coating material of core-shell nanoparticles (Lu et al., 2002; Xie et al., 2010; Yang et al., 2009a). These observations suggest that amino-groups on proteins are more readily available for NHS-mediated labeling than amino-terminated PEG chains. This may be due to favorable electrostatic interactions between the protein and the fluorophore, or to fewer degrees of rotational freedom of amino-groups incorporated within the protein's tertiary structure.

I routinely obtained 6 to 8 sdAbs per nanoparticle, which is in the range of conjugation densities achieved by other investigators on similar-sized IONPs from Ocean NanoTech or other sources (Chen et al., 2009a; Schellenberger et al., 2004; Veiseh et al., 2009; Yang et al., 2009b; Yang et al., 2009c). I confirmed specificity of EG2-IONPs to immobilized EGFR-ECD by surface plasmon resonance (Figure 3-5). The slow dissociation is in agreement with avidity occurring from simultaneous binding of EG2 units on the nanoparticle to several EGF receptors on the chip surface. Similar SPR binding profiles were previously shown for other immunoparticle/antigen interactions (Kocbek et al., 2007).

Phantom study

The local iron content is the crucial determinant of the ability to generate contrast in MRI. Therefore, the relaxivity of magnetic nanoparticles has typically been modulated by their core size, often in the range of 4 - 20 nm. Recently, a detailed study by LaConte and coworkers demonstrated that coating thickness around the iron oxide core can significantly impact r_2-relaxivities of IONPs (LaConte et al., 2007).

Previously, T_2-relaxation measurements on Ocean NanoTech iron oxide nanoparticles with 10 nm Fe_2O_3 cores in agarose phantoms generated r_2 values of 124 mM^{-1} s^{-1} and 190 mM^{-1} s^{-1} in 3 T and 7 T MRI scanners, respectively (Chen et al., 2009a; Yang et al., 2009c). In contrast, the phantom MRI study that I carried out in water generated r_2-relaxivities of 65 mM^{-1} s^{-1} and 42 mM^{-1} s^{-1} for non-targeted IONPs and EG2-IONPs, respectively (Figure 3-5 E). Experimental variables such as field strength, temperature and medium in which the

measurements are made, produce significant effects on the contrast agent. Therefore, these parameters should be considered when making comparisons of contrast agents reported in the literature (Sun et al., 2008). It is therefore possible that the differences in r_2-values could be caused by external factors, but given the large variability of other physical characteristics between individual IONP batches, the cause could also lie within the particles themselves (Figure 3-8).

I observed a decrease in r_2-relaxivities after EG2 conjugation to the particles surface, which is in agreement with LaConte's study on coating layer thickness (LaConte et al., 2007). In a report on lactoferrin-conjugated IONPs (10 nm), r_2-values of 76 mM^{-1} s^{-1} and 131 mM^{-1} s^{-1} were found for targeted and non-targeted nanoparticles, respectively (Xie et al., 2011). Clinically-investigated long-circulating iron oxide nanoparticles (Ferumoxtran-10), which are also currently explored for brain tumor imaging, have reported r_2-values of 65 mM^{-1} s^{-1} at particle diameters of 15-30 nm (Burtea et al., 2008).

3.4.3 Cytotoxicity study

For nanoparticles to move into the clinical arena it is important that nanotoxicology research understands how the multiple factors such as nanoparticle size and composition, surface coating, different cell lines, incubation time and colorimetric assays influence the toxicity of nanoparticles in order to avoid their undesirable properties. Even though *in vitro* experiments must have *in vivo* validation in order to be meaningful, simple *in vitro* toxicity models and assays may provide a general estimate of toxicity in a relatively short time and assist subsequent toxicity risk assessment of nanoparticles (Choi et al., 2010).

In this study, I tested IONP concentrations up to 300 µg/ml, since the blood volume of a mouse is about 1 ml and the injection dose for the animal study was planned to be 10 mg Fe/kg body weight, i.e. in a mouse of 25 g, a total of 0.25 mg Fe would be injected. As a result, a concentration of 250-300 µg/ml would be representative of the short time exposure time of most cells encountered by the circulating IONPs in the blood stream. However, liver and spleen cells are likely to be exposed to much higher concentrations, since they are known to sequester

iron oxide nanoparticles *in vivo* (Bae et al., 2011). Liver cirrhosis and hepatocellular carcinoma could develop if the iron concentration exceeds 4000 µg/g wet weight (Jain et al., 2008).

I carried out a standard Alamar Blue® viability assay, which is similar to the better known MTT assay that monitors the metabolic conversion of a non-fluorescent compound into a fluorescent product through a process mediated by enzymes in the mitochondrial membrane. My findings are similar to the results obtained by Xie and coworkers and Hadjipanayis *et al.* on nanoparticles from the same commercial source. They did not observe any cytotoxicity for cells exposed to maximal nanoparticle concentrations of 100 µg/ml and 300 µg/ml, respectively (Hadjipanayis et al., 2010; Xie et al., 2009).

Other frequently employed *in vitro* cytoxicity assays are the lactate dehyrodgenase (LDH) leakage assays, detection of reactive oxygen species (ROS) or measurement of cytokine production. LDH is a cytoplasmic enzyme, which becomes released if the cell membrane integrity is compromised. ROS production is significantly increased under oxidative stress conditions, resulting in subsequent alteration of membrane lipids, protein and nucleic acids (Choi et al., 2010; Lewinski et al., 2008; Ryman-Rasmussen et al., 2007). Most of these assays are based on the chemical conversion of a non-fluorescent reagent into a fluorescent product and therefore they can be carried out conveniently in multi-well plates, thus allowing for the analysis of multiple cell lines and concentrations in parallel. In addition, a hemolysis assay is considered an important approach to investigate the biosafety of intravenously administered nanoparticles, since erythrocytes are among the first cells that come into contact with foreign materials in the blood system (Kim et al., 2005; Wu et al., 2011).

The nanoparticles used in this study have been injected *in vivo* in at least seven studies (including my own) using immuno-supressed nude mice, in which the animals were monitored up to 96 hours without any reported toxicity. Nevertheless, in order to reveal potential immunogenic effects, the long term fate of IONPs from Ocean NanoTech and their effects on liver and spleen functionality would need to be investigated in immuno-competent model systems.

For example, monocrystalline iron oxide nanoparticles (MION-46) were shown to induce seizures, which was attributed to decreased particle break down in the brain due to a lack of response from local macrophages and reactive astrocytes (Muldoon et al., 2005). This demonstrates that while the major constituents of all these particle are biocompatible, size and physical coating can induce varying physiological localization followed by diverging host responses (Yang et al., 2008). Indisputably, the surface characteristic of nanoparticles is a crucial factor that not only determines the biocompatibility of these magnetic materials but also plays an important role in their cell adhesion and internalization.

3.4.4 Cell binding studies

EGFR-targeted nanoparticles were previously shown to enter cells in *in vitro* cell binding assays (Benhabbour et al., 2011; Bhattacharyya et al., 2010; Kullberg et al., 2003; Lee et al., 2010; Oliveira et al., 2010; Yang et al., 2009b). I carried out confocal microscopy experiments with fluorescently labeled nanoparticles in order to investigate binding and internalization of EG2-IONPs versus non-targeted control particles into EGFR over-expressing U87MG cells (Figure 3-6, Figure 3-7).

The internalization of nanoparticles into mammalian cells depends on the physicochemical properties of the particles including size, shape and surface charge. The size may furthermore affect the endocytotic uptake mechanism. Generally, clathrin-mediated endocytosis is considered the predominant pathway for the uptake of small particles below 200 nm, whereas the uptake of larger particles up to a size of 500 nm seems to be caveolae-mediated (Jain and Stylianopoulos, 2010; Sung et al., 2009; Wohlfart et al., 2011). Other possible ways of nanoparticle uptake into cells are via macropinocytosis or lipid rafts, which allow endocytosis of particles > 150 nm (Mailander and Landfester, 2009; Parkar et al., 2009). The fate of targeted IONPs after cell internalization is still controversial, with most reports showing that nanoparticles enter into endosomes and are then degraded in lysosomes, while other studies have shown that they can escape from the endosomes and locate in the cytoplasm or around the nucleus. It

seems that conjugated ligands and surface coatings affect the distribution of particles within cells (Peng et al., 2008).

The EGF receptor is internalized by receptor-mediated endocytosis into clathrin-coated vesicles. However, when stimulated with high doses of EGF, the EGF receptor is ubiquitinated and is endocytosed through a clathrin-independent, lipid raft-dependent pathway (Sigismund et al., 2005). Therefore, EGFR-targeted IONPs could enter cells via at least two different endocytic pathways. It was previously shown that endocytosis can be triggered by multivalent binding of several receptors to one particle (Fearon et al., 1981; Huet et al., 1980; Schreiber et al., 1983; Schwartz et al., 1986).

Chithrani and coworkers investigated the effect of particle size and shape on internalization by monitoring the uptake of negatively charged gold nanoparticle at sizes between 14 and 100 nm of varying aspect ratios. In their study, maximum uptake into mammalian cells occurred with 50 nm spherical particles (Chithrani et al., 2006). In view of these findings, the internalization of the targeted and non-targeted IONPs investigated in my thesis, which demonstrated hydrodynamic diameters of 95 nm and 56 nm, respectively, should be readily observed (Figure 3-5 D). However, in my confocal microscopy experiments, the observed nanoparticle internalization was weak, suggesting that there must be other critical factors, besides size, contributing to IONP internalization (Figure 3-6 B).

It is possible that low and inconsistent IONP internalization observed in my study was due to insufficient amounts of sdAbs on the particle surface. For example, Benhabbour *et al.* demonstrated that EGFR-targeted liposomes were increasingly internalized with increasing numbers of heptameric affibodies conjugated to the surface (Benhabbour et al., 2011). And Zhou and coworkers demonstrated that increasing the scFv density on a liposome surface had much greater impact on internalization of the nanoprobe than the affinity of the individual scFv fragments. They subsequently postulated that the effect of intrinsic antibody affinity on quantitative cellular uptake might be relatively unimportant, if multiple copies of antibody fragment are present on the surface of the immunolipsosomes (Zhou et al., 2007).

Nevertheless, the ideal ligand-particle ratio may also depend on the number of receptors on the target cell surface. Tseng *et al.* demonstrated that higher cellular uptake rate via receptor-mediated endocytosis of EGF-conjugated nanoparticles was proportional to the number of EGF receptors on the cell surface (Tseng et al., 2007). In another study, critical antigen surface concentration was reported to be about 4×10^4 sites per single cell. After this value a further increase in antigen density was found to be not important (Torchilin, 2010).

In my experiments, I obtained 6 - 8 EG2 sdAbs/particle, which is in the range of what has been achieved by Yang *et al.* for EGFR-targeted nanoparticles of similar size, who subsequently observed internalization (Yang et al., 2009b). In addition, the U87MG.EGFR cell line expresses approximately 10^6 receptors/cell and antigen density should therefore be sufficiently above the critical threshold (Nishikawa et al., 1994). I therefore postulate that the amount of EG2 conjugated to the nanoparticle surface should have been sufficient to allow for EGFR-mediated endocytosis and that the reason for impaired internalization is likely to lie elsewhere. Probable causes will be discussed in the following paragraphs.

The surface charge of IONPs influences protein adsorption and internalization.

Surface charge and hydrophobicity also influence the particle uptake and/or the rate of transcytosis. In cell-based assays, higher internalization rates are associated with positively charged particles because of the negatively charged composition of the cell membranes (Harush-Frenkel et al., 2007; Wohlfart et al., 2011).

In order to determine the charge of the Ocean NanoTech IONPs, I measured the zeta potential of particles disbursed in buffers of pH 4 to pH 10 and obtained an average isoelectric point (pI) of the non-targeted nanoparticles at pH 5.7 ± 5, i.e. these particles would be charged negatively at physiological pH (Figure 3-8 D). This appears surprising at first, since the presence of free amino-groups on the particle surface is expected to contribute to an overall positive charge, comparable to a reported pI-value of 8.6 for amino-functionalized nanoparticles published by Chen and coworkers (Chen et al., 2008). However, the amphiphilic copolymer coating of Ocean NanoTech nanoparticles, onto which the

functionalized PEG chains are grafted, contains negatively charged carboxyl-groups and these particles display zeta potential values of -30 to – 50 mV versus amino-PEGylated NPs with potentials of – 3 to -28 mV (values provided by Ocean NanoTech and my own results, respectively; Figure 3-8 C). The different zeta potentials observed for individual batches could therefore be indicative of different degrees of PEGylation, since this would alter the ratio between negatively charged COOH- and positively charged NH_2-groups. Indeed, I observed that the amount of amino-groups determined in the fluorescamine assay generally correlated with the zeta potential values of the individual IONP batches, e.g. batch 2 and 3 showed less free amino-groups in the fluorescamine assay and consequently more negative zeta potential values (Figure 3-8 B and C). I therefore propose that altered ratios of amino- and carboxyl-groups on the nanoparticle surface could have caused the variability in nanoparticle internalization. The following reports are in support of this hypothesis. Mailander and Landfester found that, while carboxyl-functionalized nanoparticles of a size of 100 nm only showed a slight increase of total particle uptake into HeLa cells after 24 h compared to non-functionalized particles of the same size, amino-functionalized particles showed a more than 40-fold increase in uptake (Mailander and Landfester, 2009). Likewise, Ryman-Rasmussen et al. (2007) showed that carboxylic acid coated quantum dots (QDs) demonstrated very different patterns of cytoplasmic localization compared to QDs coated with PEG or PEG-amines (Ryman-Rasmussen et al., 2007). Several other investigators also found that modulation of nanoparticle surface charge can influence the mechanism of intracellular uptake (Arvizo et al., 2010; Leroueil et al., 2007; Verma and Stellacci, 2010).

I showed that conjugation of EG2 to the nanoparticle surface rendered their zeta potential more negative, suggesting that the pI of the nanoparticle suspension might also be altered between targeted versus non-targeted IONPs prepared from the same batch (Figure 3-5 B). Since EG2cys has a calculated isoelectric point of 6.21, it would be unlikely that sdAb conjugation would flip the nanoparticle charge at physiological pH from overall negative to overall positive and therefore

I conclude that both the targeted and non-targeted nanoparticles carried an overall negative charge at a pH of 7.2.

Nevertheless, negatively charged nanoparticles can also yield efficient uptake rates, especially after adsorption of serum proteins or covalent coupling of targeting ligands (Bertorelle et al., 2006; Wohlfart et al., 2011). It is assumed that hydrophobic and ionic interactions are the two principal driving forces for protein adsorption, combined with an entropy gain caused by conformational changes of the proteins during adsorption (Vonarbourg et al., 2006). Wiogo *et al.* analyzed the spectrum of serum proteins that adsorb onto the nanoparticle surface and observed that the surface charge of the particles impacts the type of the proteins adsorbed and that these interactions were likely based on electrostatic forces (Wiogo et al., 2011). Chen *et al.* investigated the adsorption of proteins from fetal bovine serum (FBS) onto the surface of silanes-magnetite nanoparticles functionalized with either amino groups, polyethylene glycol, or carboxylic acid and found that protein adsorption was highest for the particles having carboxylic acid groups on the surface (Chen et al., 2008). Similarly, a study by Mu *et al.* demonstrated that magnetic nanoparticles with carboxylic acid groups on their surfaces bound more serum protein compared to particles with aminated surfaces (Mu et al., 2010). These findings suggest that the varying ratios of surface amino- and carboxyl-groups of the different Ocean NanoTech nanoparticle batches could have influenced the quantity and type of adsorbed serum proteins, which in turn could have affected their ability to become internalized.

I observed that Ocean NanoTech IONPs showed almost no binding to cell surfaces on fixed cells, which could have been caused by electrostatic repulsion between the negatively charged cell membrane and the negatively charged particles (Figure 3-6 A). These experiments were carried out in PBS/0.1% BSA, which suggests that BSA could have been adsorbed to the particle surface. BSA itself has a pI of 5.1, and hence the overall charge of the IONPs would still remain negative and contribute to the repulsive forces between particle and membrane. In contrast, the incubation of live cells with EG2-IONPs or non-targeted IONPs resulted, at least for some batches, in cell surface binding and internalization

(Figure 3-6 B). Several factors might have contributed to this outcome. First, the experiments were carried out in full medium, containing 10% fetal bovine serum (FBS). As a result, a plethora of serum proteins could have non-specifically adsorbed to the particles surface. In relation to this, it has been demonstrated that despite the large quantities of albumin in serum, BSA can be competed from the nanoparticle surface by lower abundance serum proteins that exhibit higher affinities for the particle (Bertrand and Leroux, 2011). The adsorption of protein onto the surface of nanoparticles has previously been shown to proceed immediately upon contact with the physiological environment, forming a "corona" around the particles (Wiogo et al., 2011). Therefore, these specific adsorption profiles could have produced significant variability in the internalization properties of different nanoparticle batches.

It is generally accepted that the presence of localized charged or hydrophobic surface areas on proteins are crucial for their biological function e.g. in protein-enzyme, ligand-receptor, and antigen-antibody complexes. Therefore, I predict that heterogeneous charge distribution on colloidal surfaces could further contribute to the complexity of nanoparticle interactions with biological systems, especially for batches in which surface modification is not absolutely uniform. In conclusion, I postulate that correlating the isoelectric point and/or zeta potential of nanoparticle solutions to their biological fate may only be of limited value as long as the heterogeneity of their individual surfaces is not known.

Effect of PEGylation on target recognition and internalization

Today, PEGylation is the gold standard to generate nanoparticles with extended systemic circulation times. Even so, the hydrophilic coating never totally abrogates protein deposition and complement activation; therefore differential adsorption of serum proteins onto PEGylated nanoparticles affects their *in vivo* distribution and translocation across cellular membranes (Bertrand and Leroux, 2011). Kim *et al.* investigated the adsorption pattern on PEGylated versus non-PEGylated nanoparticles and showed that immunoglobulin G, an opsonizing protein was only adsorbed on the bare particle, thus confirming the protective role of the PEG chains against opsonins, whereas the serum proteins

ApoA and ApoB-100 were more associated with the PEGylated particles (Kim et al., 2007).

Contradicting results have been obtained for the relationship of PEGylation and nanoparticle internalization. Some groups reported that immobilization of PEG on nanoparticles increases their uptake into cancer cells in comparison to unmodified particles (Gupta and Curtis, 2004). However, most other investigators suggested that one of the major problems associated with PEGylation is the low binding and uptake of the carriers into the target cells, which is believed to be one barrier against sufficient nanoparticle delivery to tumor cells. This phenomenon has also been termed "PEG dilemma" (Fang et al., 2011; Harush-Frenkel et al., 2007; Hatakeyama et al., 2011; Torchilin, 2010). In addition, diminished antigen binding has been observed for antibodies conjugated to PEGylated liposomes. This effect was dependent on amount of incorporated PEG and length of the polymer chains (Kontermann, 2006). Schnyder and Huwyler found that the PEG-mediated shielding effect reduced *in vivo* target recognition of immunoliposomes by up to 50% and was highly dependent on PEG chain length. In their study, the effect of PEGylation was less pronounced or not present at PEG molecular masses of 2000 and 750 kDa (Schnyder and Huwyler, 2005). Torchilin and colleagues proposed that a Tat peptide moiety conjugated to the distal end of 3400 Dalton PEG chain was removed from the "above the surface" configuration and moved closer to the nanoparticle core, which resulted in its inability to interact directly with the cell surface. This "folding in" property was not observed for PEGs with 1000 Da molecular weight. In agreement with this study, Sun and colleagues used heterobifunctional PEG 600 to coat the surface of IONPs and subsequently conjugated folic acid (FA) to the nanoparticles through an amide linkage at the free terminus of PEG. Their results showed that folate receptor-positive human cervical carcinoma cells (HeLa) took up about 12-fold more FA-IONPs than non-targeted IONPs, suggesting the folate presentation on the particle surface was effective (Sun et al., 2006).

Soluble polymers with a flexible main chain (e.g. PEG) in aqueous solutions have a strong tendency to fold into a statistical globule rather than maintain a stretched

conformation (Sawant et al., 2008). Direct measurement of PEG-tethered ligand-receptor interaction potentials confirm a thickness of 5 nm for 2 kDa PEG in its coiled state and an overall length of an extended PEG chain of 15 nm (Schnyder and Huwyler, 2005; Wang and Thanou, 2010). These considerations suggest that a corona of 5-kDa PEGs on the Ocean NanoTech IONP surface could substantially block the access of the surface-conjugated 15 kDa sdAbs to their targets, if they become "folded into" the PEG corona. Therefore, the possibility should be considered that the surface-conjugated 5 kDa amino-functionalized PEGs could interfere with EG2/EGFR recognition in my study (Figure 3-11). In addition, nanoparticles with carboxyl-functionalized surfaces are acidic in nature due to the dissociable OH-group and could therefore interact strongly with positively charged amino-groups in the EG2 protein sequence. In conclusion, the lack of specificity of EG2-IONPs for cell surface expressed EGFR could be caused by coiled-in PEG chains, which subsequently could mask the activity of the sdAb fragments as illustrated in Figure 3-11. The use of short PEGs (e.g. MW <1000) or insertion of protease sensitive peptides between PEGs and nanoparticles may be effective strategies to overcome the PEG dilemma (Fang et al., 2011).

Some other factors might have contributed to the variability of the cell-labeling results in the confocal microscopy study. Up to batch 4, the IONPs were directly labeled with NHS-reactive Alexa Fluor® 488. Anti-PEG backbone antibodies were commercially available only later thereby enabling me to start to use these for nanoparticle detection. It is possible that this difference in detection could have contributed to the altered cell-labeling profile between IONP and IONP-488 batches. For example, Kuan *et al.* showed that the method of mAb labeling had a major influence on the selectivity and specificity of mAb distribution *in vivo*. N-succinimidyl 5-iodo-3 pyridine carboxylate (SIPC), which binds to the lysine amino groups on mAbs, carries a positive charge on the nitrogen atom of its pyridine ring at lysosomal pH, and was shown to remain trapped inside lysosomes because of this charge (Kuan et al., 2000). However, since the labeling efficiency of fluorophore to particles was approximately 1 to 1, I consider it unlikely that a

single fluorophore on a large particle surface will have a crucial effect on IONP distribution.

Another reason for the apparently weak labeling efficiency could be simply that the fluorophores are being quenched in proximity to the metal core of the IONPs (Bertorelle et al., 2006). Quenching of the fluorophore by iron oxide has also been observed for a Cy5.5 dye conjugated to the surface of iron oxide nanoparticles (Josephson et al., 2002). The same group noted that conjugation of fluorescein to the nanoparticles resulted in a profound quenching effect and postulated that the fluorescence quenching of magnetic nanoparticles may be due to non-radiative energy transfer between the dye and iron oxide. In the case of colloidal gold, non-radiative energy transfer is believed to be the dominant mechanism of fluorescence quenching. Fluorophores ranging from fluorescein (ex 494, em 520) to Cy5 (ex 649, em 670) were highly quenched by colloidal gold (Dubertret et al., 2001). Malicka and Gryczynski also found that proximity of metallic surfaces resulted in decreased fluorophore lifetimes (Malicka et al., 2003).

In summary, my findings, once more, illustrate the complexity of colloidal surfaces, their molecular architecture and charge distribution, as well as consequences of ligand attachment. My data emphasizes the urgent need for well-characterized nanoparticle surface chemistries, as well as an increase in the understanding of the interaction of these surfaces with blood components and the resulting impact on cellular internalization and *in vivo* distribution. Reproducible physical and chemical properties are essential for successful application of nanoparticulate contrast agents or drug carriers in the treatment of human disease.

3.4.5 *In vivo* distribution of targeted EG2-IONP-680 and non-targeted IONP-680

The epidermal growth factor receptor is a well-established tumor target and *in vivo* imaging of EGFR expressing cancer cells using radio- and fluorophore-labeled ligands (Adams et al., 2007; Ke et al., 2003), antibodies and antibody fragments (Mishra et al., 2004; Takahashi et al., 1987), affibodies (Friedman et al., 2008), and immunoparticles (Benhabbour et al., 2011; Diagaradjane et al.,

2008; Feng et al., 2009; Hadjipanayis et al., 2010; Mamot et al., 2003; Oliveira et al., 2010; Tsutsui et al., 2007; Yang et al., 2009b) has been demonstrated in numerous subcutaneous and orthotopic xenograft models.

In vivo optical imaging of EGFR-targeted IONPs

The nanoparticles in this study were labeled with DyLight 680 fluorophores. The quantity of intravenously injected nanoparticles in my experiments was identical to other reports on Ocean NanoTech nanoparticles and IONPs from different sources (Chen et al., 2009a; Glaus et al., 2010; Xie et al., 2010). Fluorescence in the animals was monitored for 72 hours at which point the study was terminated (Figure 3-9). PEGylated iron oxide nanoparticles have previously demonstrated prolonged blood half-lives compared to their non-PEGylated counterparts (Alexis et al., 2008; Dunn et al., 1994; Wu et al., 2011). In my study, I observed similar levels of fluorescence at all post-injection imaging time points, which suggests that either a large fraction of PEGylated EG2-IONPs and control IONPs remained in circulation or that the nanoparticles non-specifically adsorbed onto the vessel wall. A pharmacokinetic analysis would provide detailed information about blood circulation times and clearance profiles of EG2-IONPs and the non-targeted IONPs. For example, a two-step clearance mechanism has been described for PEGylated nanoparticles by Wenger and coworkers. In their study, half-lives of 30 minutes were found for a fraction of PEGylated and non-PEGylated particles (~30 % IA), with a large fraction of nanoparticles observed as having a much longer half-life at 120 h post-injection (Wenger et al., 2011). The long duration of fluorescence observed in the animals in my study are in agreement with their findings. Thus, non-targeted PEGylated Ocean NanoTech IONPs could potentially find application as blood pool contrast agent for increased visibility of blood vessels by cerebromicroangiography (Wu et al., 2011).

Cross-reactivity of EG2 with murine EGFR has not been investigated, and binding to endogenous EGFR on mouse endothelial cells and in the liver could in theory contribute to the sequestration of the IONPs. This is a drawback that is recognized for all currently approved therapeutic anti-EGFR antibodies, which

bind wild-type EGFR expressed in normal tissues including skin, liver, and gut. Not only does this pool of EGFR in normal tissue represent a large sink for the antibodies, but also it makes the use of antibody/cytotoxic conjugates risky (Garrett et al., 2009). However, this effect could not be discerned under my experimental conditions.

In this study I observed enhanced accumulation of targeted as well as non-targeted IONPs in the tumor-carrying flank of the animals, with no significant difference between them, which suggests that in both cases retention was mediated by the EPR-effect (Figure 3-9). This outcome was not unexpected, because previous studies have also shown that the presence of the tumor cell-targeting ligands on IONPs does not necessarily result in their increased accumulation in solid tumors (Bae et al., 2011; Wang and Thanou, 2010). For example, a study by Kirpotin and coworkers showed that anti-Her2 immunoliposomes display a similar biodistribution, including tumor accumulation, to non-targeted liposomes and thus appear to be less dependent on molecular targeting for actual biodistribution and tumor localization (Kirpotin et al., 2006). As described previously in this thesis, tumor penetration is a passive process that requires a long circulating half-life to allow extravasation of the particle across the hyperpermeable tumor vessels and effective diffusion through the tumor interstitial space. The addition of targeting ligands increases the size and biological reactivity of the particle, which could potentially amplify the problem of transport across these barriers (Jain and Stylianopoulos, 2010). However, besides its size, the constitution of the nanoparticle surface is a crucial determinant of *in vivo* distribution and retention of nanoparticles at the tumor site. The surface charge of IONPs should ideally be maintained close to neutral for imaging and drug delivery (Peng et al., 2008). Therefore, the overall negative charge of EG2-IONPs and control IONPs in this study could have contributed to their *in vivo* distribution profile.

Ex vivo imaging of tumor tissues and organs

Ex vivo imaging of the organs and the tumor tissue revealed low overall fluorescence in the tumors comparable to non-target organs, such as heart and

kidneys (Figure 3-10). These findings suggested that although the EPR effect caused selective accumulation of IONPs in tumors relative to other tissues at the same depth in the animals, it was not powerful enough to achieve accumulation of large amounts of targeted and non-targeted IONPs in the tumor tissue relative to other organs.

Tumor angiogenesis is reported to begin as the tumor diameter becomes larger than 0.8 – 1.0 mm, and the neovasculature being formed maintains the tumor blood supply (Fang et al., 2011). In my study, IONPs were administered when the tumors reached volumes of 100 mm^3 suggesting that vascularization of the tumors must have had occurred at this point. In addition, previous reports showed that subcutaneous U87MG tumors are well vascularized (Abourbeh et al., 2007; Claes et al., 2008). In general, the EPR-effect is undoubtedly much larger in tumors in animal models than in patients, simply because most rodent tumors grow much faster. Because of this rapid growth, blood vessels in mouse tumors generally do not develop properly and they consequently tend to be much more leaky than their human counterparts. Nevertheless, the EPR effect is a highly heterogeneous phenomenon, which varies substantially from tumor model to tumor model, as well as from patient to patient. In addition, tumors growing subcutaneously are anatomically and physiologically very different form tumors growing in their native (orthotopic) environment. One of the major pitfalls in the field of tumor-targeted delivery relates to the fact that the EPR effect is often overrated and/or misinterpreted (Lammers et al., 2011). While the EPR effect may be in effect for intravenously administered nanoparticles, the majority (> 95%) of administered nanoparticles are known to accumulate in other organs, in particular the liver, spleen and lungs (Bae et al., 2011; Koo et al., 2006). The large size of nanoparticles along with the uniformly elevated interstitial fluid pressure in tumors may hinder transport across the vessel walls and compromise the benefits of the EPR effect (Jain and Stylianopoulos, 2010).

Consistent with most reports on *in vivo* distribution of iron oxide nanoparticles of this size, the highest particle accumulation is observed in the liver and the spleen (Diagaradjane et al., 2008; Jain et al., 2008; Yang et al., 2009a). The liver receives

blood from the gut and the heart via the portal vein and hepatic artery, respectively. Blood circulates through a permeable discontinuous capillary network, the sinusoids, to reach the central and hepatic veins. Inside the sinusoid capillaries, the Kupffer cells are responsible for phagocytic activity of the liver. These cells belong to the MPS and represent 80 to 90% of the total body macrophage population, explaining the large uptake of opsonized nanoparticles. The architecture of the splenic parenchyma is highly tortuous and its reticular fiber meshwork decreases the blood shear rate, maximizing interactions between blood components and splenocytes. Moreover, extravasated colloids must squeeze through the elongated fenestrations of the sinusoid to reenter the venous circulation. Physiologically, this process results in splenic retention. For nanoparticles, physicochemical factors that limit passage through the sinusoidal sieve (high rigidity, large size (>200 nm) and elongated or irregular shapes) will therefore contribute to their sequestration in the spleen (Bertrand and Leroux, 2011). Pretreatment with lovastatin before the injection of targeted IONPs may provide a new method to decrease the nonspecific uptake of targeted nanoparticles by the liver or spleen and increases their concentration at the tumor site (Peng et al., 2008).

Furthermore, I observed increased accumulation of EG2-IONPs in the lungs compared to non-targeted IONPs (Figure 3-10). From the injection site, the nanoparticles are transported directly to the heart via the venous network. Blood is delivered into the right ventricle and continues on to the pulmonary circulation. Lung capillaries are among the smallest blood vessels in the body with diameters between 2 and 13 μm in humans and rodents alike. Therefore they constitute the first sieving constraint for nanoparticulate contrast agents. Rigid particles with a diameter of 10 μm remain permanently trapped; particles with a size of 3-6 μm are initially caught in lung capillaries but eventually escape to reach the systemic circulation, while smaller particles (< 3 μm) avoid pulmonary retention (Bertrand and Leroux, 2011). The fact that only the targeted IONPs were retained in the lung suggests that they must be larger than the non-targeted nanoparticles. However, the measured hydrodynamic diameter of EG2-IONPs was below 100

nm. Therefore, adsorption of large serum proteins or even *in vivo* aggregation may have taken place in order to attain EG2-IONP dimensions that resulted in retention in the lung tissue. The low amount of fluorescence detected in the kidneys of the animals suggested that the fluorophore/IONPs conjugates remained stable in circulation for at least 72 hours, because dissociation of the polymer coating would have generated smaller degradation products, or even free fluorophore, that would have accumulated in the kidneys.

Chen *et al.* demonstrated optical and MR imaging of RGD-conjugated Ocean NanoTech nanoparticles in a subcutaneous U87MG xenograft tumor model. This is the only other study besides my own that was carried out with PEGylated Ocean NanoTech IONPs (Chen et al., 2009a). In contrast to the results of my own study, they observed enhanced accumulation of targeted IONPs over non-targeted particles in the tumor. Interestingly, however, they also saw increased accumulation of the targeted nanoparticles in the lungs, similar to my own observations (Figure 3-10). Yang and coworkers reported high accumulation in liver and spleen for anti-EGFR scFv-conjugated nanoparticles and non-targeted control nanoparticles in an orthotopic pancreas xenograft model. In addition, some accumulation in kidneys and lungs for the non-targeted nanoparticles were reported (Yang et al., 2009b). In the latter case, charge differences may have contributed to a differential serum protein adsorption pattern or aggregation *in vivo*, thus leading to a significantly increased size for non-targeted IONPs over their targeted counterparts.

In two of the published Ocean NanoTech IONP distribution studies, the authors also targeted the epidermal growth factor receptor. Non-pegylated Ocean NanoTech nanoparticles conjugated with anti-EGFRvIII mAbs showed preferential tumor accumulation over non-targeted nanoparticles by convection enhanced delivery (CED) in an orthotopic U87MG.EGFRvIII xenograft mouse brain tumor model (Hadjipanayis et al., 2010). Interestingly, in this study, the EGFRvIII-targeted particles were not internalized, which is in agreement with the slow internalization rate of EG2-hFc bound to EGFRvIII that I observed for this cell line (Figure 2-22 A). In the second study, Ocean NanoTech nanoparticles

conjugated with anti-EGFR scFv demonstrated specificity to EGFR-over-expressing MIA-Paca pancreatic cells and intracellular localization of the targeted, but not the non-targeted IONPs (Yang et al., 2009b). In both of the above studies, labeling of the nanoparticles with the anti-EGFR targeting moieties was achieved by cross-linking amines of the targeting proteins to carboxyl-groups in the polymer coating in the absence of polyethylene glycol.

The molecular weight of PEG can significantly affect the distribution of PEG-coated IONPs *in vivo*. Thus it is critical to select the ratio and molecular weight of PEG when designing IONPs for targeted delivery (Peng et al., 2008). Effects of targeting ligands have primarily been observed for non-PEGylated nanoparticles. Since PEGylation increases circulation times, differences between targeted and non-targeted particles may no longer be visible (Pirollo and Chang, 2008). Several studies have shown a >100% increase in tumor accumulation of nanoparticles following PEGylation. While this appears to be dramatic, the majority of intravenously administered nanoparticles still ends up in the liver and the spleen, with a lesser extent being in lungs and kidneys (Bae et al., 2011).

However, the lack of EG2-IONP specificity for U87MG.EGFR tumor cells observed in my study, may have also resulted from impaired target recognition and subsequent internalization due to the shielding effect generated by unfavorable PEG chain length and/or density on these particles, which I discussed in detail in the previous paragraph (see "3.4.4 Cell binding studies", page 140). Furthermore, heterogeneous PEGylation of the IONP surface could have contributed to undesired opsonization effects and/or unfavorable charge interactions between the particle and the cell membrane, which may also account for the lack of specificity observed for EG2-IONPs.

In another study on targeted Ocean NanoTech IONPs against a different molecular target (uPAR) in a pancreatic tumor model, *ex vivo* optical imaging showed highest accumulation of fluorescence in liver and spleen after 48 hours with no visible fluorescence in the other organs and the tumor. Subsequent histological staining nevertheless confirmed the presence of targeted iron oxide nanoparticles in the tumor and no staining for the non-targeted nanoparticles

(Yang et al., 2009a). It would therefore be interesting to follow up on the distribution of targeted EG2-IONPs and non-targeted IONPs within the tumor tissue. The organs and tumors from my study were frozen in OTC media and are currently stored at -80°C. I plan to stain tissue sections for iron content using Prussian Blue reagent. While optical imaging should be indicative of the whereabouts of fluorescently-labeled polymer coating, Prussian Blue staining is a true reflection of IONP distribution.

Molecular targeting ligands on the surface of IONPs were demonstrated to influence the cellular distribution of the nanoparticle (Diagaradjane et al., 2008; Xie et al., 2011). I also intend to carry out an immunohistological study to detect vessel and tumor cell distribution of targeted and non-targeted nanoparticles using anti-PEG (backbone) antibodies to detect the particles, and anti-CD31 and anti-EGFR antibodies to detect vessels and tumor cells, respectively.

Finally, it would have also been interesting to investigate the organ and tumor distribution of targeted and non-targeted IONPs by *ex vivo* imaging at earlier time points, since the imaging of the whole animal indicated less liver fluorescence at the 30 minute and 1 hour time points compared to later acquisitions, which is in agreement with observations by Wenger *et al*. and Lutz *et al.* (Lutz et al., 2006; Wenger et al., 2011). Furthermore, highest tumor accumulation was observed at 24 and 48 hours for IONPs and EG2-IONPs, respectively, which was also reported in by other investigators (Koo et al., 2006).

3.5 Conclusion

In this study, I investigated the physical properties, such as size, zeta potential and surface functionalization, of PEGylated iron oxide nanoparticles from two different commercial sources, Ocean NanoTech and Genovis. In addition, I analyzed the effect of these IONPs on cell viability in a three-day growth assay. I showed that both initial particle samples were monodisperse in aqueous solution, demonstrating narrow size distribution and average hydrodynamic diameters of 36 nm for Ocean NanoTech nanoparticles and 56 nm for Genovis IONPs. The zeta potential of the two particle samples was comparable with averages of -6.9 ± 4.2

mV and -4.4 ± 0.7 mV over the first 3 months after arrival for Ocean NanoTech and Genovis IONPs, respectively. The cytotoxicity profile of the IONPs from both sources was comparable and only the highest concentration (300 μg/ml) caused a cell-line dependent decrease of 20 – 40 % in cell viability.

I designed a conjugation strategy to attach the anti-EGFR single domain antibody EG2 to the IONP surface and developed a customized production and purification approach. The sequence of the sdAb was modified by introducing an additional cysteine at the C-terminus (EG2cys), so that uniformly oriented attachment to the particle surface was achieved. This was done by our collaborators at the IBS-NRC. Using SPR biosensor technology, I subsequently validated that affinity and specificity of EG2cys for EGFR were retained. EGFR is a readily accessible cell surface receptor, and when over-expressed, provides a basis for selective antibody-based targeting of tumor cells (Mamot et al., 2003). The final decision to pursue EG2 conjugation with the IONPs from Ocean NanoTech was based on the significantly higher degree of amino-functionalization on these particles, as well as on their smaller size and narrower size distribution profile.

Using a protein assay, I determined that 6 - 8 sdAbs were conjugated per EG2-IONP, which is in the range of conjugation densities commonly achieved for proteins of similar molecular weight. Consequently, I observed an increase in hydrodynamic diameter, a change in zeta potential and a decrease in r_2-relaxivity upon EG2 conjugation compared to the non-conjugated particles. A competition binding experiment using SPR biosensor technology demonstrated specificity of binding of EG2-IONPs for immobilized EGFR-ECD and furthermore suggested a significant avidity contribution to the affinity of the multivalent nanoplatform for the EGF receptors on the chip surface.

Next, I studied the ability of the targeted and non-targeted nanoparticles to interact with cell surfaces by confocal microscopy. I demonstrated that overall binding to cells was low and cell-labeling patterns varied greatly between nanoparticle batches. Subsequently, I identified differences in particle surface chemistry as the most probable cause. I observed that more negative zeta potentials correlated with the detection of fewer amino-groups in the

fluorescamine assay. Since the polyethylene glycol chains grafted on the particle surface are amino-functionalized, I concluded that the predominant difference between the individual nanoparticle batches was most likely based on their PEG grafting density. I speculated that changes in particle internalization patterns could have arisen from altered adsorption profiles of serum proteins. It has been demonstrated by others that changes in nanoparticle surface charge, which in turn affect the protein adsorption spectra, may lead to differences in the cellular uptake of nanoparticles (Mailander and Landfester, 2009). In addition, conflicting reports on the ability of PEG to increase or decrease internalization of nanoparticles suggest that there is an urgent requirement to better understand the relationship between nanoparticle surface composition, serum protein adsorption and subsequent cell surface interaction. I would therefore recommend carrying out PEGylation optimization steps (modifying length and density) in order to achieve a better balance between the positive attributes of PEGylation (decrease in opsonization) and its unfavorable steric effects ("PEG dilemma").

I furthermore carried out an optical imaging study in mice bearing subcutaneous U87MG.EGFR xenograft tumors and analyzed the distribution of fluorescently labeled targeted EG2-IONPs and non-targeted control IONPs *in vivo*. For both particles, fluorescence in the whole animal was detected up to 72 hours when the study was terminated, indicating long-circulating properties of the PEGylated nanoprobes. An increase in fluorescence in the tumor-bearing flank of the animal was observed for targeted and non-targeted IONPs, but no difference in tumor retention was seen between them over the investigated time period. My findings are in agreement with recent reports by other investigators saying that targeting ligands (e.g. antibodies) do not contribute to IONP accumulation in the tumor, which is primarily mediated by the EPR effect, but can result in enhanced cellular uptake and retention of the nanoprobe, due to interaction of the targeting ligand with receptors on the cell surface. Whether internalization of EG2-IONPs and IONPs into U87MG.EGFR cancer cells occurred in my study remains to be confirmed by histological analysis of the tumor tissue.

I also imaged the tumor tissue and organs of the animals *ex vivo* at 72 hours after IONP injection. As expected, the majority of the targeted and non-targeted IONPs were cleared by the liver and spleen, rendering the amount of fluorescence seen in the tumor and other organs proportionally insignificant, which is why differences among these were not detected under the chosen imaging settings. Tumor accumulation of nanoparticle quantities of less than 5% of the injected dose are not surprising and have been previously reported in other solid tumor models (Bae et al., 2011). Throughout evolution, complex living organisms have perfected their defenses towards the recognition and clearance of exogenous nano- and micro-sized pathogens, and multiple physiological mechanisms overlap to maintain homeostasis. Hence, despite all efforts to decrease biofouling and host reaction, the human body still perceives organic and inorganic nanoparticles as foreign material (Bertrand and Leroux, 2011).

In my study, accumulation of EG2-IONPs, but not control IONPs, was observed in the lung, suggesting that the targeted nanoparticles were larger than the non-targeted nanoparticles and subsequently sequestered in the delicate vessel bed of the lungs.

3.5.1 Future outlook

The outcome of this study shows that several points remain to be addressed in order to improve the sdAb/nanoparticle formulation to achieve enhanced delivery of the iron oxide contrast agent to EGFR over-expressing tumor cells. Whereas I demonstrated that EG2 is a suitable targeting ligand, due to its small size, high stability and rapid receptor-mediated internalization into EGFR over-expressing glioblastoma cells, the presentation of the single domain antibody on the nanoparticle surface is probably far from ideal. The relatively long polyethylene glycol chains on the Ocean NanoTech nanoparticles (5 kDa), in addition to potentially sparse PEG density, could provoke coiling of the polymer chains as described by Torchilin and colleagues (Sawant et al., 2008), thus sterically obstructing the EG2 sdAb/EGF receptor interaction. The negatively charged

polymer coating could further contribute to this phenomenon through electrostatic interactions with positively charged groups in the sdAb sequence.

My study furthermore shows that the production of commercial core-shell IONPs with reproducible surface characteristics has not yet been achieved and the subsequent cell binding and *in vivo* distribution studies emphasize the shortcomings of ill-defined nanoparticle surfaces. Similar observations are increasingly entering the literature (Lutz et al., 2006; Moghimi et al., 2011). In my opinion, gaining control of the variability between and within individual nanoparticle batches is the prerequisite for meaningful studies on IONP interactions with biological membranes *in vitro* and *in vivo,* and will be the foundation on which additional surface functionalization (conjugation of targeting ligands, fluorophore, *etc.*) may later be built. Recent advances in macromolecular engineering and polymer chemistry make this an attainable goal (Lutz et al., 2006).

Considering the vast number of contradicting reports on internalization and biodistribution of IONPs, which can be found in the current literature, it becomes furthermore obvious that extensive studies are needed to understand the effect of particle size, biopolymer coating, and surface charge/hydrophobicity on the interaction with biological membranes *in vitro* and *in vivo*. Once these problems are solved, new strategies could be pursued, such as the incorporation of additional BBB-specific single domain antibodies in the nanoparticle shell (Muruganandam et al., 2002). Herein, the generation of sdAbs against the lactoferrin or LDL receptor could potentially result in a valuable combination, together with EG2, to obtain bifunctional IONPs targeted to EGFR-over-expressing intracranial tumors (Wohlfart et al., 2011; Xie et al., 2011). The production of nanoprobes conjugated with two different monoclonal antibodies has been reported previously (Tan et al., 2003; Zhang et al., 2002). However, using VHH fragments instead of full-length antibodies would avoid Fc receptor-mediated effects, reduce the overall size of the targeted nanoparticles, and lower their production costs.

Furthermore, it has been proposed that endothelial cell-targeted nanomedicines possess significantly more potential for improving antitumor efficacy than do cancer cell-targeted nanomedicines (Lammers et al., 2011), further supporting the incorporation of VHH fragments against vascular targets into bifunctional IONPs as an interesting approach to pursue.

Currently, the major limitation of multimodal nanoprobes is their low specificity and limited internalization by glioma cells (Veiseh et al., 2005). For targeted as much as for non-targeted delivery, the EPR effect is undoubtedly the most important contributor to successful accumulation of the nanoparticles in tumors (Lammers et al., 2011). Strategies to optimize the EPR effect are currently being investigated and harbor significant potential to not only improve the application of nanoparticulate drug carriers for the treatment of solid tumors, but also to increase contrast agent accessibility to the tumor site in pre- and intra-operative imaging settings. In addition, glioblastomas appear to be rather rapidly growing tumors and the fact that current contrast agents are administered and accumulate non-specifically could provide hope that passive targeting and the associated EPR effect could be sufficient to enhance nanoparticles retention at the tumor site.

Recently, breast MRI was recommended by the American Cancer Society as a screening approach, adjunct to mammography for the early detection of breast cancer in women at high risk for this disease (Saslow et al., 2007). For reasons of current costs and availability, it is not conceivable that MR imaging will be used on a mass screening level. In view of the greatly superior diagnostic power of breast MR imaging that has been documented across virtually all possible clinical scenarios, the use of breast MRI was, however, recommended as an adjunct to mammography for individualized screening in women at average risk (Kuhl, 2007a; Kuhl, 2007b). Although breast MRI shows high sensitivity in detecting small breast lesions, a major challenge is its low specificity when using a non-targeted contrast agent such as gadolinium chelates, resulting in a high false-positive rate and unnecessary biopsy and mastectomy. Therefore, the development of molecularly targeted MRI contrast agents may increase the specificity of MRI (Yang et al., 2009c). The epidermal growth factor receptor is over-expressed in 50

% of breast tumors, and therefore the targeted iron oxide contrast agent designed in this study could potentially be employed in MRI-based breast cancer screening (Normanno et al., 2006).

Nanoscale materials possess novel properties as a direct consequence of their size, which may have unique consequences for toxicology (Ryman-Rasmussen et al. 2006). In general, these effects are insufficiently explored, for example long-term toxicity studies of brain-targeted iron oxide nanoparticles are still missing and herein, the effect of core-stabilizing polymer shells will need to be taken into consideration (Zolnik and Sadrieh, 2009).

Finally, increased costs and effort required for conjugation, in addition to increased complexity and problems associated with up-scaling, are currently standing in the way of industrial exploitation of ligand-conjugated nanoparticles. No actively targeted liposomes, polymers, micelles and nanoparticles have thus far been approved for clinical use and only very few are in clinical trials (Lammers et al., 2011; Wang et al., 2012).

Table 2. Overview of experiments carried out on the different nanoparticle batches

Iron oxide nanoparticles (SHA-10, Ocean NanoTech, Springdale, AR, USA) were investigated by dynamic light scattering (DLS), zeta potential measurements, cytotoxicity (Alamar Blue® assay), laser scanning microscopy, fluorescamine assay (number of amino-groups), magnetic resonance imaging (phantom study), animal study (optical imaging).

Batch	DLS	Zeta potential	Cyto-toxicity	LSM microscopy	# NH_2	MRI	Animal study
1 (03/2008)	✓	✓	✓	✓	✓		
2 (02/2009)	✓	✓	✓		✓		
3 (05/2009)	✓	✓		✓	✓		
4 (11/2009)				✓	✓		
5 (03/2010)	✓			✓	✓		
6 (08/2010)	✓	✓		✓		✓	✓
7 (11/2010)	✓	✓		✓			✓
8 (03/2011)	✓			✓		✓	

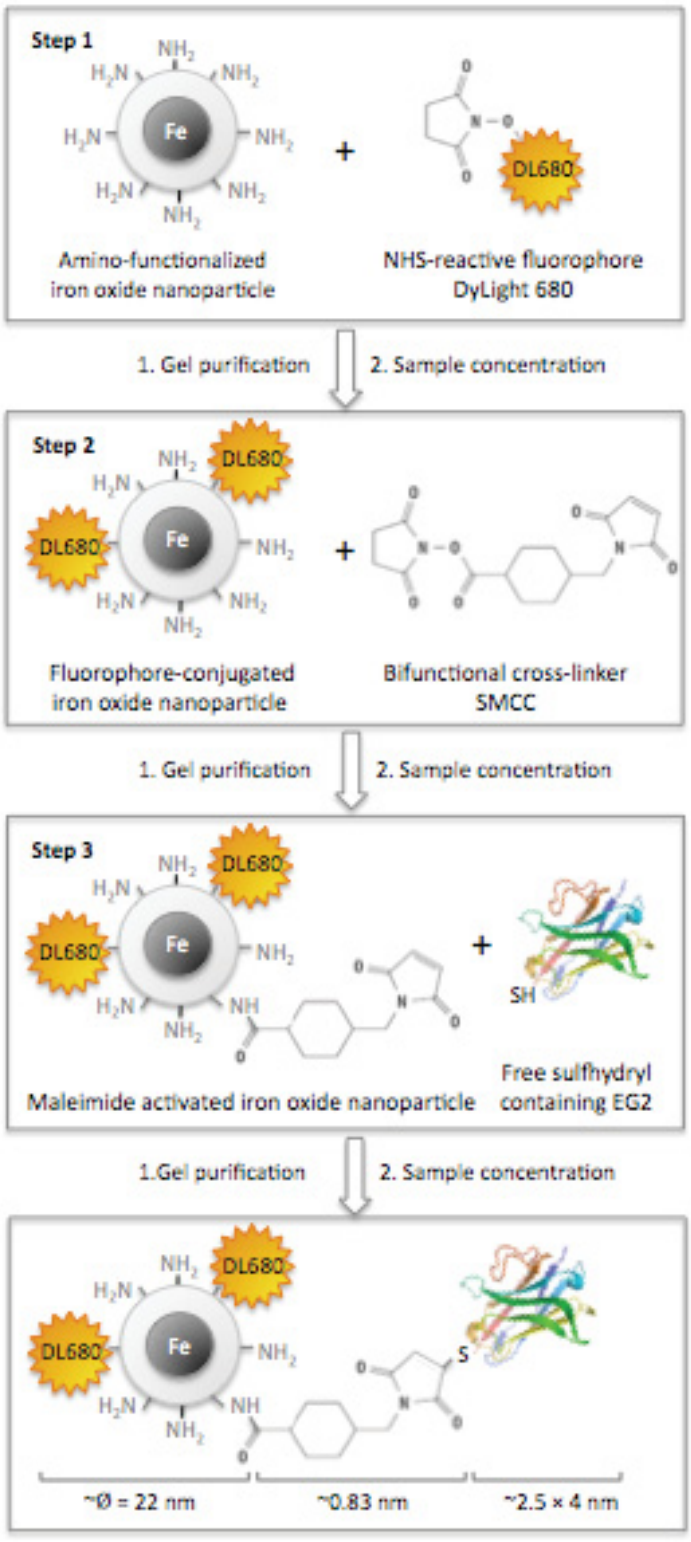

Figure 3-1 Nanoparticle conjugation scheme.

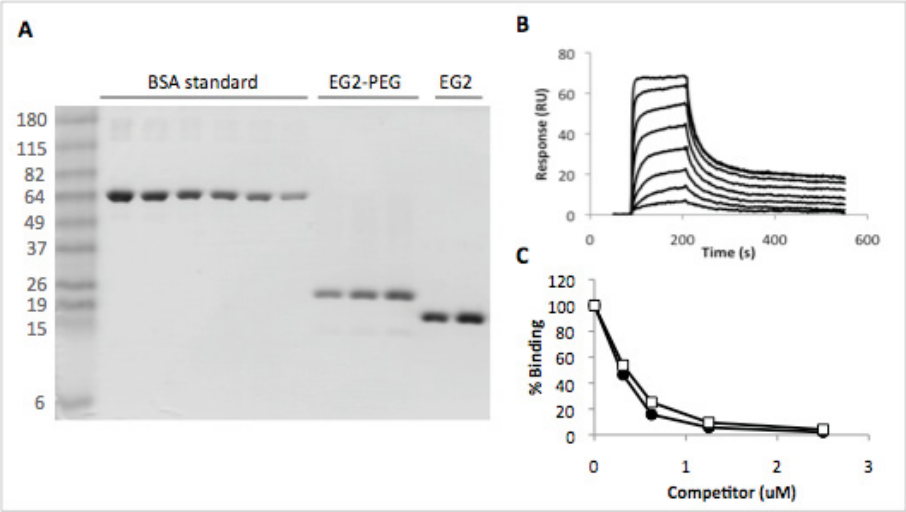

Figure 3-2 Production and purification of EG2-PEG.

(A) The inset shows the products of EG2cys reacted with different ratios of 2-kDa, monofunctional maleimide PEG. The reaction products were separated on a Superdex 75™ column at a flow rate of 0.5 µl/min. Absorbance was measured at 230 nm (black line) and 280 nm (grey line). 1 (EG2cys (D), dimer), 2 (EG2cys (M), monomer), 3 (10 x PEG), 4 (20 x PEG), 5 (40 x PEG). (B) Coomassie stained gel comparing the molecular weight and purity of EG2-PEG versus the original EG2 antibody without the additional cysteine cloned to the C-terminus. (C) SPR analysis. Serial dilutions of EG2-PEG (3.9 nM – 1 µM) were injected over immobilized EGFRvIII-ECD at 20 µl/min. (D) Competition experiment for EGFR-ECD (500 nM) binding to immobilized EG2 in the presence of increasing concentrations of competitor (0.25 – 5 µM). EG2 (●), EG2-PEG(□).

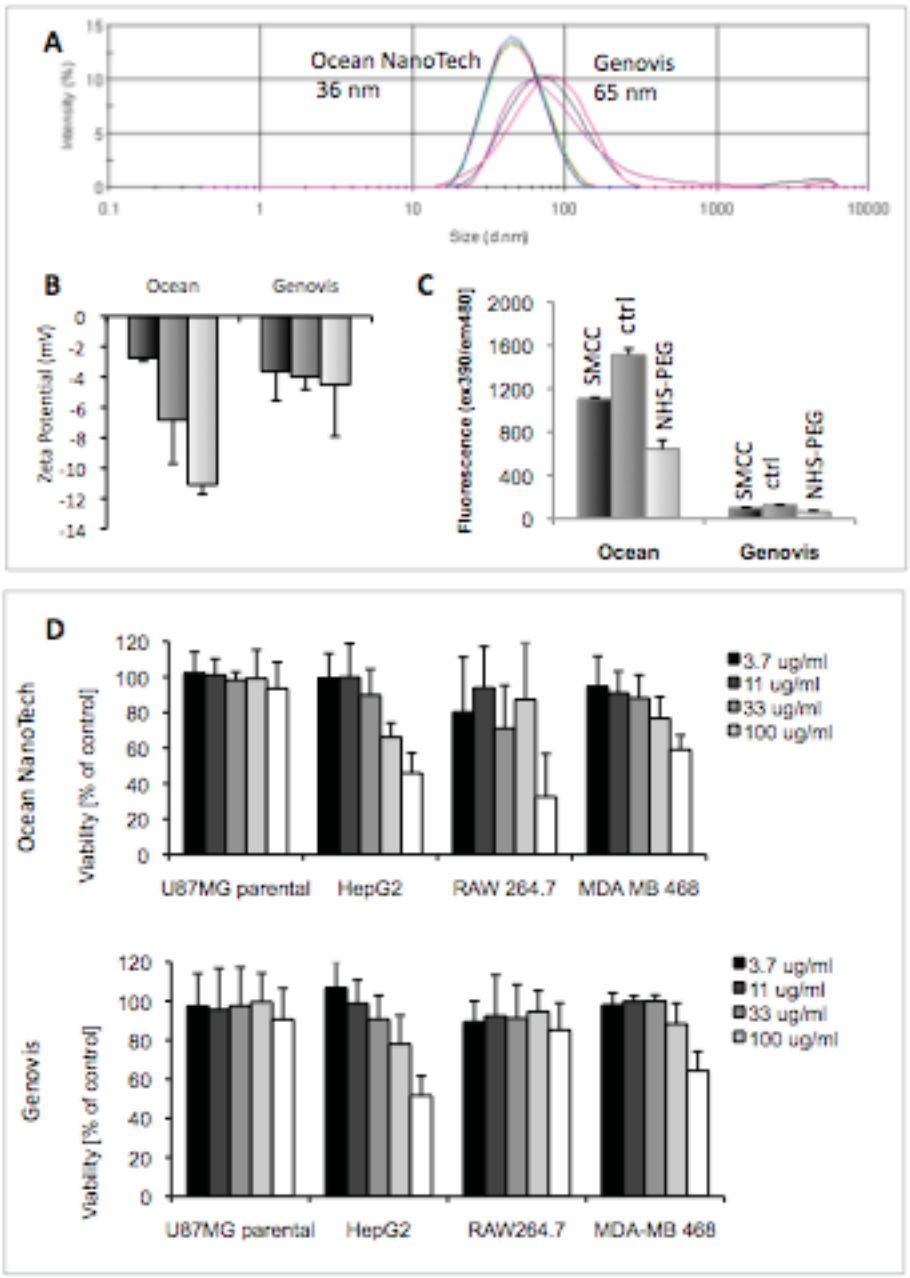

Figure 3-3. Comparison of the physical properties of Ocean NanoTech and Genovis nanoparticles with amine surface functionalization.

(A) Determination of the hydrodynamic diameter by DLS. (B) Zeta potential measuremnts. (C) Quantification of the relative reduction in free amino groups on the nanoparticle after conjugation of the bifunctional cross-linker SMCC or monofunctional NHS-activated PEG (2 kDa). (D) Four cell lines presenting target and non-target tissue were exposed to a range of particle concentrations for 72 hours. The viability of the cells at the end of the incubation period was measured in an Alamar Blue® assay.

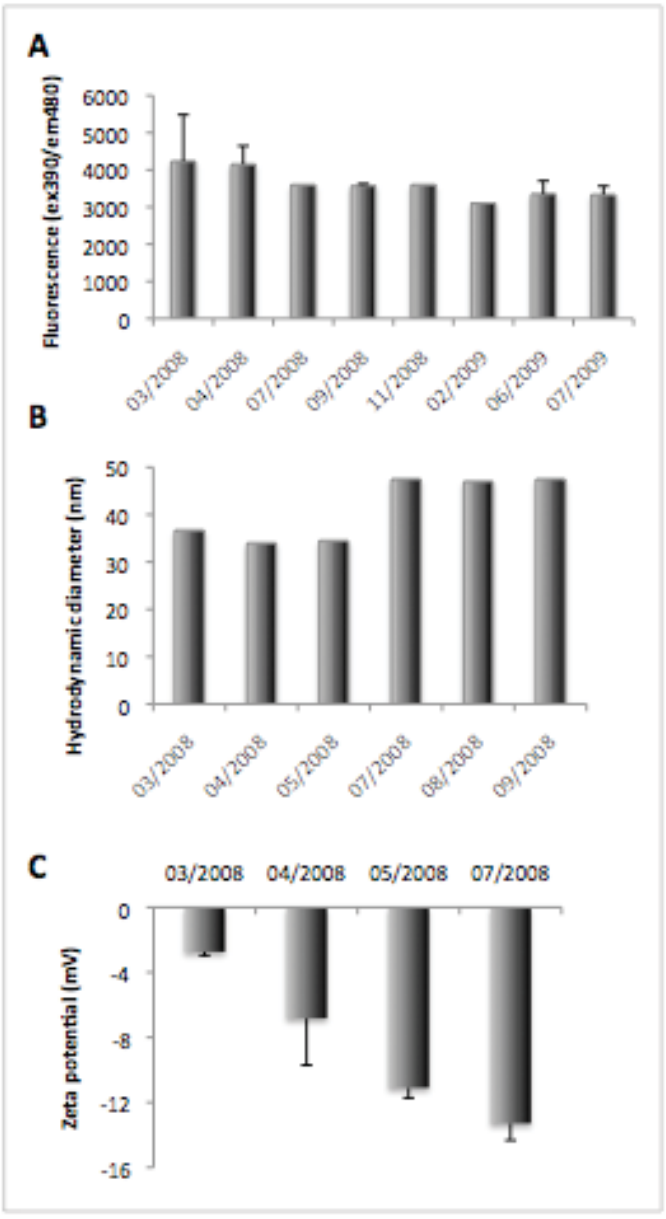

Figure 3-4. Determination of Ocean NanoTech nanoparticle stability.

(A). Quantification of free amino groups on the particle surface over a period of 16 months. (B) Hydrodynamic diameter measurements over a period of 6 months. (C) Zeta potential measurements over a period of 4 months.

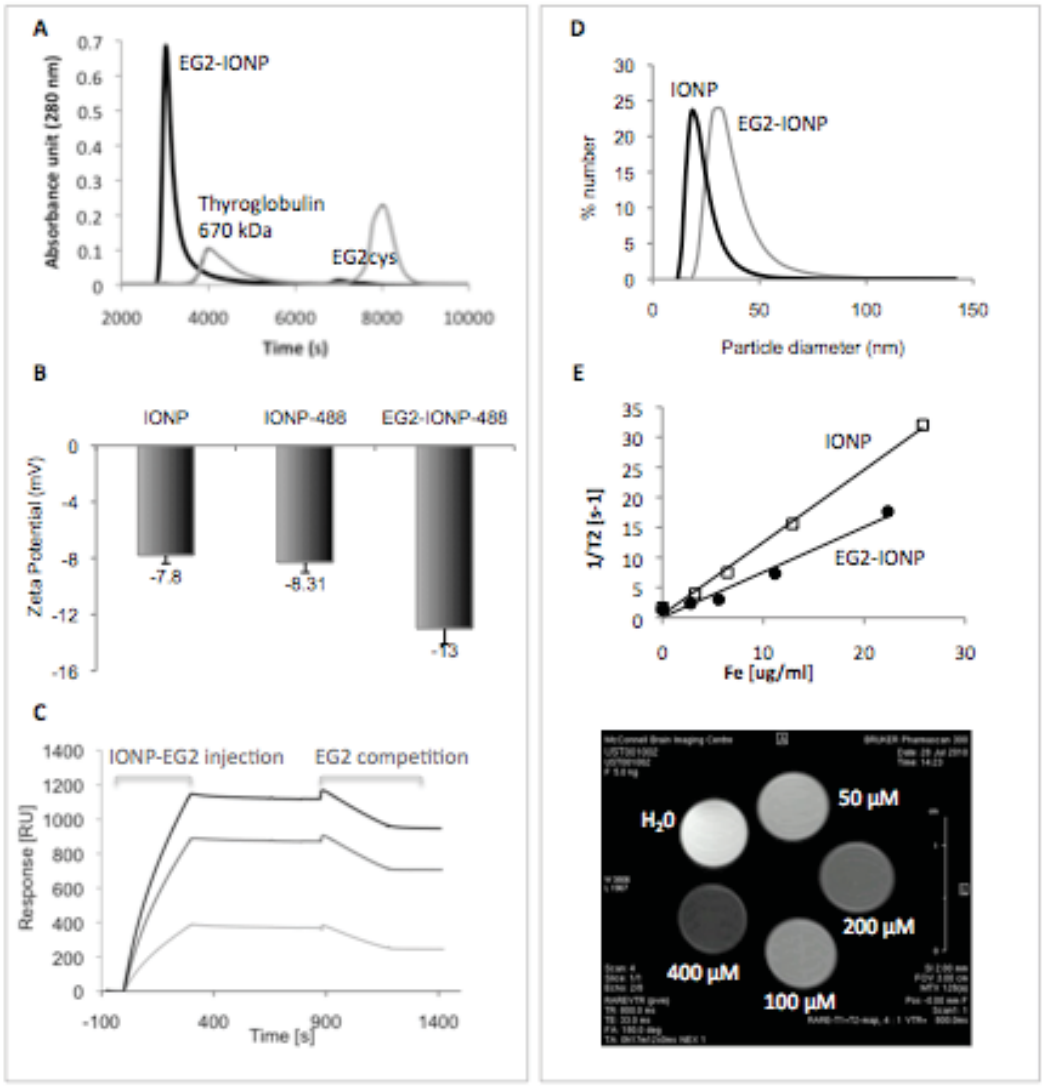

Figure 3-5. Conjugation of EG2cys to Ocean NanoTech IONPs. Determination of conjugation efficiency and changes in physical properties of the IONPs upon sdAb attachment.

(A) Purification of EG2-IONPs by gel filtration. The significant size difference between unconjugated EG2cys (16 kDa, diameter 3-4 nm) and the IONPs (diameter ~30 nm) provides excellent separation. EG2-IONPs elute in the void volume of the column and comparison to the elution profile of thyroglobulin indicates that their theoretical molecular weight is above 670 kDa. (B) The zeta potential changes after conjugation of fluorophore and single domain antibody, confirming the modification of the surface. (C) Biacore analysis. EG2-IONPs were injected over three different EGFR-ECD surfaces. The EG2-IONPs showed very slow dissociation in agreement with avidity generated by multimerization. The injection of excess amounts of EG2 accelerated EG2-IONP dissociation. (D) The hydrodynamic diameter of the particle increased form 56 to 95 nm after EG2cys conjugation. (E) MRI phantom experiments. IONP-EG2 showed decreased r_2 relaxivity compared to the control IONP.

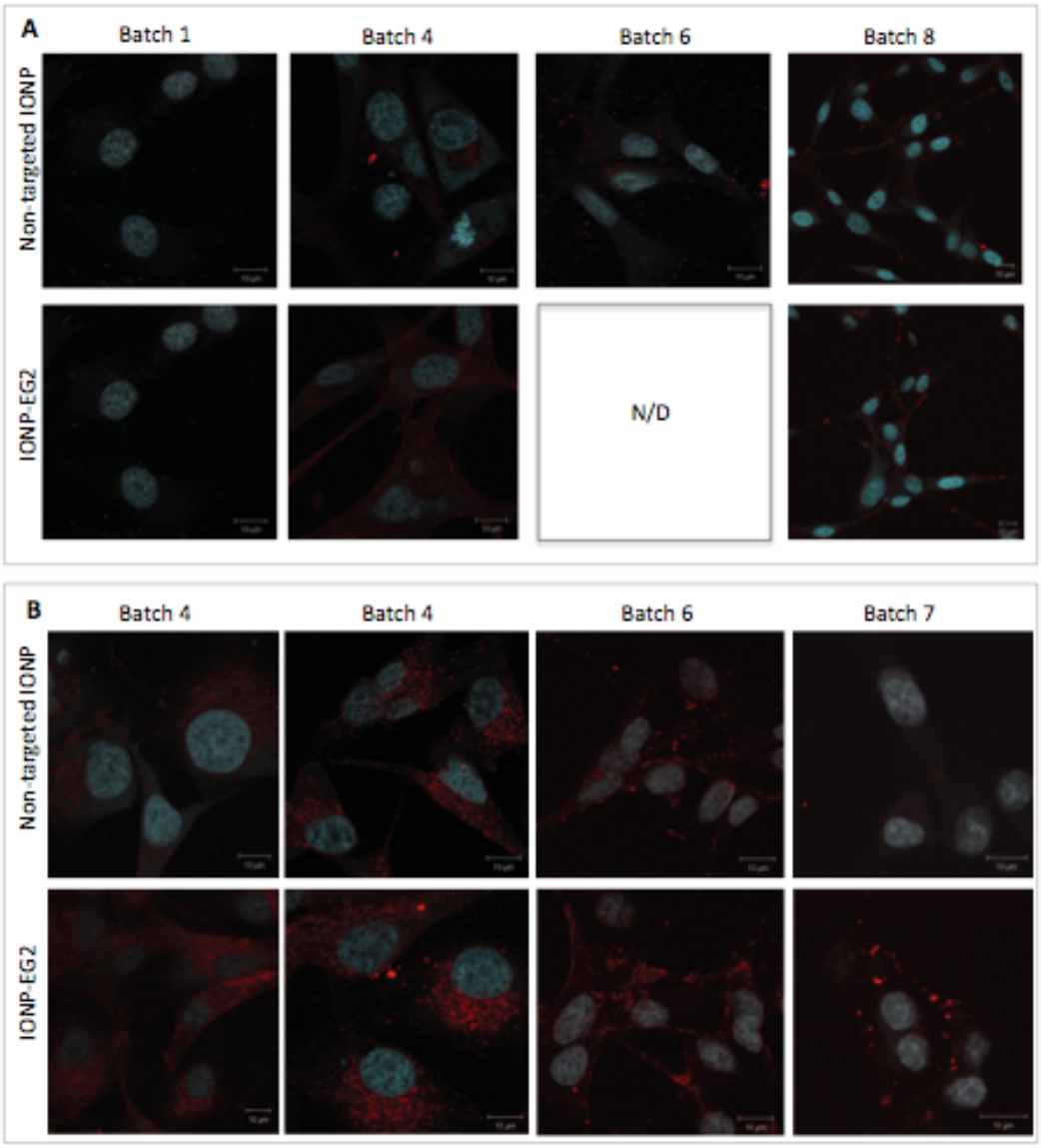

Figure 3-6. Confocal microscopy images of U87MG.EGFR cells labeled with targeted and non-targeted IONPs.

(A) Fixed U87MG.EGFR glioblastoma cells were incubated with 0.1 mg/ml EG2-IONPs or non-targeted control IONPs in PBS/0.1% BSA for 2 hours at room temperature. (B) Live U87MG.EGFR were incubated with EG2-IONPs or control IONPs in complete medium for 3 hours at 37°C. In general the association of the nanoparticles with the cells was very low, but difference in distribution can nevertheless be observed.

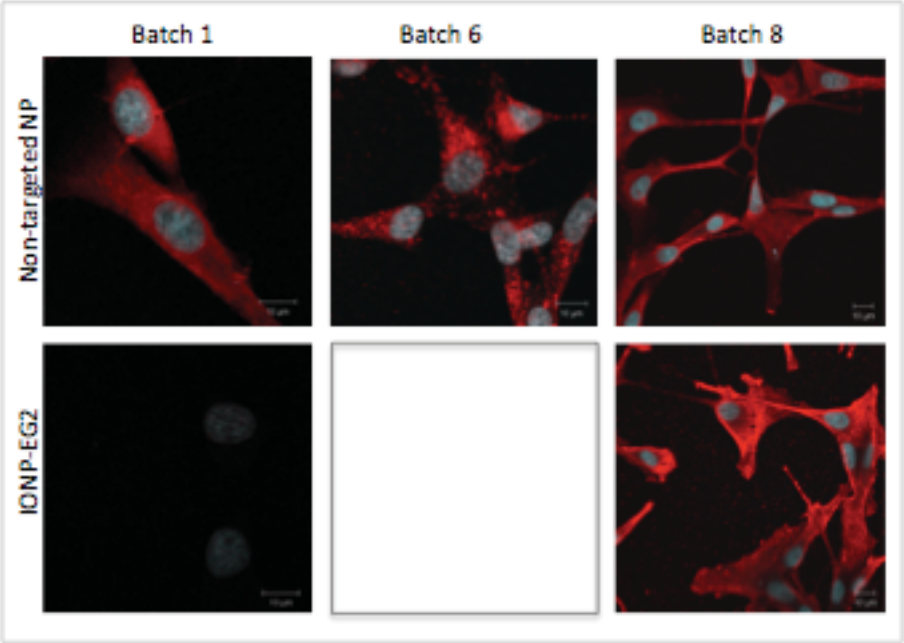

Figure 3-7. Confocal microscopy images of fixed and permeabilized U87MG.EGFR cells labeled with targeted and non-targeted IONPs from different nanoparticle batches.

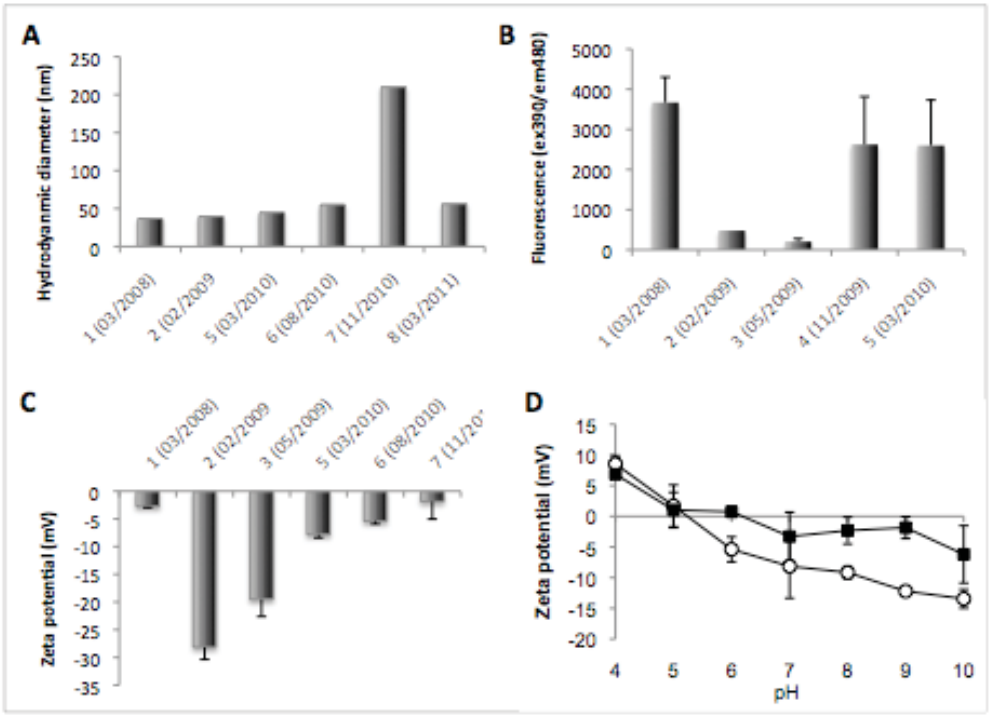

Figure 3-8 Comparison of different batches of Ocean NanoTech IONPs.

(A) Six out of the eight batches that I received from the manufacturers were compared for their average hydrodynamic diameters. Most of the IONP batches demonstrated sizes between 36 – 56 nm, except for batch seven, which consisted of multiple particle populations of different sizes. (B) The amount of amino-functionalization was assessed in the fluorescamine assay for five different batches and showed extreme variability between them. The error bars are the standard deviation of at least three independent measurements. (C) The zeta potential values for six batches was determined shortly after reception of the shipments and also showed significant differences. (D). The isoelectric point (pI) was determined for batch 1 (○) and batch 3 (■) by disbursing the particles in buffer solutions ranging from pH 4 to pH10. The pI value of batch 1 was approximately 5.2 and batch 3 was charged neutral charge at pH 6.2.

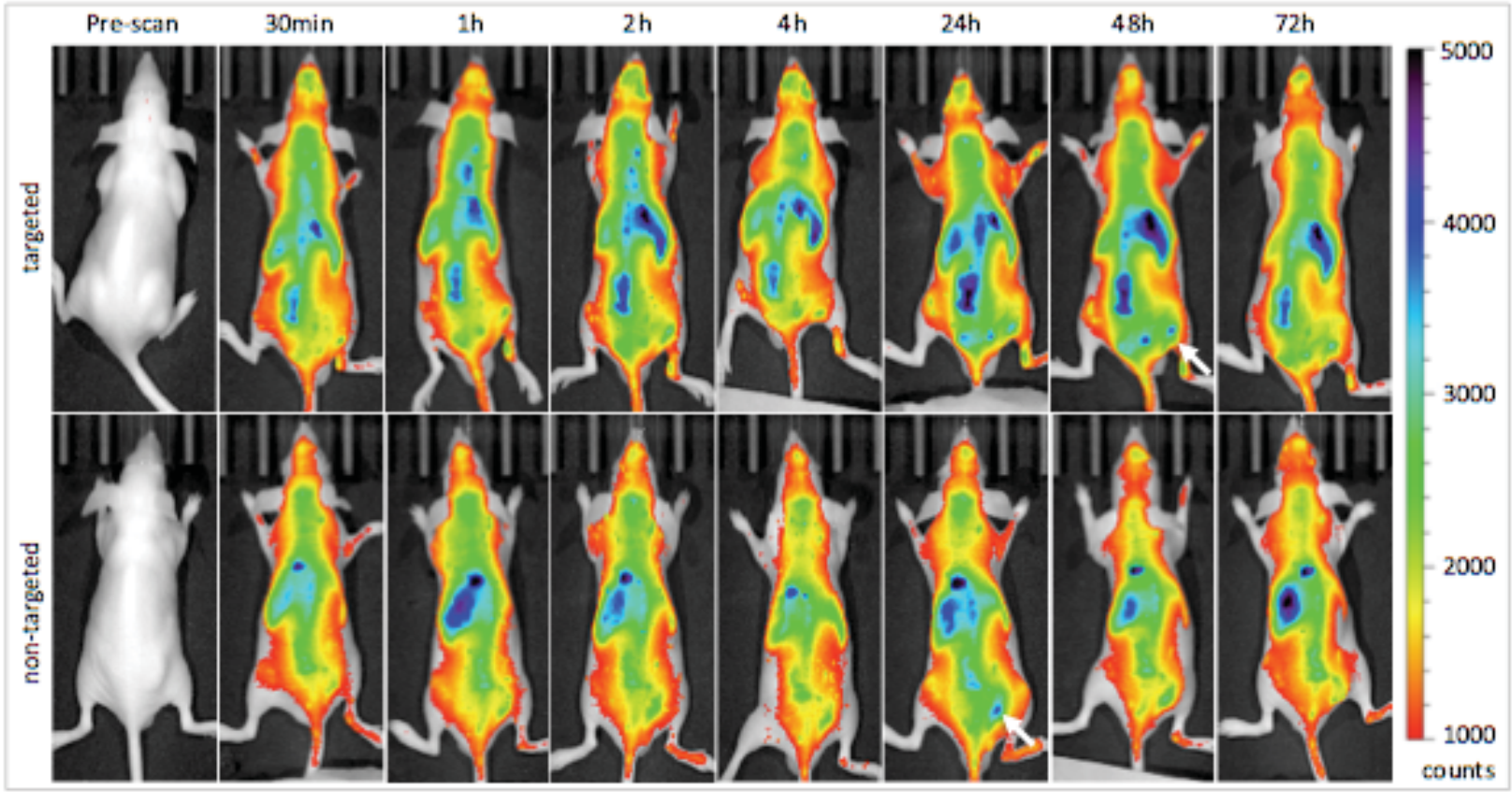
Pre-scan
30min
1h
2h
4h
24h
48h
72h
targeted
non-targeted
5000
4000
3000
2000
1000
counts

Figure 3-9. *In vivo* distribution of targeted and non-targeted IONP.

Targeted EG2-IONP-680 and non-targeted IONP-680 were injected at 10 mg Fe/kg body weight into animals bearing subcutaneous U87MG.EGFR xenograft tumors on their left flank. The distribution of the particles within the animal was measured over several time points up to 72 hours. Highest accumulation of IONPs in the tumor-bearing flank was observed at 48 hours for targeted and at 24 hours for non-targeted particles (white arrows). The fluorescence remained high until the study was terminated suggesting long-circulating properties of these PEGylated iron oxide nanoparticles *in vivo*.

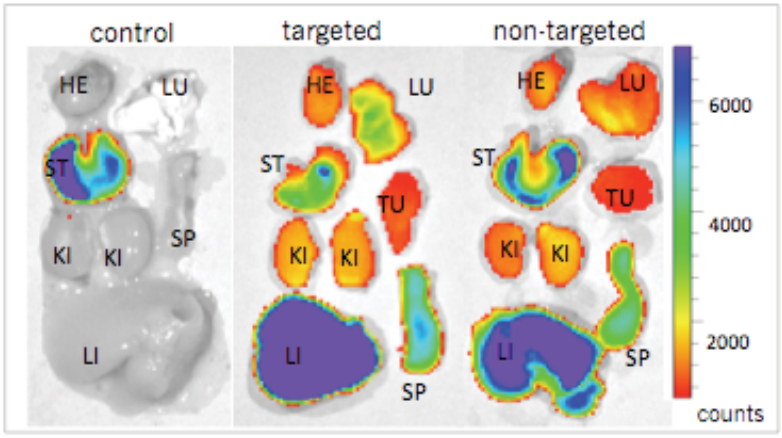

Figure 3-10. *Ex vivo* fluorescence imaging of organs and tumor tissue.

The organs and tumor tissue of animals injected with targeted EG2-IONP-680, and non-targeted IONPs-680 were imaged at the same settings as the animals. In addition the tissues of a control animal that had not been injected with nanoparticles was carried out to assess background fluorescence. The stomach content of all three animals showed non-specific fluorescence. All injected animals demonstrated the highest amount of fluorescence in liver and spleen, which are the common filter organs for particles with sizes above renal glomerular filtration threshold. In the animal injected with EG2-IONP-EG2 accumulation in the lungs was additionally observed. (HE – heart, LU – lung, ST – stomach, TU – tumor, KI – kidney, LI – liver, SP – spleen)

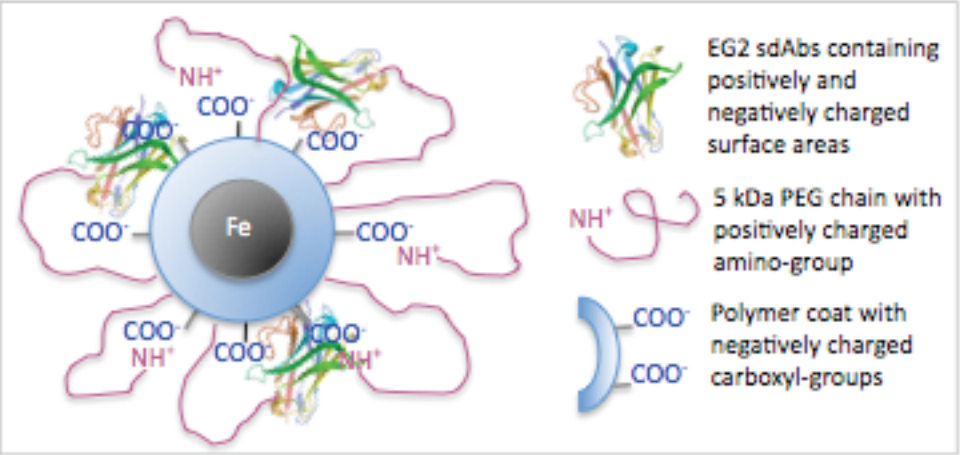

Figure 3-11. Schematic illustrating the potential charge interactions occurring on the surface of EG2-conjugated Ocean NanoTech iron oxide nanoparticles.

Non-conjugated 5 kDa PEG chains coil toward the polymer coating due to electrostatic interactions between the terminal amino-group and the negatively charged IONP surface. EG2-conjugated PEGs coil towards the surface due to charged surface areas on the protein that may interact with the carboxyl-groups on in the polymer coating.

4 Thermodynamic analysis of EGFR extracellular domain binding to EGF versus binding to EG2 sdAb.

4.1 Introduction

The correlation between structural and thermodynamic data is still difficult to predict, despite significant research efforts towards this objective due to its relevance in drug design. Databases such as pdbcal (http://www.pdbcal.org) and SCORPIO (http://scorpio.biophysics.ismb.lon.ac.uk/scorpio.html) have been generated to improve understanding of how the balance between the different thermodynamic parameters (enthalpy and entropy) guides molecular recognition processes. It is generally agreed that enthalpy reflects energetic contributions to the strength of the interaction mediated by van der Waals forces, hydrogen bonds and salt bridges, whereas entropy contributions to a binding event reflect changes in the translational and rotational degrees of freedom, solvent organization, and phenomena of conformational dynamics (Leavitt and Freire, 2001).

The correlation between aberrant activation of EGFR and the development and progression of human cancers is well established, and has made this receptor an intensely researched therapeutic and diagnostic target. Several anti-EGFR directed drugs have been approved for the treatment of human cancer over the last decade, with several more currently undergoing clinical testing. Especially antibodies against the extracellular domain have been the focus of intense research and the identification of some of their binding epitopes provided important insight into the conformational rearrangements of the extracellular domain (Schmitz and Ferguson, 2009). Although the crystal structure of the EGFR-ECD/EGF ligand-receptor complex is known, dimerization and tyrosine kinase activation remains not fully understood and the thermodynamic forces mediating this interaction have not been investigated in detail. To my knowledge, two other experimental thermodynamic studies on EGFR-ECD have been carried out. Lemmon *et al*. used isothermal calorimetry (ITC) to investigate EGF binding to the soluble EGFR-ECD, and Alvarenga *et al.* studied the interaction using SPR biosensor as well as

ITC (Alvarenga et al., 2012; Lemmon et al., 1997). In well-designed experiments, thermodynamic SPR biosensor studies have been shown to be capable of generating enthalpy and entropy values comparable to those obtained from ITC experiments. In addition, thermodynamic biosensor studies enable a prediction of the transition state of the interaction by providing measurements of temperature effects on the kinetic rate constants k_a and k_d (Day et al., 2002; Ely et al., 2006; Myszka et al., 2003; Navratilova et al., 2007; Roos et al., 1998).

Here, I present a detailed SPR biosensor characterization of the thermodynamic driving forces contributing to complex formation between EGFR-ECD and two proteins; the human EGF ligand (hEGF) and the 15-kDa anti-EGFR sdAb EG2. The thermodynamic analysis of EG2 binding to the receptor mutant EGFRvIII-ECD was included in this study, because structural differences are anticipated to occur between the extracellular domain of the wild-type and the mutant receptor, which could potentially impact their thermodynamic binding profiles (Schmitz and Ferguson, 2009). It was reported that camelid antibodies recognize novel epitopes that are not accessible to conventional antibodies, because of the size of the VH-VL binding site (Lauwereys et al., 1998; Transue et al., 1998). Therefore, sdAbs could potentially provide information on additional conformational states of the extracellular domain. The thermodynamic analysis of the receptor/sdAb interaction agreed with other reported thermodynamic profiles for antigen-antibody interactions, which are typically enthalpy-driven (Baerga-Ortiz et al., 2004; De Genst et al., 2004; Maenaka et al., 2001; Roos et al., 1998; Zeder-Lutz et al., 1997). In contrast, the interaction of hEGF with EGFR-ECD was mediated by entropy contributions, which generally confirmed the results of the two previous thermodynamic studies (Alvarenga et al., 2012; Lemmon et al., 1997). In addition, the transition states of the receptor/ligand and receptor/sdAb interactions were analyzed using the Eyring theory, and the contribution of electrostatic steering to complex formation was investigated by kinetic analysis of the interactions at increasing salt concentrations.

The following chapter also attempts to reconcile the thermodynamic data obtained in this study with current views on mechanisms of ligand-induced receptor

activation. Furthermore, these findings are expected to contribute to the accumulating information on correlation between protein structure and thermodynamic processes, which is expected to be useful for the improvement of thermodynamic scoring functions used in computational drug design (Li et al., 2008).

4.1.1 Ligand-mediated receptor activation

The structure of EGFR-ECD has been investigated by crystallography, which significantly improved our understanding of the conformations of the individual subdomains and their associated roles in receptor signaling (Ferguson et al., 2003; Ogiso et al., 2002). The extracellular domain of EGFR consists of four subdomains (I, II, III, and IV, Figure 4-a). Subdomain I and III are involved in ligand-receptor interactions, whereas large parts of domain II constitute the dimerization arm. The function of subdomain IV is still debated, but it is generally accepted that this domain is involved in dimerization as well as in high affinity ligand binding and potentially contributes additional auto-inhibitory mechanisms (Ferguson et al., 2003; Lemmon, 2009). In the absence of ligand, the extracellular domain is thought to be constrained to a tethered (inactive) conformation in which residues of domain II and IV interact, thereby pulling subdomain I and III apart so that bivalent ligand binding is no longer possible (Ferguson et al., 2003). In contrast, the ligand-bound extracellular domain is locked in the extended (active) state, i.e. the intra-molecular tether between domain II and IV is released and the ligand-binding pocket becomes reconstituted. The dimer exhibits a 2:2 stoichiometry, in which each ligand only contacts one receptor, with no contact to the other receptor or ligand (Ogiso et al., 2002). Receptor dimerization brings the intracellular regions into close proximity, thereby promoting the allosteric activation of the kinase domains (Zhang et al., 2006).

Ligand-binding studies on cell-surface expressed EGFR consistently demonstrate concave-up Scatchard plots, which can either be explained by the presence of heterogeneous binding sites or, alternatively, by negative cooperativity, i.e. the first EGF molecule would bind the dimeric receptor with higher affinity than the

second (Lemmon, 2009). A multitude of studies aimed at supporting these two theories have been conducted and gave rise to several receptor activation models. Nevertheless, there is still insufficient experimental evidence to corroborate either one of these possibilities (Alvarado et al., 2010; Lemmon, 2009; Lu et al., 2010; Mayawala et al., 2005; Teramura et al., 2006). Currently the predominant view proposes that the receptor oscillates between these two (and possibly more) conformational states on the cell surface, with 85-97% of receptors presented in the tethered conformation. Ligand binding eventually shifts the equilibrium towards the extended conformation, thereby promoting dimerization (Burgess et al., 2003; Ferguson, 2004; Lemmon, 2009). However, it has also been suggested that EGFRs mostly exist as dimers, oligomers and clusters, whereas monomers of EGFR are unstable (Kawashima et al., 2010). The identification of the tethered and extended forms of the EGF receptor first led to the suggestion that they represented the low- and high-affinity states of the receptor, respectively. However mathematical modeling of this idea fails to produce the observed concave-up Scatchard plots. In addition, the binding properties of receptor mutants in which the tether was weakened or deleted were not consistent with the assignment of the high-affinity state to the extended form of the receptor (Macdonald and Pike, 2008). The formation of predimers (homo- and heterodimers) in the absence of ligand, as well as EGFR association with other membrane proteins elevate the level of complexity of ligand-induced receptor activation and, as a result, add unknown variables to the interpretation of Scatchard data obtained from cell-binding studies (Engelman and Cantley, 2008; Farin et al., 2009; Moriki et al., 2001; Yu et al., 2002).

The successes in structure determination have lead to a dramatic increase in mechanistic understanding of the initial steps of receptor tyrosine kinase dimerization. However, the exact mechanism of signal transduction across the membrane (i.e. the mechanism through which the interaction between the two ligand-bound extracellular domains leads to phosphorylation within the catalytic domain) remains uncertain (Chen et al., 2009b). A merely untethered state and ligand-independent dimers are not capable to activate the receptor (Cymer and

Schneider, 2010; Dawson et al., 2007; Yu et al., 2002). These findings suggest that other factors are contributing to EGF receptor activation and that ligand binding must do more than simply expose the dimerization arm in order to promote receptor-receptor interactions.

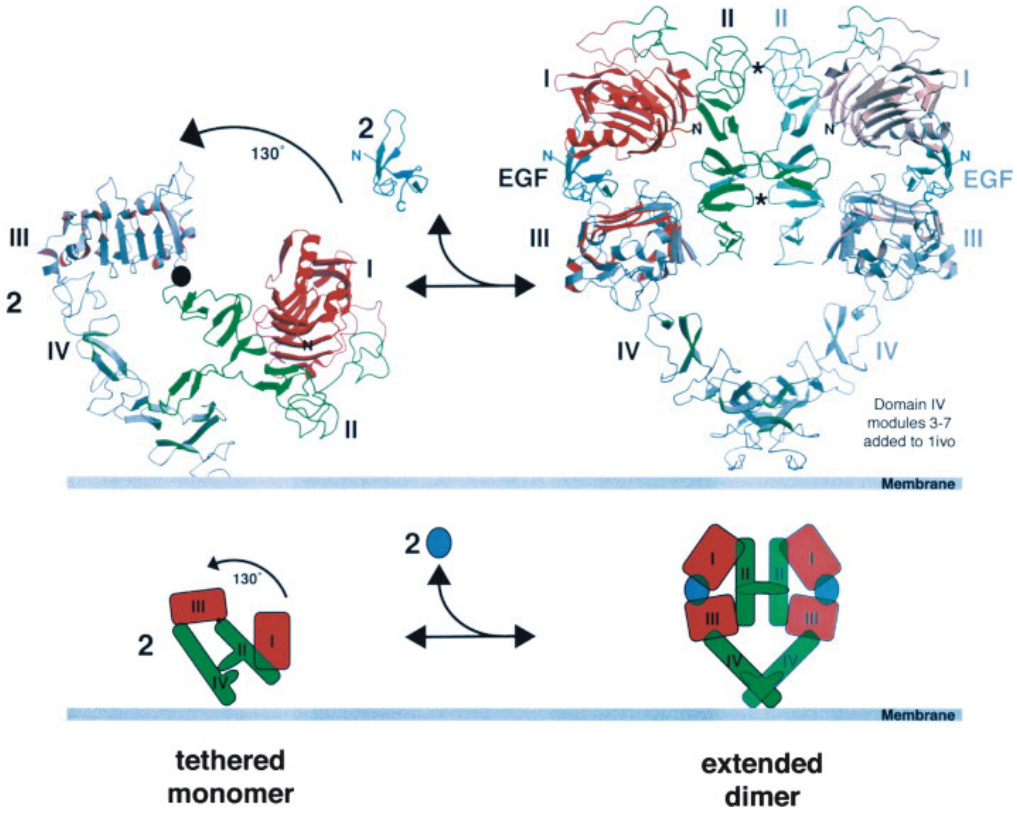

Figure 4-a. Schematic of ligand-induced conformational changes in EGFR-ECD dimerization. A transition between two EGFR-ECD structures is shown in both ribbons and cartoon representations. The unactivated (tethered) EGFR-ECD structure (PDB identity no. 1NQL) is shown on the left. A model of the EGF-induced dimer is shown on the right. This model uses the coordinates of Ogiso *et al.*, which lacked 5 of the 7 disulfide-bonded modules of subdomain IV (PDB identity no. 1IVO). In this figure, Burgess et al added the missing modules of subdomain IV using the structure of tethered EGFR-ECD, and assuming that the subdomain III/IV relationship is unaltered upon ligand binding. EGF binding is proposed to induce a 130° rotation of a rigid body containing subdomains I and II. This exposes the dimerization arm and allows dimerization of EGFR-ECD, as depicted on the right. See text for further details. *Figure:* (Burgess et al., 2003).

Lu *et al.* showed that EGFR trans-membrane domains are constitutively unassociated and associate only upon stimulation with EGF (Lu et al., 2010). In agreement with the involvement of the intracellular domain of EGFR in tyrosine

kinase activation is the finding that EGF binding to isolated extracellular domains generates linear Scatchard plots (Macdonald and Pike, 2008). Another question that currently remains unanswered is how different ligands modulate the downstream cellular response. For example, EGF stimulates abundant EGFR phosphorylation at Tyr1045, whereas the EGR ligand amphiregulin does not (Gilmore et al., 2009). Herein, Dawson and colleagues proposed a model in which the plane of the dimerization surface was predicted to be bent in a ligand–specific way, thereby promoting certain types of hetero- and homodimerization (Dawson et al., 2007). Also Wilson *et al.* hypothesized that binding of different ligands could slightly alter the conformation of the extracellular domain of the dimer, affecting the intracellular conformation as well, which then results in a changed pattern of intracellular phosphorylation thereby creating a unique signaling signature (Wilson et al., 2009).

The mutant EGF receptor variant EGFRvIII is characterized by a truncated extracellular domain lacking almost the entire subdomain I and large parts of subdomain II (Johns et al., 2007). Technically, that leaves the ligand-binding site on subdomain III intact, but most investigators agree that EGFRvIII fails to bind ligand in cell models (Cavenee, 2002; O'Rourke et al., 1998; Tang et al., 2000). The intracellular tyrosine kinase is constitutively activated suggesting that the conformation of the extracellular domain influences the activation status of the receptor (Sugawa et al., 1990). There is currently no crystal structure available for EGFRvIII-ECD.

4.1.2 Investigation of thermodynamic parameters using SPR biosensors

The Gibbs free energy (ΔG) is the most important thermodynamic description of binding, since it determines the stability of any given biological complex. The interplay of the two major interacting energy components of protein-protein interfaces, namely electrostatic and hydrophobic, is best understood by a detailed study of the thermodynamic parameters of the interaction. The enthalpy change (ΔH) of binding reflects the loss of protein solvent hydrogen bonds and van der Waals interactions, formation of protein-ligand bonds, salt bridges and van der

Waals contacts and solvent reorganization near surfaces. The main factors contributing to the entropy change (ΔS) of complex formation are the release of solvent water from the binding interface and the changes in rotational degrees of freedom upon complex formation. As a consequence of both forces being heavily dependent on the properties of the solvent water, enthalpy-entropy compensation is frequently observed in protein binding (Perozzo et al., 2004).

The change in free energy (ΔG°) for the receptor-sdAb (EGFR(vIII)-ECD/EG2) and receptor-ligand (EGFR-ECD/hEGF) interactions is related to their enthalpy (ΔH°), entropy (ΔS°) and equilibrium dissociation constant (K_D) according to the van't Hoff equation

$$\Delta G° = \Delta H° - T\Delta S° = RT \, ln \, K_D \quad (1)$$

where R = 1.987 cal K^{-1} mol^{-1} is the gas constant and T the temperature in Kelvin. The use of the van't Hoff equation implies that the reaction is of simple bimolecular type. If the enthalpy change does not vary with temperature, the van't Hoff plot of ln K_D and 1/T will be linear and the enthalpy change can be derived from the slope ΔH/R.

$$ln \, K_D = \Delta H/RT + \Delta S/R \quad (2)$$

The change in entropy is indicated by the y-intercept however it is more common to calculate it according to equation (2). However, in cases where enthalpy and entropy are affected by temperature the changes can be accounted for in the heat capacity ΔC_P by nonlinear fitting of the data using the integrated van't Hoff equation (de Mol et al., 2005; Dhalluin et al., 2005). It is expected that for most protein-protein interactions the values deviate from linearity according to the heat capacity change ΔC_P (Myszka, 2000). The heat capacity change is generally negative for protein-protein interactions, indicating that enthalpic effects become more favorable and entropic effects less favorable as temperature increases (van der Merwe, 2000). However, heat capacity change values obtained from SPR and ITC studies rarely agree (de Mol et al., 2005; Freyer et al., 2006; Thomson et al., 1998; Zeder-Lutz et al., 1997). In addition, in most SPR thermodynamic studies the minor contribution of ΔC_P over the investigated temperature range can be neglected and the calculation of ΔH from linear van't Hoff plots is sufficient to

characterize the thermodynamic driving forces of the interaction (Perozzo et al., 2004; Roos et al., 1998).

In order to further dissect the driving forces involved in complex formation the Eyring theory is applied. For the thermodynamic analysis of transition states (sometimes also referred to as encounter state) in complex formation, the rate constants can be represented graphically according to the Eyring equation, which results in a plot with a straight line of slope –H*/R and intercept dS*/R:

$$\ln (k\, h/k_B\, T) = -\Delta H^*/ RT + \Delta S^*/ R \qquad (3)$$

where h = 1.58 x 10^{-34} cal s and k_B = 3.3 x 10^{-24} cal K are the Planck and Boltzmann constants, respectively. *k* stands for, either the forward or reverse kinetic rate constant k_a or $k_{d,}$, respectively. The superscript '*' denotes that the thermodynamic constants are in the transition state. The Gibb's free energy, enthalpy and entropy change at equilibrium can be determined from the transition state by subtracting the energies derived from the association rate constant from the energies derived from the dissociation rate constant:

$$\begin{aligned} \Delta G_{eq} &= \Delta G^*_{ass} - \Delta G^*_{diss} \\ &= (\Delta H^*_{ass} - \Delta H^*_{diss}) - T\,(\Delta S^*_{ass} - \Delta S^*_{diss}) \end{aligned} \qquad (4)$$

The free energy barriers can be divided into enthalpy and entropy in the same way as the equilibrium shown in equation (1).

4.1.3 Ionic strength effects

SPR biosensor technology can also be employed to measure the effects of increasing ionic strength on the protein-protein interactions (Baerga-Ortiz et al., 2004; Baerga-Ortiz et al., 2000; Darling et al., 2002; Lookene et al., 1996; Nielsen et al., 2003; Shen et al., 1996). It is generally assumed that almost all protein-protein association events are governed to some extent by long-range electrostatic forces and that these forces correlate with the amount of electrostatic surface potential found on the interacting proteins (Janin, 1995; Orning et al., 2006; Schreiber and Fersht, 1996; Tang et al., 2006). This mechanism, commonly known as electrostatic steering, contributes to a favorable entropy of the interaction by maximizing the frequency of productive encounters (Baerga-Ortiz et al., 2004; Janin, 1995). Increasing the salt concentration in the running buffer

will interfere with the formation of long-range electrostatic forces and can provide an estimate about how important these contributions are for complex formation. Generally, interactions demonstrating fast association rate constants that are above diffusion mediated association are expected to show strong dependence on electrostatic steering, whereas other complexes could be considered relatively insensitive to variations over a wide range of salt concentrations (Schreiber and Fersht, 1996; Tang et al., 2006). One major caveat of this approach is however, that in some cases, interruption of salt bridges might be energetically neutral for the reason that charged residues interact favorably with polar solvents such as water and the net contribution will be frequently equivalent, despite the fact that the specificity of the interaction would be compromised (Davis et al., 1998).

4.2 Experimental procedures

Preparation of sensor surfaces

HBS buffer (10 mM Hepes, 150 mM NaCl, 3.4 mM EDTA, 0.005% p20, pH 7.4) was used as running buffer in all experiments unless specified otherwise. Purified recombinant human epidermal growth factor (hEGF) (Austral Biological, San Ramon, CA, USA) was immobilized by standard amino-coupling at densities of 17, 57, and 85 RU. EG2 sdAb was bound to a maleimide-activated surface through an additional cysteine, at the C-terminus of this protein as described in Chapter 3 of this thesis (see "3.2 Experimental procedures", page 115).

Kinetic measurements and data analysis

Each interaction was analyzed in at least two independent experiments, each consisting of triplicate repeats ("runs"). All sensorgrams were collected at a flow rate of 40 µl/min. EGFR-ECD dilutions from 1.5 – 1000 nM and EGFRvIII dilutions from 1.5 – 200 nM including two buffer blanks were injected in random order over EG2 and hEGF surfaces. Association times between 100 – 120 s and dissociation times of 300 s were monitored. After each analyte injection the sensor chip surface was regenerated for 30 sec with 50 mM HCl. This treatment did not denature the protein immobilized on the chip surface, since comparable

signals were obtained for duplicate injections of receptor. Sensorgrams were globally fit to the 1:1 Langmuir model, which requires that both the analyte and the immobilized protein are monovalent and homogenous. Herein, the resulting kinetic constants (K_D-values) were calculated from the association and dissociation rate constants (k_d/k_a) derived from iterative non-linear regression. The standard deviations were obtained from at least four independent data sets. The affinity of EGFR-ECD binding to hEGF was additionally determined at equilibrium binding using the BIAevaluation software and by Scatchard analysis. For the equilibrium binding analysis, the plateau RU values for each sensorgram were obtained by applying the average fit function in the software. These values were then used to generate saturation plots, and the K_D was determined by non-linear regression using the steady state affinity model in the BIAevaluation software. Scatchard plots were obtained by plotting bound (RU)/[analyte] over bound (RU). According to the Scatchard theory the equilibrium affinity constant K_D can be derived from the slope and R_{max} from the y-intercept of the linear fit (Scatchard, 1949). As mentioned previously (see "2.1 Introduction to surface plasmon resonance", page 28), Scatchard plots alone should not be used to estimate affinity constants in SPR biosensor studies, since they place inappropriate weight on the data with the lowest analyte concentrations, which are generally the least reliable (van der Merwe, 2000). Values below 5% of the Langmuir-derived R_{max}-values were therefore omitted in the plot.

Thermodynamic analysis

In order to investigate the thermodynamic profiles of the EGFR-ECD/hEGF and EGFR(vIII)-ECD/EG2 interactions, the SPR biosensor experiments were carried out at different temperatures. The interactions were studied in the temperature range from 5 to 32°C, incremented into four to five measurement temperatures. The temperature change during the experiment was linear starting from low to high. Each series of injection per temperature was preceded by a glycerol normalization step. Data sets obtained for each temperature were analyzed individually in the BIAevaluation software in the same way as described for the kinetic analysis in the previous paragraph. The resulting

data was used to generate van't Hoff and Eyring plots to determine the amount of enthalpy and entropy contributions to the individual binding steps, as described in the introduction to this chapter (see "4.1.2 Investigation of thermodynamic parameters using SPR biosensors", page 180).

Ionic strength dependence

EGF receptor extracellular domain binding to immobilized hEGF and EG2 single domain antibody was monitored in the presence of increasing concentrations of NaCl (100 – 350 mM) in order to investigate the ionic strength dependence of the interactions. HBS running buffer was prepared at 100, 150, 175, 200, 250 and 350 mM NaCl. The EGFR-ECD samples were diluted in each running buffer, so that the ionic strength of injected analyte and running buffer corresponded. Eight different EGFR-ECD concentrations (15.6 nM – 1 μM) and two buffer blanks were analyzed for each salt concentration at a flow rate of 40 μl/min. The association rate constants (k_a) from three independent runs were used to generate the reported standard deviations.

4.3 Results

4.3.1 Kinetic analysis of EGFR-ECD/hEGF and EGFR(vIII)-ECD/EG2 interactions showed that these systems can be described by a simple bimolecular binding model.

In order to avoid as much as possible the introduction of artifacts during the kinetic analysis, the biosensor community has recently provided recommendations for the generation of high quality SPR data, which I described in detail in Chapter 2 of this thesis (see "2.1 Introduction to surface plasmon resonance", page 28). I carried out the following experiments with respect to these recommendations. Hence, prior to the analysis of the kinetic and thermodynamic properties of the receptor-ligand and receptor-antibody interactions, the analytes (EGFR-ECD and EGFRvIII-ECD) were purified by size exclusion chromatography (SEC) to remove protein aggregates that could result in deviation away from a simple bimolecular interaction (data not shown). Towards the same objective, both

investigated binding partners (EG2 and hEGF) were conjugated to the SPR chip surface in ways that would promote conformational homogeneity. As described earlier, an additional cysteine was introduced at the C-terminus of the EG2 anti-EGFR single domain antibody ("EG2cys"), allowing for its site-specific immobilization onto the sensor chip surface via a covalent maleimide-bond (see "3.3.2 Characterization of EG2cys", page 123). Recombinant hEGF surfaces were generated using the standard amino-coupling chemistry, which is anticipated to yield a single configuration of active ligand (Domagala et al., 2000). In order to reduce mass transport and rebinding effects, low surface densities (15 - 160 RU for EG2 and 17 - 84 RU for hEGF) were generated, and the experiments were carried out at high flow rates, 40 µl/min. This rate was chosen, because a preliminary experiment revealed flow rate-dependent variations in the association rate constant (k_a) at flow rates below 40 µl/min (data not shown). For all surfaces prepared in the course of my study I obtained consistent surface activities of ~40% for EG2 and ~15% for hEGF.

Figure 4-1 A, D and E show nonlinear curve fitting of a simple Langmuir binding model of the association (A + B -> AB) to the SPR data obtained at 25°C for the receptor-ligand (EGFR-ECD/hEGF) and receptor-antibody (EGFR-ECD/EG2 and EGFRvIII-ECD) interactions. In agreement with previous reports on cell binding studies, the mutant receptor variant EGFRvIII did not bind to immobilized hEGF under the given experimental conditions (Cavenee, 2002) (data not shown). The kinetic parameters derived from these experiments are shown in Table 3. Affinity constants of 45 ± 2 nM for EGFR-ECD/EG2 and 32 ± 3 nM for EGFRvIII-ECD/EG2 were obtained from global analysis using the 1:1 Langmuir model. These values compare well with the results obtained from the SPR biosensor studies reported in Chapter 2 of this thesis (see "2.4.2 Determination of binding kinetics of four novel sdAbs", page 59). In those, opposite to this study, the mutant and wild-type receptors were immobilized on the chip surface and EG2 was injected as analyte at serial dilutions (EG2/EGFR-ECD: K_D = 50 ± 6 nM, EG2/EGFRvIII-ECD: K_D = 98 ± 10 nM).

Equilibrium binding and Scatchard analysis were additionally carried out for the EGFR-ECD/hEGF interaction. For equilibrium binding analysis the SPR data was fitted to the steady state affinity model using the BIAevaluation software (Figure 4-1 B). In addition, a linear Scatchard plot was obtained, which supports the simple bimolecular binding mechanism postulated for this interaction (van der Merwe, 2000) (Figure 4-1 C). These complementary methods of affinity determination produced results that were in good agreement with the K_D-values derived from non-linear regression using the Langmuir binding model (Figure 4-1 A). Specifically, affinities of 333 nM from linear Scatchard analysis, 415 ± 271 nM from the steady state model, and 294 ± 133 nM from the 1:1 Langmuir model were obtained. Steady state affinities could not be determined for the EGFR-ECD/EG2 and EGFRvIII-ECD/EG2 interactions, since equilibrium was not established in these systems during the experimental association times used in my study.

Effects of temperature on association and dissociation rate constants

Figure 4-2 shows overlaid sensorgrams of the 500 nM injections for the interaction of EGFR-ECD with immobilized recombinant hEGF (A) and immobilized EG2 sdAb (B) at the five investigated temperatures (5 - 32°C). When comparing the amount of bound EGFR-ECD at the end of the association phase a continuous increase was seen on the hEGF surface with increasing temperature. In contrast, EGFR-ECD binding to immobilized EG2 demonstrated the inverse relationship, i.e. a decrease in the bound fraction at the end of the association phase with increasing temperature. Next, I normalized the individual sensorgrams in the two data sets in order to improve the visualization of changes in association and dissociation rate (illustrated by black arrows).

Whereas the association rate (k_a) of EGFR-ECD for EG2 increased only by a factor of approximately 2.5, a 7-fold increase in k_a was observed for binding to hEGF over the investigated temperature range (Table 3). The dissociation rate (k_d) increased 14-fold for EG2 sdAb, but only 1.4-fold for hEGF. Figure 4-3 quantitatively illustrates the relationship between temperature and kinetic rate constants (k_a, k_d) for the two investigated systems. The interaction of the mutant

EGF receptor variant EGFRvIII with EG2 was included in the analysis and compared well with the binding profile observed for the wild-type receptor. As a result of these changes in rate constants, the affinities of EGFR-ECD and EGFRvIII-ECD for EG2 sdAb decreased with increasing temperature, whereas the affinity of EGFR-ECD towards hEGF increased (Table 3).

4.3.2 Thermodynamic analysis of EGFR-ECD/hEGF and EGFR(vIII)-ECD/EG2 binding revealed that opposing thermodynamic forces are driving the receptor-ligand and the receptor-antibody interaction.

The Gibb's free energy (ΔG) values calculated from equation (1) were -9.0 ± 0.2 kcal mol^{-1} for EGFR-ECD/hEGF, -10.1 ± 0.2 kcal mol^{-1} for EGFR-ECD/EG2 and -10.2 ± 0.1 kcal mol^{-1} for EGFRvIII-ECD/EG2 (Table 4). Figure 4-4 shows linear van't Hoff plots for EGFR and EGFRvIII extracellular domain binding to EG2 sdAb ($R^2 > 0.92$ and $R^2 > 0.96$) and EGFR-ECD binding to hEGF ($R^2 > 0.98$). The equilibrium binding constants (K_Ds) were derived from global analysis of the SPR data using the 1:1 Langmuir model in the BIAevaluation software as described in the previous paragraph. For the receptor-ligand interaction affinity constants derived from the steady state binding model are included in Figure 4-4 for comparison. I observed that the deviation in values obtained from the two fitting approaches was not significant (Table 3, Table 4). The kinetic and thermodynamic constants obtained for mutant receptor EGFRvIII-ECD to EG2 were comparable to the values obtained for wild-type EGFR-ECD (Figure 4-4, Table 3, Table 4). On a side note, the error bars in the van't Hoff plots represent the inter-experimental standard deviation, which was consistently higher than the errors determined between individual experimental runs within the same experiment. The greater differences observed between experiments are probably related to physicochemical factors, such as fluctuations in analyte concentration, due to independent protein determination of each gel-purified sample as well as variability between different protein production batches. These results therefore indicate good reproducibility of the data obtained for the investigated interactions.

The enthalpy ΔH estimated from the slope of the van't Hoff plot was 13.4 ± 3.4 kcal mol^{-1} for EGFR-ECD binding to hEGF and -11.0 ± 1.1 kcal mol^{-1} for binding to EG2, thus suggesting that the interaction between EGFR-ECD (or EGFRvIII-ECD) and the antibody fragment is enthalpy-driven (negative ΔH). The calculated entropy contributions (TΔS, equation (2)) were -0.8 ± 1.2 kcal mol^{-1} for EG2 and 22.3 ± 3.6 kcal mol^{-1} for hEGF (Table 4). Therefore, in the case of the EGFR-ECD/hEGF interaction, the unfavorable enthalpy was compensated by a favorable gain in entropy.

An additional level of analysis is to use Eyring plots to investigate the transition state of each system, which provides insight into the amount of activation energy ($\Delta G°_{association}$) required to achieve binding. Herein, the formation of the transition state generally correlates with the association rate, i.e. the larger the barrier the slower the k_a (Roos et al., 1998). Figure 4-5 and Figure 4-6, as well as Table 4 show the results of this approach. Similar $\Delta G°_{association}$ values were obtained for the receptor-ligand and receptor-sdAb (hEGF: 3.6 ± 0.4 kcal mol^{-1}, EG2: 3.7 ± 0.2 kcal mol^{-1}). Despite these similarities the individual thermodynamic driving forces governing the two investigated interactions varied greatly. Favorable entropy forces ($T\Delta S°_{association}$) counterbalance the large unfavorable enthalpy contribution ($\Delta H°_{association}$) to mediate the formation of the EGFR-ECD/hEGF encounter complex. In contrast, the calculated values contributing to enthalpy-entropy compensation during EGFR-ECD/EG2 encounter complex formation are approximately three-fold lower (Table 4).

4.3.3 Ionic strength effects on the EGFR-ECD/hEGF and EGFR-ECD/EG2 interactions indicate a low degree of electrostatic steering.

The effect of ionic strength on EGF receptor binding to immobilized hEGF and EG2 sdAb was analyzed by surface plasmon resonance under conditions of increasing NaCl concentrations in the running buffer. Increasing the salt concentration in the running buffer will interfere with the formation of long-range electrostatic forces and can provide an estimate about how important these contributions are during encounter complex formation. The contribution to the

Gibb's free energy contribution provided by electrostatic steering ($\Delta G_{long\text{-}range}$) can be derived from linear Debye-Hückel plots. Figure 4-7 illustrates the changes in the association rate constant (k_a) for the receptor-ligand and receptor-antibody interaction over buffer salt concentrations ranging from 100 to 350 mM.

The slopes obtained from Debye-Hückel plots are frequently used to compare binding systems investigated for the electrostatic contribution to ΔG. According to equation (5), the slope 2 $Z_A Z_B$ is the product of the effective charges of interacting proteins A and B (Baerga-Ortiz et al., 2004):

$$\log k_a = \log k_0 + 2\, Z_A Z_B \sqrt{I} \qquad (5)$$

where k_0 corresponds to the value of k_a extrapolated to an ionic strength I = 0 (y-intercept), which should represent the nonelectrostatic component of the interactions (Lookene et al., 1996). In the case of single electrolyte solutions, such as NaCl, the ionic strength (I) is equal to the concentration. I obtained slopes of −0.48 for EGFR-ECD/hEGF and −0.07 for EGFR-ECD/EG2 (Table 5).

The quantitative estimation of the contribution of electrostatic enhancement to ΔG can be obtained from equation (6) (Baerga-Ortiz et al., 2004):

$$\Delta G_{long\text{-}range} = RT \ln (k_0/k_\infty) \qquad (6)$$

where R = 1.987 cal K^{-1} mol^{-1} is the gas constant, T the temperature in Kelvin and k_∞ an estimate taken from the k_a at the highest NaCl concentration (350 mM NaCl), which was 1.03 ± 0.11 × 10^5 M^{-1} sec^{-1} and 0.43 ± 0.03 × 10^5 M^{-1} sec^{-1} for hEGF and EG2, respectively (Table 5). Using these values, the contribution to the overall ΔG from electrostatic steering for the EGFR-ECD/hEGF interaction was 0.31 kcal mol^{-1}, while the contribution of this term to EGFR-ECD/EG2 is 0.09 kcal mol^{-1}. These findings suggest a minor role of long-range electrostatic forces during complex formation.

4.4 Discussion

4.4.1 Kinetic Analysis

Over the past two decades surface plasmon resonance technology has become the most prevalent technology for determining kinetic rate constants of protein-

protein interactions. This label-free biosensor technology allows for the measurement of kinetic constants over almost the entire range of affinities identified in biological systems (Myszka et al., 1997; Ohlson et al., 1997).

In my study, an equilibrium dissociation constant of 294 ± 133 nM was obtained for the interaction of EGFR-ECD with hEGF, which is in good agreement with previous SPR biosensor studies that reported average affinities of 468 ± 91 nM (Domagala et al., 2000; Elleman et al., 2001; Nice et al., 2004; Wade et al., 2001; Zhou et al., 1993). The soluble extracellular domain of EGFR (residues 1-621) is able to form dimers in the presence of EGF with a reported dimerization affinity in the low micromolar range (Dawson et al., 2005; Lemmon et al., 1997; Odaka et al., 1997). In support of a low dimerization affinity, ultracentrifugation studies have shown that the receptor does not dimerize at concentrations between 0.1 – 1 μM in the presence of ligand, which corresponds to EGFR concentrations used in my study (Greenfield et al., 1989; Gunther et al., 1990). Additionally, it has been concluded that receptor concentrations above 10 μM are necessary to generate substantial amounts of receptor dimers in solution (Odaka et al., 1997). Since I deliberately created very low EGF density chip surfaces in the SPR study (17 – 84 RU), in order to avoid mass transport and rebinding effects, I would expect dimerization of surface bound EGFR-ECD to be negligible. In my study, the binding of EGFR-ECD to immobilized hEGF or EG2 could be described by global fitting of the binding data to the 1:1 Langmuir model ($Chi^2 < 1$), which supports the hypothesis that EGFR dimerization does not occur on the SPR chip surface (Figure 4-1 A - C). In further support of the simple bimolecular interaction model is the fact that in my study the K_D-values derived from the rate constants obtained from non-linear global curve fitting are consistent with the K_Ds obtained from the calculation of steady state measurements (Figure 4-1). In addition, linear Scatchard plots were obtained, which supports the accuracy of the 1:1 binding model (van der Merwe, 2000). I therefore conclude that more complex models are not appropriate to represent the binding mechanism under these experimental conditions.

In contrast to the K_D-values determined by SPR biosensor analysis, EGF binding to cell-surface expressed EGF receptors is characterized by affinities < 1 nM. Kinetic rate constants of $k_a = 1 - 5 \times 10^6\ M^{-1}\ s^{-1}$ and $k_d = 2 - 50 \times 10^{-3}\ s^{-1}$ have been reported from cell-binding studies (Carraway and Cerione, 1993; Knauer et al., 1984). Herein, the dissociation rate is comparable to the value determined by SPR in this study, but the association rate is about 10-fold higher for EGF binding to EGFR on the cell surface. The reasons for this significant difference in EGF ligand affinity between the soluble extracellular domain and the full-length receptor on cells are still uncertain, but involvement of the cytoplasmic domain in binding, receptor dimerization, and membrane-associated diffusion effects have been suggested (Klein et al., 2004).

The affinity of EG2 for EGFR-ECD is in the range of what is expected for a single domain antibody fragment (Muyldermans, 2001). In addition, the obtained affinities of EGFR-ECD and EGFRvIII-ECD binding to immobilized EG2 (Figure 4-1 B and C, respectively) corresponded to my previous findings on these interactions (see "2.4.2 Determination of binding kinetics of four novel sdAbs", page 59). In contrast to the experiments presented here, the receptors were immobilized on the sensor chip surface and the sdAbs were injected over the surface (Bell et al., 2010; Iqbal et al., 2010b). Inverse orientation of the binding partners in an SPR biosensor study is considered an excellent internal control for experimental artifacts, since a discrepancy in affinity due to heterogeneous surface presentation would become apparent. Herein, I furthermore confirmed my previous observation that EG2 sdAb does not differentiate between wild-type EGFR and mutant EGFRvIII (Iqbal et al., 2010b).

With regards to the measured kinetic rate constants, similar k_a-values were obtained for the EGFR-ECD/hEGF and EGFR(vIII)-ECD/EG2 interactions (Table 3). Association rates of this magnitude are considered to be predominantly controlled by rotational and translational diffusion (Schreiber and Fersht, 1996). In these cases, the association rate varies according to the temperature-related changes in buffer viscosity (Roos et al., 1998).

4.4.2 Thermodynamic Analysis

With the introduction of temperature-controlled SPR instruments, Zeder-Lutz and coworkers carried out the first thermodynamic analysis using Biosensor technology in 1997 (Zeder-Lutz et al., 1997). Since then, thermodynamic data obtained from SPR thermodynamic experiments has repeatedly been shown to be in good agreement with data obtained by ITC (Day et al., 2002; Myszka et al., 2003; Navratilova et al., 2007).

The ΔG values determined for the EGFR-ECD/hEGF (−9.0 ± 0.2 kcal mol^{-1}) and the EGFR-ECD/EG2 (-10.0 ± 0.2 kcal mol^{-1}) interaction in this study are in the range of the average free binding energy reported for protein-protein interactions ($\Delta G_{average}$ = −10.4 ± 2.49 kcal mol^{-1}, Table 4) (Stites, 1997). Both interactions produced linear van't Hoff plots with opposite ΔH values of 13.4 ± 3.4 kcal mol^{-1} for hEGF and −11.0 ± 1.1 kcal mol^{-1} for EG2, which suggest that the receptor/sdAb interaction is enthalpy driven whereas the receptor/ligand interaction is experiencing significant enthalpy penalty. The calculated entropy values (TΔS) were 22.3 ± 3.6 kcal mol^{-1} for EGF and −0.8 ± 1.2 kcal mol^{-1} for EG2 at 25°C (Table 4). Thus, the interaction between the antibody and the receptor is primarily enthalpy-driven. These findings are in agreement with thermodynamic driving forces determined for other camelid single domain antibodies and conventional antibodies as well as their fragments, which generally demonstrated enthalpy-driven thermodynamic profiles ($\Delta H_{average}$ = −9.8 ± 4.2 kcal mol^{-1}) with small positive or negative entropic contributions ($T\Delta S_{average}$ = 3.0 ± 3.8 kcal mol^{-1}) (Baerga-Ortiz et al., 2004; De Genst et al., 2004; Maenaka et al., 2001; Roos et al., 1998; Zeder-Lutz et al., 1997). In contrast, binding of EGFR-ECD to hEGF is entropy-driven, which is in agreement with previously published ITC data on EGF binding to soluble EGFR-ECD (Alvarenga et al., 2012; Lemmon et al., 1997). Therefore, this study constitutes another example in which thermodynamic data from SPR studies are comparable to results obtained by ITC. In the first ITC study on EGFR-ECD binding to EGF, the investigators attributed the observed entropy gain to additional solvent release upon receptor dimerization, since the experiments were carried out at concentrations that would

allow for dimerization to occur (Lemmon et al., 1997). In contrast, the authors of the second study proposed conformational changes in the receptor extracellular domain as source of the measured entropy gain (Alvarenga et al., 2012). In their study the thermodynamic parameters obtained from SPR biosensor experiments did, however, not agree with the results from the ITC experiments, which they carried out in parallel. Interestingly, the thermodynamic data obtained for the receptor/ligand interaction in my own study, corresponded exactly to the ITC data in Alvarenga's study. This discrepancy could potentially originate from differences in the design between the two thermodynamic SPR analyses and emphasizes the importance of optimizing the experimental conditions in order to obtain meaningful data.

Correlation of thermodynamic and structural data

The observed entropy-driven binding of EGFR-ECD to its ligand EGF is supported by the physical composition of the binding interface reported in the x-ray crystal structure. The ligand/receptor interface consists of three contact sites, each of which is governed by hydrophobic forces and displays high degrees of shape complementarity, superior to what has been reported for antibody/antigen interfaces (Klein et al., 2008; Ogiso et al., 2002). The release of large amounts of solvent water molecules from these complementary hydrophobic surfaces could generate significant entropy contributions to the overall binding energy (Creighton, 1993; Tanford, 1978). Pre-shaped complementary interfaces are furthermore expected to result in decreased conformational entropic penalty upon binding (Todd et al., 2000). Currently, few reports on entropy-mediated interactions are found in the literature compared to a vast number of documented enthalpy-driven interactions (pdbcal, SCORPIO). Therefore, the opportunity to compare the thermodynamic binding profile of the EGFR-ECD/hEGF interaction to reports on other protein-protein interactions was very limited. In addition, most of the previously reported entropy-mediated interactions were formed between ligands of molecular weight below 1000 Da and their target proteins and as a result, this specific thermodynamic profile could potentially be more frequent in protein-peptide interactions. This thinking may, however, be biased since the

analysis of thermodynamic driving forces has traditionally been employed in research focused on the development of small molecule drug candidates. Nevertheless, there are some examples of similar entropy-mediated interactions for protein-protein complexes that are involved in biological processes. Entropy-mediated binding was, for example, shown for the association of thrombin (36 kDa) with thrombomodulin (74 kDa), as well as for the binding of the acidic transcriptional activators VP16 to the TATA binding protein (Baerga-Ortiz et al., 2004; Ferreira et al., 2005). Of note, the thrombomodulin protein consists of three EGF-like domains, which were proposed to mediate the interaction between thrombomodulin and thrombin (Baerga-Ortiz et al., 2000).

Transition state analysis

The individual thermodynamic parameters mediating the formation of the encounter and subsequent docking complexes were determined by Eyring analysis of the kinetic rate constants (k_a and k_d) of the receptor/ligand and receptor/sdAb interactions (Figure 4-5). The resulting binding profiles are illustrated in Figure 4-6. At association the molecules have to overcome a free energy barrier, in order to reach the transition state from which they decay into a complex at much lower free energy (Roos et al., 1998). The energetic barrier ($\Delta G°_{association}$) of the encounter step is similar for EGFR-ECD binding to immobilized hEGF and to immobilized EG2, which is in agreement with the comparable association rate constants (k_as) for the two complexes (Table 4). However, in contrast to hEGF, the affinity of EGFR-ECD to EG2 decreases at increasing temperature, suggesting that the individual thermodynamic driving forces mediating the formation of the encounter and docking complexes exhibit differential sensitivities to temperature change. Eyring analysis of EGFR-ECD/hEGF showed that both the encounter and the final complex are mediated by entropy. Interestingly, during the encounter step a large gain in entropy is needed to balance the large positive $\Delta H°_{association}$ value that disfavors the interaction. The docking step then demonstrates favorable enthalpy, which could be associated to the establishment of short-range electrostatic interactions at the ligand/receptor interface. In support of this hypothesis is the observation that binding events resulting in favorable ΔH are

rate limiting for the dissociation reaction and take place once the complex is formed (Baerga-Ortiz et al., 2004). Furthemore, pH sensitivity for EGF binding to EGFR-ECD was demonstrated in an SPR biosensor study by Ferguson *et al.*, who attributed this pH dependence to protonation of three histidine residues involved in the protein-ligand interface on subdomain III (Ferguson et al., 2003). These observations are in agreement with the formation short-range electrostatic interactions at the EGFR-ECD/hEGF interface upon docking complex formation (Schreiber, 2002). However, for EGFR-ECD binding to hEGF, entropy is also the major driving force of the docking step.

In contrast, the entropy contribution to the encounter step is significantly smaller for the EGFR-ECD/EG2 interaction, and enthalpy is shown to mediate the formation of the docking step. For this interaction, the observed entropy penalty during docking complex formation ($T\Delta S°_{dissociation}$) could originate from the establishment of short-range electrostatic interactions that subsequently decrease the conformational and rotational degrees of freedom of side chains in the receptor/sdAb interface ("rigidification").

The above results suggest that entropy and enthalpy effects are differentially influenced by temperature. In agreement with previous reports, large variations in dissociation rate constants (k_ds) are only observed in the enthalpy-mediated complex formation step of the EGFR-ECD/EG2 complex, 14-fold versus 1.4-fold for EGFR-ECD/hEGF, which indicates that factors affecting the enthalpy (e.g. van der Waals forces, hydrogen bonds, electrostatic forces) of an interaction are more temperature-sensitive than the entropy-mediated binding component of an interaction (i.e. hydrophobic interactions, desolvation) (Baerga-Ortiz et al., 2004; Ferreira et al., 2005; Lipschultz et al., 2002).

4.4.3 Analysis of the EGFR-ECD/hEGF and EGFR-ECD/EG2 interactions demonstrates minor contributions of long-range electrostatic forces to complex formation.

It is generally assumed that almost all protein-protein association events are governed to some extent by long-range electrostatic forces and that these forces

correlate with the amount of electrostatic surface potential found on the interacting proteins (Janin, 1995; Orning et al., 2006; Schreiber and Fersht, 1996; Tang et al., 2006). This mechanism, commonly known as electrostatic steering, contributes to the favorable entropy of interactions by maximizing the frequency of productive encounters (Janin, 1995). For example, the dominantly entropy-driven interaction of thrombin with thrombomodulin was shown to be highly sensitive to changes in ionic strength, which supports the idea that electrostatic steering is occurring in that case (Baerga-Ortiz et al., 2004; Baerga-Ortiz et al., 2000).

In my study, both, the receptor/ligand and the receptor/sdAb interaction demonstrated minor salt dependence in their association rate constants over the investigated range of salt concentrations (100 - 350 mM). I calculated that electrostatic steering contributed 0.31 kcal mol^{-1} and 0.09 kcal mol^{-1} for EGFR-ECD binding to hEGF and EG2, respectively. The slope of the Debye-Hückel plot is generally used for comparison of the ionic strength dependence between different protein-protein complexes. I obtained Debye-Hückel slopes of -0.48 for EGFR-ECD/hEGF and -0.07 for EGFR-ECD/EG2, whereas values of -0.5 to -6 were reported for other protein-protein interactions (Baerga-Ortiz et al., 2000). All of these complexes, however, demonstrated significantly faster association rate constants by at least one magnitude compared to the k_a-values observed for the EGF receptor-ligand and receptor-sdAb interactions investigated in my study (k_a = 3 x 10^5 M^{-1} s^{-1} for hEGF and k_a = 1.5 x 10^5 $M^{-1}s^{-1}$ for EG2, Table 3). Schreiber and Fersht, as well as Clore and colleagues demonstrated for several protein-protein complexes that long-range electrostatic interactions are essential for the encounter complex formation (Schreiber and Fersht, 1996; Tang et al., 2006). My findings are in agreement with this observation, since the interactions investigated in my study are characterized by slow association rates and correspondingly exhibited minor contributions of electrostatic steering to encounter complex formation. Nevertheless, it has been pointed out that interruption of salt bridges might be energetically neutral for the reason that charged residues interact favorably with polar solvents such as water and the net contribution will be

frequently equivalent, however, in this case the specificity of the interaction would be compromised (Davis et al., 1998). It is therefore possible that the contribution of electrostatic steering could be generally underestimated, since a decrease in specificity would be difficult to observe.

The moderate effect of ionic strength on EGF binding to EGFR over the investigated salt concentration agrees well with the evolutionary conserved biological role of EGF receptor signaling in species other than mammals (Yarden, 2001). EGF has been identified as a homolog to the Lin-3 ligand in the nematode *Caenorhabditis elegans* (Hill and Sternberg, 1992). Since *C. elegans* is dependent on osmoregulation to stabilize its shape in the absence of bone structures, it follows that under environmental conditions of different ionic strength the intracellular fluid is exposed to significant changes in osmolality (Choe and Strange, 2007). Hence, for EGFR signaling to function properly under these changing conditions it would be necessary that it is able to regulate its activity without being dependent on the ionic strength of the environment.

In summary, my data suggests that EGFR-ECD binding to EGF is predominantly mediated through entropy-driven thermodynamic forces. However, enthalpy contributions occur during the establishment of the final docking complex. Favorable surface complementarity of hydrophobic regions on the receptor/ligand interface and the release of solvent water could be contributing to the observed gain in entropy. In addition, fluctuations in protein dynamics have recently been proposed as sources of entropy that could mediate allosteric activation of receptor-ligand complexes. This compelling hypothesis will be discussed in the following paragraph.

Dynamic allostery

Ligand binding typically accomplishes a rigidification residues in the binding interface, however if a concomitant conformational change allows another area in the protein to become less densely packed that area may gain flexibility and thus compensate for the entropy loss upon binding (Kern and Zuiderweg, 2003). In support of this hypothesis, Williams and co-workers suggested that an endothermic profile is a direct result of an increase in disorder

within the receptor-ligand complex, for example, resulting from loosening of the receptor's internal structure, a change in its oligomerization state, or through the induction of conformational changes. Large entropic driving forces therefore favor the interaction and positive enthalpies are expected to occur. In a biological perspective these considerations are in agreement with the behavior expected from allosteric proteins, in which internal changes need to occur in order to alter the receptor configuration at a distant site (Williams et al., 2004).

The large favorable entropy observed for EGFR-ECD binding to immobilized hEGF in my study might not be generated solely by exchange of solvent water molecules in the binding site and surface complementarity, the possibility of a gain in conformational and/or dynamic entropy could also be considered. Previously, the large positive TΔS value found in the ITC study by Lemmon *et al.* was attributed to additional release of surface hydrogens upon receptor dimerization, however the experimental conditions in the present study are expected to primarily represent EGF binding to monomeric EGFR-ECD in the absence of dimer formation (Lemmon et al., 1997). The activation of the EGF receptor is considered a truly allosteric event, since ligand binding promotes conformational changes at distal sites in the protein, e.g. release of the intramolecular tether between subdomain II and IV of the extracellular domain. These ligand-induced changes promote receptor dimerization and activation of the intracellular domain. By measuring the amount of water released during ligand binding the entropy contribution from desolvation could be quantitatively assessed, which would allow for the estimation of the remaining entropic forces needed to drive complex formation (Baerga-Ortiz et al., 2004). In a study on endothermically-driven homo-oligomerization of chaperonin proteins it was shown that more than half of the contributed entropy gain was attributed to structural loosening and half to desolvation effects (Luke et al., 2005). This report furthermore suggests that entropy-driven complex formation events are likely to consist of more than one favorable entropic-force.

There is considerable experimental evidence in the current literature on EGF-induced signaling as well as on other allosteric receptor systems that would

support the presence of conformational, as well as, dynamic entropy forces during high affinity complex formation. Growing evidence points towards the existence of additional populations of intermediate conformational states of the EGFR extracellular domain. The presence of conformational, as well as, dynamic entropy forces during high affinity complex formation appears intuitive, since the extracellular domain was shown to fluctuate between two significantly different conformations, requiring large shifts and rotation between the individual subdomains (Figure 4-a). The most direct experimentally supported evidence, for additional conformational states came from studies on the binding properties of the monoclonal antibody (mAb) 806. MAb 806 was found to bind to subpopulations of receptor present on EGFR over-expressing cells, which lead to the conclusion that the antibody recognizes an intermediate conformational state (Sivasubramanian et al., 2006). Furthermore, single-molecule FRET imaging of drosophila EGFR extracellular domain indicated the presence of additional dimer configurations on the cell surface (Tynan et al., 2011). Also, Teramura and coworkers mathematically modeled the kinetics of EGF-binding to EGFR and, based on their findings, they proposed the presence of a novel kinetic intermediate during EGFR dimerization (Teramura et al., 2006). Lastly, early cross-linking studies also identified ligand-receptor contacts that could not be reconciled with any of the interactions seen in the two published crystal structures (Ogiso et al., 2002). Tobi and Bahar showed by Gaussian network modeling (GNM) that fluctuations in protein dynamics correlate with experimentally observed conformational changes and proposed that the intrinsic mobilities in a protein's structure near its substrate binding site potentially represents a general phenomenon in ligand-receptor interactions (Tobi and Bahar, 2005). In their study on tenascin binding to EGFR extracellular domain they showed that the ligand binding pocket of EGFR between domain I and III is highly mobile in the absence of ligand, allowing easy access and the occurrence of local rearrangements to accommodate ligand binding (De Crescenzo et al., 2000; Iyer et al., 2007). Current literature is therefore generally in agreement with the presence of multiple intermediate conformations. Furthermore, the idea that dynamic fluctuations are at

the basis of these conformational oscillations, is gaining ground. Already in 1984, Cooper and Dryden proposed that in allosteric proteins, ligand binding affects the frequencies and amplitudes of macromolecular thermal fluctuations across the molecule. Dynamic allostery would therefore be primarily entropy-mediated and cooperativity would be a key characteristic. They furthermore suggested that ligand-induced changes in both the conformation and the dynamics are to be expected, and even in cases where large conformational changes are known to occur, the underlying dynamic fluctuations may still be the actual source of the observed allosteric effect (Cooper and Dryden, 1984). It has furthermore been suggested by several investigators that dynamic activation of protein function is more common than thought (Henzler-Wildman and Kern, 2007; Henzler-Wildman et al., 2007; Lee and Wand, 2001; Tzeng and Kalodimos, 2009).

Recent technological advances in solution NMR spectroscopy have permitted for the experimental validation of the concept of entropy-driven allosteric interactions (Frederick et al., 2007). Several elastic models have been generated to predict the dynamics of allosteric effects based on the available structural information of beginning and endpoint of the conformational change (Daily and Gray, 2009; London et al., 2011).

It may furthermore be plausible to interpret the presence of ligand induced dynamic flexibility as a means of additional autoinhibitory control of receptor activation. This view was proposed previously by Kuriyan and colleagues who suggested that one role of the extracellular domain of the EGF receptor might be to hold the transmembrane helices apart in the predimerized form of the receptor to prevent formation of the activating asymmetric kinase dimers (Jura et al., 2009). In favor of this view is the observation that to date no EGFR mutants with the ability to promote dimerization in the absence of ligand have been found, which indicates that it is not a simple structural event, switching between an open and shut conformation, but a complex chain of thermodynamically linked events that mediate activation of the intracellular kinase. Furthermore, dynamic fluctuations would not need to be propagated across the cell membrane, but releasing the extracellular autoinhibitor would automatically activate the

intracellular domains. In favor of this view, is the observation that rotations in the TM dimer interface lead to periodic oscillations in kinase activity (Lu et al., 2010).

Interestingly, increased dynamic fluctuations upon ligand binding could potentially result in negative cooperativity in EGF binding to EGFR on cell surfaces (Williams et al., 2004). The direct detection of a contribution to negative cooperativity by dynamics has recently been provided by backbone amide NMR relaxation experiments performed for the anti-cooperative binding of CTP to the dimeric enzyme CT:glycerol-3-phosphate cytidylyltransferase (Stevens et al., 2001). Recent technological advances in experimentally assessing dynamic processes by ultrafast laser technologies, NMR, and low-temperature X-ray crystallography, together with steady increases in computational power now open a new field of studying the dynamic processes involved in allosteric protein interactions. It will be of interest to carry out these kinds of studies on the EGFR extracellular domain.

4.5 Conclusions

In agreement with the findings of Lemmon *et al*. and Alvarenga *et al.*, I confirmed in this study that the interaction between EGF and EGFR-ECD is entropy-driven and endothermic. The contribution of desolvation versus other entropic forces (rotational freedom or dynamic fluctuations) in ligand binding remains to be determined. In contrast, the EGFR-ECD/EG2 and EGFRvIII-ECD/EG2 interactions were enthalpy-driven and exothermic, which is in agreement with thermodynamic binding profiles typically observed for antibody-antigen interactions (Alvarenga et al., 2012; Baerga-Ortiz et al., 2004; De Genst et al., 2004; De Genst et al., 2006; Dumoulin et al., 2002; Roos et al., 1998). Further analysis of the transition states as well as of the salt dependence of the kinetic rate constants for receptor-ligand and receptor-antibody interactions suggested a minor role for long-range electrostatic forces in the binding and dissociation steps.

This study also contributes to the increasing number of published complexes for which thermodynamic and structural data is available and which will eventually

allow for large-scale, systematic investigation of the question how enthalpy and entropy are balanced during molecular recognition processes involving biological systems (Whitesides and Krishnamurthy, 2005). This information furthermore contributes to the understanding of thermodynamic parameters enabling their incorporation into scoring functions to predict affinities during lead optimization in drug development (Li et al., 2008).

Two models of full-length EGFR have recently been generated by the groups of Springer (Mi et al., 2008) and Leahy (Qiu et al., 2009); however, their investigations were largely focused on activation of the intracellular kinase. These full-length receptors would be interesting to explore in thermodynamic studies, in order to investigate the contribution of transmembrane and intracellular domains to the thermodynamic driving forces during ligand binding. Recent advances in SPR experimental design has allowed for studies on membrane-bound receptors (Mozsolits et al., 2003). It would be interesting to carry out studies of EGF-binding to membrane-bound EGFR to investigate whether the high and low affinity binding site, negative cooperativity and conformational entropy-driven binding would be observed.

Table 3. Kinetic data derived from Langmuir fitting of SPR data for EGFR-ECD/rhEGF, EGFR-ECD/EG2 sdAb and EGFRvIII-ECD/EG2 sdAb interactions.

The kinetic rate constants k_a and k_d and the affinity constant K_D are derived from global analysis of the SPR data to a 1:1 Langmuir binding model in the BIAevaluation software. In addition the affinities were determined by steady state analysis for the EGFR-ECD/hEGF interaction (K_D^S). The error bars represent the standard deviation from at least four independent data sets.

	T (°C)	k_a (10^5 M^{-1} s^{-1})	k_d (10^{-3} s^{-1})	K_D (10^{-9} M^{-1})	K_D^S (10^{-9} M^{-1})
EGFR/hEGF	5	0.3 ± 0.1	35.0 ± 3.3	1430 ± 372	1839 ± 959
	15	0.9 ± 0.1	37.3 ± 1.8	436 ± 95	927 ± 614
	20	1.0 ± 0.8	33.0 ± 3.4	425 ± 285	697 ± 496
	25	1.6 ± 0.9	40.8 ± 8.2	294 ± 133	415 ± 271
	32	3.1 ± 2.7	50.2 ± 7.4	239 ± 183	429 ± 317
EGFR/EG2	5	0.7 ± 0.2	0.9 ± 0.2	15 ± 5	
	15	1.0 ± 0.3	2.2 ± 0.7	23 ± 8	
	20	1.5 ± 0.1	4.0 ± 0.2	26 ± 2	ND
	25	1.4 ± 0.5	5.7 ± 1.2	45 ± 2	
	32	1.6 ± 0.6	13.0 ± 2.2	94 ± 4	
EGFRvIII/EG2	5	1.1 ± 0.1	1.2 ± 0.02	11 ± 1	
	15	1.7 ± 0.001	3.0 ± 0.1	18 ± 1	
	25	2.0 ± 0.1	6.4 ± 1.1	32 ± 3	ND
	32	2.0 ± 0.1	16.7 ± 3.2	91 ± 16	

Table 4. Calculated thermodynamic parameters for the EGFR-ECD/hEGF, EGFR-ECD/EG2 and EGFRvIII-ECD/EG2 interactions obtained from linear van't Hoff analysis.

The values for the transition states (°) were derived from Eyring analysis. The standard deviation is calculated from the thermodynamic values obtained from at least four independent data sets. Parameters determined independently by steady state analysis are shown for comparison (^{S}).

Thermodynamic parameters at 25°C	**EGFR/hEGF**	**EGFR/hEGF^{S}**	**EGFR/EG2**	**EGFRvIII/EG2**
ΔG (kcal mol^{-1})	-9.0 ± 0.2	-8.8 ± 0.3	-10.1 ± 0.2	-10.2 ± 0.1
ΔH (kcal mol^{-1})	13.4 ± 3.4	11.1 ± 1.9	-11.0 ± 1.1	-12.3 ± 0.4
$-T\Delta S$ (kcal mol^{-1})	-22.3 ± 3.6	-19.9 ± 2.3	0.8 ± 1.2	2.0 ± 0.4
$\Delta G°_{association}$ (kcal mol^{-1})	3.6 ± 0.4		3.7 ± 0.2	2.4 ± 1.8
$\Delta H°_{association}$ (kcal mol^{-1})	16.5 ± 3.7		6.6 ± 0.7	5.3 ± 1.4
$-TdS°_{association}$ (kcal mol^{-1})	-12.9 ± 4.0		-2.9 ± 0.7	-1.8 ± 1.5
$\Delta G°_{dissociation}$ (kcal mol^{-1})	12.6 ±0.1		13.7 ± 0.1	13.6 ± 0.1
$\Delta H°_{dissociation}$ (kcal mol^{-1})	5.3 ± 1.4		17.3 ± 1.2	16.4 ± 1.4
$-TdS°_{dissociation}$ (kcal mol^{-1})	7.3 ± 1.4		-3.5 ± 1.1	-2.8 ± 1.5

Table 5. Kinetic data obtained from the analysis of ionic strength dependence.

	NaCl (mM)	k_a (10^5 M^{-1} s^{-1})	k_d (10^{-3} s^{-1})	K_D (10^{-9} M^{-1})	2 $Z_A Z_B$	$\Delta G_{long\text{-}range}$ (kcal mol^{-1})
EGFR/hEGF	100	1.36 ± 0.12	54.57 ± 11.03	401 ± 46	-0.48	0.31
	150	1.26 ± 0.19	58.57 ± 8.09	467 ± 72		
	175	1.01 ± 0.22	59.13 ± 12.91	594 ± 129		
	200	0.88 ± 0.06	52.70 ± 1.80	603 ± 31		
	250	0.96 ± 0.17	61.75 ± 10.39	643 ± 7		
	350	1.03 ± 0.11	58.77 ± 5.31	577 ± 107		
EGFR/EG2	100	0.46 ± 0.01	4.61 ± 0.03	100 ± 1	-0.07	0.09
	150	0.48 ± 0.04	5.72 ± 0.14	120 ± 8		
	175	0.46 ± 0.01	6.15 ± 0.11	135 ± 2		
	200	0.47 ± 0.01	6.47 ± 0.03	139 ± 5		
	250	0.49 ± 0.02	7.08 ± 0.10	145 ± 6		
	350	0.43 ± 0.03	8.53 ± 0.39	198 ± 20		

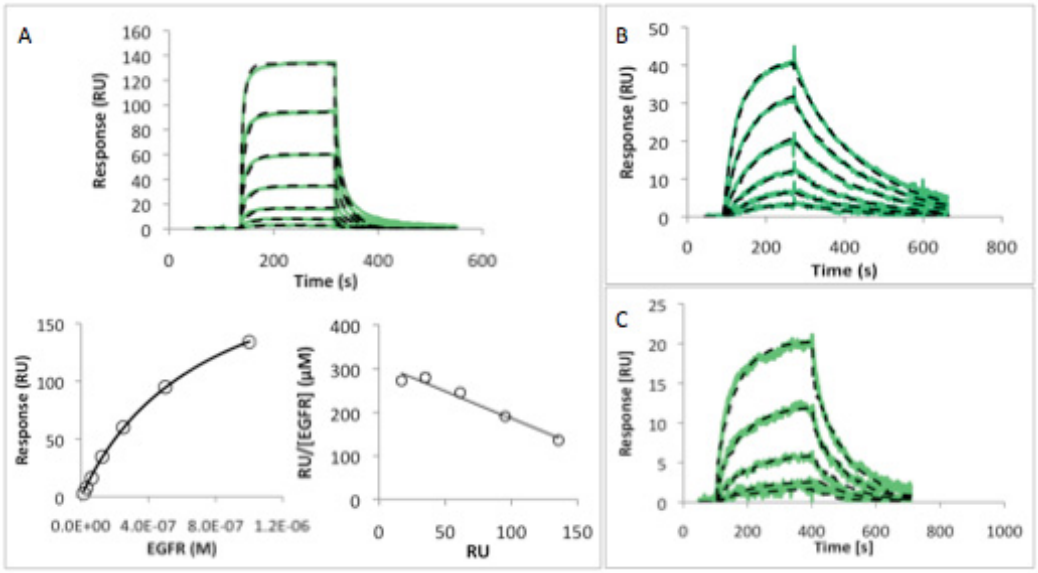

Figure 4-1. SPR biosensor analysis.

Representative sensorgrams showing the global fit of the SPR data to the 1:1 Langmuir binding model: EGFR-ECD/EGF (A), EGFR-ECD/EG2 sdAb (B) and EGFRvIII-ECD/EG2 sdAb (C). The receptor extracellular domain was injected at concentrations ranging from 1.5 nM to 1 µM over 57 RU rhEGF (A), 40 RU EG2 sdAb (D) and 24 RU EG2 sdAb (E) sensor chip surfaces. The interaction of EGFR with EGF was additionally determined using the steady state model in the BiaEvaluation software (left) as well as by linear regression according to the Scatchard theory (right). Affinities for EGFR/EGF of 197 nM , 295 nM and 333 nM were obtained by Langmuir, steady state and Scatchard analysis, respectively. EGFR and EGFRvIII bound EG2 with similar affinities of 76.8 ± 0.2 nM and 34.3 ± 0.3 nM.

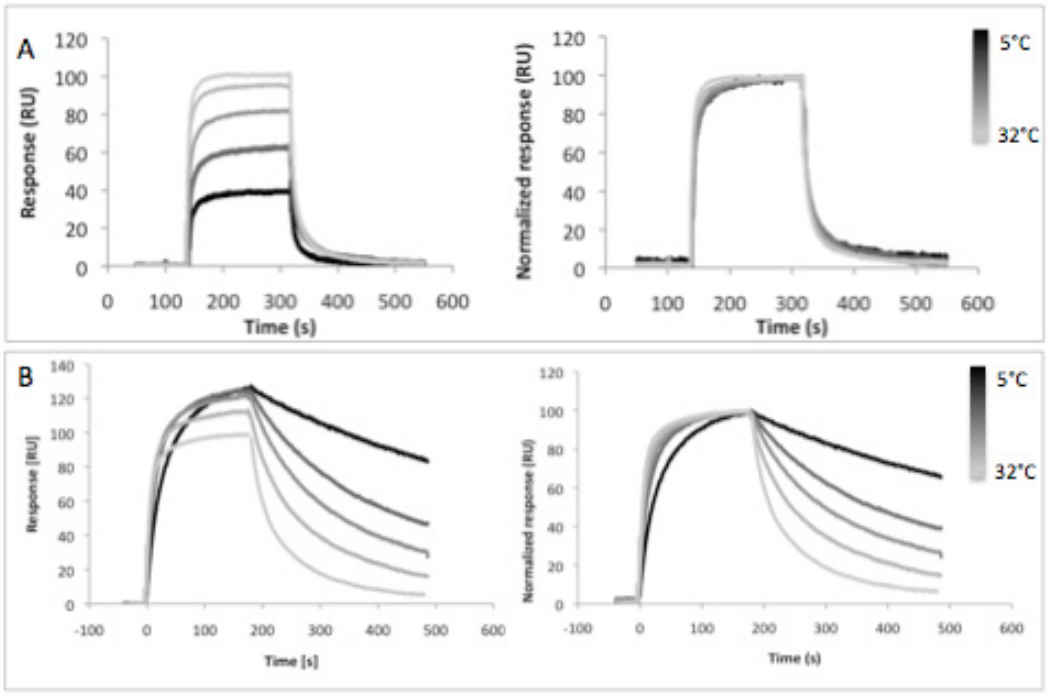

Figure 4-2. Temperature dependence of the EGFR-ECD/hEGF and EGFR-ECD/EG2 sdAb interactions

Representative sensorgrams showing binding of 500 nM EGFR-ECD to immobilized recombinant hEGF (A) and EG2 sdAb (B) for all five experimental temperatures (5 - 32°C); original data (left), normalized sensorgrams (right).

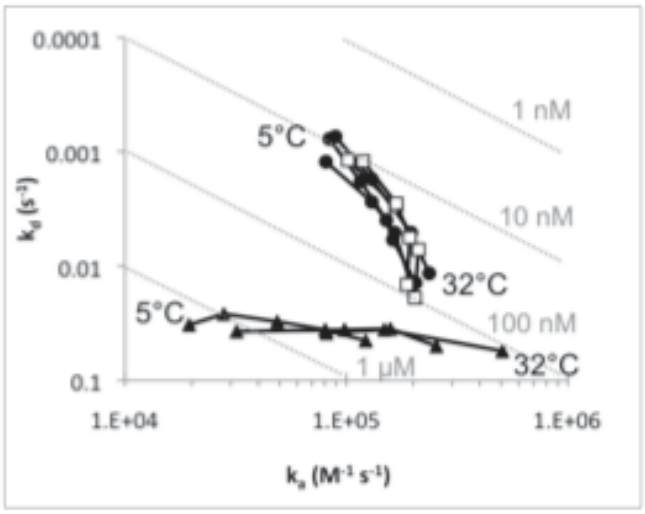

Figure 4-3. Temperature dependence of kinetic rate constants measured for the receptor-ligand and receptor-antibody interactions.

The kinetic parameters derived from the 1:1 Langmuir model of all three interactions (EGFR-ECD/hEGF (▲), EGFR-ECD/EG2 (●), EGFRvIII-ECD/EG2 (□) were determined at temperatures between 5 and 32°C.

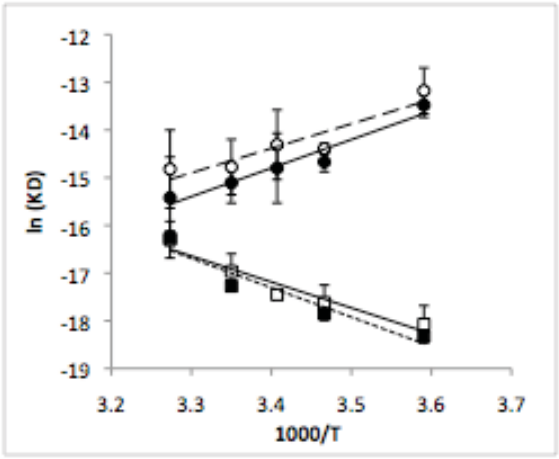

Figure 4-4. Linear van'Hoff plot assuming a temperature-independent ΔH.

Van't Hoff plots of SPR biosensor data derived from global fitting to the 1:1 Langmuir binding model: EGFR-ECD/EG2 (□), EGFRvIII-ECD/EG2 (■), EGFR-ECD/hEGF (●), and from fitting steady state affinities: EGFR-ECD/hEGF (○). ΔH was determined from $\ln K_D = \Delta H/RT + \Delta S/R$, ΔH/R being the slope. ΔG for the binding was calculated at 25°C from $\Delta G = RT \ln K_D$, where R = 1.987 cal K^{-1} mol^{-1} is the gas constant and T the temperature in Kelvin. The error bars represent the standard deviations of at least four, for EGFRvIII-ECD/EG2 two, independent determinations of each K_D-value.

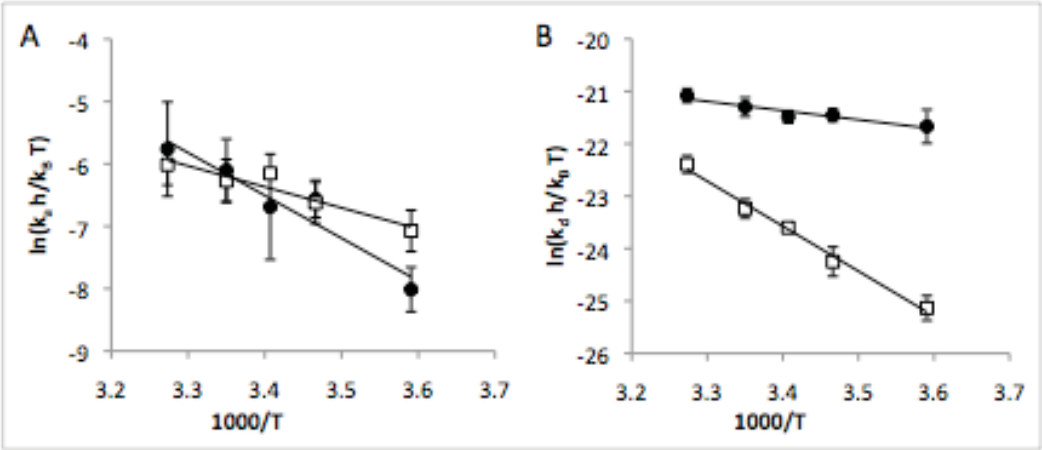

Figure 4-5. Eyring plots.

Eyring plots of the kinetic constants k_a (A) and k_d (B) determined by SPR biosensor analysis for the EGFR-ECD/hEGF (●) and EGFR-ECD/EG2 sdAb (□) interactions. The error bars are the standard deviation of at least four independent determinations of each kinetic constant.

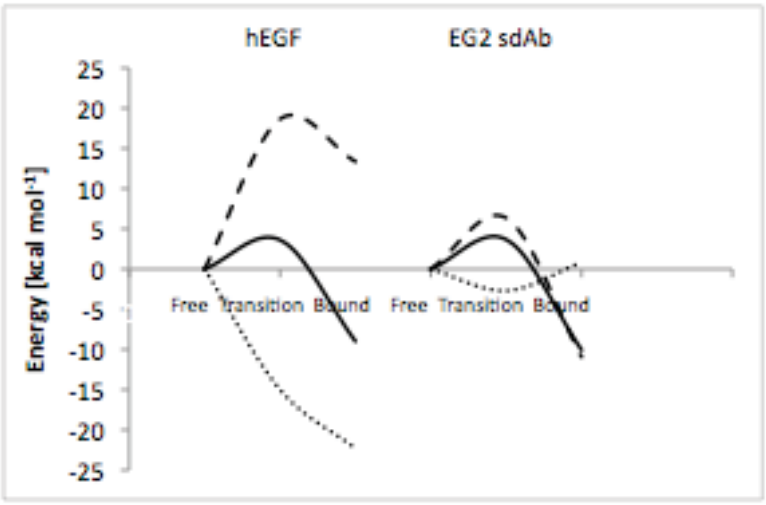

Figure 4-6. Graphical representation of transition state energies at 25°C derived from the van'Hoff and Eyring analyses.

Plots show ΔG (solid line), ΔH (dashed line) and -TΔS (dotted line) for EGFR-ECD interactions with hEGF and EG2 sdAb.

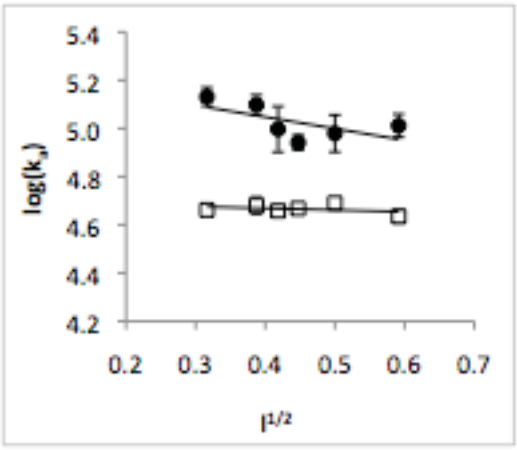

Figure 4-7. Ionic strength dependence of the association rate constants (k_a).

Ionic strength dependence of the k_a is represented by Debye- Hückel plots for the EGFR-ECD/hEGF (●) and EGFR-ECD/EG2 sdAb (□) interactions. The error bars on both plots are the standard deviation for three independent determinations of each k_a.

References

Abourbeh, G., Dissoki, S., Jacobson, O., Litchi, A., Ben Daniel, R., Laki, D., Levitzki, A., and Mishani, E. (2007). Evaluation of radiolabeled ML04, a putative irreversible inhibitor of epidermal growth factor receptor, as a bioprobe for PET imaging of EGFR-overexpressing tumors. Nucl Med Biol *34*, 55-70.

Adams, G.P., Schier, R., McCall, A.M., Simmons, H.H., Horak, E.M., Alpaugh, R.K., Marks, J.D., and Weiner, L.M. (2001). High affinity restricts the localization and tumor penetration of single-chain fv antibody molecules. Cancer Res *61*, 4750-4755.

Adams, K.E., Ke, S., Kwon, S., Liang, F., Fan, Z., Lu, Y., Hirschi, K., Mawad, M.E., Barry, M.A., and Sevick-Muraca, E.M. (2007). Comparison of visible and near-infrared wavelength-excitable fluorescent dyes for molecular imaging of cancer. J Biomed Opt *12*, 024017.

Al-Nedawi, K., Meehan, B., Micallef, J., Lhotak, V., May, L., Guha, A., and Rak, J. (2008). Intercellular transfer of the oncogenic receptor EGFRvIII by microvesicles derived from tumour cells. Nat Cell Biol *10*, 619-624.

Albrecht, H., Burke, P.A., Natarajan, A., Xiong, C.Y., Kalicinsky, M., DeNardo, G.L., and DeNardo, S.J. (2004). Production of soluble ScFvs with C-terminal-free thiol for site-specific conjugation or stable dimeric ScFvs on demand. Bioconjug Chem *15*, 16-26.

Alexis, F., Pridgen, E., Molnar, L.K., and Farokhzad, O.C. (2008). Factors affecting the clearance and biodistribution of polymeric nanoparticles. Mol Pharm *5*, 505-515.

Alvarado, D., Klein, D.E., and Lemmon, M.A. (2010). Structural basis for negative cooperativity in growth factor binding to an EGF receptor. Cell *142*, 568-579.

Alvarenga, M.L., Kikhney, J., Hannewald, J., Metzger, A.U., Steffens, K.J., Bomke, J., Krah, A., and Wegener, A. (2012). In-depth biophysical analysis of interactions between therapeutic antibodies and the extracellular domain of the epidermal growth factor receptor. Anal Biochem *421*, 138-151.

Arbabi Ghahroudi, M., Desmyter, A., Wyns, L., Hamers, R., and Muyldermans, S. (1997). Selection and identification of single domain antibody fragments from camel heavy-chain antibodies. FEBS Lett *414*, 521-526.

Arteaga, C.L. (2002). Overview of epidermal growth factor receptor biology and its role as a therapeutic target in human neoplasia. Semin Oncol *29*, 3-9.

Arvizo, R.R., Miranda, O.R., Thompson, M.A., Pabelick, C.M., Bhattacharya, R., Robertson, J.D., Rotello, V.M., Prakash, Y.S., and Mukherjee, P. (2010). Effect of nanoparticle surface charge at the plasma membrane and beyond. Nano Lett *10*, 2543-2548.

Azad, R., Gupta, R.K., Kumar, S., Pandey, C.M., Prasad, K.N., Husain, N., and Husain, M. (2003). Is neurocysticercosis a risk factor in coexistent intracranial disease? An MRI based study. J Neurol Neurosurg Psychiatry *74*, 359-361.

Bae, K.H., Chung, H.J., and Park, T.G. (2011). Nanomaterials for cancer therapy and imaging. Mol Cells *31*, 295-302.

Baerga-Ortiz, A., Bergqvist, S., Mandell, J.G., and Komives, E.A. (2004). Two different proteins that compete for binding to thrombin have opposite kinetic and thermodynamic profiles. Protein Sci *13*, 166-176.

Baerga-Ortiz, A., Rezaie, A.R., and Komives, E.A. (2000). Electrostatic dependence of the thrombin-thrombomodulin interaction. J Mol Biol *296*, 651-658.

Ballabh, P., Braun, A., and Nedergaard, M. (2004). The blood-brain barrier: an overview: structure, regulation, and clinical implications. Neurobiol Dis *16*, 1-13.

Barentsz, J., Takahashi, S., Oyen, W., Mus, R., De Mulder, P., Reznek, R., Oudkerk, M., and Mali, W. (2006). Commonly used imaging techniques for diagnosis and staging. J Clin Oncol *24*, 3234-3244.

Becerril, B., Poul, M.A., and Marks, J.D. (1999). Toward selection of internalizing antibodies from phage libraries. Biochem Biophys Res Commun *255*, 386-393.

Behr, T.M., Goldenberg, D.M., and Becker, W. (1998). Reducing the renal uptake of radiolabeled antibody fragments and peptides for diagnosis and therapy: present status, future prospects and limitations. Eur J Nucl Med *25*, 201-212.

Beier, D., Rohrl, S., Pillai, D.R., Schwarz, S., Kunz-Schughart, L.A., Leukel, P., Proescholdt, M., Brawanski, A., Bogdahn, U., Trampe-Kieslich, A*., et al.* (2008). Temozolomide preferentially depletes cancer stem cells in glioblastoma. Cancer Res *68*, 5706-5715.

Bell, A., Wang, Z.J., Arbabi-Ghahroudi, M., Chang, T.A., Durocher, Y., Trojahn, U., Baardsnes, J., Jaramillo, M.L., Li, S., Baral, T.N*., et al.* (2009). Differential tumor-targeting abilities of three single-domain antibody formats. Cancer Lett.

Bell, A., Wang, Z.J., Arbabi-Ghahroudi, M., Chang, T.A., Durocher, Y., Trojahn, U., Baardsnes, J., Jaramillo, M.L., Li, S., Baral, T.N*., et al.* (2010). Differential tumor-targeting abilities of three single-domain antibody formats. Cancer Lett *289*, 81-90.

Benhabbour, S.R., Luft, J.C., Kim, D., Jain, A., Wadhwa, S., Parrott, M.C., Liu, R., Desimone, J.M., and Mumper, R.J. (2011). In vitro and in vivo assessment of targeting lipid-based nanoparticles to the epidermal growth factor-receptor (EGFR) using a novel Heptameric Z(EGFR) domain. J Control Release.

Bertorelle, F., Wilhelm, C., Roger, J., Gazeau, F., Menager, C., and Cabuil, V. (2006). Fluorescence-modified superparamagnetic nanoparticles: intracellular uptake and use in cellular imaging. Langmuir *22*, 5385-5391.

Bertrand, N., and Leroux, J.C. (2011). The journey of a drug-carrier in the body: An anatomo-physiological perspective. J Control Release.

Besenicar, M., Macek, P., Lakey, J.H., and Anderluh, G. (2006). Surface plasmon resonance in protein-membrane interactions. Chem Phys Lipids *141*, 169-178.

Bhattacharyya, S., Bhattacharya, R., Curley, S., McNiven, M.A., and Mukherjee, P. (2010). Nanoconjugation modulates the trafficking and mechanism of antibody induced receptor endocytosis. Proc Natl Acad Sci U S A *107*, 14541-14546.

Biernat, W., Huang, H., Yokoo, H., Kleihues, P., and Ohgaki, H. (2004). Predominant expression of mutant EGFR (EGFRvIII) is rare in primary glioblastomas. Brain Pathol *14*, 131-136.

Binello, E., and Germano, I.M. (2009). Tonsillary carcinoma after temozolomide treatment for glioblastoma multiforme: treatment-related or dual-pathology? J Neurooncol *94*, 145-148.

Bolton, A.E., and Hunter, W.M. (1973). The labelling of proteins to high specific radioactivities by conjugation to a 125I-containing acylating agent. Biochem J *133*, 529-539.

Brown, P.M., Debanne, M.T., Grothe, S., Bergsma, D., Caron, M., Kay, C., and O'Connor-McCourt, M.D. (1994). The extracellular domain of the epidermal growth factor receptor. Studies on the affinity and stoichiometry of binding, receptor dimerization and a binding-domain mutant. Eur J Biochem *225*, 223-233.

Bulte, J.W., and Kraitchman, D.L. (2004). Iron oxide MR contrast agents for molecular and cellular imaging. NMR Biomed *17*, 484-499.

Burgess, A.W. (2008). EGFR family: structure physiology signalling and therapeutic targets. Growth Factors *26*, 263-274.

Burgess, A.W., Cho, H.S., Eigenbrot, C., Ferguson, K.M., Garrett, T.P., Leahy, D.J., Lemmon, M.A., Sliwkowski, M.X., Ward, C.W., and Yokoyama, S. (2003). An open-and-shut case? Recent insights into the activation of EGF/ErbB receptors. Mol Cell *12*, 541-552.

Burtea, C., Laurent, S., Vander Elst, L., and Muller, R.N. (2008). Contrast agents: magnetic resonance. Handb Exp Pharmacol, 135-165.

Campa, M.J., Kuan, C.T., O'Connor-McCourt, M.D., Bigner, D.D., and Patz, E.F., Jr. (2000). Design of a novel small peptide targeted against a tumor-specific receptor. Biochem Biophys Res Commun *275*, 631-636.

Carraway, K.L., 3rd, and Cerione, R.A. (1993). Fluorescent-labeled growth factor molecules serve as probes for receptor binding and endocytosis. Biochemistry *32*, 12039-12045.

Carter, P., and Merchant, A.M. (1997). Engineering antibodies for imaging and therapy. Curr Opin Biotechnol *8*, 449-454.

Carter, P.J. (2006). Potent antibody therapeutics by design. Nat Rev Immunol *6*, 343-357.

Cavenee, W.K. (2002). Genetics and new approaches to cancer therapy. Carcinogenesis *23*, 683-686.

Chapman, A.P. (2002). PEGylated antibodies and antibody fragments for improved therapy: a review. Adv Drug Deliv Rev *54*, 531-545.

Chen, K., Xie, J., Xu, H., Behera, D., Michalski, M.H., Biswal, S., Wang, A., and Chen, X. (2009a). Triblock copolymer coated iron oxide nanoparticle conjugate for tumor integrin targeting. Biomaterials *30*, 6912-6919.

Chen, L., Merzlyakov, M., Cohen, T., Shai, Y., and Hristova, K. (2009b). Energetics of ErbB1 transmembrane domain dimerization in lipid bilayers. Biophys J *96*, 4622-4630.

Chen, P.I., Kong, C., Su, X., and Stahl, P.D. (2009c). Rab5 isoforms differentially regulate the trafficking and degradation of epidermal growth factor receptors. J Biol Chem *284*, 30328-30338.

Chen, Z., Xu, R., Zhang, Y., and Gu, N. (2008). Effects of proteins from culture medium on surface property of silanes- functionalized magnetic nanoparticles. Nanoscale Res Lett *4*, 204-209.

Chertok, B., Moffat, B.A., David, A.E., Yu, F., Bergemann, C., Ross, B.D., and Yang, V.C. (2008). Iron oxide nanoparticles as a drug delivery vehicle for MRI monitored magnetic targeting of brain tumors. Biomaterials *29*, 487-496.

Chithrani, B.D., Ghazani, A.A., and Chan, W.C. (2006). Determining the size and shape dependence of gold nanoparticle uptake into mammalian cells. Nano Lett *6*, 662-668.

Choe, K.P., and Strange, K. (2007). Molecular and genetic characterization of osmosensing and signal transduction in the nematode Caenorhabditis elegans. FEBS J *274*, 5782-5789.

Choi, J.Y., Lee, S.H., Na, H.B., An, K., Hyeon, T., and Seo, T.S. (2010). In vitro cytotoxicity screening of water-dispersible metal oxide nanoparticles in human cell lines. Bioprocess Biosyst Eng *33*, 21-30.

Ciardiello, F., and Tortora, G. (2008). EGFR antagonists in cancer treatment. N Engl J Med *358*, 1160-1174.

Citri, A., and Yarden, Y. (2006). EGF-ERBB signalling: towards the systems level. Nat Rev Mol Cell Biol *7*, 505-516.

Claes, A., Gambarota, G., Hamans, B., van Tellingen, O., Wesseling, P., Maass, C., Heerschap, A., and Leenders, W. (2008). Magnetic resonance imaging-based detection of glial brain tumors in mice after antiangiogenic treatment. Int J Cancer *122*, 1981-1986.

Cochran, J.R., Kim, Y.S., Olsen, M.J., Bhandari, R., and Wittrup, K.D. (2004). Domain-level antibody epitope mapping through yeast surface display of epidermal growth factor receptor fragments. J Immunol Methods *287*, 147-158.

Cooper, A., and Dryden, D.T. (1984). Allostery without conformational change. A plausible model. Eur Biophys J *11*, 103-109.

Coppieters, K., Dreier, T., Silence, K., de Haard, H., Lauwereys, M., Casteels, P., Beirnaert, E., Jonckheere, H., Van de Wiele, C., Staelens, L.*, et al.* (2006). Formatted anti-tumor necrosis factor alpha VHH proteins derived from camelids show superior potency and targeting to inflamed joints in a murine model of collagen-induced arthritis. Arthritis Rheum *54*, 1856-1866.

Corsi, K., Chellat, F., Yahia, L., and Fernandes, J.C. (2003). Mesenchymal stem cells, MG63 and HEK293 transfection using chitosan-DNA nanoparticles. Biomaterials *24*, 1255-1264.

Cortez-Retamozo, V., Backmann, N., Senter, P.D., Wernery, U., De Baetselier, P., Muyldermans, S., and Revets, H. (2004). Efficient cancer therapy with a nanobody-based conjugate. Cancer Res *64*, 2853-2857.

Cortez-Retamozo, V., Lauwereys, M., Hassanzadeh Gh, G., Gobert, M., Conrath, K., Muyldermans, S., De Baetselier, P., and Revets, H. (2002). Efficient tumor targeting by single-domain antibody fragments of camels. Int J Cancer *98*, 456-462.

Creighton, T.E. (1993). Proteins: Structures and Molecular Properties., Vol 2nd Ed. (Freeman, New York).

Cvrljevic, A.N., Akhavan, D., Wu, M., Martinello, P., Furnari, F.B., Johnston, A.J., Guo, D., Pike, L., Cavenee, W.K., Scott, A.M.*, et al.* (2011). Activation of Src induces mitochondrial localisation of de2-7EGFR (EGFRvIII) in glioma cells: implications for glucose metabolism. J Cell Sci *124*, 2938-2950.

Cymer, F., and Schneider, D. (2010). Transmembrane helix-helix interactions involved in ErbB receptor signaling. Cell Adh Migr *4*, 299-312.

Daily, M.D., and Gray, J.J. (2009). Allosteric communication occurs via networks of tertiary and quaternary motions in proteins. PLoS Comput Biol *5*, e1000293.

Dard, N., and Peter, M. (2006). Scaffold proteins in MAP kinase signaling: more than simple passive activating platforms. Bioessays *28*, 146-156.

Darling, R.J., Kuchibhotla, U., Glaesner, W., Micanovic, R., Witcher, D.R., and Beals, J.M. (2002). Glycosylation of erythropoietin affects receptor binding kinetics: role of electrostatic interactions. Biochemistry *41*, 14524-14531.

Davis, S.J., Davies, E.A., Tucknott, M.G., Jones, E.Y., and van der Merwe, P.A. (1998). The role of charged residues mediating low affinity protein-protein recognition at the cell surface by CD2. Proc Natl Acad Sci U S A *95*, 5490-5494.

Dawson, J.P., Berger, M.B., Lin, C.C., Schlessinger, J., Lemmon, M.A., and Ferguson, K.M. (2005). Epidermal growth factor receptor dimerization and activation require ligand-induced conformational changes in the dimer interface. Mol Cell Biol *25*, 7734-7742.

Dawson, J.P., Bu, Z., and Lemmon, M.A. (2007). Ligand-induced structural transitions in ErbB receptor extracellular domains. Structure *15*, 942-954.

Day, Y.S., Baird, C.L., Rich, R.L., and Myszka, D.G. (2002). Direct comparison of binding equilibrium, thermodynamic, and rate constants determined by surface- and solution-based biophysical methods. Protein Sci *11*, 1017-1025.

De Crescenzo, G., Grothe, S., Lortie, R., Debanne, M.T., and O'Connor-McCourt, M. (2000). Real-time kinetic studies on the interaction of transforming growth factor alpha with the epidermal growth factor receptor extracellular domain reveal a conformational change model. Biochemistry *39*, 9466-9476.

De Genst, E., Handelberg, F., Van Meirhaeghe, A., Vynck, S., Loris, R., Wyns, L., and Muyldermans, S. (2004). Chemical basis for the affinity maturation of a camel single domain antibody. J Biol Chem *279*, 53593-53601.

De Genst, E., Saerens, D., Muyldermans, S., and Conrath, K. (2006). Antibody repertoire development in camelids. Dev Comp Immunol *30*, 187-198.

De Groeve, K., Deschacht, N., De Koninck, C., Caveliers, V., Lahoutte, T., Devoogdt, N., Muyldermans, S., De Baetselier, P., and Raes, G. (2010). Nanobodies as tools for in vivo imaging of specific immune cell types. J Nucl Med *51*, 782-789.

de Mol, N.J., Dekker, F.J., Broutin, I., Fischer, M.J., and Liskamp, R.M. (2005). Surface plasmon resonance thermodynamic and kinetic analysis as a strategic tool in drug design. Distinct ways for phosphopeptides to plug into Src- and Grb2 SH2 domains. J Med Chem *48*, 753-763.

Decanniere, K., Desmyter, A., Lauwereys, M., Ghahroudi, M.A., Muyldermans, S., and Wyns, L. (1999). A single-domain antibody fragment in complex with RNase A: non-canonical loop structures and nanomolar affinity using two CDR loops. Structure *7*, 361-370.

Decanniere, K., Muyldermans, S., and Wyns, L. (2000). Canonical antigen-binding loop structures in immunoglobulins: more structures, more canonical classes? J Mol Biol *300*, 83-91.

Dechant, M., Weisner, W., Berger, S., Peipp, M., Beyer, T., Schneider-Merck, T., Lammerts van Bueren, J.J., Bleeker, W.K., Parren, P.W., van de Winkel, J.G., *et al.* (2008). Complement-dependent tumor cell lysis triggered by combinations of epidermal growth factor receptor antibodies. Cancer Res *68*, 4998-5003.

Delgado, C., Pedley, R.B., Herraez, A., Boden, R., Boden, J.A., Keep, P.A., Chester, K.A., Fisher, D., Begent, R.H., and Francis, G.E. (1996). Enhanced tumour specificity of an anti-carcinoembrionic antigen Fab' fragment by poly(ethylene glycol) (PEG) modification. Br J Cancer *73*, 175-182.

Delikatny, E.J., and Poptani, H. (2005). MR techniques for in vivo molecular and cellular imaging. Radiol Clin North Am *43*, 205-220.

Dennis, M.S., Jin, H., Dugger, D., Yang, R., McFarland, L., Ogasawara, A., Williams, S., Cole, M.J., Ross, S., and Schwall, R. (2007). Imaging tumors with an albumin-binding Fab, a novel tumor-targeting agent. Cancer Res *67*, 254-261.

Dennis, M.S., Zhang, M., Meng, Y.G., Kadkhodayan, M., Kirchhofer, D., Combs, D., and Damico, L.A. (2002). Albumin binding as a general strategy for improving the pharmacokinetics of proteins. J Biol Chem *277*, 35035-35043.

Deyev, S.M., and Lebedenko, E.N. (2008). Multivalency: the hallmark of antibodies used for optimization of tumor targeting by design. Bioessays *30*, 904-918.

Dhalluin, C., Ross, A., Huber, W., Gerber, P., Brugger, D., Gsell, B., and Senn, H. (2005). Structural, kinetic, and thermodynamic analysis of the binding of the 40 kDa PEG-interferon-alpha2a and its individual positional isomers to the extracellular domain of the receptor IFNAR2. Bioconjug Chem *16*, 518-527.

Diagaradjane, P., Orenstein-Cardona, J.M., Colon-Casasnovas, N.E., Deorukhkar, A., Shentu, S., Kuno, N., Schwartz, D.L., Gelovani, J.G., and Krishnan, S. (2008). Imaging epidermal growth factor receptor expression in vivo: pharmacokinetic and biodistribution characterization of a bioconjugated quantum dot nanoprobe. Clin Cancer Res *14*, 731-741.

Domagala, T., Konstantopoulos, N., Smyth, F., Jorissen, R.N., Fabri, L., Geleick, D., Lax, I., Schlessinger, J., Sawyer, W., Howlett, G.J., *et al.* (2000). Stoichiometry, kinetic and binding analysis of the interaction between epidermal growth factor (EGF) and the extracellular domain of the EGF receptor. Growth Factors *18*, 11-29.

Downward, J., Yarden, Y., Mayes, E., Scrace, G., Totty, N., Stockwell, P., Ullrich, A., Schlessinger, J., and Waterfield, M.D. (1984). Close similarity of epidermal growth factor receptor and v-erb-B oncogene protein sequences. Nature *307*, 521-527.

Dreher, M.R., Liu, W., Michelich, C.R., Dewhirst, M.W., Yuan, F., and Chilkoti, A. (2006). Tumor vascular permeability, accumulation, and penetration of macromolecular drug carriers. J Natl Cancer Inst *98*, 335-344.

Dubertret, B., Calame, M., and Libchaber, A.J. (2001). Single-mismatch detection using gold-quenched fluorescent oligonucleotides. Nat Biotechnol *19*, 365-370.

Dumoulin, M., Conrath, K., Van Meirhaeghe, A., Meersman, F., Heremans, K., Frenken, L.G., Muyldermans, S., Wyns, L., and Matagne, A. (2002). Single-domain antibody fragments with high conformational stability. Protein Sci *11*, 500-515.

Dunn, S.E., Brindley, A., Davis, S.S., Davies, M.C., and Illum, L. (1994). Polystyrene-poly (ethylene glycol) (PS-PEG2000) particles as model systems for site specific drug delivery. 2. The effect of PEG surface density on the in vitro cell interaction and in vivo biodistribution. Pharm Res *11*, 1016-1022.

Ekstrand, A.J., Sugawa, N., James, C.D., and Collins, V.P. (1992). Amplified and rearranged epidermal growth factor receptor genes in human glioblastomas reveal deletions of sequences encoding portions of the N- and/or C-terminal tails. Proc Natl Acad Sci U S A *89*, 4309-4313.

Elleman, T.C., Domagala, T., McKern, N.M., Nerrie, M., Lonnqvist, B., Adams, T.E., Lewis, J., Lovrecz, G.O., Hoyne, P.A., Richards, K.M.*, et al.* (2001). Identification of a determinant of epidermal growth factor receptor ligand-binding specificity using a truncated, high-affinity form of the ectodomain. Biochemistry *40*, 8930-8939.

Els Conrath, K., Lauwereys, M., Wyns, L., and Muyldermans, S. (2001). Camel single-domain antibodies as modular building units in bispecific and bivalent antibody constructs. J Biol Chem *276*, 7346-7350.

Ely, L.K., Beddoe, T., Clements, C.S., Matthews, J.M., Purcell, A.W., Kjer-Nielsen, L., McCluskey, J., and Rossjohn, J. (2006). Disparate thermodynamics governing T cell receptor-MHC-I interactions implicate extrinsic factors in guiding MHC restriction. Proc Natl Acad Sci U S A *103*, 6641-6646.

Emerich, D.F., and Thanos, C.G. (2007). Targeted nanoparticle-based drug delivery and diagnosis. J Drug Target *15*, 163-183.

Engelman, J.A., and Cantley, L.C. (2008). A sweet new role for EGFR in cancer. Cancer Cell *13*, 375-376.

Enochs, W.S., Harsh, G., Hochberg, F., and Weissleder, R. (1999). Improved delineation of human brain tumors on MR images using a long-circulating, superparamagnetic iron oxide agent. J Magn Reson Imaging *9*, 228-232.

Ewert, S., Cambillau, C., Conrath, K., and Pluckthun, A. (2002). Biophysical properties of camelid V(HH) domains compared to those of human V(H)3 domains. Biochemistry *41*, 3628-3636.

Fahmy, T.M., Samstein, R.M., Harness, C.C., and Mark Saltzman, W. (2005). Surface modification of biodegradable polyesters with fatty acid conjugates for improved drug targeting. Biomaterials *26*, 5727-5736.

Fang, L., Barekati, Z., Zhang, B., Liu, Z., and Zhong, X.Y. (2011). Targeted therapy in breast cancer: what's new? Swiss Med Wkly *141*, w13231.

Farin, K., Di Segni, A., Mor, A., and Pinkas-Kramarski, R. (2009). Structure-function analysis of nucleolin and ErbB receptors interactions. PLoS One *4*, e6128.

Fearon, D.T., Kaneko, I., and Thomson, G.G. (1981). Membrane distribution and adsorptive endocytosis by C3b receptors on human polymorphonuclear leukocytes. J Exp Med *153*, 1615-1628.

Felder, S., Zhou, M., Hu, P., Urena, J., Ullrich, A., Chaudhuri, M., White, M., Shoelson, S.E., and Schlessinger, J. (1993). SH2 domains exhibit high-affinity binding to tyrosine-phosphorylated peptides yet also exhibit rapid dissociation and exchange. Mol Cell Biol *13*, 1449-1455.

Feng, B., Tomizawa, K., Michiue, H., Miyatake, S., Han, X.J., Fujimura, A., Seno, M., Kirihata, M., and Matsui, H. (2009). Delivery of sodium borocaptate to glioma cells using immunoliposome conjugated with anti-EGFR antibodies by ZZ-His. Biomaterials *30*, 1746-1755.

Ferguson, K.M. (2004). Active and inactive conformations of the epidermal growth factor receptor. Biochem Soc Trans *32*, 742-745.

Ferguson, K.M., Berger, M.B., Mendrola, J.M., Cho, H.S., Leahy, D.J., and Lemmon, M.A. (2003). EGF activates its receptor by removing interactions that autoinhibit ectodomain dimerization. Mol Cell *11*, 507-517.

Ferguson, K.M., Darling, P.J., Mohan, M.J., Macatee, T.L., and Lemmon, M.A. (2000). Extracellular domains drive homo- but not hetero-dimerization of erbB receptors. EMBO J *19*, 4632-4643.

Ferreira, M.E., Hermann, S., Prochasson, P., Workman, J.L., Berndt, K.D., and Wright, A.P. (2005). Mechanism of transcription factor recruitment by acidic activators. J Biol Chem *280*, 21779-21784.

Foroglou, N., Zamani, A., and Black, P. (2009). Intra-operative MRI (iop-MR) for brain tumour surgery. Br J Neurosurg *23*, 14-22.

Frederick, K.K., Marlow, M.S., Valentine, K.G., and Wand, A.J. (2007). Conformational entropy in molecular recognition by proteins. Nature *448*, 325-329.

Frederick, L., Wang, X.Y., Eley, G., and James, C.D. (2000). Diversity and frequency of epidermal growth factor receptor mutations in human glioblastomas. Cancer Res *60*, 1383-1387.

Frenken, L.G., van der Linden, R.H., Hermans, P.W., Bos, J.W., Ruuls, R.C., de Geus, B., and Verrips, C.T. (2000). Isolation of antigen specific llama VHH antibody fragments and their high level secretion by Saccharomyces cerevisiae. J Biotechnol *78*, 11-21.

Freyer, M.W., Buscaglia, R., Nguyen, B., Wilson, W.D., and Lewis, E.A. (2006). Binding of netropsin and 4,6-diamidino-2-phenylindole to an A2T2 DNA hairpin: a comparison of biophysical techniques. Anal Biochem *355*, 259-266.

Friedman, M., Orlova, A., Johansson, E., Eriksson, T.L., Hoiden-Guthenberg, I., Tolmachev, V., Nilsson, F.Y., and Stahl, S. (2008). Directed evolution to low nanomolar affinity of a tumor-targeting epidermal growth factor receptor-binding affibody molecule. J Mol Biol *376*, 1388-1402.

Funaro, A., Horenstein, A.L., Santoro, P., Cinti, C., Gregorini, A., and Malavasi, F. (2000). Monoclonal antibodies and therapy of human cancers. Biotechnol Adv *18*, 385-401.

Gadji, M., Crous, A.M., Fortin, D., Krcek, J., Torchia, M., Mai, S., Drouin, R., and Klonisch, T. (2009). EGF receptor inhibitors in the treatment of glioblastoma multiform: old clinical allies and newly emerging therapeutic concepts. Eur J Pharmacol *625*, 23-30.

Gainkam, L.O., Huang, L., Caveliers, V., Keyaerts, M., Hernot, S., Vaneycken, I., Vanhove, C., Revets, H., De Baetselier, P., and Lahoutte, T. (2008). Comparison of the biodistribution and tumor targeting of two 99mTc-labeled anti-EGFR nanobodies in mice, using pinhole SPECT/micro-CT. J Nucl Med *49*, 788-795.

Gambarota, G., and Leenders, W. (2011). Characterization of tumor vasculature in mouse brain by USPIO contrast-enhanced MRI. Methods Mol Biol *771*, 477-487.

Gan, H.K., Kaye, A.H., and Luwor, R.B. (2009). The EGFRvIII variant in glioblastoma multiforme. J Clin Neurosci *16*, 748-754.

Gao, X., Cui, Y., Levenson, R.M., Chung, L.W., and Nie, S. (2004). In vivo cancer targeting and imaging with semiconductor quantum dots. Nat Biotechnol *22*, 969-976.

Garrett, T.P., Burgess, A.W., Gan, H.K., Luwor, R.B., Cartwright, G., Walker, F., Orchard, S.G., Clayton, A.H., Nice, E.C., Rothacker, J.*, et al.* (2009). Antibodies specifically targeting a locally misfolded region of tumor associated EGFR. Proc Natl Acad Sci U S A *106*, 5082-5087.

Getz, E.B., Xiao, M., Chakrabarty, T., Cooke, R., and Selvin, P.R. (1999). A comparison between the sulfhydryl reductants tris(2-carboxyethyl)phosphine and dithiothreitol for use in protein biochemistry. Anal Biochem *273*, 73-80.

Gilmore, J.L., Gonterman, R.M., Menon, K., Lorch, G., Riese, D.J., 2nd, Robling, A., and Foley, J. (2009). Reconstitution of amphiregulin-epidermal growth factor receptor signaling in lung squamous cell carcinomas activates PTHrP gene expression and contributes to cancer-mediated diseases of the bone. Mol Cancer Res *7*, 1714-1728.

Glaser, R.W. (1993). Antigen-antibody binding and mass transport by convection and diffusion to a surface: a two-dimensional computer model of binding and dissociation kinetics. Anal Biochem *213*, 152-161.

Glaus, C., Rossin, R., Welch, M.J., and Bao, G. (2010). In vivo evaluation of (64)Cu-labeled magnetic nanoparticles as a dual-modality PET/MR imaging agent. Bioconjug Chem *21*, 715-722.

Goldstein, N.I., Prewett, M., Zuklys, K., Rockwell, P., and Mendelsohn, J. (1995). Biological efficacy of a chimeric antibody to the epidermal growth factor receptor in a human tumor xenograft model. Clin Cancer Res *1*, 1311-1318.

Gottlin, E.B., Xiangrong, G., Pegram, C., Cannedy, A., Campa, M.J., and Patz, E.F., Jr. (2009). Isolation of novel EGFR-specific VHH domains. J Biomol Screen *14*, 77-85.

Graham, J., Muhsin, M., and Kirkpatrick, P. (2004). Cetuximab. Nat Rev Drug Discov *3*, 549-550.

Grandal, M.V., Zandi, R., Pedersen, M.W., Willumsen, B.M., van Deurs, B., and Poulsen, H.S. (2007). EGFRvIII escapes down-regulation due to impaired internalization and sorting to lysosomes. Carcinogenesis *28*, 1408-1417.

Greenfield, C., Hiles, I., Waterfield, M.D., Federwisch, M., Wollmer, A., Blundell, T.L., and McDonald, N. (1989). Epidermal growth factor binding induces a conformational change in the external domain of its receptor. EMBO J *8*, 4115-4123.

Guillamo, J.S., de Bouard, S., Valable, S., Marteau, L., Leuraud, P., Marie, Y., Poupon, M.F., Parienti, J.J., Raymond, E., and Peschanski, M. (2009). Molecular mechanisms underlying effects of epidermal growth factor receptor inhibition on invasion, proliferation, and angiogenesis in experimental glioma. Clin Cancer Res *15*, 3697-3704.

Gunther, N., Betzel, C., and Weber, W. (1990). The secreted form of the epidermal growth factor receptor. Characterization and crystallization of the receptor-ligand complex. J Biol Chem *265*, 22082-22085.

Gupta, A.K., and Curtis, A.S. (2004). Surface modified superparamagnetic nanoparticles for drug delivery: interaction studies with human fibroblasts in culture. J Mater Sci Mater Med *15*, 493-496.

Gupta, A.K., and Gupta, M. (2005). Synthesis and surface engineering of iron oxide nanoparticles for biomedical applications. Biomaterials *26*, 3995-4021.

Gupta, P., Han, S.Y., Holgado-Madruga, M., Mitra, S.S., Li, G., Nitta, R.T., and Wong, A.J. (2010). Development of an EGFRvIII specific recombinant antibody. BMC Biotechnol *10*, 72.

Hadjipanayis, C.G., Machaidze, R., Kaluzova, M., Wang, L., Schuette, A.J., Chen, H., Wu, X., and Mao, H. (2010). EGFRvIII antibody-conjugated iron oxide nanoparticles for magnetic resonance imaging-guided convection-enhanced delivery and targeted therapy of glioblastoma. Cancer Res *70*, 6303-6312.

Hagihara, Y., Mine, S., and Uegaki, K. (2007). Stabilization of an immunoglobulin fold domain by an engineered disulfide bond at the buried hydrophobic region. J Biol Chem *282*, 36489-36495.

Hamad, I., and Moghimi, S.M. (2008). Critical issues in site-specific targeting of solid tumours: the carrier, the tumour barriers and the bioavailable drug. Expert Opin Drug Deliv *5*, 205-219.

Hamers-Casterman, C., Atarhouch, T., Muyldermans, S., Robinson, G., Hamers, C., Songa, E.B., Bendahman, N., and Hamers, R. (1993). Naturally occurring antibodies devoid of light chains. Nature *363*, 446-448.

Harmsen, M.M., and De Haard, H.J. (2007). Properties, production, and applications of camelid single-domain antibody fragments. Appl Microbiol Biotechnol *77*, 13-22.

Harmsen, M.M., Ruuls, R.C., Nijman, I.J., Niewold, T.A., Frenken, L.G., and de Geus, B. (2000). Llama heavy-chain V regions consist of at least four distinct subfamilies revealing novel sequence features. Mol Immunol *37*, 579-590.

Harmsen, M.M., van Solt, C.B., Fijten, H.P., van Keulen, L., Rosalia, R.A., Weerdmeester, K., Cornelissen, A.H., De Bruin, M.G., Eble, P.L., and Dekker, A. (2007). Passive immunization of guinea pigs with llama single-domain antibody fragments against foot-and-mouth disease. Vet Microbiol *120*, 193-206.

Harmsen, M.M., Van Solt, C.B., Fijten, H.P., and Van Setten, M.C. (2005). Prolonged in vivo residence times of llama single-domain antibody fragments in pigs by binding to porcine immunoglobulins. Vaccine *23*, 4926-4934.

Harush-Frenkel, O., Debotton, N., Benita, S., and Altschuler, Y. (2007). Targeting of nanoparticles to the clathrin-mediated endocytic pathway. Biochem Biophys Res Commun *353*, 26-32.

Hatakeyama, S., Sugihara, K., Shibata, T.K., Nakayama, J., Akama, T.O., Tamura, N., Wong, S.M., Bobkov, A.A., Takano, Y., Ohyama, C*., et al.* (2011). Targeted drug delivery to tumor vasculature by a carbohydrate mimetic peptide. Proc Natl Acad Sci U S A *108*, 19587-19592.

Heimberger, A.B., Hlatky, R., Suki, D., Yang, D., Weinberg, J., Gilbert, M., Sawaya, R., and Aldape, K. (2005). Prognostic effect of epidermal growth factor receptor and EGFRvIII in glioblastoma multiforme patients. Clin Cancer Res *11*, 1462-1466.

Heitner, T., Moor, A., Garrison, J.L., Marks, C., Hasan, T., and Marks, J.D. (2001). Selection of cell binding and internalizing epidermal growth factor receptor antibodies from a phage display library. J Immunol Methods *248*, 17-30.

Henzler-Wildman, K., and Kern, D. (2007). Dynamic personalities of proteins. Nature *450*, 964-972.

Henzler-Wildman, K.A., Thai, V., Lei, M., Ott, M., Wolf-Watz, M., Fenn, T., Pozharski, E., Wilson, M.A., Petsko, G.A., Karplus, M., *et al.* (2007). Intrinsic motions along an enzymatic reaction trajectory. Nature *450*, 838-844.

Hill, R.J., and Sternberg, P.W. (1992). The gene lin-3 encodes an inductive signal for vulval development in C. elegans. Nature *358*, 470-476.

Hoeller, D., Volarevic, S., and Dikic, I. (2005). Compartmentalization of growth factor receptor signalling. Curr Opin Cell Biol *17*, 107-111.

Holliger, P., and Hudson, P.J. (2005). Engineered antibody fragments and the rise of single domains. Nat Biotechnol *23*, 1126-1136.

Hoogenboom, H.R., Henderikx, P., and de Haard, H. (1998). Creating and engineering human antibodies for immunotherapy. Adv Drug Deliv Rev *31*, 5-31.

Hosokawa, S., Tagawa, T., Niki, H., Hirakawa, Y., Nohga, K., and Nagaike, K. (2003). Efficacy of immunoliposomes on cancer models in a cell-surface-antigen-density-dependent manner. Br J Cancer *89*, 1545-1551.

http://www.ablynx.com.

Huang, L., Gainkam, L.O., Caveliers, V., Vanhove, C., Keyaerts, M., De Baetselier, P., Bossuyt, A., Revets, H., and Lahoutte, T. (2008). SPECT imaging with 99mTc-labeled EGFR-specific nanobody for in vivo monitoring of EGFR expression. Mol Imaging Biol *10*, 167-175.

Huang, R., Han, L., Li, J., Liu, S., Shao, K., Kuang, Y., Hu, X., Wang, X., Lei, H., and Jiang, C. (2011). Chlorotoxin-modified macromolecular contrast agent for MRI tumor diagnosis. Biomaterials *32*, 5177-5186.

Hudson, P.J., and Souriau, C. (2003). Engineered antibodies. Nat Med *9*, 129-134.

Huet, C., Ash, J.F., and Singer, S.J. (1980). The antibody-induced clustering and endocytosis of HLA antigens on cultured human fibroblasts. Cell *21*, 429-438.

Huh, Y.M., Jun, Y.W., Song, H.T., Kim, S., Choi, J.S., Lee, J.H., Yoon, S., Kim, K.S., Shin, J.S., Suh, J.S., *et al.* (2005). In vivo magnetic resonance detection of cancer by using multifunctional magnetic nanocrystals. J Am Chem Soc *127*, 12387-12391.

Hyeon, T., Lee, S.S., Park, J., Chung, Y., and Na, H.B. (2001). Synthesis of highly crystalline and monodisperse maghemite nanocrystallites without a size-selection process. J Am Chem Soc *123*, 12798-12801.

Hynes, N.E., and MacDonald, G. (2009). ErbB receptors and signaling pathways in cancer. Curr Opin Cell Biol *21*, 177-184.

Iqbal, U., Albaghdadi, H., Luo, Y., Arbabi, M., Desvaux, C., Veres, T., Stanimirovic, D., and Abulrob, A. (2010a). Molecular imaging of glioblastoma multiforme using anti-insulin-like growth factor-binding protein-7 single-domain antibodies. Br J Cancer *103*, 1606-1616.

Iqbal, U., Trojahn, U., Albaghdadi, H., Zhang, J., O'Connor-McCourt, M., Stanimirovic, D., Tomanek, B., Sutherland, G., and Abulrob, A. (2010b). Kinetic analysis of novel mono- and multivalent VHH-fragments and their application for molecular imaging of brain tumours. Br J Pharmacol *160*, 1016-1028.

Islam, T., and Josephson, L. (2009). Current state and future applications of active targeting in malignancies using superparamagnetic iron oxide nanoparticles. Cancer Biomark *5*, 99-107.

Iyer, A.K., Tran, K.T., Borysenko, C.W., Cascio, M., Camacho, C.J., Blair, H.C., Bahar, I., and Wells, A. (2007). Tenascin cytotactin epidermal growth factor-like repeat binds epidermal growth factor receptor with low affinity. J Cell Physiol *211*, 748-758.

Jain, K.K. (2005). Role of nanobiotechnology in developing personalized medicine for cancer. Technol Cancer Res Treat *4*, 645-650.

Jain, M., Kamal, N., and Batra, S.K. (2007). Engineering antibodies for clinical applications. Trends Biotechnol *25*, 307-316.

Jain, R.K., and Stylianopoulos, T. (2010). Delivering nanomedicine to solid tumors. Nat Rev Clin Oncol *7*, 653-664.

Jain, T.K., Reddy, M.K., Morales, M.A., Leslie-Pelecky, D.L., and Labhasetwar, V. (2008). Biodistribution, clearance, and biocompatibility of iron oxide magnetic nanoparticles in rats. Mol Pharm *5*, 316-327.

Jang, S.H., Wientjes, M.G., Lu, D., and Au, J.L. (2003). Drug delivery and transport to solid tumors. Pharm Res *20*, 1337-1350.

Janin, J. (1995). Principles of protein-protein recognition from structure to thermodynamics. Biochimie *77*, 497-505.

Jaramillo, M.L., Leon, Z., Grothe, S., Paul-Roc, B., Abulrob, A., and O'Connor McCourt, M. (2006). Effect of the anti-receptor ligand-blocking 225 monoclonal antibody on EGF receptor endocytosis and sorting. Exp Cell Res *312*, 2778-2790.

Jason-Moller, L., Murphy, M., and Bruno, J. (2006). Overview of Biacore systems and their applications. Curr Protoc Protein Sci *Chapter 19*, Unit 19 13.

Jenkinson, M.D., Du Plessis, D.G., Walker, C., and Smith, T.S. (2007). Advanced MRI in the management of adult gliomas. Br J Neurosurg *21*, 550-561.

Jevsevar, S., Kunstelj, M., and Porekar, V.G. (2010). PEGylation of therapeutic proteins. Biotechnol J *5*, 113-128.

Johns, T.G., Perera, R.M., Vernes, S.C., Vitali, A.A., Cao, D.X., Cavenee, W.K., Scott, A.M., and Furnari, F.B. (2007). The efficacy of epidermal growth factor receptor-specific antibodies against glioma xenografts is influenced by receptor levels, activation status, and heterodimerization. Clin Cancer Res *13*, 1911-1925.

Johns, T.G., Stockert, E., Ritter, G., Jungbluth, A.A., Huang, H.J., Cavenee, W.K., Smyth, F.E., Hall, C.M., Watson, N., Nice, E.C*., et al.* (2002). Novel monoclonal antibody specific for the de2-7 epidermal growth factor receptor (EGFR) that also recognizes the EGFR expressed in cells containing amplification of the EGFR gene. Int J Cancer *98*, 398-408.

Johnsson, B., Lofas, S., Lindquist, G., Edstrom, A., Muller Hillgren, R.M., and Hansson, A. (1995). Comparison of methods for immobilization to carboxymethyl dextran sensor surfaces by analysis of the specific activity of monoclonal antibodies. J Mol Recognit *8*, 125-131.

Jonker, D.J., O'Callaghan, C.J., Karapetis, C.S., Zalcberg, J.R., Tu, D., Au, H.J., Berry, S.R., Krahn, M., Price, T., Simes, R.J.*, et al.* (2007). Cetuximab for the treatment of colorectal cancer. N Engl J Med *357*, 2040-2048.

Josephson, L., Kircher, M.F., Mahmood, U., Tang, Y., and Weissleder, R. (2002). Near-infrared fluorescent nanoparticles as combined MR/optical imaging probes. Bioconjug Chem *13*, 554-560.

Jun, Y.W., Huh, Y.M., Choi, J.S., Lee, J.H., Song, H.T., Kim, S., Yoon, S., Kim, K.S., Shin, J.S., Suh, J.S.*, et al.* (2005). Nanoscale size effect of magnetic nanocrystals and their utilization for cancer diagnosis via magnetic resonance imaging. J Am Chem Soc *127*, 5732-5733.

Junghans, R.P. (1997). Finally! The Brambell receptor (FcRB). Mediator of transmission of immunity and protection from catabolism for IgG. Immunol Res *16*, 29-57.

Jura, N., Endres, N.F., Engel, K., Deindl, S., Das, R., Lamers, M.H., Wemmer, D.E., Zhang, X., and Kuriyan, J. (2009). Mechanism for activation of the EGF receptor catalytic domain by the juxtamembrane segment. Cell *137*, 1293-1307.

Kalinin, N.L., Ward, L.D., and Winzor, D.J. (1995). Effects of solute multivalence on the evaluation of binding constants by biosensor technology: studies with concanavalin A and interleukin-6 as partitioning proteins. Anal Biochem *228*, 238-244.

Kamat, V., Donaldson, J.M., Kari, C., Quadros, M.R., Lelkes, P.I., Chaiken, I., Cocklin, S., Williams, J.C., Papazoglou, E., and Rodeck, U. (2008). Enhanced EGFR inhibition and distinct epitope recognition by EGFR antagonistic mAbs C225 and 425. Cancer Biol Ther *7*, 726-733.

Karlsson, R. (1999). Affinity analysis of non-steady-state data obtained under mass transport limited conditions using BIAcore technology. J Mol Recognit *12*, 285-292.

Karlsson, R., and Falt, A. (1997). Experimental design for kinetic analysis of protein-protein interactions with surface plasmon resonance biosensors. J Immunol Methods *200*, 121-133.

Katsamba, P.S., Navratilova, I., Calderon-Cacia, M., Fan, L., Thornton, K., Zhu, M., Bos, T.V., Forte, C., Friend, D., Laird-Offringa, I.*, et al.* (2006). Kinetic analysis of a high-affinity antibody/antigen interaction performed by multiple Biacore users. Anal Biochem *352*, 208-221.

Kawashima, N., Nakayama, K., Itoh, K., Itoh, T., Ishikawa, M., and Biju, V. (2010). Reversible dimerization of EGFR revealed by single-molecule fluorescence imaging using quantum dots. Chemistry *16*, 1186-1192.

Ke, S., Wen, X., Gurfinkel, M., Charnsangavej, C., Wallace, S., Sevick-Muraca, E.M., and Li, C. (2003). Near-infrared optical imaging of epidermal growth factor receptor in breast cancer xenografts. Cancer Res *63*, 7870-7875.

Kern, D., and Zuiderweg, E.R. (2003). The role of dynamics in allosteric regulation. Curr Opin Struct Biol *13*, 748-757.

Kim, D., El-Shall, H., Dennis, D., and Morey, T. (2005). Interaction of PLGA nanoparticles with human blood constituents. Colloids Surf B Biointerfaces *40*, 83-91.

Kim, H.R., Andrieux, K., Delomenie, C., Chacun, H., Appel, M., Desmaele, D., Taran, F., Georgin, D., Couvreur, P., and Taverna, M. (2007). Analysis of plasma protein adsorption onto PEGylated nanoparticles by complementary methods: 2-DE, CE and Protein Lab-on-chip system. Electrophoresis *28*, 2252-2261.

Kircher, M.F., Mahmood, U., King, R.S., Weissleder, R., and Josephson, L. (2003). A multimodal nanoparticle for preoperative magnetic resonance imaging and intraoperative optical brain tumor delineation. Cancer Res *63*, 8122-8125.

Kircher, M.F., Weissleder, R., and Josephson, L. (2004). A dual fluorochrome probe for imaging proteases. Bioconjug Chem *15*, 242-248.

Kirpotin, D.B., Drummond, D.C., Shao, Y., Shalaby, M.R., Hong, K., Nielsen, U.B., Marks, J.D., Benz, C.C., and Park, J.W. (2006). Antibody targeting of long-circulating lipidic nanoparticles does not increase tumor localization but does increase internalization in animal models. Cancer Res *66*, 6732-6740.

Klein, D.E., Stayrook, S.E., Shi, F., Narayan, K., and Lemmon, M.A. (2008). Structural basis for EGFR ligand sequestration by Argos. Nature *453*, 1271-1275.

Klein, P., Mattoon, D., Lemmon, M.A., and Schlessinger, J. (2004). A structure-based model for ligand binding and dimerization of EGF receptors. Proc Natl Acad Sci U S A *101*, 929-934.

Knauer, D.J., Wiley, H.S., and Cunningham, D.D. (1984). Relationship between epidermal growth factor receptor occupancy and mitogenic response. Quantitative analysis using a steady state model system. J Biol Chem *259*, 5623-5631.

Knight, D.M., Jordan, R.E., Kruszynski, M., Tam, S.H., Giles-Komar, J., Treacy, G., and Heavner, G.A. (2004). Pharmacodynamic enhancement of the anti-platelet antibody fab abciximab by site-specific pegylation. Platelets *15*, 409-418.

Kocbek, P., Obermajer, N., Cegnar, M., Kos, J., and Kristl, J. (2007). Targeting cancer cells using PLGA nanoparticles surface modified with monoclonal antibody. J Control Release *120*, 18-26.

Kolkman, J.A., and Law, D.A. (2010). Nanobodies ‚Äì from llamas to therapeutic proteins. Drug Discovery Today: Technologies *7*, e139-e146.

Kontermann, R.E. (2006). Immunoliposomes for cancer therapy. Curr Opin Mol Ther *8*, 39-45.

Koo, Y.E., Reddy, G.R., Bhojani, M., Schneider, R., Philbert, M.A., Rehemtulla, A., Ross, B.D., and Kopelman, R. (2006). Brain cancer diagnosis and therapy with nanoplatforms. Adv Drug Deliv Rev *58*, 1556-1577.

Kremer, S., Pinel, S., Vedrine, P.O., Bressenot, A., Robert, P., Bracard, S., and Plenat, F. (2007). Ferumoxtran-10 enhancement in orthotopic xenograft models of human brain tumors: an indirect marker of tumor proliferation? J Neurooncol *83*, 111-119.

Kuan, C.T., Wikstrand, C.J., and Bigner, D.D. (2000). EGFRvIII as a promising target for antibody-based brain tumor therapy. Brain Tumor Pathol *17*, 71-78.

Kubetzko, S., Sarkar, C.A., and Pluckthun, A. (2005). Protein PEGylation decreases observed target association rates via a dual blocking mechanism. Mol Pharmacol *68*, 1439-1454.

Kuhl, C. (2007a). The current status of breast MR imaging. Part I. Choice of technique, image interpretation, diagnostic accuracy, and transfer to clinical practice. Radiology *244*, 356-378.

Kuhl, C.K. (2007b). Current status of breast MR imaging. Part 2. Clinical applications. Radiology *244*, 672-691.

Kullberg, E.B., Nestor, M., and Gedda, L. (2003). Tumor-cell targeted epiderimal growth factor liposomes loaded with boronated acridine: uptake and processing. Pharm Res *20*, 229-236.

LaConte, L.E., Nitin, N., Zurkiya, O., Caruntu, D., O'Connor, C.J., Hu, X., and Bao, G. (2007). Coating thickness of magnetic iron oxide nanoparticles affects R2 relaxivity. J Magn Reson Imaging *26*, 1634-1641.

Lacroix, M., Abi-Said, D., Fourney, D.R., Gokaslan, Z.L., Shi, W., DeMonte, F., Lang, F.F., McCutcheon, I.E., Hassenbusch, S.J., Holland, E.*, et al.* (2001). A multivariate analysis of 416 patients with glioblastoma multiforme: prognosis, extent of resection, and survival. J Neurosurg *95*, 190-198.

Lal, A., Glazer, C.A., Martinson, H.M., Friedman, H.S., Archer, G.E., Sampson, J.H., and Riggins, G.J. (2002). Mutant epidermal growth factor receptor up-regulates molecular effectors of tumor invasion. Cancer Res *62*, 3335-3339.

Lammers, T., Kiessling, F., Hennink, W.E., and Storm, G. (2011). Drug targeting to tumors: Principles, pitfalls and (pre-) clinical progress. J Control Release.

Lauwereys, M., Arbabi Ghahroudi, M., Desmyter, A., Kinne, J., Holzer, W., De Genst, E., Wyns, L., and Muyldermans, S. (1998). Potent enzyme inhibitors derived from dromedary heavy-chain antibodies. EMBO J *17*, 3512-3520.

Leavitt, S., and Freire, E. (2001). Direct measurement of protein binding energetics by isothermal titration calorimetry. Curr Opin Struct Biol *11*, 560-566.

Ledeboer, A.M., Bezemer, S., de Hiaard, J.J., Schaffers, I.M., Verrips, C.T., van Vliet, C., Dusterhoft, E.M., Zoon, P., Moineau, S., and Frenken, L.G. (2002). Preventing phage lysis of Lactococcus lactis in cheese production using a neutralizing heavy-chain antibody fragment from llama. J Dairy Sci *85*, 1376-1382.

Lee, A.L., and Wand, A.J. (2001). Microscopic origins of entropy, heat capacity and the glass transition in proteins. Nature *411*, 501-504.

Lee, H.Y., Li, Z., Chen, K., Hsu, A.R., Xu, C., Xie, J., Sun, S., and Chen, X. (2008). PET/MRI dual-modality tumor imaging using arginine-glycine-aspartic (RGD)-conjugated radiolabeled iron oxide nanoparticles. J Nucl Med *49*, 1371-1379.

Lee, J., Choi, Y., Kim, K., Hong, S., Park, H.Y., Lee, T., Cheon, G.J., and Song, R. (2010). Characterization and cancer cell specific binding properties of anti-EGFR antibody conjugated quantum dots. Bioconjug Chem *21*, 940-946.

Lee, J.H., Huh, Y.M., Jun, Y.W., Seo, J.W., Jang, J.T., Song, H.T., Kim, S., Cho, E.J., Yoon, H.G., Suh, J.S.*, et al.* (2007). Artificially engineered magnetic nanoparticles for ultra-sensitive molecular imaging. Nat Med *13*, 95-99.

Lemmon, M.A. (2009). Ligand-induced ErbB receptor dimerization. Exp Cell Res *315*, 638-648.

Lemmon, M.A., Bu, Z., Ladbury, J.E., Zhou, M., Pinchasi, D., Lax, I., Engelman, D.M., and Schlessinger, J. (1997). Two EGF molecules contribute additively to stabilization of the EGFR dimer. EMBO J *16*, 281-294.

Leroueil, P.R., Hong, S., Mecke, A., Baker, J.R., Jr., Orr, B.G., and Banaszak Holl, M.M. (2007). Nanoparticle interaction with biological membranes: does nanotechnology present a Janus face? Acc Chem Res *40*, 335-342.

Lewinski, N., Colvin, V., and Drezek, R. (2008). Cytotoxicity of nanoparticles. Small *4*, 26-49.

Li, L., Dantzer, J.J., Nowacki, J., O'Callaghan, B.J., and Meroueh, S.O. (2008). PDBcal: a comprehensive dataset for receptor-ligand interactions with three-dimensional structures and binding thermodynamics from isothermal titration calorimetry. Chem Biol Drug Des *71*, 529-532.

Li, S., Schmitz, K.R., Jeffrey, P.D., Wiltzius, J.J., Kussie, P., and Ferguson, K.M. (2005). Structural basis for inhibition of the epidermal growth factor receptor by cetuximab. Cancer Cell *7*, 301-311.

Lidar, Z., Mardor, Y., Jonas, T., Pfeffer, R., Faibel, M., Nass, D., Hadani, M., and Ram, Z. (2004). Convection-enhanced delivery of paclitaxel for the treatment of recurrent malignant glioma: a phase I/II clinical study. J Neurosurg *100*, 472-479.

Lin, C.R., Chen, W.S., Kruiger, W., Stolarsky, L.S., Weber, W., Evans, R.M., Verma, I.M., Gill, G.N., and Rosenfeld, M.G. (1984). Expression cloning of human EGF receptor complementary DNA: gene amplification and three related messenger RNA products in A431 cells. Science *224*, 843-848.

Lipschultz, C.A., Yee, A., Mohan, S., Li, Y., and Smith-Gill, S.J. (2002). Temperature differentially affects encounter and docking thermodynamics of antibody--antigen association. J Mol Recognit *15*, 44-52.

Liu, T.F., Tatter, S.B., Willingham, M.C., Yang, M., Hu, J.J., and Frankel, A.E. (2003). Growth factor receptor expression varies among high-grade gliomas and normal brain: epidermal growth factor receptor has excellent properties for interstitial fusion protein therapy. Mol Cancer Ther *2*, 783-787.

Lockman, P.R., Koziara, J., Roder, K.E., Paulson, J., Abbruscato, T.J., Mumper, R.J., and Allen, D.D. (2003). In vivo and in vitro assessment of baseline blood-brain barrier parameters in the presence of novel nanoparticles. Pharm Res *20*, 705-713.

London, N., Raveh, B., Cohen, E., Fathi, G., and Schueler-Furman, O. (2011). Rosetta FlexPepDock web server--high resolution modeling of peptide-protein interactions. Nucleic Acids Res *39*, W249-253.

Lookene, A., Chevreuil, O., Ostergaard, P., and Olivecrona, G. (1996). Interaction of lipoprotein lipase with heparin fragments and with heparan sulfate: stoichiometry, stabilization, and kinetics. Biochemistry *35*, 12155-12163.

Lorimer, I.A., Keppler-Hafkemeyer, A., Beers, R.A., Pegram, C.N., Bigner, D.D., and Pastan, I. (1996). Recombinant immunotoxins specific for a mutant epidermal growth factor receptor: targeting with a single chain antibody variable domain isolated by phage display. Proc Natl Acad Sci U S A *93*, 14815-14820.

Lu, C., Mi, L.Z., Grey, M.J., Zhu, J., Graef, E., Yokoyama, S., and Springer, T.A. (2010). Structural evidence for loose linkage between ligand binding and kinase activation in the epidermal growth factor receptor. Mol Cell Biol *30*, 5432-5443.

Lu, Y., Yin, Y., Mayers, B.T., and Xia, Y. (2002). Modifying the Surface Properties of Superparamagnetic Iron Oxide Nanoparticles through A Sol,àíGel Approach. Nano Letters *2*, 183-186.

Luke, K., Apiyo, D., and Wittung-Stafshede, P. (2005). Dissecting homo-heptamer thermodynamics by isothermal titration calorimetry: entropy-driven assembly of co-chaperonin protein 10. Biophys J *89*, 3332-3336.

Lutz, J.F., Stiller, S., Hoth, A., Kaufner, L., Pison, U., and Cartier, R. (2006). One-pot synthesis of pegylated ultrasmall iron-oxide nanoparticles and their in vivo evaluation as magnetic resonance imaging contrast agents. Biomacromolecules *7*, 3132-3138.

Luwor, R.B., Zhu, H.J., Walker, F., Vitali, A.A., Perera, R.M., Burgess, A.W., Scott, A.M., and Johns, T.G. (2004). The tumor-specific de2-7 epidermal growth factor receptor (EGFR) promotes cells survival and heterodimerizes with the wild-type EGFR. Oncogene *23*, 6095-6104.

Macdonald, J.L., and Pike, L.J. (2008). Heterogeneity in EGF-binding affinities arises from negative cooperativity in an aggregating system. Proc Natl Acad Sci U S A *105*, 112-117.

Maenaka, K., van der Merwe, P.A., Stuart, D.I., Jones, E.Y., and Sondermann, P. (2001). The human low affinity Fcgamma receptors IIa, IIb, and III bind IgG with fast kinetics and distinct thermodynamic properties. J Biol Chem *276*, 44898-44904.

Mailander, V., and Landfester, K. (2009). Interaction of nanoparticles with cells. Biomacromolecules *10*, 2379-2400.

Majewski, P., and Thierry, B. (2007). Functionalized Magnetite Nanoparticles‚ÄîSynthesis, Properties, and Bio-Applications. Critical Reviews in Solid State and Materials Sciences *32*, 203-215.

Malicka, J., Gryczynski, I., Geddes, C.D., and Lakowicz, J.R. (2003). Metal-enhanced emission from indocyanine green: a new approach to in vivo imaging. J Biomed Opt *8*, 472-478.

Mamot, C., Drummond, D.C., Greiser, U., Hong, K., Kirpotin, D.B., Marks, J.D., and Park, J.W. (2003). Epidermal growth factor receptor (EGFR)-targeted immunoliposomes mediate specific and efficient drug delivery to EGFR- and EGFRvIII-overexpressing tumor cells. Cancer Res *63*, 3154-3161.

Mason, W.P., Maestro, R.D., Eisenstat, D., Forsyth, P., Fulton, D., Laperriere, N., Macdonald, D., Perry, J., and Thiessen, B. (2007). Canadian recommendations for the treatment of glioblastoma multiforme. Curr Oncol *14*, 110-117.

Matsumura, Y., and Maeda, H. (1986). A new concept for macromolecular therapeutics in cancer chemotherapy: mechanism of tumoritropic accumulation of proteins and the antitumor agent smancs. Cancer Res *46*, 6387-6392.

Mayawala, K., Vlachos, D.G., and Edwards, J.S. (2005). Heterogeneities in EGF receptor density at the cell surface can lead to concave up scatchard plot of EGF binding. FEBS Lett *579*, 3043-3047.

McGowan, J.C. (2008). Basic principles of magnetic resonance imaging. Neuroimaging Clin N Am *18*, 623-636, x.

Melkko, S., Halin, C., Borsi, L., Zardi, L., and Neri, D. (2002). An antibody-calmodulin fusion protein reveals a functional dependence between macromolecular isoelectric point and tumor targeting performance. Int J Radiat Oncol Biol Phys *54*, 1485-1490.

Mendelsohn, J., and Baselga, J. (2006). Epidermal growth factor receptor targeting in cancer. Semin Oncol *33*, 369-385.

Mi, L.Z., Grey, M.J., Nishida, N., Walz, T., Lu, C., and Springer, T.A. (2008). Functional and structural stability of the epidermal growth factor receptor in detergent micelles and phospholipid nanodiscs. Biochemistry *47*, 10314-10323.

Mian, I.S., Bradwell, A.R., and Olson, A.J. (1991). Structure, function and properties of antibody binding sites. J Mol Biol *217*, 133-151.

Mishra, A.K., Panwar, P., Hosono, M., Chuttani, K., Mishra, P., Sharma, R.K., and Chatal, J.F. (2004). A new bifunctional chelating agent conjugated with monoclonal antibody and labelled with technetium-99m for targeted scintigraphy: 6-(4-isothiocyanatobenzyl)-5,7-dioxo-1,11-(carboxymethyl)-1,4,8,11-tetraaz acyclotridecane. J Drug Target *12*, 559-567.

Miyamoto, C.T., Brady, L.W., Rackover, M.A., Emrich, J., Class, R., Bender, H., Micaily, B., and Steplewski, Z. (1996). The use of epidermal growth factor receptor-425 monoclonal antibodies radiolabeled with iodine-125 in the adjuvant treatment of patients with high grade gliomas of the brain. Recent Results Cancer Res *141*, 183-192.

Moghimi, S.M., Hunter, A.C., and Andresen, T.L. (2011). Factors Controlling Nanoparticle Pharmacokinetics: An Integrated Analysis and Perspective. Annu Rev Pharmacol Toxicol.

Moghimi, S.M., Hunter, A.C., and Murray, J.C. (2001). Long-circulating and target-specific nanoparticles: theory to practice. Pharmacol Rev *53*, 283-318.

Moghimi, S.M., Hunter, A.C., and Murray, J.C. (2005). Nanomedicine: current status and future prospects. FASEB J *19*, 311-330.

Morawski, A.M., Winter, P.M., Crowder, K.C., Caruthers, S.D., Fuhrhop, R.W., Scott, M.J., Robertson, J.D., Abendschein, D.R., Lanza, G.M., and Wickline, S.A. (2004). Targeted nanoparticles for quantitative imaging of sparse molecular epitopes with MRI. Magn Reson Med *51*, 480-486.

Moriki, T., Maruyama, H., and Maruyama, I.N. (2001). Activation of preformed EGF receptor dimers by ligand-induced rotation of the transmembrane domain. J Mol Biol *311*, 1011-1026.

Moscatello, D.K., Holgado-Madruga, M., Godwin, A.K., Ramirez, G., Gunn, G., Zoltick, P.W., Biegel, J.A., Hayes, R.L., and Wong, A.J. (1995). Frequent expression of a mutant epidermal growth factor receptor in multiple human tumors. Cancer Res *55*, 5536-5539.

Mozsolits, H., Thomas, W.G., and Aguilar, M.I. (2003). Surface plasmon resonance spectroscopy in the study of membrane-mediated cell signalling. J Pept Sci *9*, 77-89.

Mu, Q., Yang, L., Davis, J.C., Vankayala, R., Hwang, K.C., Zhao, J., and Yan, B. (2010). Biocompatibility of polymer grafted core/shell iron/carbon nanoparticles. Biomaterials *31*, 5083-5090.

Muldoon, L.L., Sandor, M., Pinkston, K.E., and Neuwelt, E.A. (2005). Imaging, distribution, and toxicity of superparamagnetic iron oxide magnetic resonance nanoparticles in the rat brain and intracerebral tumor. Neurosurgery *57*, 785-796; discussion 785-796.

Muruganandam, A., Tanha, J., Narang, S., and Stanimirovic, D. (2002). Selection of phage-displayed llama single-domain antibodies that transmigrate across human blood-brain barrier endothelium. FASEB J *16*, 240-242.

Muyldermans, S. (2001). Single domain camel antibodies: current status. J Biotechnol *74*, 277-302.

Muyldermans, S., Baral, T.N., Retamozzo, V.C., De Baetselier, P., De Genst, E., Kinne, J., Leonhardt, H., Magez, S., Nguyen, V.K., Revets, H., *et al.* (2009). Camelid immunoglobulins and nanobody technology. Vet Immunol Immunopathol *128*, 178-183.

Muyldermans, S., Cambillau, C., and Wyns, L. (2001). Recognition of antigens by single-domain antibody fragments: the superfluous luxury of paired domains. Trends Biochem Sci *26*, 230-235.

Myszka, D.G. (1999). Improving biosensor analysis. J Mol Recognit *12*, 279-284.

Myszka, D.G. (2000). Kinetic, equilibrium, and thermodynamic analysis of macromolecular interactions with BIACORE. Methods Enzymol *323*, 325-340.

Myszka, D.G., Abdiche, Y.N., Arisaka, F., Byron, O., Eisenstein, E., Hensley, P., Thomson, J.A., Lombardo, C.R., Schwarz, F., Stafford, W., *et al.* (2003). The ABRF-MIRG'02 study: assembly state, thermodynamic, and kinetic analysis of an enzyme/inhibitor interaction. J Biomol Tech *14*, 247-269.

Myszka, D.G., Morton, T.A., Doyle, M.L., and Chaiken, I.M. (1997). Kinetic analysis of a protein antigen-antibody interaction limited by mass transport on an optical biosensor. Biophys Chem *64*, 127-137.

Nagane, M., Coufal, F., Lin, H., Bogler, O., Cavenee, W.K., and Huang, H.J. (1996). A common mutant epidermal growth factor receptor confers enhanced tumorigenicity on human glioblastoma cells by increasing proliferation and reducing apoptosis. Cancer Res *56*, 5079-5086.

Natarajan, A., Xiong, C.Y., Albrecht, H., DeNardo, G.L., and DeNardo, S.J. (2005). Characterization of site-specific ScFv PEGylation for tumor-targeting pharmaceuticals. Bioconjug Chem *16*, 113-121.

Natsume, A., Wakitani, M., Yamane-Ohnuki, N., Shoji-Hosaka, E., Niwa, R., Uchida, K., Satoh, M., and Shitara, K. (2006). Fucose removal from complex-type oligosaccharide enhances the antibody-dependent cellular cytotoxicity of single-gene-encoded bispecific antibody comprising of two single-chain antibodies linked to the antibody constant region. J Biochem *140*, 359-368.

Navratilova, I., Papalia, G.A., Rich, R.L., Bedinger, D., Brophy, S., Condon, B., Deng, T., Emerick, A.W., Guan, H.W., Hayden, T., *et al.* (2007). Thermodynamic benchmark study using Biacore technology. Anal Biochem *364*, 67-77.

Neuwelt, E.A., Varallyay, P., Bago, A.G., Muldoon, L.L., Nesbit, G., and Nixon, R. (2004). Imaging of iron oxide nanoparticles by MR and light microscopy in patients with malignant brain tumours. Neuropathol Appl Neurobiol *30*, 456-471.

Nguyen, V.K., Desmyter, A., and Muyldermans, S. (2001). Functional heavy-chain antibodies in Camelidae. Adv Immunol *79*, 261-296.

Nguyen, V.K., Hamers, R., Wyns, L., and Muyldermans, S. (2000). Camel heavy-chain antibodies: diverse germline V(H)H and specific mechanisms enlarge the antigen-binding repertoire. EMBO J *19*, 921-930.

Nice, E.C., and Catimel, B. (1999). Instrumental biosensors: new perspectives for the analysis of biomolecular interactions. Bioessays *21*, 339-352.

Nice, E.C., Catimel, B., Rothacker, J.A., Hall, N., Burgess, A.W., Garrett, T.P.J., McKern, N.M., and Ward, C.W. (2004). Applications of optical biosensors to structure-function studies on the EGF/EGF receptor system. Methods in Proteome and Protein Analysis, 133-164.

Nielsen, P.K., Bonsager, B.C., Berland, C.R., Sigurskjold, B.W., and Svensson, B. (2003). Kinetics and energetics of the binding between barley alpha-amylase/subtilisin inhibitor and barley alpha-amylase 2 analyzed by surface plasmon resonance and isothermal titration calorimetry. Biochemistry *42*, 1478-1487.

Nishikawa, R., Ji, X.D., Harmon, R.C., Lazar, C.S., Gill, G.N., Cavenee, W.K., and Huang, H.J. (1994). A mutant epidermal growth factor receptor common in human glioma confers enhanced tumorigenicity. Proc Natl Acad Sci U S A *91*, 7727-7731.

Normanno, N., De Luca, A., Bianco, C., Strizzi, L., Mancino, M., Maiello, M.R., Carotenuto, A., De Feo, G., Caponigro, F., and Salomon, D.S. (2006). Epidermal growth factor receptor (EGFR) signaling in cancer. Gene *366*, 2-16.

Nuttall, S.D., and Walsh, R.B. (2008). Display scaffolds: protein engineering for novel therapeutics. Curr Opin Pharmacol *8*, 609-615.

O'Rourke, D.M., Nute, E.J., Davis, J.G., Wu, C., Lee, A., Murali, R., Zhang, H.T., Qian, X., Kao, C.C., and Greene, M.I. (1998). Inhibition of a naturally occurring EGFR oncoprotein by the p185neu ectodomain: implications for subdomain contributions to receptor assembly. Oncogene *16*, 1197-1207.

Odaka, M., Kohda, D., Lax, I., Schlessinger, J., and Inagaki, F. (1997). Ligand-binding enhances the affinity of dimerization of the extracellular domain of the epidermal growth factor receptor. J Biochem *122*, 116-121.

Ogiso, H., Ishitani, R., Nureki, O., Fukai, S., Yamanaka, M., Kim, J.H., Saito, K., Sakamoto, A., Inoue, M., Shirouzu, M*., et al.* (2002). Crystal structure of the complex of human epidermal growth factor and receptor extracellular domains. Cell *110*, 775-787.

Ohgaki, H., Dessen, P., Jourde, B., Horstmann, S., Nishikawa, T., Di Patre, P.L., Burkhard, C., Schuler, D., Probst-Hensch, N.M., Maiorka, P.C*., et al.* (2004). Genetic pathways to glioblastoma: a population-based study. Cancer Res *64*, 6892-6899.

Ohlson, S., Strandh, M., and Nilshans, H. (1997). Detection and characterization of weak affinity antibody antigen recognition with biomolecular interaction analysis. J Mol Recognit *10*, 135-138.

Oliveira, S., Schiffelers, R.M., van der Veeken, J., van der Meel, R., Vongpromek, R., van Bergen En Henegouwen, P.M., Storm, G., and Roovers, R.C. (2010). Downregulation of EGFR by a novel multivalent nanobody-liposome platform. J Control Release *145*, 165-175.

Omidfar, K., Rasaee, M.J., Kashanian, S., Paknejad, M., and Bathaie, Z. (2007). Studies of thermostability in Camelus bactrianus (Bactrian camel) single-domain antibody specific for the mutant epidermal-growth-factor receptor expressed by Pichia. Biotechnol Appl Biochem *46*, 41-49.

Omidfar, K., Rasaee, M.J., Modjtahedi, H., Forouzandeh, M., Taghikhani, M., Bakhtiari, A., Paknejad, M., and Kashanian, S. (2004a). Production and characterization of a new antibody specific for the mutant EGF receptor, EGFRvIII, in Camelus bactrianus. Tumour Biol *25*, 179-187.

Omidfar, K., Rasaee, M.J., Modjtahedi, H., Forouzandeh, M., Taghikhani, M., and Golmakani, N. (2004b). Production of a novel camel single-domain antibody specific for the type III mutant EGFR. Tumour Biol *25*, 296-305.

Orning, L., Rian, A., Campbell, A., Brady, J., Fedosov, S.N., Bramlage, B., Thompson, K., and Quadros, E.V. (2006). Characterization of a monoclonal antibody with specificity for holo-transcobalamin. Nutr Metab (Lond) *3*, 3.

Padlan, E.A. (1994). Anatomy of the antibody molecule. Mol Immunol *31*, 169-217.

Papalia, G.A., Baer, M., Luehrsen, K., Nordin, H., Flynn, P., and Myszka, D.G. (2006). High-resolution characterization of antibody fragment/antigen interactions using Biacore T100. Anal Biochem *359*, 112-119.

Parkar, N.S., Akpa, B.S., Nitsche, L.C., Wedgewood, L.E., Place, A.T., Sverdlov, M.S., Chaga, O., and Minshall, R.D. (2009). Vesicle formation and endocytosis: function, machinery, mechanisms, and modeling. Antioxid Redox Signal *11*, 1301-1312.

Paul-Murphy, J., Gershwin, L.J., Thatcher, E.F., Fowler, M.E., and Habig, W.H. (1989). Immune response of the llama (Lama glama) to tetanus toxoid vaccination. Am J Vet Res *50*, 1279-1281.

Pavlinkova, G., Beresford, G., Booth, B.J., Batra, S.K., and Colcher, D. (1999). Charge-modified single chain antibody constructs of monoclonal antibody CC49: generation, characterization, pharmacokinetics, and biodistribution analysis. Nucl Med Biol *26*, 27-34.

Pedersen, M.W., Meltorn, M., Damstrup, L., and Poulsen, H.S. (2001). The type III epidermal growth factor receptor mutation. Biological significance and potential target for anti-cancer therapy. Ann Oncol *12*, 745-760.

Peng, X.H., Qian, X., Mao, H., Wang, A.Y., Chen, Z.G., Nie, S., and Shin, D.M. (2008). Targeted magnetic iron oxide nanoparticles for tumor imaging and therapy. Int J Nanomedicine *3*, 311-321.

Perlstein, B., Ram, Z., Daniels, D., Ocherashvilli, A., Roth, Y., Margel, S., and Mardor, Y. (2008). Convection-enhanced delivery of maghemite nanoparticles: Increased efficacy and MRI monitoring. Neuro Oncol *10*, 153-161.

Perozzo, R., Folkers, G., and Scapozza, L. (2004). Thermodynamics of protein-ligand interactions: history, presence, and future aspects. J Recept Signal Transduct Res *24*, 1-52.

Pirollo, K.F., and Chang, E.H. (2008). Does a targeting ligand influence nanoparticle tumor localization or uptake? Trends Biotechnol *26*, 552-558.

Porter, A.L., and Youtie, J. (2009). Where does nanotechnology belong in the map of science? Nat Nanotechnol *4*, 534-536.

Prestwich, G.D. (2008). Engineering a clinically-useful matrix for cell therapy. Organogenesis *4*, 42-47.

Prigent, S.A., Nagane, M., Lin, H., Huvar, I., Boss, G.R., Feramisco, J.R., Cavenee, W.K., and Huang, H.S. (1996). Enhanced tumorigenic behavior of glioblastoma cells expressing a truncated epidermal growth factor receptor is mediated through the Ras-Shc-Grb2 pathway. J Biol Chem *271*, 25639-25645.

Qiu, C., Tarrant, M.K., Boronina, T., Longo, P.A., Kavran, J.M., Cole, R.N., Cole, P.A., and Leahy, D.J. (2009). In vitro enzymatic characterization of near full length EGFR in activated and inhibited states. Biochemistry *48*, 6624-6632.

Ramge, P., Unger, R.E., Oltrogge, J.B., Zenker, D., Begley, D., Kreuter, J., and Von Briesen, H. (2000). Polysorbate-80 coating enhances uptake of polybutylcyanoacrylate (PBCA)-nanoparticles by human and bovine primary brain capillary endothelial cells. Eur J Neurosci *12*, 1931-1940.

Re, F., Cambianica, I., Zona, C., Sesana, S., Gregori, M., Rigolio, R., La Ferla, B., Nicotra, F., Forloni, G., Cagnotto, A.*, et al.* (2011). Functionalization of liposomes with ApoE-derived peptides at different density affects cellular uptake and drug transport across a blood-brain barrier model. Nanomedicine *7*, 551-559.

Reddy, G.R., Bhojani, M.S., McConville, P., Moody, J., Moffat, B.A., Hall, D.E., Kim, G., Koo, Y.E., Woolliscroft, M.J., Sugai, J.V.*, et al.* (2006). Vascular targeted nanoparticles for imaging and treatment of brain tumors. Clin Cancer Res *12*, 6677-6686.

Reist, C.J., Archer, G.E., Kurpad, S.N., Wikstrand, C.J., Vaidyanathan, G., Willingham, M.C., Moscatello, D.K., Wong, A.J., Bigner, D.D., and Zalutsky, M.R. (1995). Tumor-specific anti-epidermal growth factor receptor variant III monoclonal antibodies: use of the tyramine-cellobiose radioiodination method enhances cellular retention and uptake in tumor xenografts. Cancer Res *55*, 4375-4382.

Revets, H., De Baetselier, P., and Muyldermans, S. (2005). Nanobodies as novel agents for cancer therapy. Expert Opin Biol Ther *5*, 111-124.

Rich, R.L., and Myszka, D.G. (2004). Why you should be using more SPR biosensor technology. Drug Discovery Today: Technologies *1*, 301-308.

Rich, R.L., and Myszka, D.G. (2008). Survey of the year 2007 commercial optical biosensor literature. J Mol Recognit *21*, 355-400.

Roden, L.D., and Myszka, D.G. (1996). Global analysis of a macromolecular interaction measured on BIAcore. Biochem Biophys Res Commun *225*, 1073-1077.

Roos, H., Karlsson, R., Nilshans, H., and Persson, A. (1998). Thermodynamic analysis of protein interactions with biosensor technology. J Mol Recognit *11*, 204-210.

Roovers, R.C., Laeremans, T., Huang, L., De Taeye, S., Verkleij, A.J., Revets, H., de Haard, H.J., and van Bergen en Henegouwen, P.M. (2007a). Efficient inhibition of EGFR signaling and of tumour growth by antagonistic anti-EFGR Nanobodies. Cancer Immunol Immunother *56*, 303-317.

Roovers, R.C., van Dongen, G.A., and van Bergen en Henegouwen, P.M. (2007b). Nanobodies in therapeutic applications. Curr Opin Mol Ther *9*, 327-335.

Roser, M., Fischer, D., and Kissel, T. (1998). Surface-modified biodegradable albumin nano- and microspheres. II: effect of surface charges on in vitro phagocytosis and biodistribution in rats. Eur J Pharm Biopharm *46*, 255-263.

Ryman-Rasmussen, J.P., Riviere, J.E., and Monteiro-Riviere, N.A. (2007). Variables influencing interactions of untargeted quantum dot nanoparticles with skin cells and identification of biochemical modulators. Nano Lett *7*, 1344-1348.

Saerens, D., Frederix, F., Reekmans, G., Conrath, K., Jans, K., Brys, L., Huang, L., Bosmans, E., Maes, G., Borghs, G.*, et al.* (2005a). Engineering camel single-domain antibodies and immobilization chemistry for human prostate-specific antigen sensing. Anal Chem *77*, 7547-7555.

Saerens, D., Pellis, M., Loris, R., Pardon, E., Dumoulin, M., Matagne, A., Wyns, L., Muyldermans, S., and Conrath, K. (2005b). Identification of a universal VHH framework to graft non-canonical antigen-binding loops of camel single-domain antibodies. J Mol Biol *352*, 597-607.

Sampson, J.H., Akabani, G., Archer, G.E., Bigner, D.D., Berger, M.S., Friedman, A.H., Friedman, H.S., Herndon, J.E., 2nd, Kunwar, S., Marcus, S.*, et al.* (2003). Progress report of a Phase I study of the intracerebral microinfusion of a recombinant chimeric protein composed of transforming growth factor (TGF)-alpha and a mutated form of the Pseudomonas exotoxin termed PE-38 (TP-38) for the treatment of malignant brain tumors. J Neurooncol *65*, 27-35.

Sampson, J.H., Archer, G.E., Mitchell, D.A., Heimberger, A.B., and Bigner, D.D. (2008). Tumor-specific immunotherapy targeting the EGFRvIII mutation in patients with malignant glioma. Semin Immunol *20*, 267-275.

Sampson, J.H., Archer, G.E., Mitchell, D.A., Heimberger, A.B., Herndon, J.E., 2nd, Lally-Goss, D., McGehee-Norman, S., Paolino, A., Reardon, D.A., Friedman, A.H.*, et al.* (2009). An epidermal growth factor receptor variant III-targeted vaccine is safe and immunogenic in patients with glioblastoma multiforme. Mol Cancer Ther *8*, 2773-2779.

Sampson, J.H., Crotty, L.E., Lee, S., Archer, G.E., Ashley, D.M., Wikstrand, C.J., Hale, L.P., Small, C., Dranoff, G., Friedman, A.H.*, et al.* (2000). Unarmed, tumor-specific monoclonal antibody effectively treats brain tumors. Proc Natl Acad Sci U S A *97*, 7503-7508.

Sandoval, M.A., Sloat, B.R., Lansakara, P.D., Kumar, A., Rodriguez, B.L., Kiguchi, K., Digiovanni, J., and Cui, Z. (2011). EGFR-targeted stearoyl gemcitabine nanoparticles show enhanced anti-tumor activity. J Control Release.

Saslow, D., Boetes, C., Burke, W., Harms, S., Leach, M.O., Lehman, C.D., Morris, E., Pisano, E., Schnall, M., Sener, S.*, et al.* (2007). American Cancer Society guidelines for breast screening with MRI as an adjunct to mammography. CA Cancer J Clin *57*, 75-89.

Sawant, R.R., Sawant, R.M., Kale, A.A., and Torchilin, V.P. (2008). The architecture of ligand attachment to nanocarriers controls their specific interaction with target cells. J Drug Target *16*, 596-600.

Scatchard, G. (1949). THE ATTRACTIONS OF PROTEINS FOR SMALL MOLECULES AND IONS. Annals of the New York Academy of Sciences *51*, 660-672.

Schellenberger, E.A., Sosnovik, D., Weissleder, R., and Josephson, L. (2004). Magneto/optical annexin V, a multimodal protein. Bioconjug Chem *15*, 1062-1067.

Schlessinger, J. (2002). Ligand-induced, receptor-mediated dimerization and activation of EGF receptor. Cell *110*, 669-672.

Schmiedel, J., Blaukat, A., Li, S., Knochel, T., and Ferguson, K.M. (2008). Matuzumab binding to EGFR prevents the conformational rearrangement required for dimerization. Cancer Cell *13*, 365-373.

Schmitz, K.R., and Ferguson, K.M. (2009). Interaction of antibodies with ErbB receptor extracellular regions. Exp Cell Res *315*, 659-670.

Schnall, M., and Rosen, M. (2006). Primer on imaging technologies for cancer. J Clin Oncol *24*, 3225-3233.

Schnyder, A., and Huwyler, J. (2005). Drug transport to brain with targeted liposomes. NeuroRx *2*, 99-107.

Schreiber, A.B., Libermann, T.A., Lax, I., Yarden, Y., and Schlessinger, J. (1983). Biological role of epidermal growth factor-receptor clustering. Investigation with monoclonal anti-receptor antibodies. J Biol Chem *258*, 846-853.

Schreiber, G. (2002). Kinetic studies of protein-protein interactions. Curr Opin Struct Biol *12*, 41-47.

Schreiber, G., and Fersht, A.R. (1996). Rapid, electrostatically assisted association of proteins. Nat Struct Biol *3*, 427-431.

Schwartz, A.L., Ciechanover, A., Merritt, S., and Turkewitz, A. (1986). Antibody-induced receptor loss. Different fates for asialoglycoproteins and the asialoglycoprotein receptor in HepG2 cells. J Biol Chem *261*, 15225-15232.

Shen, B.J., Hage, T., and Sebald, W. (1996). Global and local determinants for the kinetics of interleukin-4/interleukin-4 receptor alpha chain interaction. A biosensor study employing recombinant interleukin-4-binding protein. Eur J Biochem *240*, 252-261.

Shen, J., Vil, M.D., Jimenez, X., Zhang, H., Iacolina, M., Mangalampalli, V., Balderes, P., Ludwig, D.L., and Zhu, Z. (2007). Single variable domain antibody as a versatile building block for the construction of IgG-like bispecific antibodies. J Immunol Methods *318*, 65-74.

Sheriff, S., and Constantine, K.L. (1996). Redefining the minimal antigen-binding fragment. Nat Struct Biol *3*, 733-736.

Shi, X., Thomas, T.P., Myc, L.A., Kotlyar, A., and Baker, J.R., Jr. (2007). Synthesis, characterization, and intracellular uptake of carboxyl-terminated poly(amidoamine) dendrimer-stabilized iron oxide nanoparticles. Phys Chem Chem Phys *9*, 5712-5720.

Sigismund, S., Woelk, T., Puri, C., Maspero, E., Tacchetti, C., Transidico, P., Di Fiore, P.P., and Polo, S. (2005). Clathrin-independent endocytosis of ubiquitinated cargos. Proc Natl Acad Sci U S A *102*, 2760-2765.

Sivasubramanian, A., Chao, G., Pressler, H.M., Wittrup, K.D., and Gray, J.J. (2006). Structural model of the mAb 806-EGFR complex using computational docking followed by computational and experimental mutagenesis. Structure *14*, 401-414.

Smith, J.S., Tachibana, I., Passe, S.M., Huntley, B.K., Borell, T.J., Iturria, N., O'Fallon, J.R., Schaefer, P.L., Scheithauer, B.W., James, C.D*., et al.* (2001). PTEN mutation, EGFR amplification, and outcome in patients with anaplastic astrocytoma and glioblastoma multiforme. J Natl Cancer Inst *93*, 1246-1256.

Sorkin, A., and Goh, L.K. (2008). Endocytosis and intracellular trafficking of ErbBs. Exp Cell Res *314*, 3093-3106.

Sorkin, A., and Goh, L.K. (2009). Endocytosis and intracellular trafficking of ErbBs. Exp Cell Res *315*, 683-696.

Sorkin, A., Westermark, B., Heldin, C.H., and Claesson-Welsh, L. (1991). Effect of receptor kinase inactivation on the rate of internalization and degradation of PDGF and the PDGF beta-receptor. J Cell Biol *112*, 469-478.

Souriau, C., Rothacker, J., Hoogenboom, H.R., and Nice, E. (2004). Human antibody fragments specific for the epidermal growth factor receptor selected from large non-immunised phage display libraries. Growth Factors *22*, 185-194.

Stenberg, E., Persson, B., Roos, H., and Urbaniczky, C. (1991). Quantitative determination of surface concentration of protein with surface plasmon resonance using radiolabeled proteins. Journal of Colloid and Interface Science *143*, 513-526.

Stevens, S.Y., Sanker, S., Kent, C., and Zuiderweg, E.R. (2001). Delineation of the allosteric mechanism of a cytidylyltransferase exhibiting negative cooperativity. Nat Struct Biol *8*, 947-952.

Stijlemans, B., Conrath, K., Cortez-Retamozo, V., Van Xong, H., Wyns, L., Senter, P., Revets, H., De Baetselier, P., Muyldermans, S., and Magez, S. (2004). Efficient targeting of conserved cryptic epitopes of infectious agents by single domain antibodies. African trypanosomes as paradigm. J Biol Chem *279*, 1256-1261.

Stites, W.E. (1997). Proteinminus signProtein Interactions: Interface Structure, Binding Thermodynamics, and Mutational Analysis. Chem Rev *97*, 1233-1250.

Stummer, W., Pichlmeier, U., Meinel, T., Wiestler, O.D., Zanella, F., and Reulen, H.J. (2006). Fluorescence-guided surgery with 5-aminolevulinic acid for resection of malignant glioma: a randomised controlled multicentre phase III trial. Lancet Oncol *7*, 392-401.

Sugawa, N., Ekstrand, A.J., James, C.D., and Collins, V.P. (1990). Identical splicing of aberrant epidermal growth factor receptor transcripts from amplified rearranged genes in human glioblastomas. Proc Natl Acad Sci U S A *87*, 8602-8606.

Sun, C., Sze, R., and Zhang, M. (2006). Folic acid-PEG conjugated superparamagnetic nanoparticles for targeted cellular uptake and detection by MRI. J Biomed Mater Res A *78*, 550-557.

Sun, C., Veiseh, O., Gunn, J., Fang, C., Hansen, S., Lee, D., Sze, R., Ellenbogen, R.G., Olson, J., and Zhang, M. (2008). In vivo MRI detection of gliomas by chlorotoxin-conjugated superparamagnetic nanoprobes. Small *4*, 372-379.

Sung, C.K., Hong, K.A., Lin, S., Lee, Y., Cha, J., Lee, J.K., Hong, C.P., Han, B.S., Jung, S.I., Kim, S.H.*, et al.* (2009). Dual-modal nanoprobes for imaging of mesenchymal stem cell transplant by MRI and fluorescence imaging. Korean J Radiol *10*, 613-622.

Takahashi, H., Herlyn, D., Atkinson, B., Powe, J., Rodeck, U., Alavi, A., Bruce, D.A., and Koprowski, H. (1987). Radioimmunodetection of human glioma xenografts by monoclonal antibody to epidermal growth factor receptor. Cancer Res *47*, 3847-3850.

Tan, P.H., Manunta, M., Ardjomand, N., Xue, S.A., Larkin, D.F., Haskard, D.O., Taylor, K.M., and George, A.J. (2003). Antibody targeted gene transfer to endothelium. J Gene Med *5*, 311-323.

Tanford, C. (1978). The hydrophobic effect and the organization of living matter. Science *200*, 1012-1018.

Tang, C., Iwahara, J., and Clore, G.M. (2006). Visualization of transient encounter complexes in protein-protein association. Nature *444*, 383-386.

Tang, C.K., Gong, X.Q., Moscatello, D.K., Wong, A.J., and Lippman, M.E. (2000). Epidermal growth factor receptor vIII enhances tumorigenicity in human breast cancer. Cancer Res *60*, 3081-3087.

Teh, Y.H., and Kavanagh, T.A. (2010). High-level expression of Camelid nanobodies in Nicotiana benthamiana. Transgenic Res *19*, 575-586.

Teis, D., and Huber, L.A. (2003). The odd couple: signal transduction and endocytosis. Cell Mol Life Sci *60*, 2020-2033.

Teramura, Y., Ichinose, J., Takagi, H., Nishida, K., Yanagida, T., and Sako, Y. (2006). Single-molecule analysis of epidermal growth factor binding on the surface of living cells. EMBO J *25*, 4215-4222.

Tereshko, V., Uysal, S., Koide, A., Margalef, K., Koide, S., and Kossiakoff, A.A. (2008). Toward chaperone-assisted crystallography: protein engineering enhancement of crystal packing and X-ray phasing capabilities of a camelid single-domain antibody (VHH) scaffold. Protein Sci *17*, 1175-1187.

Thomassen, Y.E., Verkleij, A.J., Boonstra, J., and Verrips, C.T. (2005). Specific production rate of VHH antibody fragments by Saccharomyces cerevisiae is correlated with growth rate, independent of nutrient limitation. J Biotechnol *118*, 270-277.

Thomson, J., Liu, Y., Sturtevant, J.M., and Quiocho, F.A. (1998). A thermodynamic study of the binding of linear and cyclic oligosaccharides to the maltodextrin-binding protein of Escherichia coli. Biophys Chem *70*, 101-108.

Thurber, G.M., Schmidt, M.M., and Wittrup, K.D. (2008). Factors determining antibody distribution in tumors. Trends Pharmacol Sci *29*, 57-61.

Tobi, D., and Bahar, I. (2005). Structural changes involved in protein binding correlate with intrinsic motions of proteins in the unbound state. Proc Natl Acad Sci U S A *102*, 18908-18913.

Todd, M.J., Luque, I., Velazquez-Campoy, A., and Freire, E. (2000). Thermodynamic basis of resistance to HIV-1 protease inhibition: calorimetric analysis of the V82F/I84V active site resistant mutant. Biochemistry *39*, 11876-11883.

Tomayko, M.M., and Reynolds, C.P. (1989). Determination of subcutaneous tumor size in athymic (nude) mice. Cancer Chemother Pharmacol *24*, 148-154.

Torchilin, V. (2011). Tumor delivery of macromolecular drugs based on the EPR effect. Adv Drug Deliv Rev *63*, 131-135.

Torchilin, V.P. (2010). Passive and active drug targeting: drug delivery to tumors as an example. Handb Exp Pharmacol, 3-53.

Transue, T.R., De Genst, E., Ghahroudi, M.A., Wyns, L., and Muyldermans, S. (1998). Camel single-domain antibody inhibits enzyme by mimicking carbohydrate substrate. Proteins *32*, 515-522.

Tseng, C.L., Wang, T.W., Dong, G.C., Yueh-Hsiu Wu, S., Young, T.H., Shieh, M.J., Lou, P.J., and Lin, F.H. (2007). Development of gelatin nanoparticles with biotinylated EGF conjugation for lung cancer targeting. Biomaterials *28*, 3996-4005.

Tsutsui, Y., Tomizawa, K., Nagita, M., Michiue, H., Nishiki, T., Ohmori, I., Seno, M., and Matsui, H. (2007). Development of bionanocapsules targeting brain tumors. J Control Release *122*, 159-164.

Tynan, C.J., Roberts, S.K., Rolfe, D.J., Clarke, D.T., Loeffler, H.H., Kastner, J., Winn, M.D., Parker, P.J., and Martin-Fernandez, M.L. (2011). Human epidermal growth factor receptor (EGFR) aligned on the plasma membrane adopts key features of Drosophila EGFR asymmetry. Mol Cell Biol *31*, 2241-2252.

Tzeng, S.R., and Kalodimos, C.G. (2009). Dynamic activation of an allosteric regulatory protein. Nature *462*, 368-372.

Udenfriend, S., Stein, S., Bohlen, P., Dairman, W., Leimgruber, W., and Weigele, M. (1972). Fluorescamine: a reagent for assay of amino acids, peptides, proteins, and primary amines in the picomole range. Science *178*, 871-872.

Ullrich, A., Coussens, L., Hayflick, J.S., Dull, T.J., Gray, A., Tam, A.W., Lee, J., Yarden, Y., Libermann, T.A., Schlessinger, J*., et al.* (1984). Human epidermal growth factor receptor cDNA sequence and aberrant expression of the amplified gene in A431 epidermoid carcinoma cells. Nature *309*, 418-425.

Vajkoczy, P., and Menger, M.D. (2000). Vascular microenvironment in gliomas. J Neurooncol *50*, 99-108.

Valdes, P.A., Fan, X., Ji, S., Harris, B.T., Paulsen, K.D., and Roberts, D.W. (2009). Estimation of Brain Deformation for Volumetric Image Updating in Protoporphyrin IX Fluorescence-Guided Resection. Stereotact Funct Neurosurg *88*, 1-10.

Van de Broek, B., Devoogdt, N., D'Hollander, A., Gijs, H.L., Jans, K., Lagae, L., Muyldermans, S., Maes, G., and Borghs, G. (2011). Specific cell targeting with nanobody conjugated branched gold nanoparticles for photothermal therapy. ACS Nano *5*, 4319-4328.

van der Linden, R.H., de Geus, B., Frenken, G.J., Peters, H., and Verrips, C.T. (2000). Improved production and function of llama heavy chain antibody fragments by molecular evolution. J Biotechnol *80*, 261-270.

van der Merwe, P.A. (2000). Surface Plasmon Resonance in Protein-Ligand Interactons: A Practical Approach. Oxford University Press.

Van Regenmortel, M.H., Altschuh, D., Chatellier, J., Christensen, L., Rauffer-Bruyere, N., Richalet-Secordel, P., Witz, J., and Zeder-Lutz, G. (1998). Measurement of antigen-antibody interactions with biosensors. J Mol Recognit *11*, 163-167.

Vaneycken, I., Govaert, J., Vincke, C., Caveliers, V., Lahoutte, T., De Baetselier, P., Raes, G., Bossuyt, A., Muyldermans, S., and Devoogdt, N. (2010). In vitro analysis and in vivo tumor targeting of a humanized, grafted nanobody in mice using pinhole SPECT/micro-CT. J Nucl Med *51*, 1099-1106.

Varallyay, P., Nesbit, G., Muldoon, L.L., Nixon, R.R., Delashaw, J., Cohen, J.I., Petrillo, A., Rink, D., and Neuwelt, E.A. (2002). Comparison of two superparamagnetic viral-sized iron oxide particles ferumoxides and ferumoxtran-10 with a gadolinium chelate in imaging intracranial tumors. AJNR Am J Neuroradiol *23*, 510-519.

Veiseh, O., Gunn, J.W., Kievit, F.M., Sun, C., Fang, C., Lee, J.S., and Zhang, M. (2009). Inhibition of tumor-cell invasion with chlorotoxin-bound superparamagnetic nanoparticles. Small *5*, 256-264.

Veiseh, O., Sun, C., Gunn, J., Kohler, N., Gabikian, P., Lee, D., Bhattarai, N., Ellenbogen, R., Sze, R., Hallahan, A.*, et al.* (2005). Optical and MRI multifunctional nanoprobe for targeting gliomas. Nano Lett *5*, 1003-1008.

Verma, A., and Stellacci, F. (2010). Effect of surface properties on nanoparticle-cell interactions. Small *6*, 12-21.

Veronese, F.M., and Pasut, G. (2005). PEGylation, successful approach to drug delivery. Drug Discov Today *10*, 1451-1458.

Vincke, C., Loris, R., Saerens, D., Martinez-Rodriguez, S., Muyldermans, S., and Conrath, K. (2009). General strategy to humanize a camelid single-domain antibody and identification of a universal humanized nanobody scaffold. J Biol Chem *284*, 3273-3284.

von Maltzahn, G., Ren, Y., Park, J.H., Min, D.H., Kotamraju, V.R., Jayakumar, J., Fogal, V., Sailor, M.J., Ruoslahti, E., and Bhatia, S.N. (2008). In vivo tumor cell targeting with "click" nanoparticles. Bioconjug Chem *19*, 1570-1578.

Vonarbourg, A., Passirani, C., Saulnier, P., and Benoit, J.P. (2006). Parameters influencing the stealthiness of colloidal drug delivery systems. Biomaterials *27*, 4356-4373.

Vu, K.B., Ghahroudi, M.A., Wyns, L., and Muyldermans, S. (1997). Comparison of llama VH sequences from conventional and heavy chain antibodies. Mol Immunol *34*, 1121-1131.

Wade, J.D., Domagala, T., Rothacker, J., Catimel, B., and Nice, E. (2001). Use of thiazolidine-mediated ligation for site specific biotinylation of mouse EGF for biosensor immobilisation. Letters in Peptide Science *8*, 211-220.

Waksal, H.W. (1999). Role of an anti-epidermal growth factor receptor in treating cancer. Cancer Metastasis Rev *18*, 427-436.

Wang, A.Z., Langer, R., and Farokhzad, O.C. (2012). Nanoparticle delivery of cancer drugs. Annu Rev Med *63*, 185-198.

Wang, M., and Thanou, M. (2010). Targeting nanoparticles to cancer. Pharmacol Res *62*, 90-99.

Wang, Y.X., Hussain, S.M., and Krestin, G.P. (2001). Superparamagnetic iron oxide contrast agents: physicochemical characteristics and applications in MR imaging. Eur Radiol *11*, 2319-2331.

Wells, A. (1999). EGF receptor. Int J Biochem Cell Biol *31*, 637-643.

Wenger, Y., Schneider, R.J., 2nd, Reddy, G.R., Kopelman, R., Jolliet, O., and Philbert, M.A. (2011). Tissue distribution and pharmacokinetics of stable polyacrylamide nanoparticles following intravenous injection in the rat. Toxicol Appl Pharmacol *251*, 181-190.

Whitesides, G.M., and Krishnamurthy, V.M. (2005). Designing ligands to bind proteins. Q Rev Biophys *38*, 385-395.

Wikstrand, C.J., Hale, L.P., Batra, S.K., Hill, M.L., Humphrey, P.A., Kurpad, S.N., McLendon, R.E., Moscatello, D., Pegram, C.N., Reist, C.J.*, et al.* (1995). Monoclonal antibodies against EGFRvIII are tumor specific and react with breast and lung carcinomas and malignant gliomas. Cancer Res *55*, 3140-3148.

Wikstrand, C.J., McLendon, R.E., Friedman, A.H., and Bigner, D.D. (1997). Cell surface localization and density of the tumor-associated variant of the epidermal growth factor receptor, EGFRvIII. Cancer Res *57*, 4130-4140.

Wiley, H.S., Shvartsman, S.Y., and Lauffenburger, D.A. (2003). Computational modeling of the EGF-receptor system: a paradigm for systems biology. Trends Cell Biol *13*, 43-50.

Williams, D.H., O'Brien, D.P., Sandercock, A.M., and Stephens, E. (2004). Order changes within receptor systems upon ligand binding: receptor tightening/oligomerisation and the interpretation of binding parameters. J Mol Biol *340*, 373-383.

Willuda, J., Kubetzko, S., Waibel, R., Schubiger, P.A., Zangemeister-Wittke, U., and Pluckthun, A. (2001). Tumor targeting of mono-, di-, and tetravalent anti-p185(HER-2) miniantibodies multimerized by self-associating peptides. J Biol Chem *276*, 14385-14392.

Wilson, K.J., Gilmore, J.L., Foley, J., Lemmon, M.A., and Riese, D.J., 2nd (2009). Functional selectivity of EGF family peptide growth factors: implications for cancer. Pharmacol Ther *122*, 1-8.

Winkler, M.E., O'Connor, L., Winget, M., and Fendly, B. (1989). Epidermal growth factor and transforming growth factor alpha bind differently to the epidermal growth factor receptor. Biochemistry *28*, 6373-6378.

Wiogo, H.T., Lim, M., Bulmus, V., Yun, J., and Amal, R. (2011). Stabilization of magnetic iron oxide nanoparticles in biological media by fetal bovine serum (FBS). Langmuir *27*, 843-850.

Wohlfart, S., Gelperina, S., and Kreuter, J. (2011). Transport of drugs across the blood-brain barrier by nanoparticles. J Control Release.

Wong, A.J., Ruppert, J.M., Bigner, S.H., Grzeschik, C.H., Humphrey, P.A., Bigner, D.S., and Vogelstein, B. (1992). Structural alterations of the epidermal growth factor receptor gene in human gliomas. Proc Natl Acad Sci U S A *89*, 2965-2969.

Wu, J.L., Abe, T., Inoue, R., Fujiki, M., and Kobayashi, H. (2004). IkappaBalphaM suppresses angiogenesis and tumorigenesis promoted by a constitutively active mutant EGFR in human glioma cells. Neurol Res *26*, 785-791.

Wu, S.H., Lin, C.Y., Hung, Y., Chen, W., Chang, C., and Mou, C.Y. (2011). PEGylated silica nanoparticles encapsulating multiple magnetite nanocrystals for high-performance microscopic magnetic resonance angiography. J Biomed Mater Res B Appl Biomater *99*, 81-88.

Xie, H., Zhu, Y., Jiang, W., Zhou, Q., Yang, H., Gu, N., Zhang, Y., Xu, H., and Yang, X. (2011). Lactoferrin-conjugated superparamagnetic iron oxide nanoparticles as a specific MRI contrast agent for detection of brain glioma in vivo. Biomaterials *32*, 495-502.

Xie, J., Chen, K., Huang, J., Lee, S., Wang, J., Gao, J., Li, X., and Chen, X. (2010). PET/NIRF/MRI triple functional iron oxide nanoparticles. Biomaterials *31*, 3016-3022.

Xie, J., Chen, K., Lee, H.Y., Xu, C., Hsu, A.R., Peng, S., Chen, X., and Sun, S. (2008). Ultrasmall c(RGDyK)-coated Fe3O4 nanoparticles and their specific targeting to integrin alpha(v)beta3-rich tumor cells. J Am Chem Soc *130*, 7542-7543.

Xie, J., Huang, J., Li, X., Sun, S., and Chen, X. (2009). Iron oxide nanoparticle platform for biomedical applications. Curr Med Chem *16*, 1278-1294.

Xiong, C.Y., Natarajan, A., Shi, X.B., Denardo, G.L., and Denardo, S.J. (2006). Development of tumor targeting anti-MUC-1 multimer: effects of di-scFv unpaired cysteine location on PEGylation and tumor binding. Protein Eng Des Sel *19*, 359-367.

Xu, Y.H., Richert, N., Ito, S., Merlino, G.T., and Pastan, I. (1984). Characterization of epidermal growth factor receptor gene expression in malignant and normal human cell lines. Proc Natl Acad Sci U S A *81*, 7308-7312.

Yamazaki, H., Fukui, Y., Ueyama, Y., Tamaoki, N., Kawamoto, T., Taniguchi, S., and Shibuya, M. (1988). Amplification of the structurally and functionally altered epidermal growth factor receptor gene (c-erbB) in human brain tumors. Mol Cell Biol *8*, 1816-1820.

Yamazaki, H., Ohba, Y., Tamaoki, N., and Shibuya, M. (1990). A deletion mutation within the ligand binding domain is responsible for activation of epidermal growth factor receptor gene in human brain tumors. Jpn J Cancer Res *81*, 773-779.

Yamoutpour, F., Bodempudi, V., Park, S.E., Pan, W., Mauzy, M.J., Kratzke, R.A., Dudek, A., Potter, D.A., Woo, R.A., O'Rourke, D.M.*, et al.* (2008). Gene silencing for epidermal growth factor receptor variant III induces cell-specific cytotoxicity. Mol Cancer Ther *7*, 3586-3597.

Yang, J., Gunn, J., Dave, S.R., Zhang, M., Wang, Y.A., and Gao, X. (2008). Ultrasensitive detection and molecular imaging with magnetic nanoparticles. Analyst *133*, 154-160.

Yang, K., Basu, A., Wang, M., Chintala, R., Hsieh, M.C., Liu, S., Hua, J., Zhang, Z., Zhou, J., Li, M.*, et al.* (2003). Tailoring structure-function and pharmacokinetic properties of single-chain Fv proteins by site-specific PEGylation. Protein Eng *16*, 761-770.

Yang, L., Mao, H., Cao, Z., Wang, Y.A., Peng, X., Wang, X., Sajja, H.K., Wang, L., Duan, H., Ni, C.*, et al.* (2009a). Molecular imaging of pancreatic cancer in an animal model using targeted multifunctional nanoparticles. Gastroenterology *136*, 1514-1525 e1512.

Yang, L., Mao, H., Wang, Y.A., Cao, Z., Peng, X., Wang, X., Duan, H., Ni, C., Yuan, Q., Adams, G.*, et al.* (2009b). Single chain epidermal growth factor receptor antibody conjugated nanoparticles for in vivo tumor targeting and imaging. Small *5*, 235-243.

Yang, L., Peng, X.H., Wang, Y.A., Wang, X., Cao, Z., Ni, C., Karna, P., Zhang, X., Wood, W.C., Gao, X.*, et al.* (2009c). Receptor-targeted nanoparticles for in vivo imaging of breast cancer. Clin Cancer Res *15*, 4722-4732.

Yarden, Y. (2001). The EGFR family and its ligands in human cancer. signalling mechanisms and therapeutic opportunities. Eur J Cancer *37 Suppl 4*, S3-8.

Yarden, Y., and Sliwkowski, M.X. (2001). Untangling the ErbB signalling network. Nat Rev Mol Cell Biol *2*, 127-137.

Yoshimoto, K., Dang, J., Zhu, S., Nathanson, D., Huang, T., Dumont, R., Seligson, D.B., Yong, W.H., Xiong, Z., Rao, N.*, et al.* (2008). Development of a real-time RT-PCR assay for detecting EGFRvIII in glioblastoma samples. Clin Cancer Res *14*, 488-493.

Yu, X., Sharma, K.D., Takahashi, T., Iwamoto, R., and Mekada, E. (2002). Ligand-independent dimer formation of epidermal growth factor receptor (EGFR) is a step separable from ligand-induced EGFR signaling. Mol Biol Cell *13*, 2547-2557.

Zeder-Lutz, G., Zuber, E., Witz, J., and Van Regenmortel, M.H. (1997). Thermodynamic analysis of antigen-antibody binding using biosensor measurements at different temperatures. Anal Biochem *246*, 123-132.

Zhang, J., MacKenzie, R., and Durocher, Y. (2009). Production of chimeric heavy-chain antibodies. Methods Mol Biol *525*, 323-336, xv.

Zhang, J., Tanha, J., Hirama, T., Khieu, N.H., To, R., Tong-Sevinc, H., Stone, E., Brisson, J.R., and MacKenzie, C.R. (2004). Pentamerization of single-domain antibodies from phage libraries: a novel strategy for the rapid generation of high-avidity antibody reagents. J Mol Biol *335*, 49-56.

Zhang, X., Gureasko, J., Shen, K., Cole, P.A., and Kuriyan, J. (2006). An allosteric mechanism for activation of the kinase domain of epidermal growth factor receptor. Cell *125*, 1137-1149.

Zhang, Y., Zhu, C., and Pardridge, W.M. (2002). Antisense gene therapy of brain cancer with an artificial virus gene delivery system. Mol Ther *6*, 67-72.

Zhou, M., Felder, S., Rubinstein, M., Hurwitz, D.R., Ullrich, A., Lax, I., and Schlessinger, J. (1993). Real-time measurements of kinetics of EGF binding to soluble EGF receptor monomers and dimers support the dimerization model for receptor activation. Biochemistry *32*, 8193-8198.

Zhou, Y., Drummond, D.C., Zou, H., Hayes, M.E., Adams, G.P., Kirpotin, D.B., and Marks, J.D. (2007). Impact of single-chain Fv antibody fragment affinity on nanoparticle targeting of epidermal growth factor receptor-expressing tumor cells. J Mol Biol *371*, 934-947.

Zhu, X.F., Liu, Z.C., Xie, B.F., Li, Z.M., Feng, G.K., Yang, D., and Zeng, Y.X. (2001). EGFR tyrosine kinase inhibitor AG1478 inhibits cell proliferation and arrests cell cycle in nasopharyngeal carcinoma cells. Cancer Lett *169*, 27-32.

Zolnik, B.S., and Sadrieh, N. (2009). Regulatory perspective on the importance of ADME assessment of nanoscale material containing drugs. Adv Drug Deliv Rev *61*, 422-427.

Zuo, Z., Jimenez, X., Witte, L., and Zhu, Z. (2000). An efficient route to the production of an IgG-like bispecific antibody. Protein Eng *13*, 361-367.